LONG-TERM RESPONSE OF SOILS SUBJECTED TO REPETITIVE MECHANICAL LOADS: ENGINEERING IMPLICATIONS

A Thesis
Presented to
The Academic Faculty

by

Junghee Park

In Partial Fulfillment
of the Requirements for the Degree
Doctor of Philosophy in the
School of Civil and Environmental Engineering

Georgia Institute of Technology
May 2018

LONG-TERM RESPONSE OF SOILS SUBJECTED TO REPETITIVE MECHANICAL LOADS: ENGINEERING IMPLICATIONS

Approved by:

Dr. J. Carlos Santamarina, Advisor
School of Civil and Environmental Engineering (Adjunct Professor)
Georgia Institute of Technology

Dr. Susan E. Burns
School of Civil and Environmental Engineering
Georgia Institute of Technology

Dr. J. David Frost
School of Civil and Environmental Engineering
Georgia Institute of Technology

Dr. Guillermo H. Goldsztein
School of Mathematics
Georgia Institute of Technology

Dr. Sheng Dai
School of Civil and Environmental Engineering
Georgia Institute of Technology

Date Approved: December, 7, 2017

The heart of man plans his way,

but the LORD directs his steps (Proverbs 16:9)

ACKNOWLEDGEMENTS

I would like to thank my advisor, Professor J. Carlos Santamarina for his support. Prof. Santamarina is not only an academic advisor, but also a father. I always have been impressed with his great insight, knowledge, patience, generosity, and philosophy of life. I will never forget the time when we edited a manuscript together in a KAUST library.

I would like to express special thanks to an academic advisor, Prof. Jong-Sub Lee for his support. He is more than an advisor to me. I will never forget that he took me to Atlanta in May 2012.

I am also grateful to my thesis committee, Dr. J. David Frost, Dr. Susan E. Burns, Dr. Sheng Dai, and Dr. Guillermo H. Goldsztein, for their valuable comments and feedback on my research.

I would like to thank the members of the Particulate Media Research Laboratory PMRL and Energy GeoEngineering Laboratory EGEL for their help. Special thanks to Dr. Jongmuk Won for being with me and Gabrielle E. Abelskamp for editing this thesis.

Finally, I would like to thank my mother and brother for having always believed in me with sacrifice, support, and endless love. Without their support, I could never have achieved this work.

TABLE OF CONTENTS

LIST OF TABLES

LIST OF FIGURES

SUMMARY

The long-term performance of geo-structures and energy-related geosystems depends on the soil response to all kinds of repetitive loads. These include stress cycles associated with wind, waves, and traffic, cyclic changes in pore fluid chemistry, thermal cycles, drying and wetting sequences, freeze-thaw cycles, and repetitive changes in pore water pressure. This thesis explores the mechanical response of soils (sands-to-fines) subjected to repetitive loading under various boundary conditions. Experimental studies involve various repetitive loading frames. In most cases, the vertical deformation and the shear wave velocity are continuously monitored during ten thousand repetitive loading cycles. The plastic strain accumulation is a function of the initial void ratio, the maximum stress obliquity, and the cyclic stress amplitude; data gathered in this experimental program suggest simple procedures to estimate the potential deformation geostructures may experience when subjected to repetitive mechanical loads. Experimental results show that the void ratio evolves towards the terminal void ratio as the number of load cycles increases. Furthermore, data analyses reveal that the fines in soil mixtures have a marked effect on repetitive loading-induced asymptotic contraction and small strain sediment stiffness even when the fines fraction is significantly lower than the 50% used in the Unified Soil Classification System USCS. Therefore, a Revised Soil Classification System RSCS is proposed herein for engineering purposes by providing a physics-inspired, data-driven approach that benefits from the experience gained in our discipline since the inception of current soil classification systems.

CHAPTER 1

INTRODUCTION

1.1. Motivation

Geotechnical structures often experience a large number of repetitive loading cycles. Then, design must consider the influence of repetitive loads on long-term performance, serviceability, and safety. Examples include energy-related geosystems such as pumped hydro-storage, monopiles-supported wind turbines, compressed air energy storage, and energy piles (Chai and Miura 2002; Peng et al. 2006; Anderson 2009; Pasten and Santamarina 2011).

Repetitive mechanical loads cause the accumulation of permanent deformations when the cyclic strain exceeds the threshold strain. Then, there are associated changes in void ratio, hydraulic conductivity, small strain stiffness, compression index, and friction angle (Youd, 1970; Kelly *et al*., 2006; Achmus *et al*., 2009). Consequently, repetitive mechanical loads can hinder the long-term performance of all kinds of geosystems. Furthermore, the non-linear response in plastic strain ε^{pl} versus the number of cycles challenges geotechnical engineers to accurately predict the permanent strain accumulation ε^{pl}_{acc}.

The goals of this research are to enhance the fundamental understanding of the long-term response of soils (sands-to-fines) subjected to repetitive mechanical loads and to identify the engineering implications and design considerations. The experimental study includes pore-fluid pressure oscillations, different levels of stress amplitude, very large number of cycles, and high-stress amplitude cycles.

1.2 Thesis Organization

The research presented in this thesis centers on the fundamental understanding of the long-term response of soils subjected to repetitive mechanical loads and engineering implications. This thesis consists of five main chapters.

Chapter 2 explores the volumetric and deviatoric response of contractive and dilative sands subjected to repetitive changes in pore water pressure under constant deviatoric stress with various maximum stress obliquities $\eta_{max}=q/p'$. Data analyses place emphasis on the concepts of shakedown, ratcheting, and critical state soil mechanics.

Chapter 3 investigates the quasi-static mechanical response of sands subjected to repetitive loads under zero lateral strain boundary conditions. Data gathered in this experimental program suggests a simple procedure to estimate the potential settlement a shallow foundation may experience when subjected to repetitive mechanical loads.

Chapter 4 examines the possible mechanism for the "tipping-point" observed in load-deformation response data gathered during one million loading cycles. An experimental study conducted for high stress amplitude loading cycles $\Delta\sigma$=2-to-20 MPa advances the understanding of the effect of particle crushing on repeititve loading effects.

Chapter 5 focuses on the long-term response of sand-fines mixtures subjected to repetitive loading under zero-lateral strain conditions. A robust method is proposed to capture the critical role of fines on the engineering properties of soil mixtures and successfully estimate the maximum settlement during repetitive loading.

Chapter 6 proposes a Revised Soil Classification System RSCS for engineering purposes by providing a physics-inspired and data-driven approach.

Chapter 7 summarizes salient conclusions from this study. The three appendices at the end of the thesis provide additional information related to gravimetric-volumetric analysis, additional observations about the Revised Soil Classification System (prepared with Gloria. M. Castro), and a preliminary constitutive model study for soil response under repetititve loading conditions.

CHAPTER 2

SOIL RESPONSE TO REPETITIVE CHANGES IN PORE WATER PRESSURE UNDER DEVIATORIC LOADING

2.1 Introduction

Soils often experience repetitive changes in pore water pressure, such as repetitive rising-and-falling of groundwater levels, tidal action, reservoir operation, pumped hydro storage, and aquifer management to meet water demands (Chu et al. 2003; Orense et al. 2004; Leroueil et al. 2009; Page et al. 2009; Nakata et al. 2013). Repetitive changes in pore water pressure can trigger slope instability, sediment contraction, and even static liquefaction under drained conditions (Olson et al. 2000; Chu et al. 2003; Leroueil et al. 2009; Huang 2016, Chang et al. 2017).

Furthermore, repetitive changes in pore water pressure cause soil volume contractions followed by a reduction in normal effective stress $\sigma'_n=K_o \cdot \sigma'_v$. Consequently, fluid pressure fluctuations lead to the volume change-induced strength loss which affects the potential implications to the traditional pile-soil interfaces, slope stability, aquifer storage and recovery system using pressure injection technique, compressed air energy storage, CO_2 injection and storage.

Soils will gradually deform in responses to repetitive excitations of any kind. Volumetrically, soils evolve towards a unique terminal void ratio e_T and associated internal fabric as the number of loading cycles increases. However, it remains unclear whether a critical state is the terminal void ratio for soils subjected to large-strain repetitive loading cycles (Jardin 1992; Tsuha et al. 2012). On the other hand, the soil

deviatoric response may stabilize at shakedown or continue deforming in ratcheting mode.

In this study, we explore the volumetric and deviatoric responses of contractive and dilative sands subjected to repetitive changes in pore water pressure under constant deviatoric stress with various maximum stress obliquities $\eta_{max}=q/p'$. This study starts with the characterization of the sand used in all tests, followed by the experimental program and test results.

2.2 Experimental Study

2.2.1 Tested Sand

We use the silica "KAUST 20/30 sand" for the study reported in this chapter. Table 2.1 summarizes its main characteristics, including particle shape (i.e. roundness), coefficient of uniformity C_u, and extreme void ratios e_{max} and e_{min}. Particle roundness R and coefficient of uniformity C_u determine the two extreme void ratios; predicted values are included in Table 2.1 for comparison (Youd 1973; Cho et al. 2006).

Let's define the mean effective stress $p'=(\sigma'_1+\sigma'_3)/2$ and the deviatoric stress $q=(\sigma'_1-\sigma'_3)/2$ in terms of the effective axial σ'_1 and confining stress σ'_3, and the stress obliquity as $\eta=q/p'$. Figure 2.1 shows a set of conventional consolidated-undrained CU triaxial test results in the p'-q-e-ε_d space. The critical state parameters for the KAUST 20/30 sand are listed in Table 2.1 (ϕ_{cs}=friction angle at constant volume, λ=slope and Γ=intercept in e-log p'). The critical state friction angle measured on the p'-q projection is $\phi_{cs}=31^o$; for comparison, the critical state friction angle inferred from roundness is $\phi_{cs}=$

$31^o \pm 2^o$, and the simplified angle of repose method shows a value $\phi_{cs}= 32^o$ (Note: refer to Table 2.1 for details).

2.2.2 Experimental Devices and Configuration

The triaxial system used to run repetitive pressure cycles consists of (1) a triaxial cell with a LVDT to track vertical displacement, (2) a loading frame for the application of constant deviatoric stress, and (3) a pressure panel used to generate cyclic changes in pore water pressure and to measure volume changes.

2.2.3 Sample Preparation

We prepare loose, medium-dense, and dense specimens using a combination of raining and tamping techniques to attain different initial relative densities between D_r = 15% and 70%.

2.2.4 Loading Histories

Table 2.2 summarizes the experimental study, and details the initial void ratios e_o, cyclic pressure amplitude Δu_w, and maximum stress obliquities $\eta_{max}=q/p'_{min}$ for all tests. Note that the cyclic pressure amplitudes Δu_w selected in this study are due to the consideration of typical height of tidal action, seasonally-fluctuated ground water level, and change in ground water level caused by reservoir operation (Huang 2016).

For clarity, Figure 2.2 presents a subset of the stress paths explored in this study. The loading history consists of five stages: (1) isotropic consolidation, (2) deviatoric loading to stress obliquity η= 0.33, (3) decrease pore water pressure u_w to reach η= 0.20,

(4) repetitive change in pore water pressure from η= 0.20 to η_{max}= 0.50 for N=100 loading cycles (shown in red), and (5) strain-controlled undrained axial compression from η= 0.20 to failure at a shear rate of ε_d=1%/min. A subset of cases is shown in Figure 2.2.

2.3 Experimental Results: Load-Deformation Response

We report in detail the experimental results for a subset of specimens subjected to repetitive changes in pore water pressure in order to highlight salient trends. Then, we analyze the complete dataset.

2.3.1 Maximum Stress Obliquity η_{max}

Figure 2.3 illustrates the load-deformation response of loose and medium-dense sands subjected to repetitive fluid pressure cycles to different maximum stress obliquities η_{max}=0.33, 0.40, 0.45, and 0.50. In all four specimens, the repetitive change in pore water pressure begins at p_o'= 250 kPa and η_{min}= 0.20 (Refer to Figure 2.2). Results show:

- Pre-loading. The void ratio decreases and the deviatoric strain increases during the applications of constant deviatoric stress σ_d= 100 kPa to stress obliquity η= 0.33, and during the decrease in pore water pressure to reach η= 0.20.
- Repetitive loading. All specimens exhibit (1) dilation in every decrease in mean effective stress from $\eta_{min} \rightarrow \eta_{max}$, but (2) overall contraction at the end of every cycle $i \rightarrow 100$. The fluid pressure oscillation also leads to the increase in deviatoric strain ε_d. The cumulative changes in void ratio and deviatoric strain are more significant as the maximum stress obliquity increases.

- *Undrained shear*. The undrained deviatoric loadings after N=100 loading cycles shows that all specimens reach the critical state line as shown in the p'-q-e space (Figure 2.3). These results confirm that the critical state line is not affected by the repetitive loading history (Taylor 1948; Schofield and Wroth 1968; Castro 1982; Mohamed 1985). Note that the initial void ratios e_o of all specimens were in the contractive zone before the repetitive loading cycles, however specimens subjected to high stress obliquity and large pressure cycles had become denser than critical state before undrained shear.

2.3.2 Confining Effective Stress p_o'

Figure 2.4 shows the p'-q-e-ε_d load-deformation response of three medium-dense specimens subjected to different mean principal stress p_o' (Refer to Figure 2.2 for details of the loading history before the repetitive loading initiates). The changes in void ratio and the deviatoric strain accumulation during the repetitive pressure cycles are more significant as the initial mean effective stress p_o' increases. Once again, all specimens dilate as the pressure increase in every cycle, however, the overall void ratio trend is contractive at the end of every cycle. All three specimens show dilative tendency during the final undrained shear.

2.4 Analyses and Discussion

This section presents a comprehensive analysis of the 14 tests performed in this study (Table 2.2), with emphasis on the accumulation of shear deformation and volume change during repetitive pressure cycles.

2.4.1 Shear Deformation

Shakedown is reached when the shear strain ceases to accumulate. Alternatively, ratcheting implies continued shear strain accumulation. Ratcheting is observed in specimens subjected to large stress amplitudes, and high stress obliquity, and it may be aggravated by fatigue-induced particle crushing (Kolisoja 1998; Werkmeister 2003; Alonso-Marroquin and Herrmann 2004; Werkmeister et al. 2005; Wichtmann et al. 2005; da Fonseca et al. 2013).

Figure 2.5 presents the evolution of the deviatoric strain ε_d with the number of cycles the loose, medium-dense, and dense specimens subjected to pressure cycles to various maximum stress obliquity η_{max} and initial mean effective stress p_o'. A polynomial model is fitted to all test results in Figure 2.5 (modified from Chong and Santamarina 2016):

$$\varepsilon_i^{acc} = \left[\varepsilon_1 + a(1-i^{-b}) - c(1-i^{-1}) + d(i-1)\right]\cdot 10^{-4} \qquad (2.1)$$

where a, b, c, and d are fitting parameters and i is the number of loading cycles. This model allows us to estimate the plastic deviatoric strain accumulation ε_i^{acc} at the end of i^{th} cycle in terms of the shear strain after first cycle ε_1. Shakedown response corresponds to $d = 0$, while ratcheting is matched with $d > 0$. Model parameters for all test conducted as part of this study are summarized in Table 2.2.

Observations. Trends in shear strain accumulations induced by pressure cycles can be summarized as follows:

- Particle level mechanisms such as slip-down and roll-over determine the shear-induced strain accumulation (Ishihara 1996; Mueth et al. 2000; Narsilio and

Santamarina 2008). The plastic shear strain accumulation is more pronounced (1) in earlier cycles (2) in the loose and medium-dense sands (Note: compare accumulation for η_{max} =0.45 and p'$_o$=250 kPa), and (3) for higher maximum obliquity η_{max}.

- The permanent strain accumulation ε_d^{acc} increases with increasing maximum stress obliquity η_{max} at the same p$_o$' and increasing in the mean effective stress p$_o$' with the same η_{max}.
- Loose, medium-dense, and dense specimens with the stress obliquity $0.33 \leq \eta_{max} \leq 0.53$ exhibit shakedown response (d=0). Shakedown is more obvious for smaller η_{max}.
- The dense specimen brought to post critical state conditions during pressure cycles (η_{max}= 0.56 vs. η_{max}= 0.52) exhibits a ratcheting response (d= 2.8×10^{-4}). This is unsustainable: either a sudden failure is anticipated or the specimen generates local and transient negative pore pressure that keeps it within stability conditions.

These observations indicate that plastic shear strain accumulation is a function of the initial void ratio e_o (i.e. initial packing density), maximum stress obliquity η_{max}, and cyclic pressure amplitude Δu_w which determine the features of the shear strain evolution even with a limited number of cycles N=100.

2.4.2 Volume Change

<u>*Evolution of void ratio*</u>. Figure 2.6 presents the evolution of void ratio with the number of cycles for the loose, medium-dense, and dense specimens where pressure cycles start at p'_o=250 kPa and reach different maximum stress obliquity η_{max}. The tendency to contract or dilate depends on the initial void ratio e_o. The highest rate of change in void ratio occurs during earlier cycles and are more pronounced as the maximum stress obliquity

increases. All specimens evolve towards an asymptotic terminal void ratio e_T. A hyperbolic model properly fits all void ratio datasets in terms of the e_i measure after the i_{th} cycle (Park and Santamarina 2017a):

$$e_i = e_T + (e_0 - e_T)\left[1 + \left(\frac{i}{N^*}\right)^m\right]^{-1} \qquad \text{for } m > 0 \tag{2.2}$$

where m is a fitting parameter. The model parameter N^* is the number of cycles required for a given specimen to reach half of the asymptotic volume change $(e_o - e_T)/2$. Model parameters are summarized in Table 2.2 for all tests.

Terminal void ratio. Test results in Figure 2.7 compare the initial void ratio e_o and the terminal void ratio e_T for medium-dense and dense specimens subjected to fluid pressure cycles. The three medium dense-specimens subjected to η_{max}=0.50 contract to reach terminal void ratios that are denser than critical state. On the other hand, the dense specimens dilate particularly for η_{max}=0.53 (Note: the obliquity at critical state is η_{cs}=0.52). The terminal void ratios for the dense and medium-dense specimens do not converge to a single line. Therefore, the balance between slip-down and roll-over deformation mechanism depends on maximum obliquity η_{max} and initial void ratio e_o.

Potential volume change. Results discussed above suggest that the normalized volume change $(e_o - e_T)/(e_o - e_{min})$ caused by fluid pressure cycles depends on the maximum stress obliquity as confirmed in Figure 2.8a. Note that significant volumetric dilations in dense specimens develop when the maximum stress obliquity η_{max} is greater than the critical state stress obliquity η_{cs}=0.52. However, fabric change requires strains above the elastic

threshold. The relevance of strain is explained in Figure 2.8b where volume change data are plotted versus the deviatoric strain measured at the tenth of cycle i=10. Figure 2.8(b) shows a linear relationship between the normalized volume change at terminal density and the shear strain level. Trends suggest that plastic volumetric strain accumulation ε_v^{acc} will occur while shear strain levels exceed the volumetric threshold strain $\varepsilon_{th}|^v = 2\times10^{-4}$ for the tested sand.

Ratio between horizontal-to-vertical plastic strains v^*. The polynomial fitting of shear strain and the hyperbolic fitting of void ratio allow us to compute the incremental plastic shear strain $\Delta\varepsilon_d^{pl}$ and plastic volumetric strain $\Delta\varepsilon_{vol}^{pl}$ between two consecutive cycles i and i+1 without the inherent error magnification in incremental computations with experimental data [Equations 2.1 and 2.2, and Table 2.2]:

$$\Delta\varepsilon_d^{pl}(i) = \varepsilon_d^{pl}(i+1) - \varepsilon_d^{pl}(i) \tag{2.3}$$

$$\Delta\varepsilon_{vol}^{pl}(i) = \frac{e_i - e_{i+1}}{1+e_i} \tag{2.4}$$

The ratio between the incremental horizontal-to-vertical plastic strain v^* in axisymmetric conditions is:

$$v^*(i) = \left.\frac{+\Delta\varepsilon_\perp}{-\Delta\varepsilon_{//}}\right|_{plastic} = -\frac{\Delta\varepsilon_3^{pl}}{\Delta\varepsilon_1^{pl}} = -\frac{\frac{\Delta\varepsilon_{vol}^{pl}(i) - \Delta\varepsilon_d^{pl}(i)}{2}}{\Delta\varepsilon_d^{pl}(i)} = -\frac{1}{2}\left(\frac{\Delta\varepsilon_{vol}^{pl}(i)}{\Delta\varepsilon_d^{pl}(i)} - 1\right) \tag{2.5}$$

Figure 2.9 shows the evolution of the plastic strain ratio v^* for loose, medium-dense, and dense specimens with the number of cycles. A ratio v^*= 0.5 suggests shear deformation at constant volume. A ratio $v^*\rightarrow0$ implies large vertical deformation compared to volume change (i.e. ratcheting). A negative ratio $v^* < 0$ indicates that both

vertical and horizontal contraction take place during repetitive loading, and that volumetric contraction is more dominant than shear deformation (i.e. shakedown).

Bulk skeleton stiffness B. The bulk skeleton stiffness in a cycle relates the imposed isotropic cyclic pressure to the volumetric strain $B = \Delta u_w/\varepsilon_{vol}$. Figure 2.10 plots the average bulk modulus B_{avg} during loading and unloading versus the number of loading cycles. The bulk modulus increases towards an asymptotic value in all case, with some stress obliquity effect. However, the mean effective stress p_o' plays a key role to define a bulk skeleton stiffness.

Shear wave velocity measurements for this sand at different stress levels shows that shear wave velocity V_s [m/s] = $89\text{m/s}(\sigma'_{mean}/1\text{kPa})^{0.21}$. Then, the maximum bulk skeleton stiffness $B_{max} = 2\cdot(V_s^2\rho)(1+\nu)/[3\cdot(1-2\nu)]$ is computed from the shear wave velocity assuming a small-strain Poisson's ratio ν=0.1. The three medium-dense specimens with η_{max} = 0.50 attain an asumptotic bulk skeleton stiffness ratio B_{max}/B_{avg} = 5.1 for p_o'=125 kPa, B_{max}/B_{avg} = 4.3 for p_o'=250 kPa, and B_{max}/B_{avg} = 3.7 for p_o'=375 kPa. These limited results suggest that volumetric strains computed from in-situ shear wave velocity measurements will be lower bound of the volumetric strains the soil experiences even after a large number of pressure cycles.

2.5 Conclusions

Stress obliquity, stress amplitude, and the initial void ratio control the volumetric and deviatoric response of a soil subjected to repetitive changes in pore water pressure under constant shear stress. This study selects the maximum stress obliquities $\eta_{max}=q/p'$

as a variable which affects the evolution of the void ratio and deviatoric strain in contractive and dilative sand specimens. Results suppor the following:

- The void ratio evolves towards the terminal void ratio e_T as the number of load cycles increases. The terminal void ratio is a function of the initial void ratio e_0, stress obliquity η, and cyclic pressure amplitude Δu_w.
- The soil subjected to high stress obliquity and large stress amplitude loading cycles will cross the critical state line *CSL* on *e-p'* space, tend to be denser than *CSL*, and reach a stable deformation state above the *CSL*.
- A new volumetric terminal state develops where slip-down and roll-over are balanced (i.e. constant volume) during repeititve pressure cycles.
- Plastic volumetric strain accumulations ε_v^{acc} will occur until shear strain levels exceed the volumetric threshold strain $\varepsilon_{th}|^v = 2\times10^{-4}$ for the tested sand.
- The accumulation of permanent strain ε_d^{acc} is a function of the stress obliquity η, cyclic pressure amplitude Δu_w, and the initial packing e_o. Shakedown prevails for small pressure amplitudes and at low stress obliquity. Rratcheting is dominant at high stress obliquity and for large stress amplitude cycles.
- The ratio between horizontal-to-vertical plastic strains ν^* captures the evolving shear deformations during volume contractions and expansions.
- The bulk skeleton stiffness evolves towards asymptotic values with the number of cycles. Still, the mean effective stress p_o' plays a key role to define the stiffness asymptote.

Table 2.1 Tested sand - Properties

Property	**KAUST 20/30 sand**	**Observation**	**Reference**
D [mm]	0.60 ~ 0.85		
Roundness R	0.60	Image analysis - Roundness $R = \sum r_i/N$. The average radius of curvature of surface features divided by the radius of the largest inscribed sphere r_{max}.	
C_u	1.20	An equivalent diameter that overlaps on each particle enables to estimate the volume and mass of each particle by the use of specific gravity G_s=2.65. The particle size distribution curve from this analysis results in the coefficient of uniformity C_u=1.20.	
G_s	2.65		
e_{max}	0.786	The estimated maximum void ratios using R=0.60 and C_u = 1.20 is e_{max} = 0.76	ASTM D4253 Youd 1973
e_{min}	0.533	The estimated minimum void ratios using R=0.60 and C_u = 1.20 is e_{min} = 0.46.	ASTM D4254 Youd 1973
ϕ_{cs}	31^o	Friction angle ϕ_{cs}=31^o (i.e. η=0.52). The simplified angle of repose method to estimate the critical state friction angle leads to ϕ_{cs} = 32^o. The critical state friction angle inferred from roundness R=0.60 is ϕ_{cs} = 31^o ± 2^o	Santamarina and Cho 2001 Cho et al. 2006
Γ	0.845	Intercept of *CSL* at 1 kPa in e-log p'	
λ	0.074	Slope of *CSL* in e-log p'	

Table 2.2 Experimental study: Test conditions. Note: fitting parameters correspond to models intodueced in the text.

			Repetitive Loading				CU Test		Void Ratio e (1)				Deviatoric Strain ε_d (2)				
Initial Packing Condition	Test No.	Void ratio after specimen preparation	Maximum Stress Obliquity $\eta_{max}=q/p'_{min}$	q [kPa]	p'_{max} [kPa]	Cyclic Pressure Amplitude Δu_w [kPa]	B-value	Volume change tendency during shear	Initial void ratio e_o	Terminal void ratio e_T	Model parameter m	Characteristic number N^*	Dev. Strain ε_1 at i=1	Model parameter a	Model parameter b	Model parameter c	Ratcheting parameter d
Loose	1	0.7461	0.33	50	250	100	0.972	Contractive	0.7065	0.7000	1.0	49	2.15	700	0.021	24	0
	2	0.7390	0.36	50	250	110	0.981	-	0.7027	0.6960	0.95	43	0.92	900	0.021	14	0
	3	0.7419	0.40	50	250	125	0.976	Contractive	0.7031	0.6878	1.0	22	16	2200	0.021	50	0
Medium dense	4	0.7208	0.45	50	250	140	0.977	Dilative	0.6828	0.6621	0.85	19	35	3900	0.021	93	0
	5	0.7092	0.50	50	250	150	0.976	Dilative	0.6722	0.6448	0.88	19	56	6300	0.020	100	0
	6	0.6958	0.50	25	125	75	0.984	Dilative	0.6783	0.6598	1.0	26	21	4600	0.022	120	0
	7	0.7180	0.50	75	375	225	0.981	Dilative	0.6660	0.6361	0.79	13	58	6500	0.020	0	0
Dense	8	0.6138	0.26	50	250	55	0.950		0.5900	0.5915	0.9	1	0.05	10	0.040	0.3	0
	9	0.6171	0.30	50	250	85	0.952	-	0.6021	0.6032	1.0	1	0.03	10	0.017	0	0
	10	0.6151	0.40	50	250	125	0.951	-	0.6015	0.6030	0.9	1	0.07	55	0.016	1	0
	11	0.6196	0.45	50	250	140	0.966	Dilative	0.6025	0.6029	1.0	1	16	650	0.016	2	0
	12	0.6145	0.52	50	250	153	0.977	Dilative	0.6000	0.6008	1.0	1	19	650	0.015	0	0
	13	0.6133	0.53	50	250	155	0.965	-	0.5965	0.6052	1.0	7	9	900	0.015	0	0
	14	0.6200	0.56	50	250	160	0.967	-	0.6032	0.6415	1.0	24	15	1000	0.050	0	2.8

Note: (1) Hyperbolic model: $e_i=e_T+(e_o-e_T)[1+(i/N^*)^m]^{-1}$

(2) Polynomial model: $\varepsilon_i^{acc}=[\varepsilon_1+a(1-i^{-b})-c(1-i^{-1})-d(1-i)]\cdot 10^{-4}$

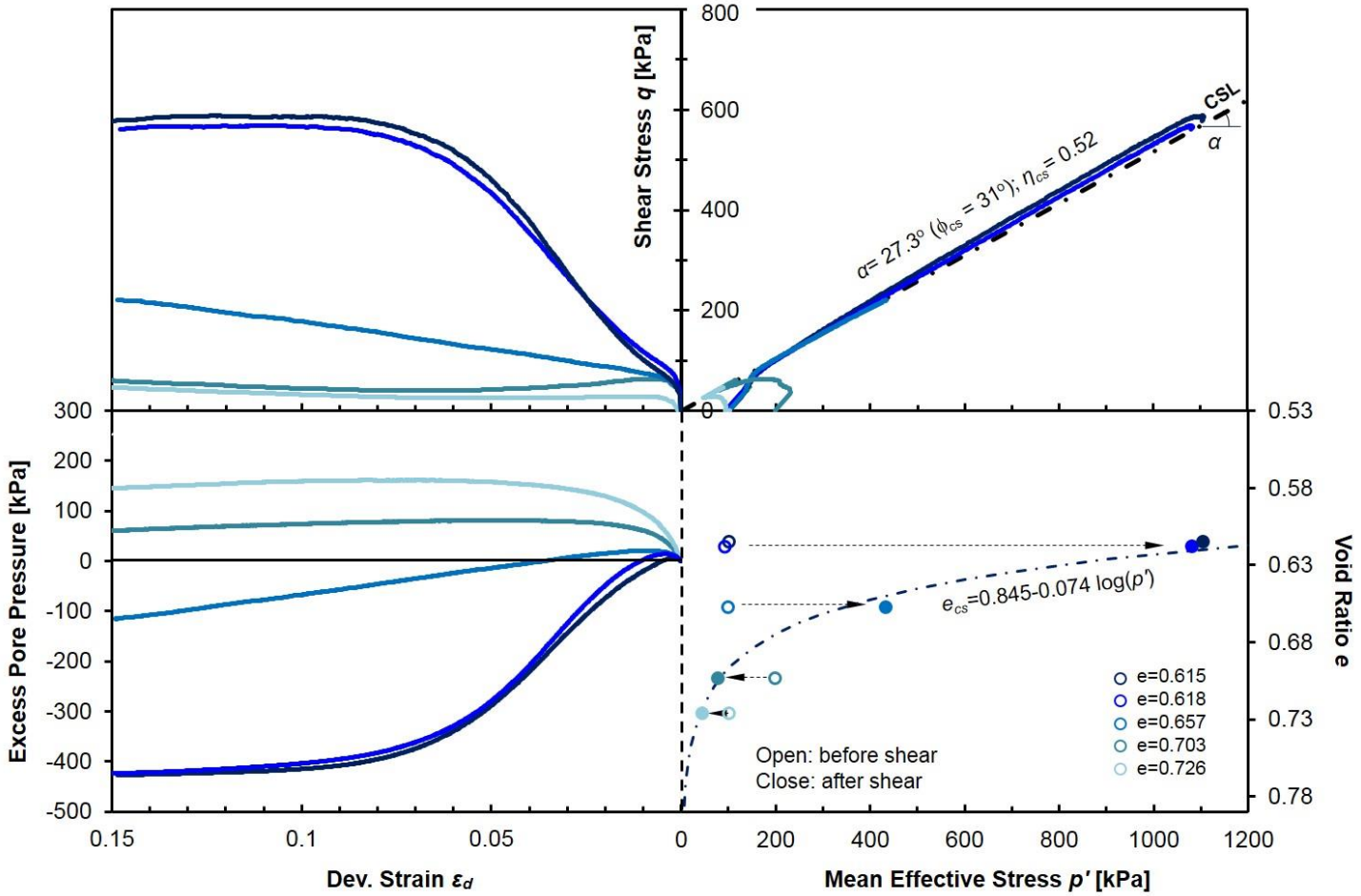

Figure 2.1 Conventional consolidated-undrained CU triaxial test results in p'-q-e-ε_d space (Shear rate: ε_d=1%/min). Notation: $p'=(\sigma_1'+\sigma_3')/2$, $q=(\sigma_1'-\sigma_3')/2$, $\phi_{cs}=\sin^{-1}(\tan\alpha)$, and stress obliquity $\eta=q/p'$. Critical state parameters for the KAUST 20/30 sand: Friction angle ϕ_{cs}=31°, intercept of CSL at 1 kPa in e-log p' = 0.845, and slope of CSL in e-logp' = 0.074. For reference, the maximum and minimum void ratios are e_{max}=0.786 and e_{min}=0.533.

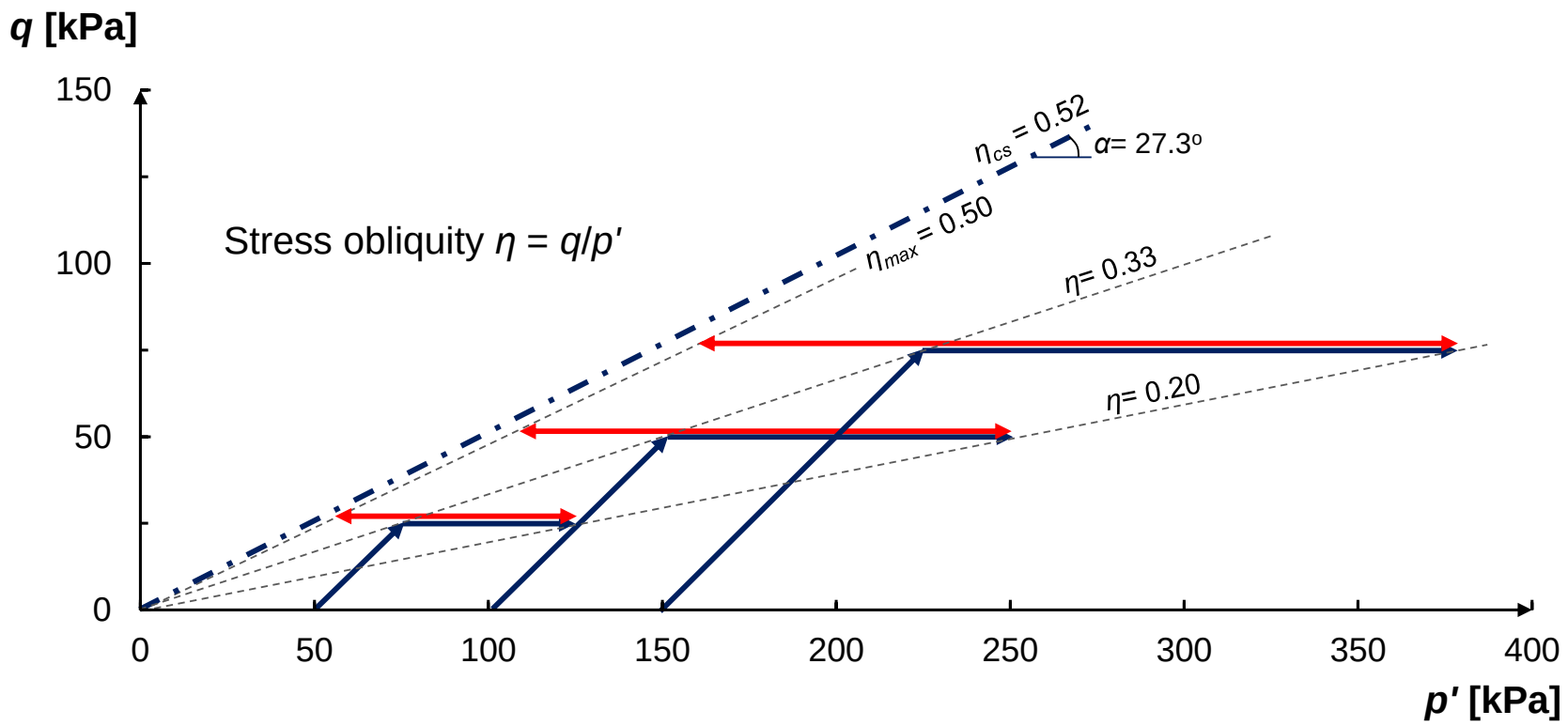

Figure 2.2 Stress paths on the p'-q space (Note: a subset of cases shown here – Refer to Table 2.1 for a complete description). The loading history consists of five stages: (1) isotropic consolidation, (2) deviatoric loading to stress obliquity η= 0.33, (3) decrease pore water pressure u_w to reach η= 0.20, (4) repetitive change in pore water pressure from η= 0.20 to η_{max}= 0.50 (shown in red), and (5) strain-controlled undrained axial compression from η= 0.20 to failure at a shear rate of ε_d=1%/min. Notation: p'=(σ_1'+σ_3')/2, q=(σ_1'-σ_3')/2, ϕ_{cs}=$\sin^{-1}$(tanα), and stress obliquity η=q/p'.

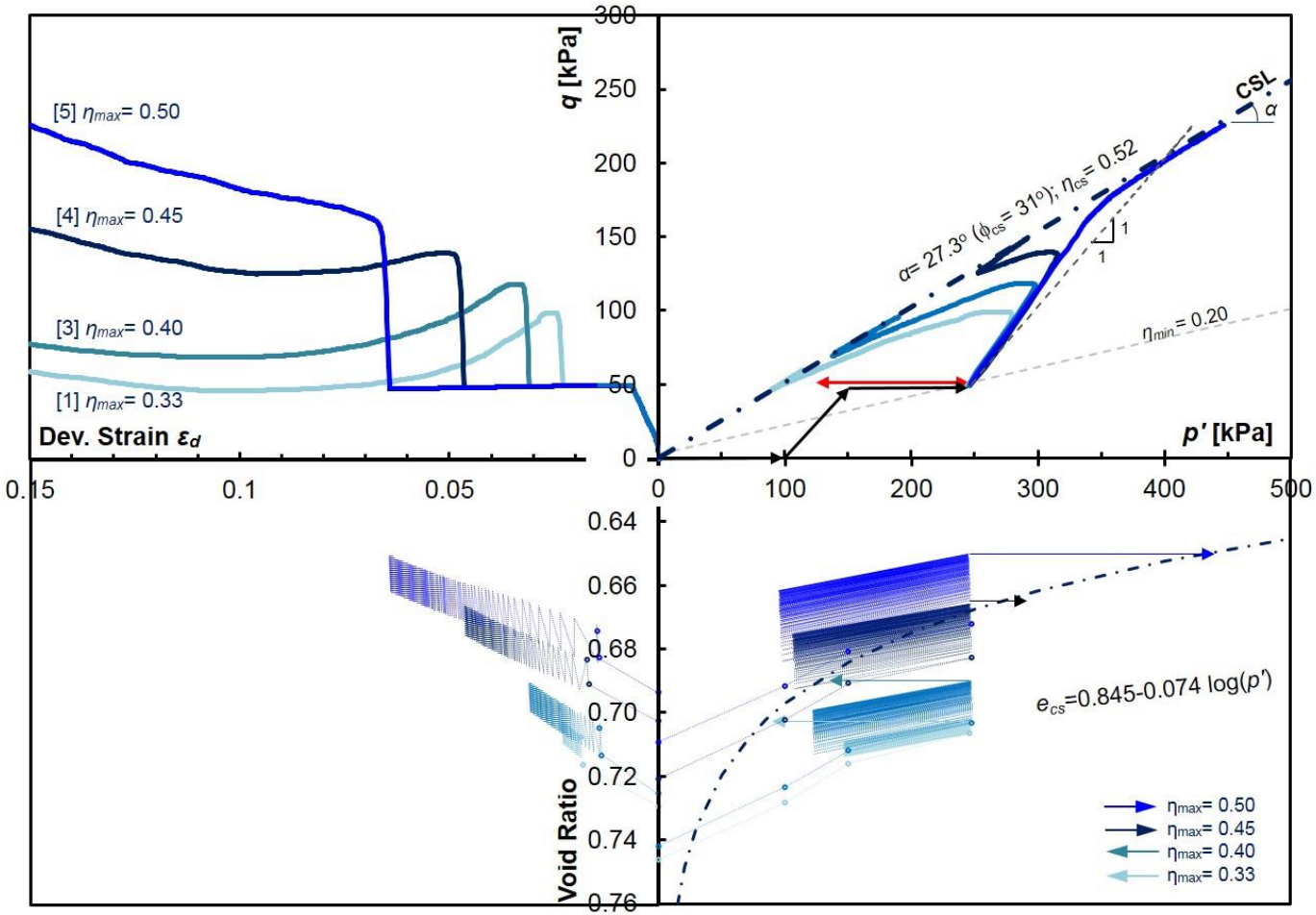

Figure 2.3 Maximum stress obliquity: Loose and medium dense sands subjected to repetitive fluid pressure cycles to different maximum stress obliquities η_{max}. In all four specimens, the pressure cycles begin at p'=250 kPa and η_{min}=0.20. Tests end with undrained axial compression from the same initial stress condition at η_{min}=0.20. Notation: $p'=(\sigma_1'+\sigma_3')/2$, $q=(\sigma_1'-\sigma_3')/2$, $\phi_{cs}=\sin^{-1}(\tan\alpha)$, and stress obliquity $\eta=q/p'$. [ ] indicates the Test No. 1, 3, 4, and 5 in Table 2.2.

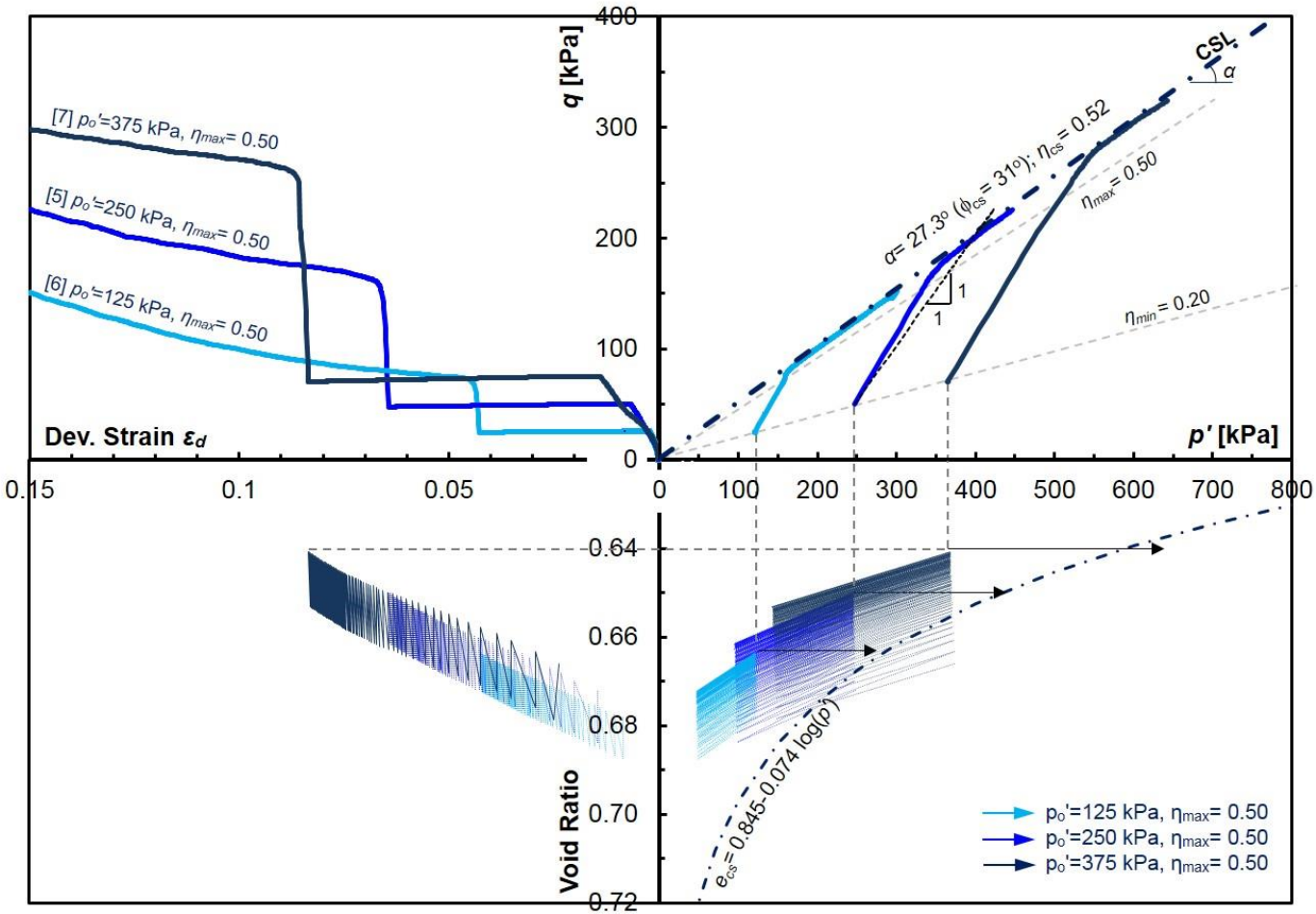

Figure 2.4 Confining effective stress: Medium dense sand specimens subjected to repetitive fluid pressure cycles between η_{min}=0.20 and η_{max}=0.50. Tests end with undrained axial compression from the same obliquity η_{min}=0.20. Figure 2.2 shows all stress paths in detail. Notation: $p'=(\sigma_1'+\sigma_3')/2$, $q=(\sigma_1'-\sigma_3')/2$, $\phi_{cs}=\sin^{-1}(\tan\alpha)$, and stress obliquity $\eta=q/p'$. [ ] indicates the Test No. 5, 6, 7 in Table 2.2.

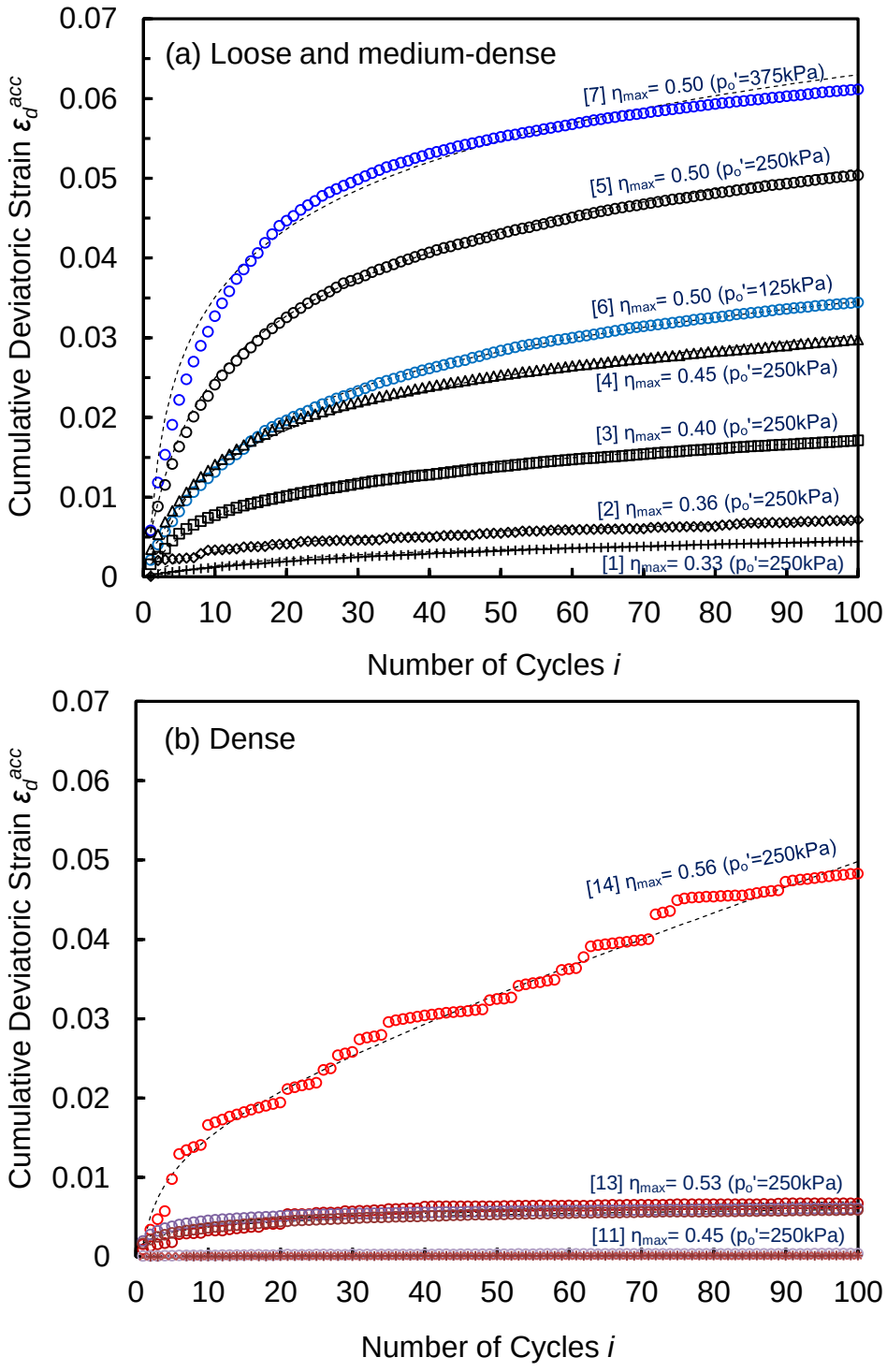

Figure 2.5 Shear Deformation: Cumulative deviatoric strain ε_d^{acc} vs. number of cycles: (a) Loose and medium-dense specimens; (b) Dense specimens. The initial mean effective stress p_o' and the maximum stress obliquity η_{max} are indicated in each case. The minimum stress obliquity is η_{min}=0.20 for all tests. Dotted lines: polynomial model fitted to test results (model parameters are summarized in Table 2.1). Note the obliquity at critical state is η_{cs}=0.52. [ ] indicates the Test No. in Table 2.2.

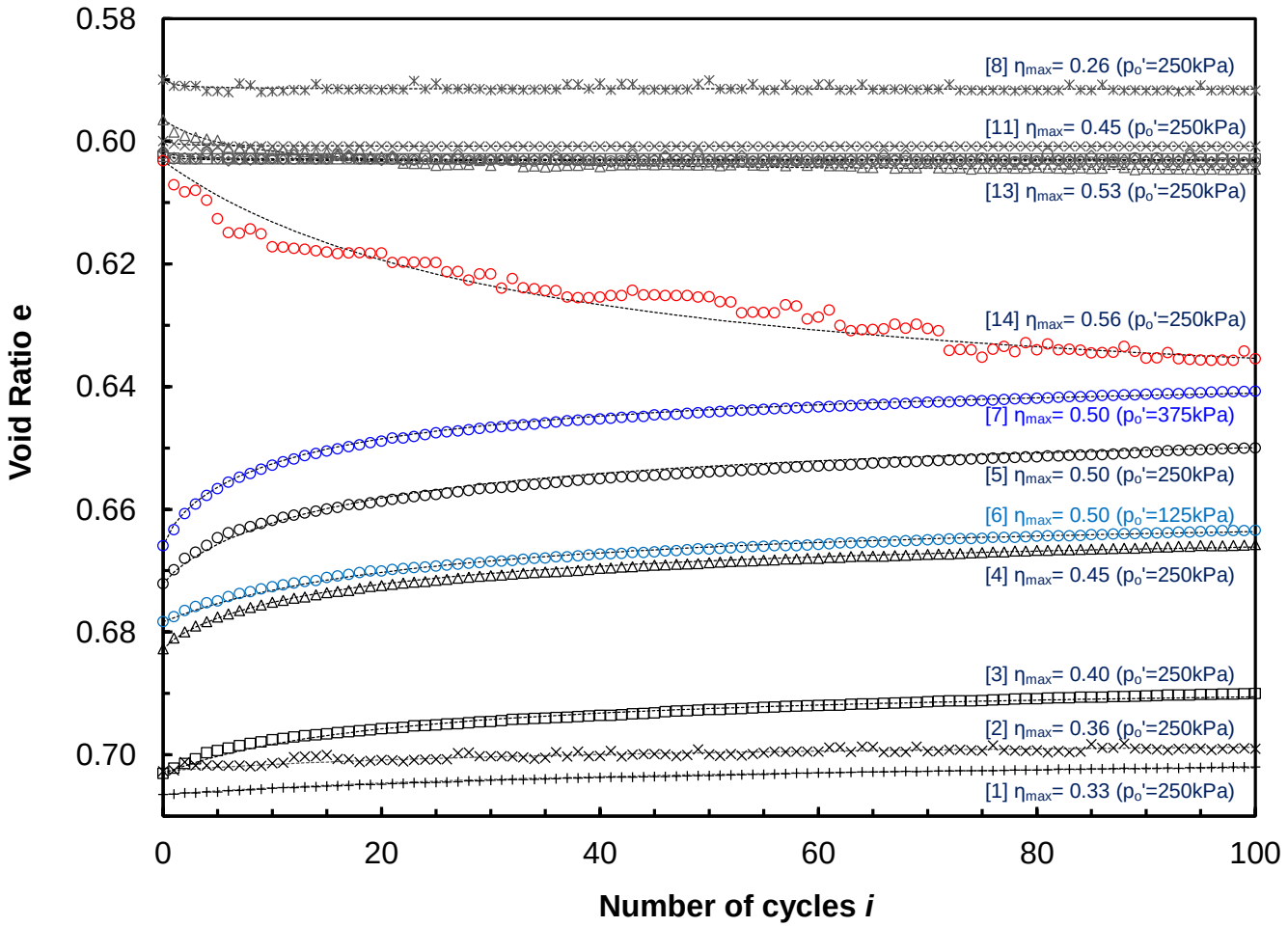

Figure 2.6 Volume change: Void ratio vs. number of cycles for loose, medium and dense specimens subjected to fluid pressure oscillations. The initial mean effective stress p_o' and the maximum stress obliquity are indicated in each case. The minimum stress obliquity is η_{min}=0.20 for all tests. Dotted lines: hyperbolic model fitted to test results (model parameters in Table 2.1). [ ] indicates the Test No. in Table 2.2.

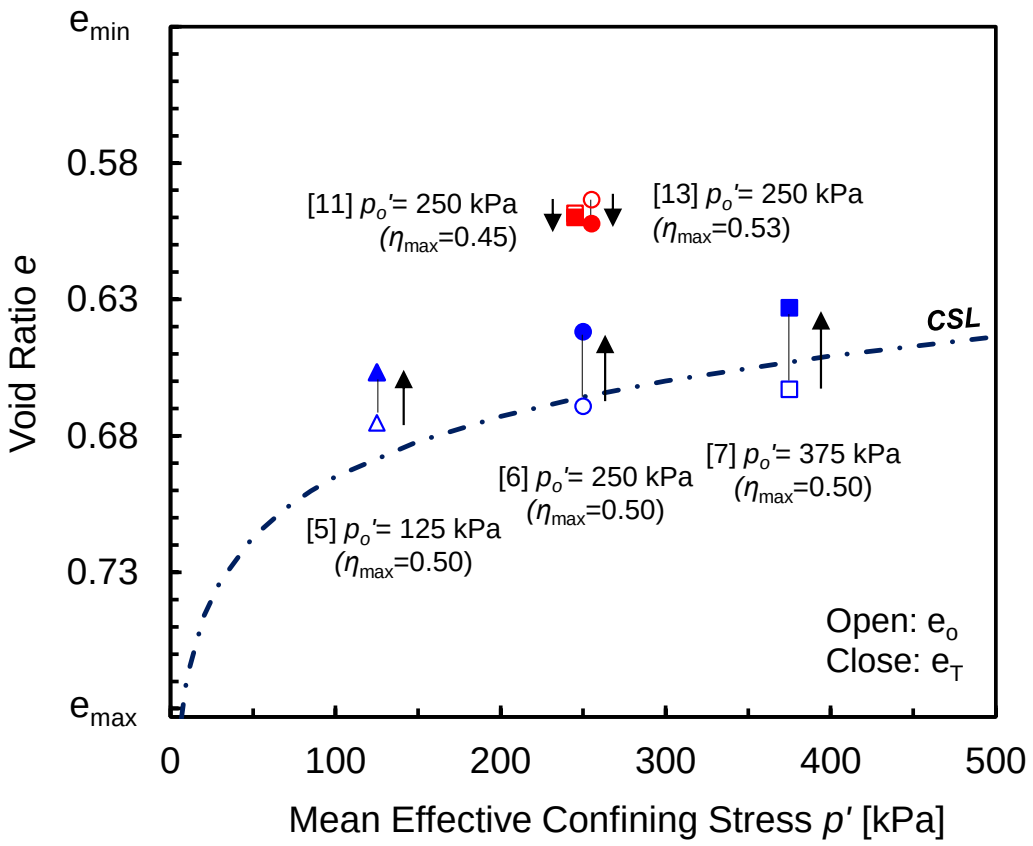

Figure 2.7 Evolution of void ratio for medium-dense (=blue) and dense sand (=red) specimens subjected to fluid pressure oscillations at different mean effective stress p_o'. In all specimens, the repetitive change in pore water pressure begins at η_{min}=0.20. Note: the critical state line CSL is e_{cs}=0.845-0.074 log(p'). [ ] indicates the Test No. 5, 6, and 7 in Table 2.2.

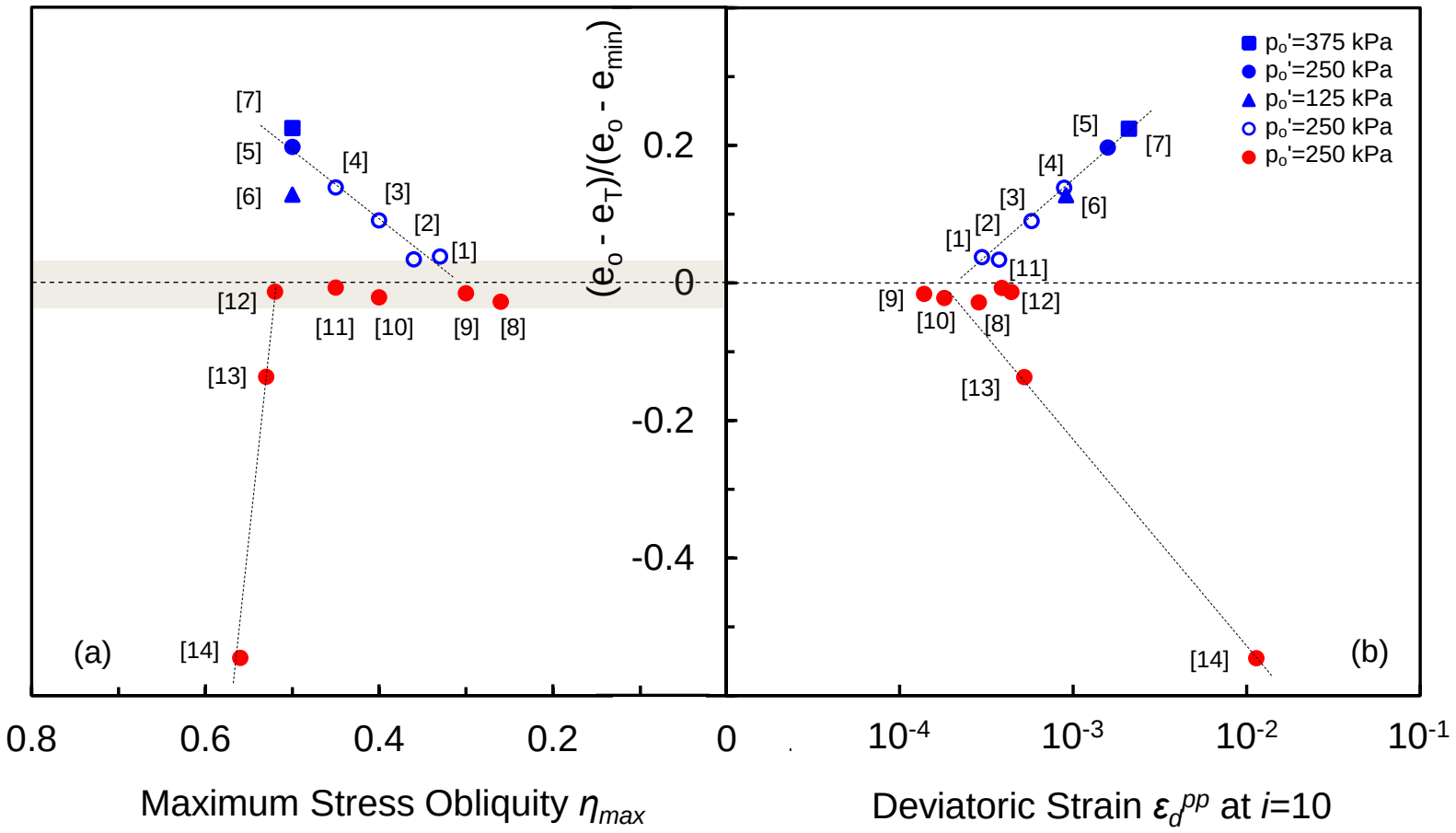

Figure 2.8 Normalized volume change (e_o - e_T)/(e_o - e_{min}) caused by fluid pressure oscillations - Loose, medium-dense, and dense sand specimens. (a) Maximum stress obliquity η_{max}, (b) Deviatoric strain level at i=10. [ ] indicates the Test No. in Table 2.2.

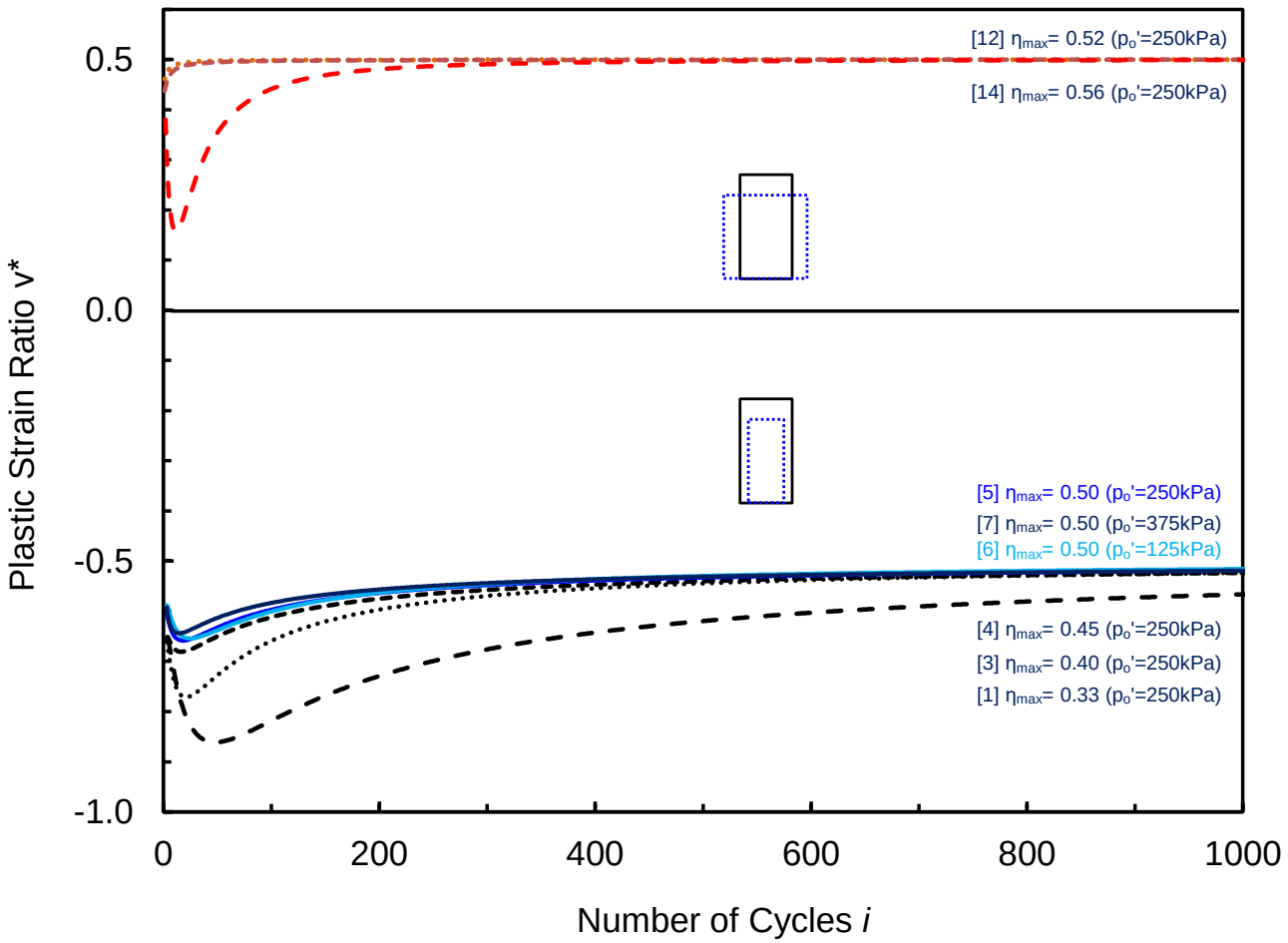

Figure 2.9 Ratio between incremental horizontal-to-vertical plastic strains ν^* (= - $\Delta\varepsilon^{pl}_{\perp}$/ $\Delta\varepsilon^{pl}_{//}$) vs. number of cycles. A negative ratio $\nu^*<0$ indicates vertical and horizontal contraction; a ratio $\nu^*=0$ implies vertical deformation at constant volume. [ ] indicates the Test No. in Table 2.2.

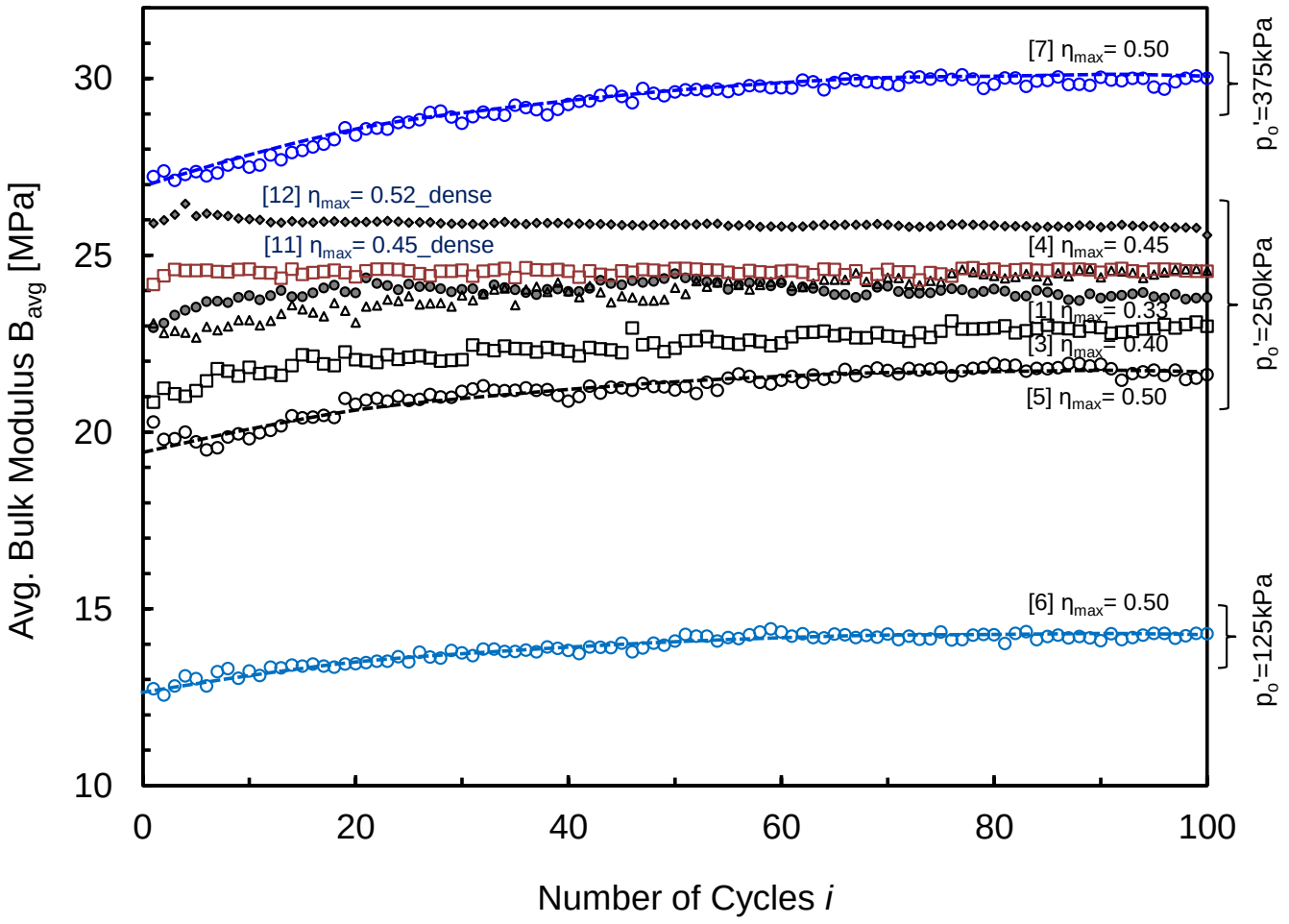

Figure 2.10 Evolution of average bulk modulus B_{avg} vs. number of cycles. Note: the instantaneous bulk modulus can be computed from the e_i-vs-i trends fitted with the hyperbolic model (refer to Figure 2.6). [ ] indicates the Test No. in Table 2.2.

CHAPTER 3

SANDS SUBJECTED TO LOW STRESS AMPLITUDE CYCLES (K_O CONDITIONS)

3.1 Introduction

The long-term performance of geotechnical systems depends on the soil response to all kinds of repetitive loads. These include stress cycles associated to wind, waves, and traffic (Long and Vanneste 1994; Peng et al. 2006; Andersen 2009; Wichtmann et al. 2010), chemical cyclic changes in pore fluid (Musso et al. 2003), thermal cycles (Pasten and Santamarina 2014; Di Donna and Laloui 2015), drying and wetting sequences (Albrecht and Benson 2001), freeze-thaw cycles (Chamberlain et al. 1990; Viklander 1998; Qi et al. 2008), and repetitive changes in pore water pressure (Orense et al. 2004; Nakata et al. 2013; Huang 2016).

The design of geo-structures for a long design-life needs to consider the influence of repetitive loads on long-term performance, serviceability, and safety. For example, this is the case of energy-related geosystems such as pumped hydro-storage, monopoles-supported wind turbines, compressed air energy storage, and energy piles (Chai and Miura 2002; Peng et al. 2006; Anderson 2009; Pasten and Santamarina 2011). The number of mechanical loading cycles in these systems can be particularly high: monopile-supported wind turbines experience more than $N=10^7$ cycles during the design-life (Achmus et al. 2009; Li et al. 2015), while tidal cycles exceed $N=10^4$ in a 30 year design-life.

Repetitive mechanical loads cause the accumulation of permanent deformations when the cyclic strain exceeds the threshold strain; then, there are associated changes in void ratio, hydraulic conductivity, small strain stiffness, compression index, and friction angle (Youd 1970; Kelly et al. 2006; Achmus et al. 2009). Consequently, repetitive mechanical loads can hinder the long-term performance of all kinds of geosystems.

This study explores the mechanical response of sands subjected to repetitive loading under zero lateral strain conditions. Basic concepts are reviewed first, followed by the experimental program and test results. The discussion provides a procedure for first-order settlement estimates that is valuable for engineering applications.

3.2 Soil Response to Repetitive Loads: Terms and Processes

The analysis and discussion of the long-term response of soils subjected to repetitive mechanical loads require terms and concepts that are not part of the standard geotechnical vocabulary. These concepts are briefly introduced next.

3.2.1 Threshold Strains

The imposed strain level determines the underlying particle-scale deformation mechanisms. If the strain level is smaller than the elastic threshold strain $\varepsilon_{th}|^{el}$, elastic deformations occur at grain contacts and the fabric remains constant (Vucetic and Dobry 1991; Vucetic 1994; Pasten et al. 2014). On the other hand, strain accumulations through particle rearrangement and fabric changes take place above the volumetric threshold strain $\varepsilon_{th}|^{v}$ (Note: $\varepsilon_{th}|^{v} \approx 30 \cdot \varepsilon_{th}|^{el}$ – Ishihara 1996). A theoretical analysis based on the Hertzian contact predicts a lower threshold strain for stiffer particles and at lower

confining stresses (Santamarina et al. 2001). It remains unclear whether the threshold strain levels obtained under quasi-static loading conditions also apply to the soil response under repetitive loading.

3.2.2 Volumetric Strain: Terminal Void Ratio

A soil subjected to repetitive loading will reach a stable asymptotic terminal void ratio (D'Appolonia and D'appolonia 1967; Narsilio and Santamarina 2008). The convergence rate towards the terminal void ratio depends on the initial packing density, particle shape, initial stress level, and cyclic stress amplitudes (Chong and Santamarina 2016).

3.2.3 Shear Strain: Shakedown or Ratcheting?

There are two distinct asymptotic trends in terms of shear strains (Sharp and Booker 1984; Collins et al. 1993; Alonso-Marroquın and Herrmann 2004; Werkmeister et al. 2005). Shakedown refers to finite shear strain accumulation, even when the strain is large enough to cause back-and-forth plastic shear strains in every cycle. On the other hand, ratcheting refers to asymptotic plastic strain accumulation in every cycle.

3.3 Experimental Study: Devices and Test Procedure

This experimental program explores the evolution of the void ratio and the small strain stiffness of sands subjected to repetitive mechanical loads under zero-lateral strain conditions. The repetitive loading system consists of an instrumented floating-ring oedometer cell and an automatic stress-controlled frame (Figure 3.1). The tall floating

ring oedometer (*ID* = 52.5 mm, 3.9 mm wall thickness, and 100 mm high) is designed to ensure the alignment of the top and bottom caps during repetitive loading (*OD* = 50.8 mm and 50.8 mm height).

3.3.1 Stress-Controlled Repetitive Loading System

The loading system consists of a rigid reaction frame, pneumatic cylinders, and peripheral control electronics. The computer sends the digitized command signal to the digital-to-analog converter DAC (Labjack U3-LV). The controller (proportional-integral-derivative controller PID - Enfield Technologies C1) activates the pneumatic valve (Enfield Technologies LS-V25s) to match the analog command signal from the DAC and the analog signal received from the pressure transducer. The loading system can operate in strain-controlled mode if the LVDT response is used as feedback signal instead of the pressure transducer.

3.3.2 Deformation Monitoring

The LVDT (TransTek DC 0242) clamped to the top and bottom caps tracks the specimen vertical deformation. LVDT data are saved by the data logger (Keysight 34970A, Figure 3.1).

3.3.3 Shear Waves: Bender Elements

The top and bottom caps include bender elements which are mounted inside removable nylon screws. We use grounded parallel-type bender elements for both source and receiver to minimize crosstalk (Lee and Santamarina 2005). The bender elements are

12.7 mm × 8 mm × 0.7 mm in size, and are mounted with a 5 mm cantilevered length (7.7 mm anchored length). The function generator sends a 10 V step signal every 50 *m*s (Keysight 33210A). Received signals go through a filter-amplifier (Krohn-Hite 3364 - 500 Hz high-pass and 200 kHz low-pass window) before they are averaged in the oscilloscope and stored. (Keysight DSOX 2014A - 1024 stacked signals - See implications of signal stacking in Santamarina and Fratta 2005).

3.3.4 Specimen Preparation

This experimental study uses Ottawa 20/30 sand (roundness= 0.9; median grain size D_{50}= 0.72 mm; maximum and minimum void ratios e_{max}= 0.742 and e_{min}= 0.502; specific gravity G_s= 2.65). The specimen preparation method involves different tamping energies to attain target relative densities between D_r = 30-and-70%.

3.3.5 Test Procedure

The loading procedure for all specimens consists of four stages: (1) static step loading to σ_0, (2) repetitive loading by N=10^4 cycles with amplitude $\Delta\sigma$, (3) static loading to the maximum vertical stress, and (4) unloading. Shear wave measurements during the repetitive loading stage take place at the same vertical effective stress $\sigma_0 + \Delta\sigma$, at the top of cycles i = 1, 10, 100, 300, 1000, 3000, and 10000. Loading cycles have a period of 12 seconds. Table 3.1 summarizes all test conditions.

3.4 Experimental Results

All 33 tests in Table 3.1 exhibit similar trends. This section presents detailed experimental results for two specimens D_r = 44% and D_r = 86%, subjected to loading cycles with stress amplitude $\Delta\sigma/\sigma_0$ = 1.3 (Table 3.1). Then, the complete dataset is analyzed in the following section.

3.4.1 Effective Stress σ'_z vs. Void Ratio e

Figure 3.2 presents the change in void ratio during the static-repetitive-static loading history followed by the static unloading stage. The void ratio for the loosely and densely packed sands decreases monotonically during the initial static loading stage. The dotted circles indicate creep deformation at constant load. Repetitive loading cycles cause higher contraction in the looser specimen.

3.4.2 Vertical Effective Stress σ'_z vs. Volumetric Strain ε_z

Figure 3.3 presents the same repetitive load-response shown in Figure 3.2 but in terms of stress and strain. The recoverable and irrecoverable strains are clearly seen in the earlier loading-unloading cycles. The plastic strain accumulation becomes negligible as the number of cycles increases, but it remains hysteretic, i.e. plastic shakedown.

3.4.3 Evolution of Void Ratio

Figure 3.4 illustrates the void ratio evolution with the number of cycles for the two specimens reported above (D_r = 44% and 86%; $\Delta\sigma/\sigma_0$ = 1.3). Once again, most changes in void ratio take place in earlier cycles and are more significant in the loosely-

packed sand. Figures 3.4a and 3.4b show a modified hyperbolic model fitted to test results (inspired by Paute et al. 1993; Werkmeister et al. 2005; modified from Chong and Santamarina 2016):

$$e_i = e_T + (e_1 - e_T)\left[1 + \left(\frac{i-1}{N^*}\right)^m\right]^{-1} \qquad \text{for } i \geq 1 \text{ and } m > 0 \tag{3.1}$$

where m is a fitting parameter and i is the number of loading cycles. The void ratio e_i is measured after the i^{th} cycle. The initial void ratio e_1 corresponds to i= 1, and the terminal void ratio e_T is the asymptotic void ratio as $i \to \infty$. Finally, the model parameter N^* is the number of cycles required for a given soil to compact to half of the asymptotic contraction, that is, $(e_1 - e_T)/2$.

3.4.4 Shear Wave Signals

Figure 3.5 shows the shear wave signal cascades recorded during the "static-repetitive-static" loading history followed by the unloading stage. The travel time decreases during the first quasi-static loading stage. Changes in the first arrival are less obvious during repetitive loading. We use the time-stretched cross-correlation method in CODA wave analysis to assess these minor changes in travel time (Snieder 2006; Dai et al. 2013). Then, the stretching factor θ allows us to determine minute changes in shear wave velocity during repetitive loading cycles.

3.5. Analyses and Discussion – Compete Dataset

In this section, we report and analyze the complete dataset produced with the 33 tests performed for this study (Table 3.1).

3.5.1 Evolution of Void Ratio: e_T and N^*

The terminal void ratio e_T and the characteristic number of cycles N^* describe the soil response to repetitive loads for engineering purposes (Equation 3.1). Figure 3.6a shows that the asymptotic terminal void ratio e_T scales with the initial void ratio e_0. In other words, specimens do not evolve to a single soil fabric but retain memory of their initial fabric even after a very large number of cycles (see also Chong and Santamarina 2016). On the other hand, the terminal density decreases as the stress amplitude ratio $\Delta\sigma/\sigma_0$ increases. In fact, the dimensionless volume contraction $\lambda = (e_T - e_{min})/(e_0 - e_{min})$ is strongly correlated to the stress amplitude ratio $\Delta\sigma/\sigma_0$ as shown in Figure 3.6b: $\lambda = 1.0 - 0.05 \cdot [\Delta\sigma/\sigma_0]$.

The characteristic number of cycles N^* required to reach half of the asymptotic volume contraction $\Delta e = (e_1 - e_T)/2$ increases with increasing initial void ratio e_0; in fact, $N^* \rightarrow 1$ for densely packed sands ($e_0 \rightarrow e_{min}$) and $N^* \rightarrow 10^3$ for loosely packed sands ($e_0 \rightarrow e_{max}$). Less obvious is the fact that N^* also increases with stress ratio $\Delta\sigma/\sigma_0$: this happens because the terminal void ratio e_T is lower for higher $\Delta\sigma/\sigma_0$, hence, a larger number of cycles is required to attain half of the asymptotic contraction $\Delta e = (e_1 - e_T)/2$. Finally, Figure 3.6d shows that the m-exponent is relatively constant, $m = 0.45 \pm 0.05$.

3.5.2 Threshold Strain

The upper and lower hyperbolic model trends fitted to test results e^u and e^l define the peak-to-peak strain in i cycle $\varepsilon_{pp}(i)$ [Figure 3.4b and Equation 3.1]:

$$\varepsilon_{pp}(i) = \frac{\Delta e_i}{1+e_i} = \frac{e_i^u - e_i^l}{1+e_i^l} \tag{3.2}$$

On the other hand, the permanent change in void ratio between two consecutive cycles defines the plastic volumetric strain $\varepsilon_v^{pl}(i)$ between i and i+1 cycles [Figure 3.4b]:

$$\varepsilon_v^{pl}(i) = \frac{e_i^l - e_{i+1}^l}{1+e_i^l} \tag{3.3}$$

Let's select the volumetric threshold strain $\varepsilon_{th}|^v$ as the peak-to-peak strain ε_{pp} that corresponds to a plastic volumetric strain of $\varepsilon_v^{pl} = 10^{-8}$ per cycle. This strain level is small enough to prevent atomic-scale displacement between neighboring particles.

Figure 3.7 presents the volumetric threshold strains $\varepsilon_{th}|^v$ determined for all tests. Values cluster into four groups as a function of initial void ratio e_0 and stress amplitude ratio $\Delta\sigma/\sigma_0$: the volumetric threshold strain increases as the initial void ratio decreases and the stress amplitude ratio increases. The volumetric threshold strain is in the range of $\varepsilon_{th}|^v \approx$ 3-to-10 $\times 10^{-4}$ for all tests. For comparison, threshold volumetric shear strain data extracted from published studies are superimposed on Figure 3.7 (Note: $\gamma \approx \varepsilon_v/2$ for oedometric conditions). Differences may be due to boundary compliance and higher fabric stability in oedometer tests.

3.5.3 Damping Ratio *D* and Constraint Modulus *M*

The damping ratio $D = \Delta W/(4\pi \cdot W)$ relates the consumed energy ΔW to the stored energy W in a σ_z-ε_z cycle. On the other hand, the constraint modulus in a cycle relates the applied cyclic stress to the peak-to-peak strain $M = \Delta\sigma/\varepsilon_v$. Figure 3.8 plots the damping ratio D_i and the constraint modulus M_i versus the number of cycles i, where both values D_i and M_i are normalized by the corresponding values in the first cycle, that is D_1 and M_1.

For clarity, values are shown at a selected number of cycles i=1, 2, 10, 100, 1000, and 10000. The damping ratio decreases while the constraint modulus increases with the number of cycles in all 33 tests. Most of the reduction in the damping ratio takes place in the first few cycles (see also Stokoe et al. 1999) while the increase in the constraint modulus continues even after a large number of cycles (see resilient modulus data in Monismith 2004; da Fonseca et al. 2013). The stress amplitude ratio $\Delta\sigma/\sigma_0$ affects the variation of constraint modulus as the number of cycles increases. Hence, repetitive mechanical loads result in denser, stiffer, and less attenuating sand fabrics under zero-later strain conditions.

3.5.4 Shear Wave Velocity during Static Loading

The shear wave velocity is a power function of the vertical σ'_z and horizontal σ'_x effective stresses (Roesler 1979; Yu and Richard 1984; Santamarina et al. 2001):

$$V_s = \alpha\left(\frac{\sigma_z^{'} + \sigma_x^{'}}{2\,kPa}\right)^{\beta} = \alpha\left(\frac{\sigma_z^{'}}{1kPa}\right)^{\beta}\left(\frac{1+K_0}{2}\right)^{\beta} \tag{3.4}$$

where the α-factor is the shear wave velocity at effective stress σ'_{mean}= 1 kPa, and the β-exponent represents the stress sensitivity of the shear wave velocity. The shear wave

velocity-stress relation captures both contact behavior and fabric changes (Cha et al. 2014).

Figure 3.9a summarizes the evolution of the shear wave velocity measured during the (1) static, (2) repetitive, and (3) static loading stages for a loose sand and a dense sand. Figure 3.9b presents the α-factors and β-exponents computed by fitting Equation 3.4 to the static load stages before and after repetitive loading for all tests. The data trend is consistent with the relationship between α and β values reported by Cha *et al*. 2014. Overall, the sand becomes stiffer (lower C_c), the α-factor increases, the β-exponent decreases and the soil fabric becomes less sensitive to stress changes after repetitive loading.

3.5.5 Shear Wave Velocity during Repetitive Loading

Figure 3.9c presents the shear wave velocity against the number of loading cycles for three loosely-packed sands subjected to different stress amplitude ratios $\Delta\sigma/\sigma_0$. The shear wave velocity increases with $\log(i)$ for all stress amplitude ratios $\Delta\sigma/\sigma_0$:

$$\frac{V_s|_i}{V_s|_1} = i^d \tag{3.5}$$

The d-exponent is a function of the shear wave velocity for the first cycle $V_s|_1$ (Figure 3.9d). Data points cluster along linear trends for each stress amplitude ratio $\Delta\sigma/\sigma_0$. In words, the rate of increase in small-strain stiffness during repetitive loading is more pronounced in looser and softer sands subjected to high stress cycles.

3.5.6 Maximum Constraint Modulus M_{max} from V_s

Figure 3.10 illustrates the comparison between the measured constraint modulus $M_i = \Delta\sigma/\varepsilon_{pp}(i)$ [Figure 3.4b and Equation 3.2] and the maximum constraint modulus M_{max} computed from the shear wave velocity $M_{max} = 2\cdot(V_s^2\rho)(1-\nu)/(1-2\nu)$ assuming a small-strain Poisson's ratio $\nu = 0.15$. Values are shown for the first cycle $i = 1$ and after $i = 10^4$ cycles. Changes in shear wave velocity track the evolution of the constraint modulus M_i during repetitive loading. In all cases, the maximum constraint modulus M_{max} remains the upper bound of stiffness.

3.5.7 Evolution of K_o

The coefficient of earth pressure K_0 at rest relates in the in-situ horizontal effective stress to the vertical effective stress under zero-lateral strain conditions (Mayne and Kulahwy 1982; Michalowski 2005). Let's analyze velocity-stress data before and after the repetitive loading stage to estimate the evolution of the coefficient of earth pressure K_0 during repetitive loading. From Equation 3.4,

$$\frac{V_s\big|_N}{V_s\big|_1} = \frac{\alpha\big|_N}{\alpha\big|_1} \frac{\left(\frac{\sigma_z^{'}\big|_N}{1kPa}\right)^{\beta|_N}}{\left(\frac{\sigma_z^{'}\big|_1}{1kPa}\right)^{\beta|_1}} \frac{\left(\frac{1+K_0\big|_N}{2}\right)^{\beta|_N}}{\left(\frac{1+K_0\big|_1}{2}\right)^{\beta|_1}} \tag{3.6}$$

Then,

$$K_0\big|_N = \frac{\sigma^{'}x}{\sigma^{'}z} = 2\left[\frac{V_s\big|_N}{V_s\big|_1}\frac{\alpha\big|_1}{\alpha\big|_N}\sigma^{'}z^{(\beta|_1-\beta|_N)}\left(\frac{1+K_0\big|_1}{2}\right)^{\beta|_1}\right]^{\frac{1}{\beta|_N}} - 1 \tag{3.7}$$

Assuming a nominal initial value $K_0|_1$=0.42, the α and β values fitted before and after repetitive loading allow us to anticipate a stress ratio $K_0|_N \approx 0.48 \pm 0.02$ immediately after repetitive loading with stress amplitude ratio $\Delta\sigma/\sigma_0$= 1.3. Hence, indirect shear wave velocity measurements suggest a gradual increase in horizontal stress during repetitive loading under zero lateral strains (see also data in Sawicki and Swidzinski 1995).

3.6 Repetitive Load-Induced Settlement

The maximum asymptotic change in void ratio $\Delta e=e_0-e_T$ induced by repetitive mechanical loading as $N\rightarrow\infty$ will cause a strain ε_T (refer to earlier results - Figures 3.6a and 3.6b):

$$\varepsilon_T = \frac{e_0 - e_T}{1+e_0} = (1-\lambda)\frac{e_0 - e_{\min}}{1+e_0} = a\frac{\Delta\sigma}{\sigma_0}\frac{e_0 - e_{\min}}{1+e_0} \tag{3.8}$$

where a= 0.05 for the sand tested in this study (Figure 3.6b). Thus, the settlement of a layer thickness H subjected to repetitive mechanical loading under zero lateral strain conditions is:

$$S_T = \int_0^H \varepsilon_T dz = \int_0^H \frac{e_0(z) - e_T(z)}{1+e_0(z)} dz = \int_0^H a\frac{e_0(z) - e_{\min}(z)}{1+e_0}\frac{\Delta\sigma(z)}{\sigma_0(z)} dz \tag{3.9}$$

This equation highlights the importance of the initial e_0 and terminal e_T void ratios. The last expression benefits from experimental results used herein to estimate e_T from $e_{\min}$ and the stress amplitude ratio $\Delta\sigma/\sigma_0$. For example, let's consider a large footing on a homogeneous sandy sediment (e_{max}=0.74, e_{min}=0.50, e_0= 0.60). The footing applies σ_0

(z=0) =100 kN/m^2 and $\Delta\sigma$= 50 kN/m^2. From Figures 3.6a and 3.6b and Equation 3.9, the settlement expected for a H= 5 m thick layer is S_T= 5.7 mm.

3.7 Conclusions

The void ratio, the state of stress, and the small strain stiffness of sands change during quasi-static repetitive mechanical loads under zero-lateral strain conditions. Notable conclusions from this study follow:

- The void ratio evolves towards the terminal void ratio e_T as the number of load cycles $i\rightarrow\infty$. The terminal void ratio e_T is a function of the initial void ratio e_0 when repetitive loads take place under K_o-condition. In other words, the soil retains memory of its initial fabric.
- The characteristic number of cycles N^* required to reach half of the asymptotic volume contraction Δe= (e_1-e_T)/2 increases with increasing initial void ratio e_0; in fact, $N^*\rightarrow$1 for densely packed sands ($e_0\rightarrow e_{min}$), and $N\rightarrow 10^3$ for loosely packed sands ($e_0\rightarrow e_{max}$).
- The volumetric threshold strain $\varepsilon_{th}|^v$ is in the range of $\varepsilon_{th}|^v \approx$ 3-to-10 × 10^{-4} for the tested sand.
- The changes in void ratio, damping ratio and constraint modulus during repetitive loading reveal that repetitive K_o-loading results in denser, stiffer, and less attenuating sand fabrics. All these changes are a function of the initial void ratio e_0 and the stress amplitude ratio $\Delta\sigma/\sigma_0$.
- Shear wave velocity-stress trends V_s= $\alpha(\sigma'_{mean}/\text{kPa})^\beta$ capture both contact behavior and fabric changes. Data show that sands become stiffer (lower C_c), the α-factor

increases, the β-exponent decreases and the soil fabric becomes less sensitive to stress changes after repetitive loading.

- Changes in shear wave velocity track the evolution of the constraint modulus M_i during repetitive loadings. The maximum constraint modulus M_{max} computed from shear wave velocity V_s remains the upper bound for the sediment stiffness.
- The increase in shear wave velocity indicates a gradual increase in horizontal stress during repetitive loading under zero lateral strains.
- Data gathered in this experimental program suggest a simple procedure to estimate the potential settlement a shallow foundation may experience when subjected to repetitive mechanical loads. The calculation method is based on the initial and terminal void ratios.

Table 3.1. Test condition

Initial vertical stress σ_0 [kPa]	Stress amplitude $\Delta\sigma$ [kPa]	Stress amplitude ratio $\Delta\sigma/\sigma_0$	Initial relative density D_r^* (number of tests)
174	$\Delta\sigma$ = 138 (174 ↔ 312)	0.8	40% (3) 70% (3)
105	$\Delta\sigma$ = 138 (105 ↔ 243)	1.3	40% (6) 70% (6)
67	$\Delta\sigma$ = 100 (67 ↔ 167)	1.5	30% (1) 50% (1) 70% (1)
105	$\Delta\sigma$ = 276 (105 ↔ 381)	2.7	40% (3) 70% (3)
105	$\Delta\sigma$ = 414 (105 ↔ 519)	4.0	40% (3) 70% (3)

*Note: target value. The measured value is used in all plots and analyses.

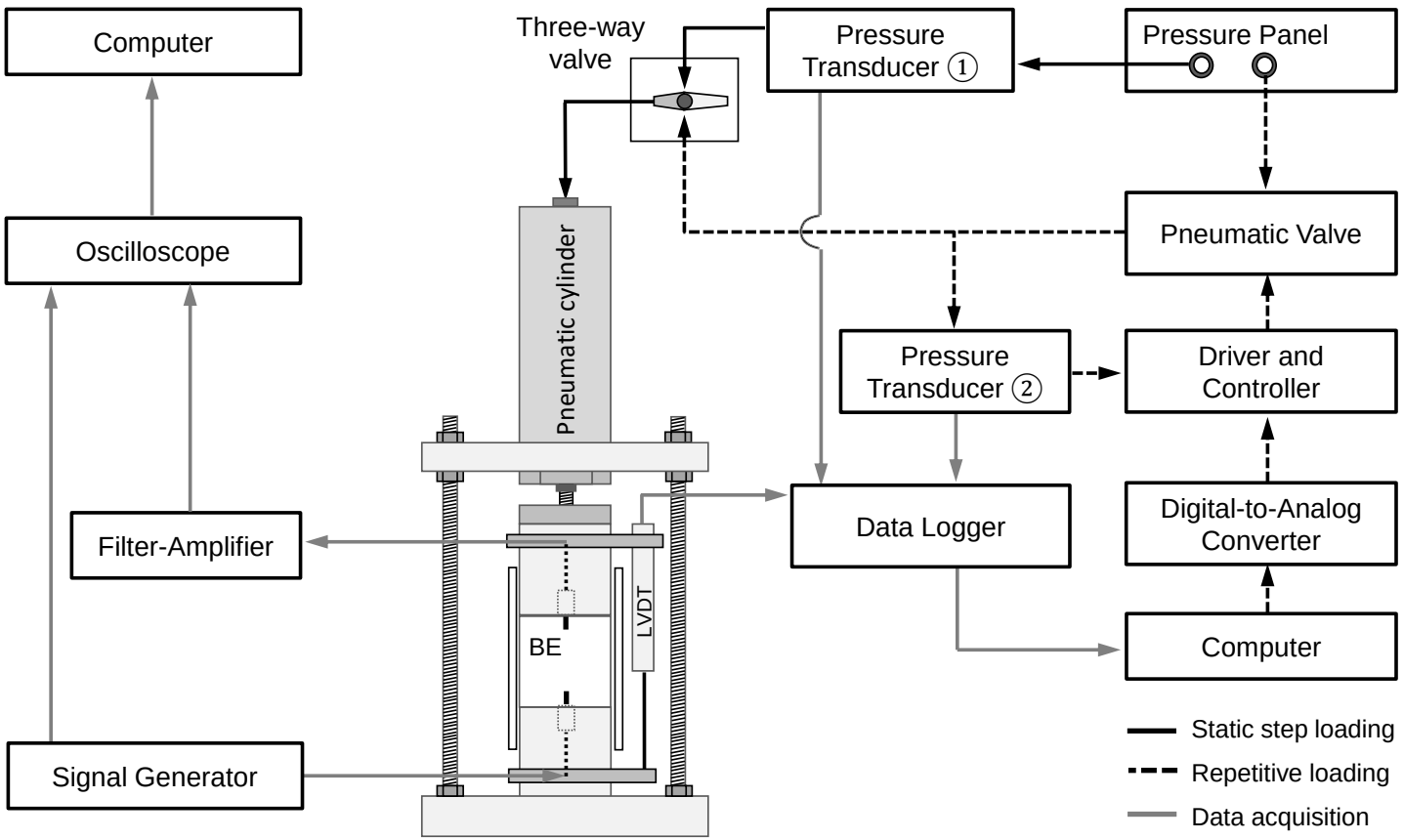

Figure 3.1. Device. Schematic diagram of the pneumatic system used for static and repetitive loading. The peripheral electronics are used to measure deformation and shear waves. The oedometer cell consists of a floating ring, top and bottom caps with bender elements BE, and LVDT clamps. Top and bottom cap dimensions: 50.8 mm diameter and 50.8 mm height. Floating ring dimensions: ID= 52.5 mm, OD= 60.3 mm, and 100 mm height.

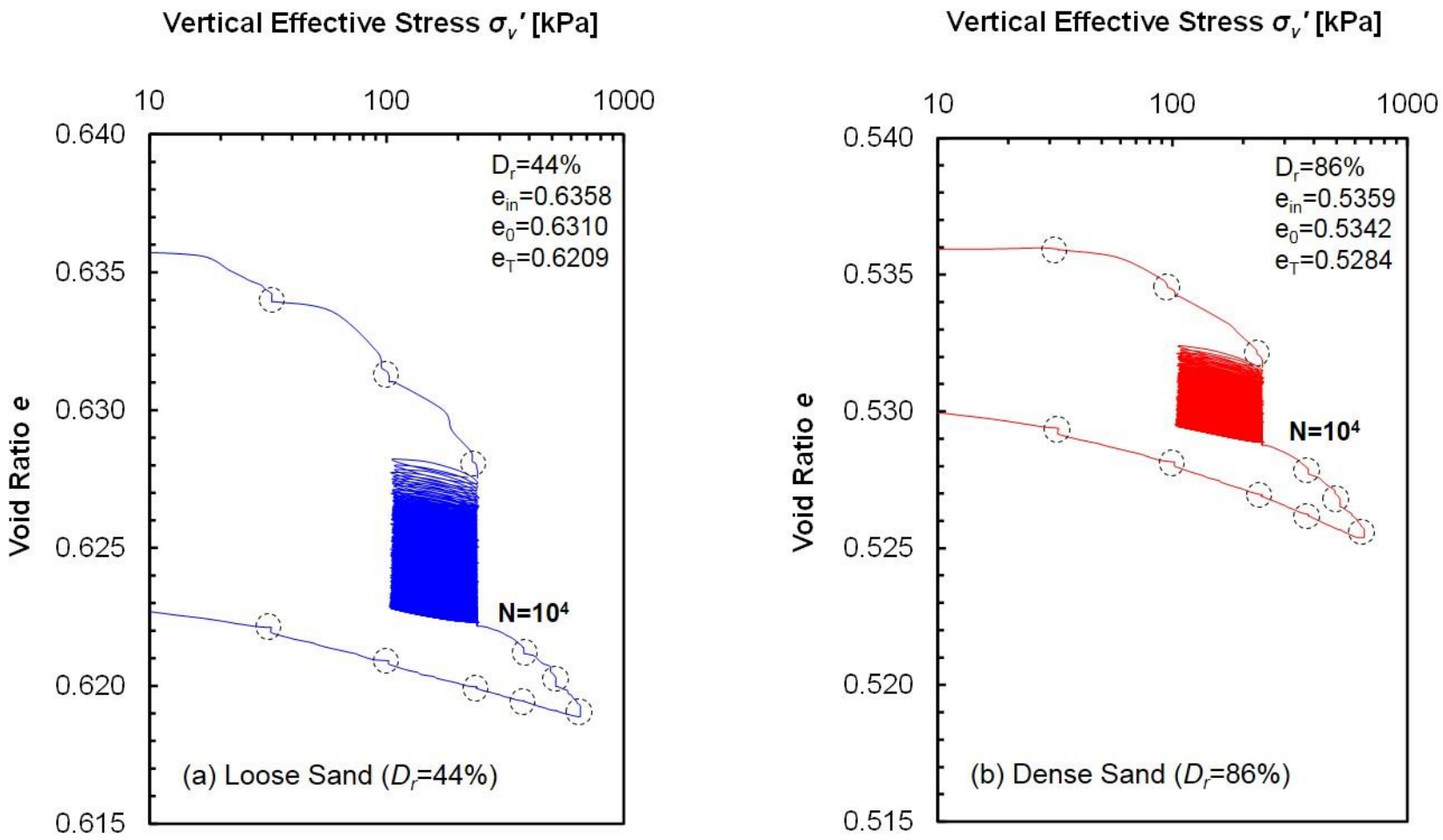

Figure 3.2. The change in void ratio during the static-repetitive-static loading history followed by the static unloading sequence. (a) Loose sand D_r=44%; (b) Dense sand D_r =86%. Test conditions: σ_0 =105 kPa, stress amplitude ratio $\Delta\sigma/\sigma_0$= 1.3 (from 105-to-243 kPa).

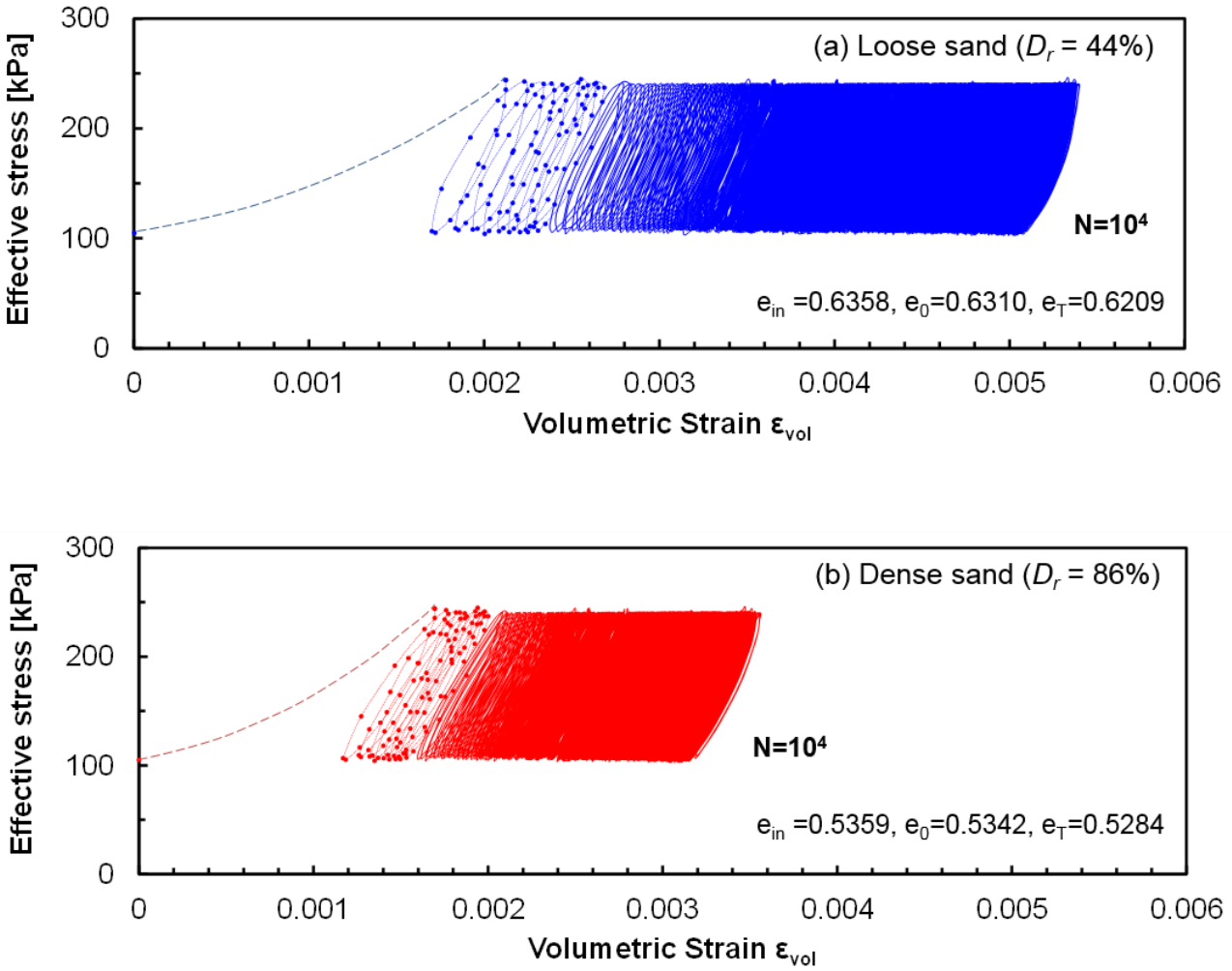

Figure 3.3. Stress-strain response during repetitive loading cycles. (a) Loose sand D_r=44%; (b) Dense sand D_r =86%. Test conditions: σ_0 =105 kPa, stress amplitude ratio $\Delta\sigma/\sigma_0$= 1.3 (from 105-to-243 kPa).

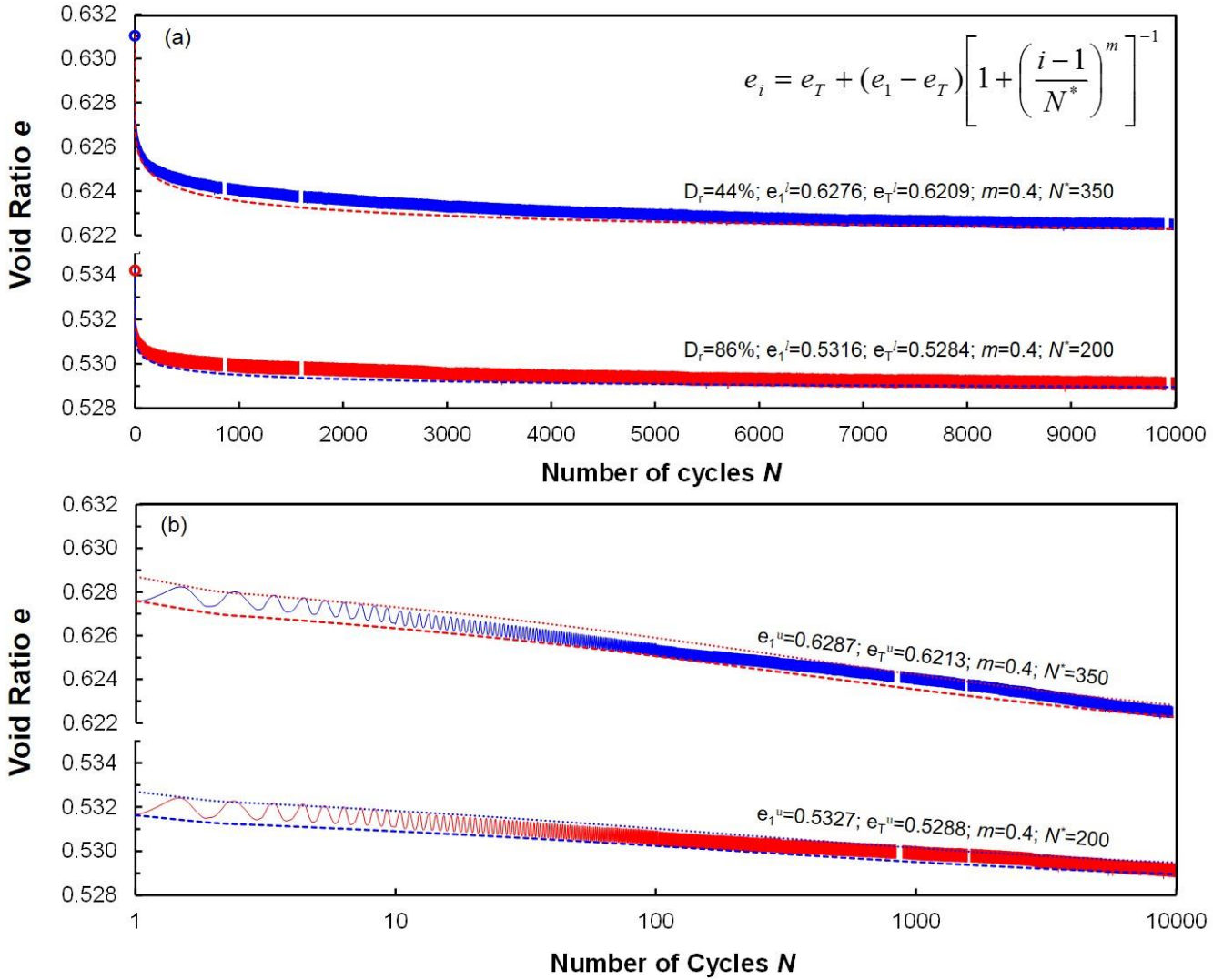

Figure 3.4. Void ratio evolution with number of cycles *i*. (a) Linear scale; (b) Logarithmic scale. Test conditions: σ_0 =105 kPa, stress amplitude ratio $\Delta\sigma/\sigma_0$= 1.3 (from 105-to-243 kPa).

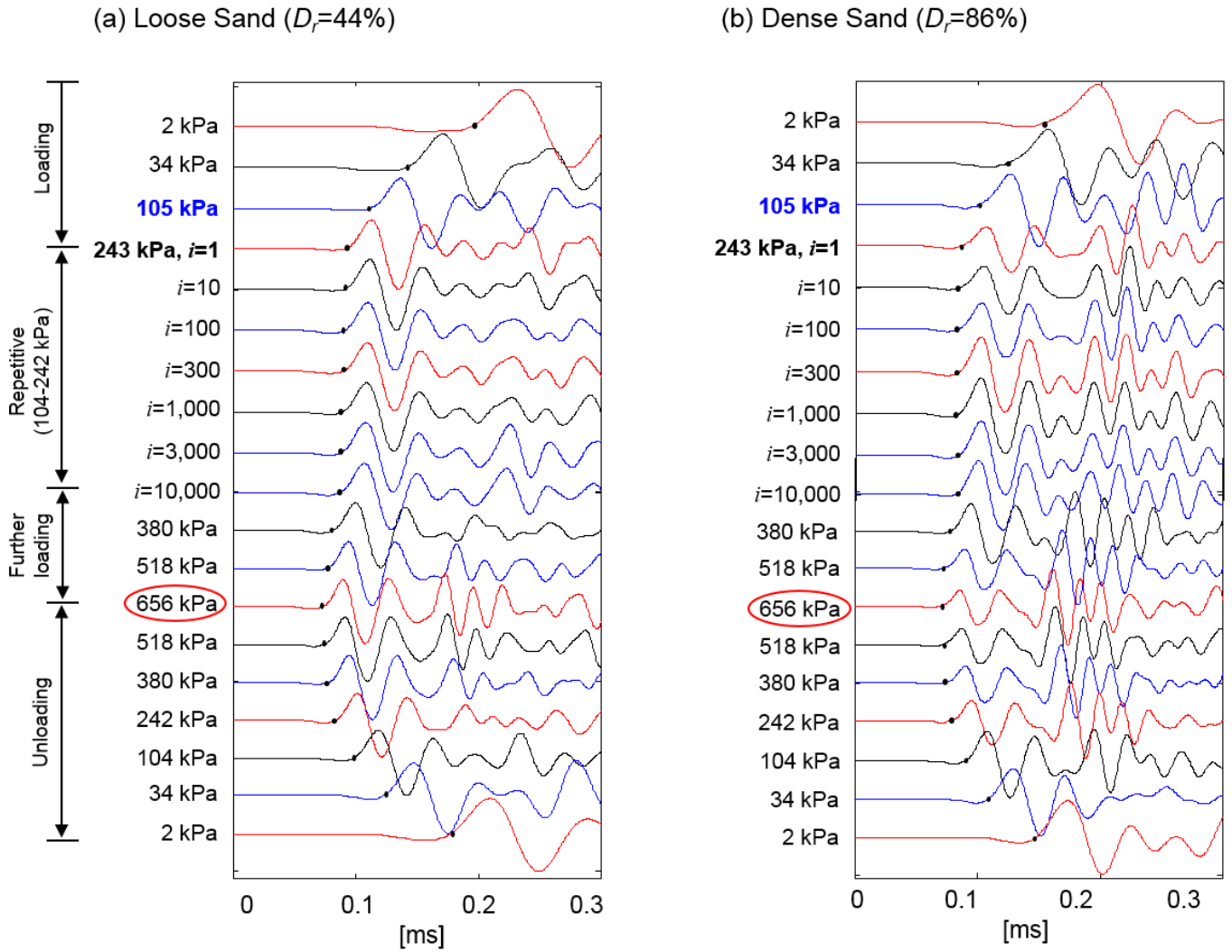

Figure 3.5. Cascade of shear wave signals captured during the "static-repetitive-static" loading history followed by unloading. (a) Loose sand D_r=44%; (b) Dense sand D_r =86%. Test conditions: σ_0 =105 kPa, stress amplitude ratio $\Delta\sigma/\sigma_0$= 1.3 (from 105-to-243 kPa).

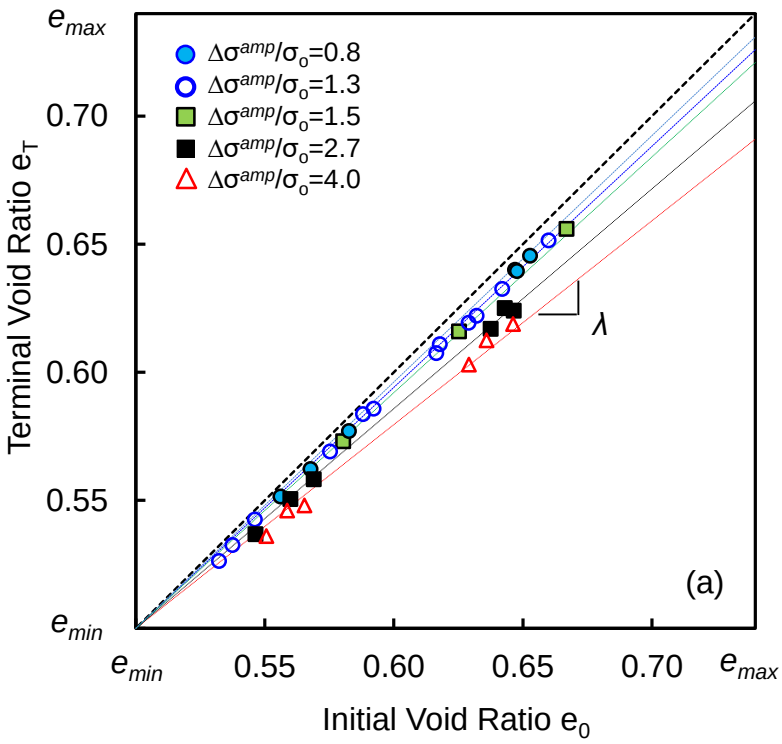
e_{max}
0.70
0.65
0.60
0.55
e_{min}
Terminal Void Ratio e_T
$\Delta\sigma^{amp}/\sigma_0$=0.8
$\Delta\sigma^{amp}/\sigma_0$=1.3
$\Delta\sigma^{amp}/\sigma_0$=1.5
$\Delta\sigma^{amp}/\sigma_0$=2.7
$\Delta\sigma^{amp}/\sigma_0$=4.0
λ
(a)
e_{min}
0.55
0.60
0.65
0.70
e_{max}
Initial Void Ratio e_0

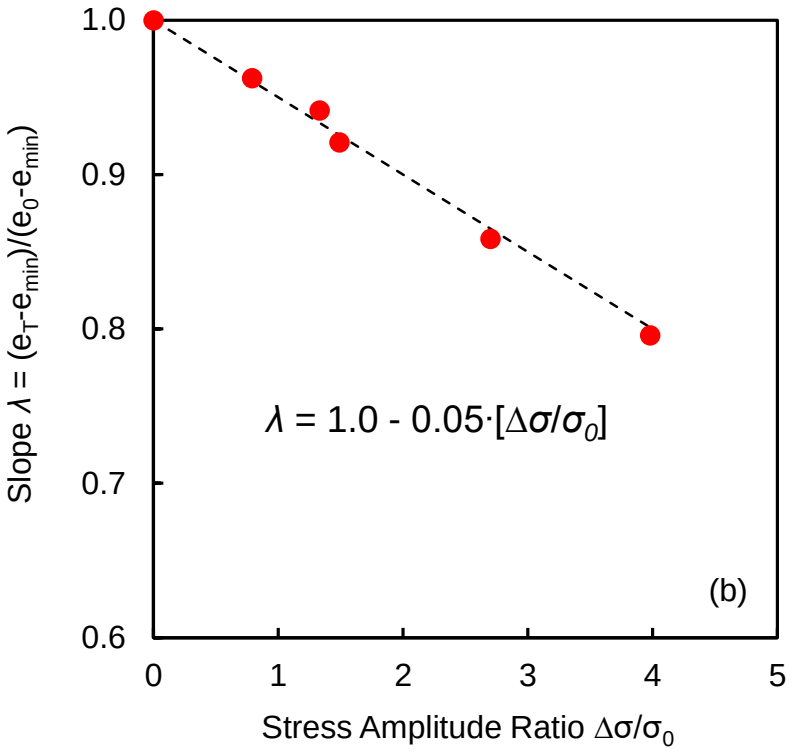
1.0
0.9
0.8
0.7
0.6
Slope $\lambda = (e_T-e_{min})/(e_0-e_{min})$
$\lambda = 1.0 - 0.05\cdot[\Delta\sigma/\sigma_0]$
(b)
0
1
2
3
4
5
Stress Amplitude Ratio $\Delta\sigma/\sigma_0$

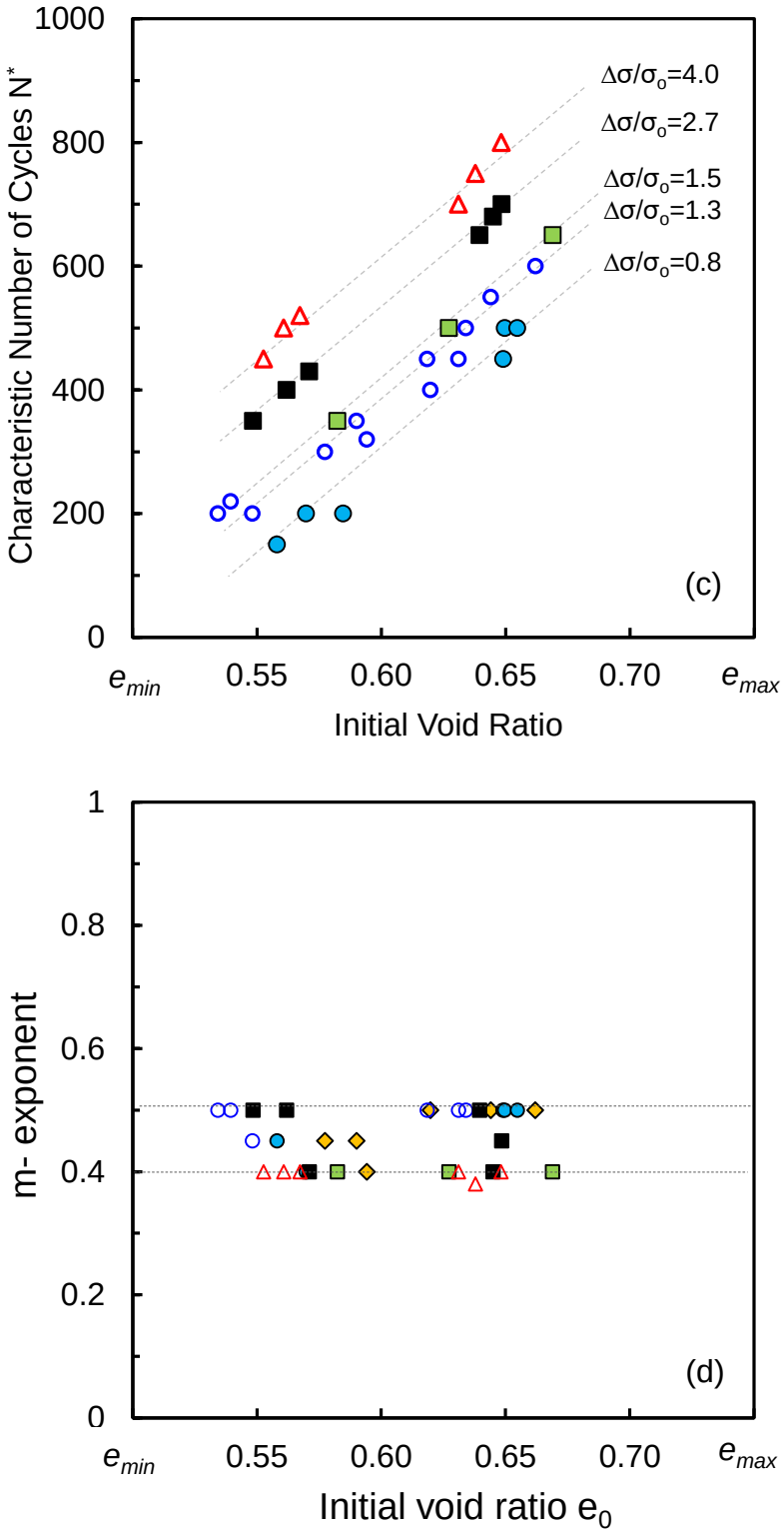

Figure 3.6. Terminal void ratio and characteristic number of cycles. (a) Terminal void ratio e_T versus initial void ratio e_0 for different stress amplitude ratios $\Delta\sigma/\sigma_0$; (b) Slope $\lambda = (e_T - e_{min})/(e_0 - e_{min})$ versus stress amplitude ratio $\Delta\sigma/\sigma_0$; (c) Characteristic number of cycles N^* versus initial void ratio e_0 as a function of stress amplitude ratio; and (d) Fitting model parameter m versus initial void ratio e_0.

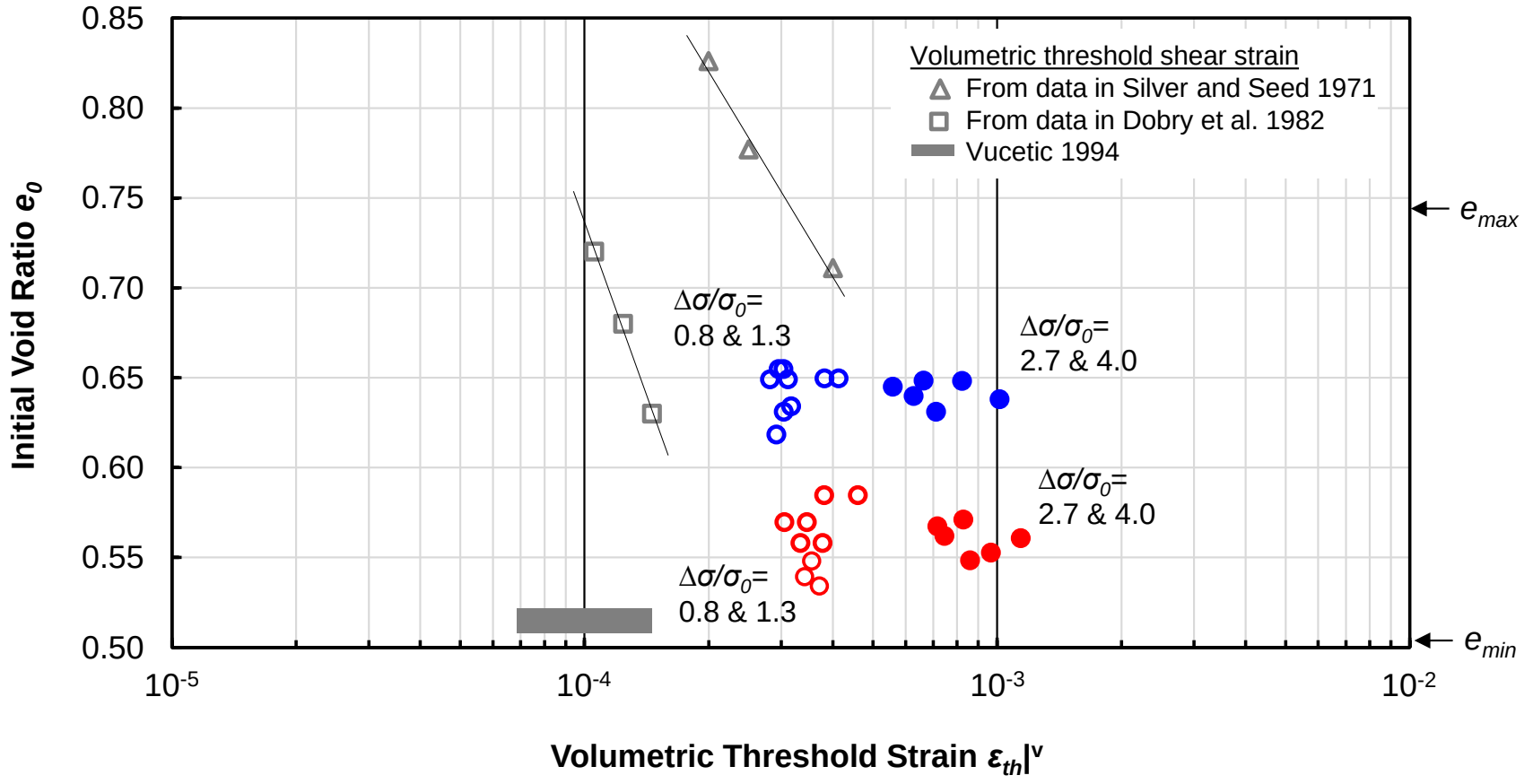

Figure 3.7. The volumetric threshold strain $\varepsilon_{th}|^{v}$ during repetitive loading under zero-lateral strain conditions. The effect of initial void ratio e_0 and stress amplitude ratio $\Delta\sigma/\sigma_0$.

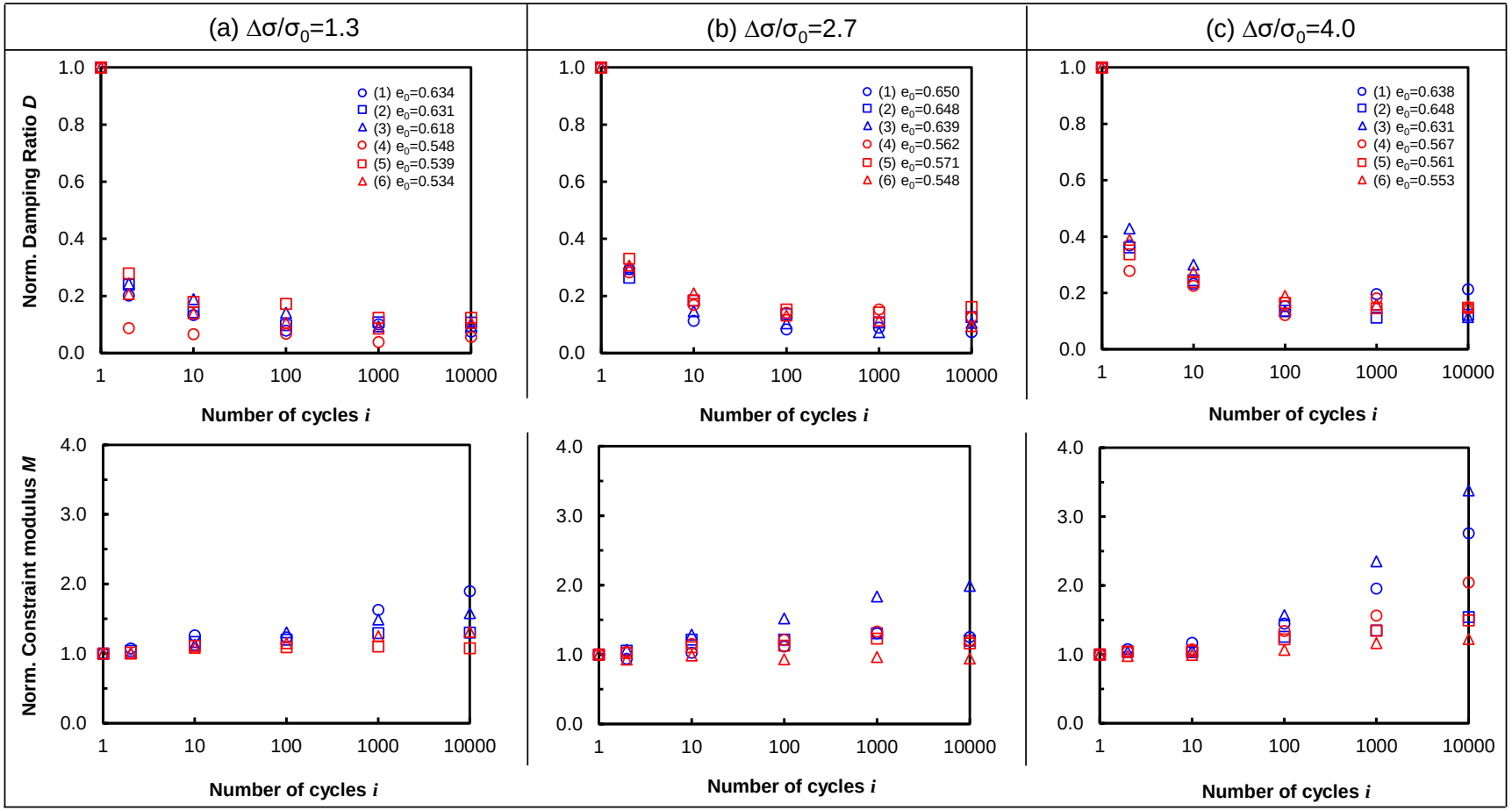

Figure 3.8. The evolution in damping ratio D and constraint modulus M versus number of cycles. Results show the normalized damping ratio and constraint modulus for different stress amplitude ratios $\Delta\sigma/\sigma_0$ and sediments with different initial void ratio e_0.

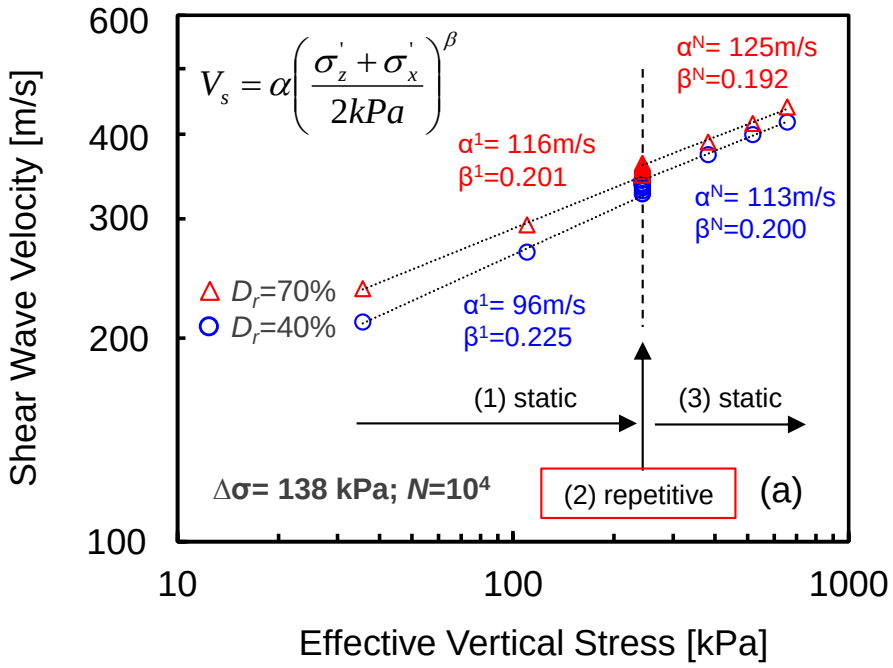
600
400
300
200
100
10
100
1000
Shear Wave Velocity [m/s]
Effective Vertical Stress [kPa]
$V_s = \alpha\left(\frac{\sigma_z' + \sigma_x'}{2kPa}\right)^{\beta}$
α^N= 125m/s
β^N=0.192
α^1= 116m/s
β^1=0.201
α^N= 113m/s
β^N=0.200
D_r=70%
D_r=40%
α^1= 96m/s
β^1=0.225
(1) static
(3) static
Δσ= 138 kPa; N=10⁴
(2) repetitive
(a)

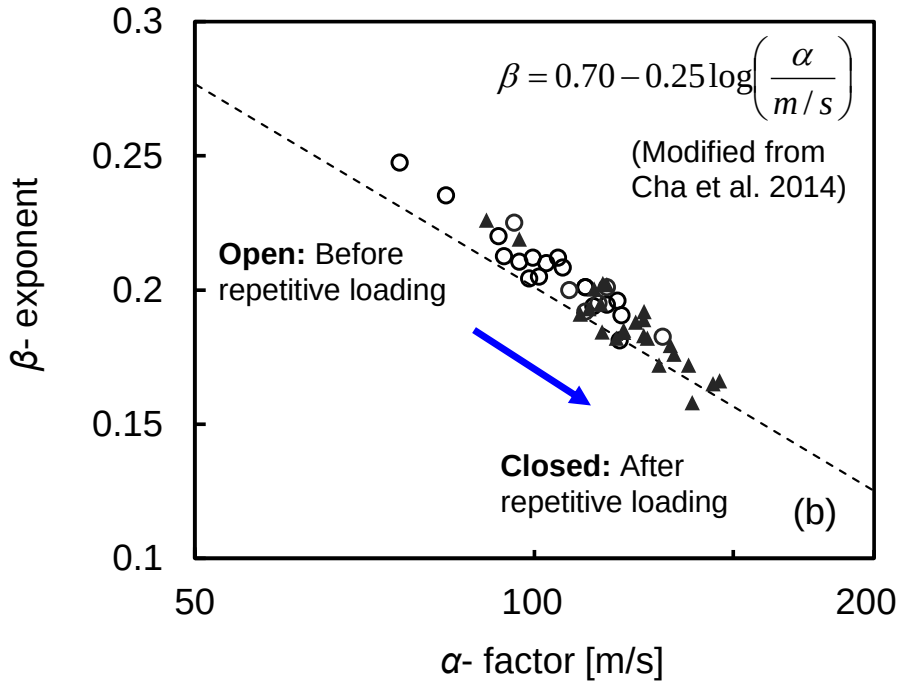
0.3
0.25
0.2
0.15
0.1
50
100
200
β- exponent
α- factor [m/s]
$\beta = 0.70 - 0.25\log\left(\frac{\alpha}{m/s}\right)$
(Modified from Cha et al. 2014)
Open: Before repetitive loading
Closed: After repetitive loading
(b)

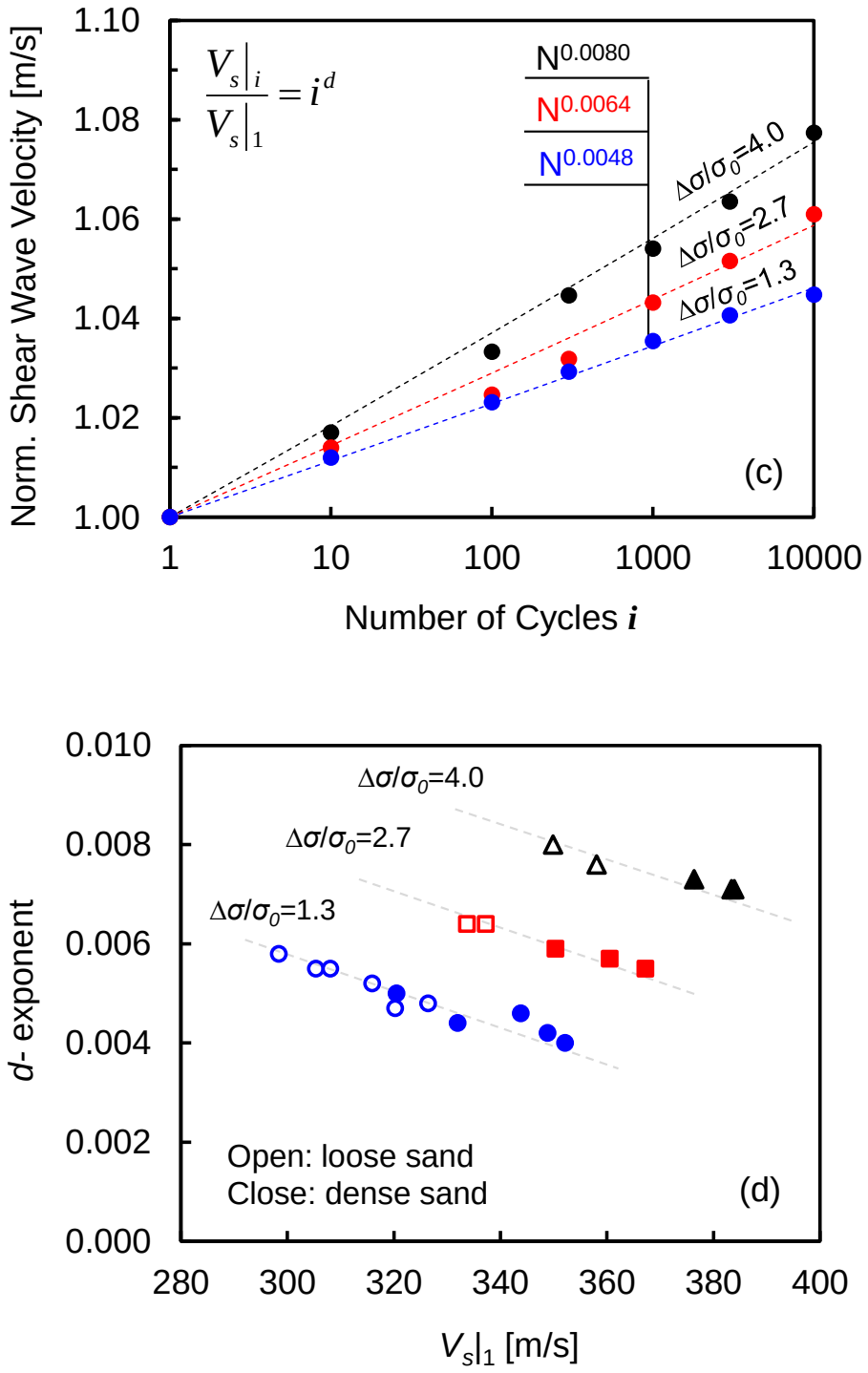

Figure 3.9. The evolution of shear wave velocity during static and repetitive loading stages - Particle contact and fabric change. (a) Shear wave velocity versus stress, (b) The α-factor and β-exponent before and after repetitive mechanical loading, (c) Normalized shear wave velocity versus number of cycles, and (d) The d-exponent versus shear wave velocity at the beginning of repetitive loading $V_s|_1$.

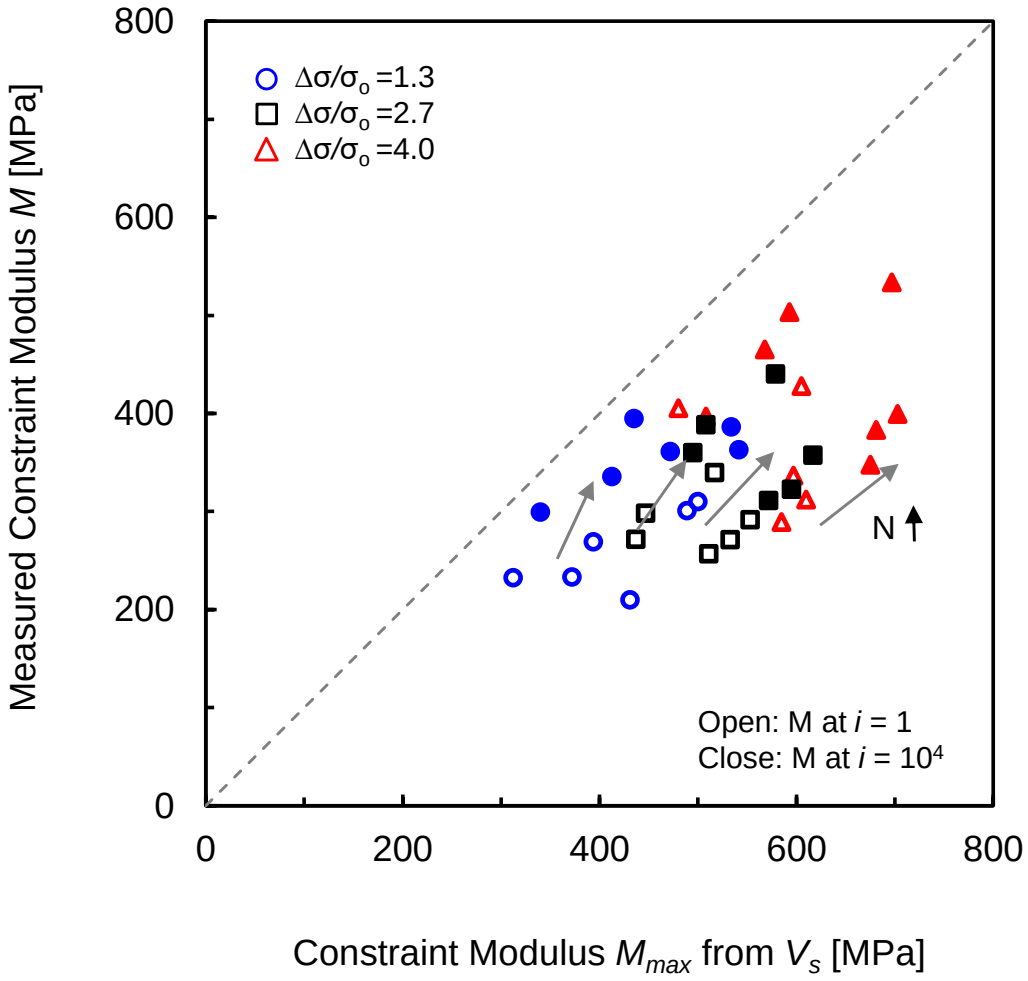

Figure 3.10. Measured constraint modulus M versus maximum constraint modulus M_{max} computed from shear wave velocity $M_{max}= 2\cdot(V_s^2\rho)(1-\nu)/(1-2\nu)$. Note: Small-strain Poisson's ratio ν= 0.15.

CHAPTER 4

SANDS SUBJECTED TO HIGH STRESS AMPLITUDE AND HIGH NUMBER OF CYCLES

4.1 Introduction

Particle crushing occurs in soils that experience high effective stress conditions such as deep foundations, earth dams, and reservoirs during oil extraction. Particle crushing increases the difficulties in predicting the shear strength and compressibility (Lade and Yamamuro 1996; Feda 2002; Uygar and Doven 2006; Sadrekarimi and Olson 2010). Furthermore, produced fines decrease the hydraulic conductivity due to the decrease in pore size, increase in specific surface, and the consequence of fines migration, entrapment, bridging, and clogging. In fact, fines produced during repetitive loading may trigger the undrained failure of railway ballast (Indraratna et al. 1997).

Particle crushing can result from high static stress as well as fatigue induced by repetitive loading. The amount of fines produced by repetitive loading may exceed the fines caused by high static stress. One could speculate that particle crushing mechanisms depend on the stress amplitude level and the number of cycles. For example, asperity breakage may prevail at large number of cycles while particle crushing or splitting should be dominant for high stress amplitude. Data show "tipping points" in the load-deformation response at a large number of cycles, despite relatively low levels of stress amplitudes (see data in Suiker et al. 2005; Indraratna et al. 2003; Werkmeister 2003; Wichtmann 2005; Werkmeister 2005; Indraratna et al. 2006; Fonseca et al. 2013;

Indraratna and Nimbalkar 2013). The non-linear response in the plastic strain ε^{pl} versus number of cycles challenges the prediction of permanent strain accumulation ε^{pl}_{acc}.

The purpose of this study is to advance the understanding of "tipping-points" in the load-deformation response of soils subjected to a large number of low stress amplitude cycles, and fewer number of but of high stress amplitude.

4.2 Experimental Study

The experimental program investigates the load-deformation response of sands under zero-later strain conditions subjected to: (1) one million loading cycles N=10^6 at a low stress amplitude of $\Delta\sigma$=100 kPa, and (2) hundred loading cycles N=100 at a high stress amplitude of $\Delta\sigma$=2, 4, 8, 12, and 20 MPa.

4.2.1 Tested Sand

Tested materials are "Ottawa 20/30 sand" and "KAUST 20/30 sand". Table 4.1 summarizes their index properties including the coefficient of uniformity C_u, particle shape (i.e. roundness), and extreme void ratios e_{max} and e_{min}.

4.2.2 Instrumented Oedometer Cells

This study uses two different sizes of oedometer cells to maintain the zero-lateral strain condition during repetitive loading. The dimensions of two oedometer cells with a floating ring system follow:

- Low stress amplitude cycles (Figure 4.1, floating ring: ID = 52.5 mm, wall thickness t=3.9 mm, and height H=100 mm; caps: OD = 50.8 mm and height h = 50.8 mm).

- High stress amplitude cycles Δσ=2-to-20 MPa (Figure 4.1, floating ring: ID = 76.2 mm, wall thickness t=35 mm, and height H=158 mm; caps: OD = 75 mm and height h = 76.2 mm).

The top and bottom caps for both cells involve parallel-type bender elements to minimize crosstalk and attain better shielding (Lee and Santamarina 2005). The dimensions of the bender elements are 12.7×8×0.7 (length × width × thickness in mm). A 5 mm cantilevered length of bender elements ensures better contact in soils. An LVDT (TransTek DC 0242) clamped to the top and bottom caps tracks changes in specimen height.

4.2.3 Stress-controlled Repetitive Loading System and Data Acquisition Systems

Figure 4.1 presents the stress-controlled repetitive loading system for one million loading cycles and high stress amplitude cycles.

- *Low stress amplitude cycles*. Figure 4.1(a) illustrates the repetitive loading system for one million cycles. This test setup consists of a stiff reaction frame, the tall floating ring oedometer cell, a pneumatic cylinder, and peripheral electronics. The PID controller (Proportional-integral-derivative controller) activates the sinusoidal stress amplitudes for the repetitive vertical loadings (see details in Park and Santamarina 2017a).
- *High stress amplitude cycles.* Figure 4.1(b) presents the repetitive loading system for high stress amplitude Δσ=2-to-20 MPa. The ISCO pump connected to the hydraulic jack (Enerpac, RSM-1000) generates the rectangular cyclic pressures to control the stress imposed on sands.

- *Data acquisition.* Figure 4.1 also shows the data acquisition system for vertical deformation and shear wave measurement. The LVDTs (TransTek, DC 0242) continuously monitor the vertical deformation of specimens which are saved by the data logger (Keysight 34970A). For shear waves, the function generator sends step input signals (freq=20 Hz, V=10 volt, Keysight 33210A). The mechanically-transformed shear waves pass through soils. The filter-amplifier establishes a 500 Hz high-pass and 200 kHz low-pass window (Krohn-Hite 3364). The computer saves the electrically-converted shear wave on the oscilloscope after stacking of 1024 signals (Keysight DSOX 2014A-stacking in Santamarina and Fratta 2005). Dimensions of bender elements are 12.7 × 8 × 0.7 (length × width × thickness in mm) with a 5 mm cantilevered length.

4.2.4 Specimen Preparation

This study uses Ottawa 20/30 sand and KAUST 20/30 sand for the one million loading cycles. The specimen preparation method involves different tamping energies to attain the target relative densities D_r = 30%, 50%, and 70%. The maximum and minimum void ratios data assist with the target relative densities (Table 4.1). On the other hand, we test KAUST 20/30 sand only for high stress amplitude cycles. The initial target relative density is $D_r \approx 75\%$ for all specimens. Note that the shear stiffness for test sand is G=29MPa for Ottawa 20/30 sand and G≈15GPa for KAUST 20/30 sand.

4.2.5 Test Procedures

The loading procedures for both the one million loading cycles and high stress amplitude cycles involve the "static-to-repetitive" loading history.

- *Low stress amplitude cycles*. The loading process involves: Static step loading up to 67 kPa (=σ_o) → Repetitive: 167 kPa…67 kPa (i.e. $\Delta\sigma$=100 kPa, stress amplitude ratios $\Delta\sigma/\sigma_o$ = 1.50) → Static step loading up to 507 kPa. When the number of load cycles successfully reaches one million N=10^6, the vertical effective stress monotonically increases to the maximum vertical stress, and then reduces in the reverse order for the static unloading. Loading cycles have a period of T=12 seconds for all specimens.
- *High stress amplitude cycles.* The loading process depends on five initial effective stresses σ_o (=0.5, 1, 2, 3, and 5 MPa). For example, static step loading up to σ_o = 5 MPa → Repetitive: 25 MPa…5 MPa (i.e. $\Delta\sigma$=20 MPa, stress amplitude ratios $\Delta\sigma/\sigma_o$ = 4). The test finishes when the number of load cycles reach N=100 to exclude the effect of a further increase in the static loads on particle crushing. The stress amplitude ratio is $\Delta\sigma/\sigma_o$=4 with a cyclic loading period T= 60 seconds for all specimens. Note that a monotonic oedometer test results up to σ'_v=24 MPa compares the load-deformation responses between static and repetitive loadings.

During the loading cycles, shear waves of the specimens are continuously measured at the same vertical effective stress $\sigma_o + \Delta\sigma$, at the top of cycles (i.e. i = 1, 10, 100, 300, 1000, … N=10^6). Table 4.2 summarizes all test conditions.

4.2.6 Sieve Analysis, Optical Microscopy, and Scanning Electron Microscopy SEM

This study tracks the changes in the particle size distribution of all specimens after repetitive loading tests. A sieve analysis provides the general information of particle size distribution associated with particle crushing. However, this may not capture a particle broken in half during crushing and still retained on its parent size sieve. The sieve analysis may consider this particle as fresh. Therefore, we employ optical microscopy and scanning electron microscopy to provide supplementary information.

4.3 Experimental Results

This section presents detailed experimental results for sand specimens subjected to low stress amplitude cycles (one million cycles; $\Delta\sigma$=100 kPa for $\Delta\sigma/\sigma_o$=1.50), and (2) high stress amplitude cycles (100 cycles; $\Delta\sigma$=2, 4, 8, 12, and 20 MPa for $\Delta\sigma/\sigma_o$=5).

4.3.1 Effective Stress σ'_v vs. Void ratio e

Figure 4.2 presents the change in void ratio for the five KAUST 20/30 sand specimens subjected to high stress amplitude cycles during static and high stress amplitude repetitive loadings history followed by the static unloading stage. The monotonic loading test (illustrated with an orange straight line) indicates that the yield stress is $\sigma_{yield}\approx$10MPa. The void ratio for all specimens decreases monotonically during the first static loading. Repetitive loading cycles result in more significant volume contraction as the stress amplitude $\Delta\sigma$ increases from 2 MPa-to-20 MPa. The void ratios of two specimens with $\Delta\sigma$=12 MPa and $\Delta\sigma$=20 MPa are even smaller than the minimum void ratio e_{min}=0.533 when the load cycles successfully reach N=100. For comparison,

Figure 4.2 also illustrates the change in void ratios for a KAUST sand specimen during one million loading cycles (black dotted square).

4.3.2 Evolution of Void Ratio

This section displays results that are strongly associated with the void ratio evolution during one million loading cycles and high stress amplitude cycles.

- *Low stress amplitude cycles.* Figure 4.3 shows that the change in the void ratio e versus the number of cycles i for three Ottawa 20/30 and three KAUST 20/30 sands. In the e-log(i) plot, the measured void ratios for both sands decrease linearly to the number of cycles $i \approx 10^4$, yet exhibit pronounced reduction after $i \approx 10^4$ cycles. The non-linear trend becomes more significant with a higher initial void ratio.
- *High stress amplitude cycles.* Figure 4.4 presents the void ratio evolution with the number of cycles for the five KAUST 20/30 sand specimens. Notable changes in the void ratio occur in the first 10 cycles and the volume contraction becomes more pronounced as the stress amplitude $\Delta\sigma$ increases from 2 MPa-to-20 MPa. In linear-log scale [Figure 4.4(b)], the void ratios for the stress amplitudes $\Delta\sigma$=12MPa and 20MPa show the significant deviation from linear trend. The onset of deviation occurs at the smaller number of loading cycles with a higher stress amplitude.

- *Terminal void ratio e_T.* Soil will attain an asymptotic void ratio when subjected to all kinds of repetitive loads. Figure 4.4 also plots a modified hyperbolic model (red dotted line) matched to the test results to estimate the terminal void ratio e_T as $i \rightarrow \infty$ (Modified from Chong and Santamarina 2016; Park and Santamarina 2017a). This model anticipates the void ratio e_i after a given number of loading cycle i as follows:

$$e_i = e_T + (e_1 - e_T)\left[1 + \left(\frac{i-1}{N^*}\right)^m\right]^{-1} \qquad \text{for } i \geq 1 \text{ and m} > 0 \qquad (4.1)$$

where m is a fitting constant, e1 is measured after the 1st cycle. The model parameter N* corresponds to the number of cycles where the asymptotic contraction in half (e1-eT)/2 occurs. This model fits the evolution of the void ratio well with the exception of the cases with stress amplitude Δσ=12 MPa Δσ=20MPa. However, this study accepts the terminal void ratio estimated for Δσ=12 and Δσ=20MPa from the lower boundary of the terminal-density perspective (Figures 4.3 and 4.4).

4.3.3 Shear Wave Signals

Figure 4.5 presents the typical shear wave signal cascades recorded during the "static-repetitive-static" loading history followed by an unloading sequence. The first arrival times of shear waves in two test conditions decrease during the first static step loading. The change in the first arrival time is more pronounced for high stress amplitude Δσ=5-to-25 MPa. The first arrival time slightly decreases as the number of cycles increases. However, minimal changes in the first arrival times hinder the accurate determination of the shear wave velocity during repetitive load cycles. Thus, we use CODA wave analysis for signal processing to determine the shear wave velocities (Snieder 2006; Dai et al. 2013).

4.4 Analyses and Discussion

In this section, we report and analyze the complete dataset produced with the 11 tests performed for this study (Table 4.1).

4.4.1 Particle Size

Figure 4.6 presents particle size distribution curves obtained from one million cycles and high stress amplitude loading cycles for 2-to20MPa. The particle size distribution after crushing exhibits a linear trend in log-log scale. The amount of fines produced during crushing increases with a higher stress amplitude. The repetitive load with $\Delta\sigma$=20MPa results in more fines compared with the monotonic load at a similar stress level. Furthermore, the amount of fines produced increases with more angular particle shapes and higher initial void ratio (Lee and Farhoomand 1967; Sadrekarimi and Olson 2010). Details follow in the next section.

4.4.2 Particle Crushing in Granular Packing

The particle crushing mechanism depends on two opposing factors: size *d* and coordination number *CN* (Valdes 2002; Guimaraes et al. 2007). A smaller size of particle has a higher mean tensile strength when subjected to an axial force *F* ($\sigma_{yield} = F/d^2$). However, the particle size distribution curve in Figure 4.6 indicates that the fines produced results from particle crushing without significant changes in the particle size distribution of its parent sand. This observation further underlines the importance of the coordination number on the particle crushing mechanism. In other words, the smaller particles in a granular packing typically attain a lower coordination number, therefore

possess a higher probability of crushing (McDowell 1999; Coop et al. 2004; Guimaraes et al. 2007; Sadrekarimi and Olson 2010). The production of finer particles is accelerated once smaller particles produced by particle splitting or asperity breakage exist in a given granular packing.

4.4.3 Particle Shape

An optical microscopy and scanning electron microscopy SEM capture further insight of the underlying deformation mechanism associated with the "tipping point" that may result from asperity breakage, particle slitting and crushing. Figure 4.7 shows the microscopic images of sand particles after repetitive loading with $\Delta\sigma$=20MPa. It is clear that the finer the particle size produced, the more angular the particle shapes.

Figure 4.8 displays the SEM images of particles. The SEM images capture the abrasion on the particle surface, asperity breakage, micro fractures, the clean cross-sectional area due to the particle splitting, and plate- or blade-like finer particles with sharper edges. This image analysis indicates that sand particles tend to split through the inherent cleavage planes as the shape becomes more angular and the size becomes finer due to the relatively smaller coordination number.

We match the particle shape after crushing and sphericity and roundness in Krumbein and Sloss 1963 the according to the particle size. Figure 4.9 indicates that the finer the particle size produced, the more angular the particle shape (see similar results in Guimaraes et al. 2007; Sadrekarimi and Olson 2010). The flat and blady geometry of fines leads to the higher probability of bridge formation in the clogging mechanism.

4.4.4 Terminal Void Ratio e_T

A soil will reach a stable asymptotic terminal void ratio e_T when subjected to repetitive loading (D'Appolonia and D'appolonia 1967; Narsilio and Santamarina 2008). Figure 4.10 presents the terminal void ratio e_T against the initial void ratio e_o [in Figures 4.3 and 4.4, Equation 4.1]. The terminal void ratio of sands for one million cycles varies with the initial void ratio e_o (red circle and red triangle, $\Delta\sigma/\sigma_o = 1.50$). On the other hand, the terminal void ratio for high stress amplitude indicates that the asymptotic volume contraction $\Delta e=e_o-e_T$ under the similar initial packing condition depends on not only stress amplitude ratio $\Delta\sigma/\sigma_o$, but also the stress amplitude $\Delta\sigma$ if a load-deformation process involves particle crushing with higher stress levels. We use this observation to estimate the repetitive load-induced maximum settlement in the next section.

4.4.5 Maximum Change in Relative Density ΔD_T

The ratio between the asymptotic contraction $\Delta e=e_o-e_T$ to the attainable void ratio range $e_{max}-e_{min}$ assists with estimates of the maximum change in relative density ΔD_T at $i\rightarrow\infty$ with the initial relative density $D_{i=0}$ at $i=0$ during repetitive loading (Chong and Santamarina 2016):

$$\Delta D_T = \frac{e_{i=o} - e_T}{e_{\max} - e_{\min}} \tag{4.2}$$

$$D_{i=0} = \frac{e_{\max} - e_{i=0}}{e_{\max} - e_{\min}} \tag{4.3}$$

Figure 4.11(a) presents ΔD_T versus $D_{i=0}$ for six specimens for one million cycles and five specimens mixtures for high stress amplitudes. Once again, the stress amplitude ratio $\Delta\sigma/\sigma_o$ and stress amplitude $\Delta\sigma$ control the anticipated maximum asymptotic

contraction during repetitive loading. The terminal densities for stress amplitudes $\Delta\sigma$= 12MPa and 20 MPa will be even higher than D_r=100%.

Figure 4.11(a) also displays a curve fitting model to predict the maximum change in relative density ΔD_T that is a function of the stress amplitude ratio $\Delta\sigma/\sigma_o$, stress amplitude $\Delta\sigma$, and initial relative density $D_{i=0}$ (note: we assume that a volume contraction does not take place at the minimum void ratio e_{min} if $\sigma_o + \Delta\sigma < \sigma_{yield} \sim 10$MPa):

$$\Delta D_T = \frac{\left(\frac{\Delta\sigma}{\sigma_0}\right)\left[1 - D_{i=0}\right]^n}{M} = \frac{\left(\frac{\Delta\sigma}{\sigma_0}\right)\left[1 - D_{i=0}\right]^n}{14 - 0.6 \cdot \Delta\sigma} \tag{4.4}$$

where *M* is a model parameter determined by matching the fitting model to test results, and this is a function of stress amplitude $\Delta\sigma$. The *n*-parameter determines the curvature of the model. The underlying assumption for the estimation of ΔD_T is that there is no repetitive load-induced volume contraction if the stress $\sigma_o + \Delta\sigma < \sigma_{yield}$. This assumption leads to gain four *M*-parameters for the stress amplitude $\Delta\sigma$=0.1, 2, 4, and 8 MPa which provide a linear trend for m=14 – 0.6·$\Delta\sigma$ [Figure 4.11(b)]. The linear guideline bounds the two *M*-parameters for the stress amplitude $\Delta\sigma$=12 MPa and 20 MPa which estimate the ΔD_T in the range of $D_{i=0}$ = 0-to-0.95.

4.4.6 Volumetric Strain: Tipping Point

Figure 4.12 plots the volumetric strain ε_{vol} versus the number of cycles during one million repetitive loading cycles. The evolution of the volumetric strain for all sand specimens during one million cycles implies that soils retain memory of their initial

fabric even after a very large number of cycles. In other words, a loosely packed-soil exhibit a “tipping point” at an earlier number of cycles.

For comparison, volumetric strain data extracted from published studies are superimposed on Figure 4.12. The non-linear trend observed in linear-log scale supports that a large number of cycles imposed on particle contacts may cause an emergent deformation mechanism such as fatigue-induced asperity breakage.

4.4.7 Load-Deformation - Relevant Analogues

Fatigue-induced asperity breakage is analogous to particle splitting or crushing. It describes a possible deformation mechanism associated with “tipping point” for engineering purposes. Two straight lines imposed on Figures 4.13(a) and (b) emphasize progressive repetitive load-deformation processes during one million cycles (Zone I and II) and during high stress amplitude cycles (Zone III and IV):

- *Zone* I. It involves the collapse of an unstable array of particles, particle sliding and rolling into the pore spaces, shear deformation and compaction due to the skeleton deformation, and denser packing induced by particle rearrangement (Lambe and Whitman 1969; Omidvar et al. 2012). Note that local contact stresses in a granular packing will be generally much greater than the mean stresses at the end of *Zone* I (Djordjevic and Morrison 2006; Sadrekarimi and Olson 2010).
- *Zone* II. The soil reaches a quite stable deformation state after $i \approx 2\times10^4$ [Figure 4.13(a)]. However, the higher stress concentration fluctuated during a large number of loading cycles remains on local particle contacts. Eventually, the accumulated fatigue

results in a yielding of local contacts followed by the onset of asperity breakage. This particle-level deformation leads to the second part of volume contraction.

- *Zone* III. Particle splitting and crushing prevail the deformation mechanism that involves a significant fines generation (Level III damage, Mesri and Vard 2009). The fines produced by high stress amplitude cycles may exhibit two different processes: (1) void-filling if its size is small enough to fit into pores between parent particles, or (2) resources for subsequent crushing events and production of much finer particles.
- *Zone* IV. The fines produced begin to fill the pores and the void-filling becomes dominant. This leads to the increase in coordination numbers. The change in void ratio while i=10→20 is a half of the volume contraction for the first ten cycles. The soil fabric becomes more stable as the number of cycles increase.

From the engineering perspective, the deformation responses in *Zone* II and *Zone* III require special attention due to the abrupt change in a sediment settlement when subjected to a large number of cycles or high stress amplitude cycles.

4.4.8 Shear Wave Velocity

The shear wave velocity is a power function of the vertical σ'_z and horizontal σ'_x effective stresses (Roesler 1979; Yu and Richard 1984; Santamarina et al. 2001):

$$V_s = \alpha\left(\frac{\sigma'_z + \sigma'_x}{2\,kPa}\right)^{\beta} = \alpha\left(\frac{\sigma'_z}{1kPa}\right)^{\beta}\left(\frac{1+K_0}{2}\right)^{\beta} \tag{4.5}$$

where the α-factor is the shear wave velocity at effective stress σ'_{mean}= 1 kPa, and the β-exponent represents the stress sensitivity of the shear wave velocity. The shear wave

velocity-stress relation captures both contact behavior and fabric changes (Cha et al. 2014).

Figure 4.14(a) presents the evolution of the shear wave velocity measured during the (1) static, (2) repetitive (N=10^6), and (3) static loading stages for three KAUST 20/30 sand specimens. The sand becomes stiffer with a higher α-factor and a lower β-exponent and the soil fabric becomes less sensitive to stress changes after repetitive loading.

Figure 4.14(b) plots the change in shear wave velocity measured during the static loading states for five KAUST 20/30 sand specimens [refer to test procedure, Note: the arrow in Figure 4.14(b) indicates the initiation of the loading cycle and for clarity, the evolution of the shear wave velocity during the repetitive loading stage will follow in the next section]. The shear wave velocity-effective stress relationship exhibits a linear trend in log-log scale at σ_v < 10 MPa. However, the relationship shows a higher α-factor and a lower β-exponent in the stress level above σ_v > 10 MPa (i.e. test procedures for $\Delta\sigma$=12 MPa and 20 MPa). This observation indicates that particle crushing significantly enhances the particle contact and fabric stability (refer to Figure 4.6). Furthermore, the shear wave velocity-effective stress relationship captures the yield stress of sediments under high stress conditions.

4.4.9 Shear Wave Velocity Evolution

Figure 4.15(a) presents the shear wave velocity against the number of loading cycles for three Ottawa 20/30 sand and three KAUST 20/30 sand specimens subjected to subjected to one million loading cycles. The evolution of the shear wave velocity for all specimens depends on the initial packing condition. The drastic increase in small strain

stiffness at the number of cycles $i \approx 10^4$ results from the asperity breakage, and becomes more pronounced as the initial void ratio increases.

Figure 4.15(b) illustrates the evolution of the shear wave velocity measured during the hundred loading cycles with stress amplitudes ranging from 2-to-20 MPa for five KAUST 20/30 sand specimens. In the linear-log scale, the shear wave velocity evolves linearly with the number of cycles for the three stress amplitude $\Delta\sigma$=2 MPa, 4 MPa, and 8 MPa. However, the shear wave velocity for the stress amplitudes $\Delta\sigma$=12 MPa and 20 MPa deviates from the linear trend after i > 40. This observation involves a dominant pore-filling mechanism, enhanced particle contacts, and reinforced soil fabrics associated with all fines produced by particle crushing under a high stress condition $\sigma_o + \Delta\sigma > \sigma_{yield}$. The evolution of the shear wave velocity captures the role of fines produced on sediment small strain stiffness.

4.5 Conclusions

This study investigated the repetitive load-deformation response of soils subjected to a large number of cycles or high stress amplitude loading cycles. The main conclusions follow:

- Optical microscopy and scanning electron microscopy SEM reveal that the finer the particle sizes produced, the more angular the particles are.
- Sand particles subjected to a large number of cycles or high stress amplitude cycles tend to split through the inherent cleavage planes with more angular particle shape, finer particle size, and higher initial void ratio. The lower coordination number in a looser granular packings lead to a higher probability of crushing.

- The soil reaches a stable asymptotic terminal void ratio e_T when subjected to repetitive loading and retains memory of its initial fabric even after a very large number of cycles or high stress amplitude cycles. In particular, a loosely packed sand exhibits a “tipping point” at an earlier number of cycles.
- Fatigue-induced asperity breakage and particle splitting or crushing are associated with a “tipping point” in the deformation-cycle response.
- The evolution of the shear wave velocity during one million cycles depends on the initial packing conditions. The significant increase in small strain stiffness as the number of cycles approaches $i \approx 10^4$ reflects the asperity breakage, and becomes more pronounced as the initial void ratio increases.
- The fines produced during high stress amplitude cycles contribute to pore-filling, markedly enhance particle contacts, and reinforce the soil fabric. The evolution of the shear wave velocity during high stress amplitude cycles captures the role of produced fines on the sediment small strain stiffness.

Table 4.1. Tested sand – Properties.

Property	KAUST 20/30 sand	Ottawa 20/30 sand
Particle size D [mm]	0.60 ~ 0.85	0.60 ~ 0.85
Roundness R	0.60	0.90
Coefficient of uniformity C_u	1.20	1.20
Specific gravity G_s	2.65	2.65
Maximum void ratio e_{max}	0.786	0.742
Minimum void ratio e_{min}	0.533	0.502
Critical state friction angle ϕ_{cs}	31^o	27^o
Intercept (in e-log p') Γ	0.845	0.802
Slope (in e-log p') λ	0.074	0.047

Table 4.2. Test conditions

	No.	σ_o [MPa]	$\Delta\sigma$ [MPa]	$\sigma' = \sigma_o + \Delta\sigma$ [MPa]	σ'/σ_o	Tested sand	Initial void raito $e_{initial}$	Void ratio at i=0 e_o
One million cycles	[1]	0.067	0.1	0.167	2.5	Ottawa 20/30	0.673	0.669
	[2]	0.067	0.1	0.167	2.5	Ottawa 20/30	0.631	0.627
	[3]	0.067	0.1	0.167	2.5	Ottawa 20/30	0.583	0.582
	[4]	0.067	0.1	0.167	2.5	KAUST 20/30	0.735	0.731
	[5]	0.067	0.1	0.167	2.5	KAUST 20/30	0.694	0.696
	[6]	0.067	0.1	0.167	2.5	KAUST 20/30	0.639	0.638
High stress amplitude cycles	[7]	0.5	2	2.5	5	KAUST 20/30	0.597	0.587
	[8]	1	4	5	5	KAUST 20/30	0.589	0.577
	[9]	2	8	10	5	KAUST 20/30	0.589	0.572
	[10]	3	12	15	5	KAUST 20/30	0.590	0.568
	[11]	5	20	25	5	KAUST 20/30	0.591	0.561

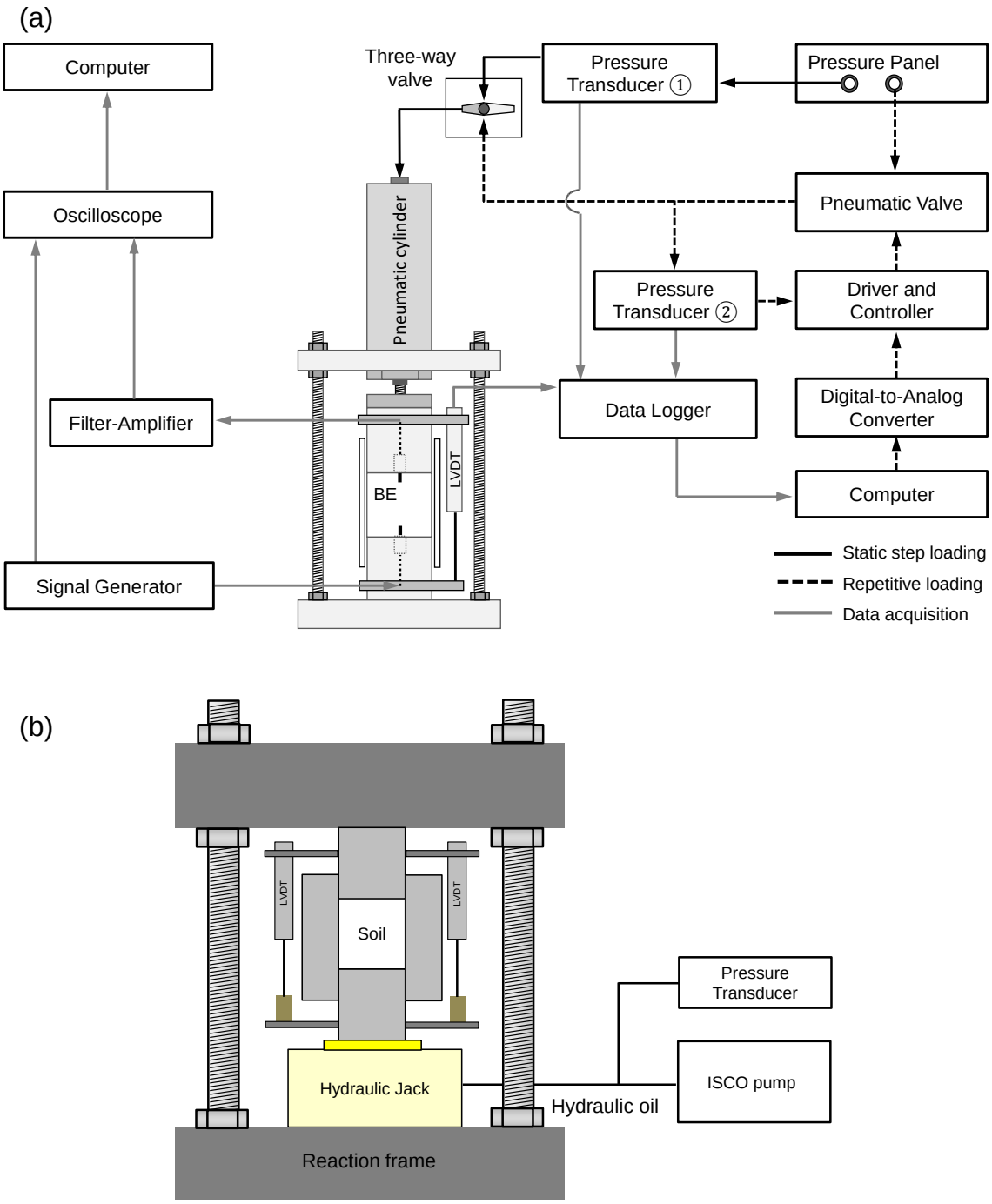

Figure 4.1. Instrumented oedometer cells with floating ring, top and bottom caps, bender elements BE, and LVDT clamps. (a) One million loading cycles. Top and bottom cap: 50.8 mm diameter and 50.8 mm height. Floating ring: ID= 52.5 mm, OD= 60.3 mm, and 100 mm height, Schematic diagram of the pneumatic system used for static and repetitive loading is also described here. (b) High stress amplitude cycles. Floating ring: ID = 76.2 mm, wall thickness t=35 mm, and height H=158 mm; caps: OD = 75 mm and height h = 76.2 mm. The peripheral electronics are used to measure deformation and shear waves.

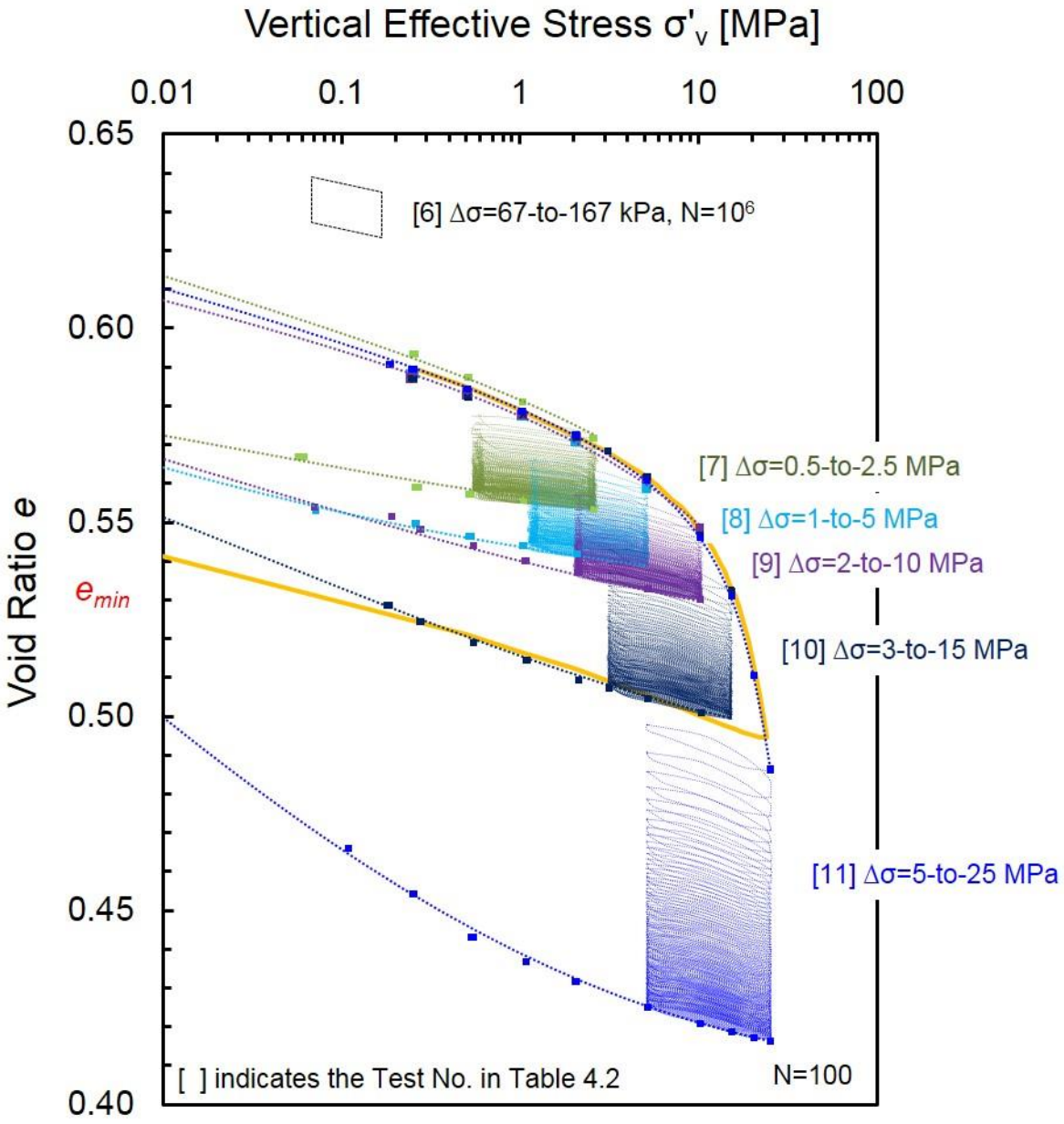

Figure 4.2. The change in void ratio during the static and high stress amplitude repetitive loading history followed by the static unloading sequence. Black dotted square indicates the change in the void ratio for a KAUST sand specimen during one million loading cycles. [ ] indicates the Test No. 6, 7, 8, 9, 10, and 11 in Table 4.2 (note: minimum void ratio for KAUST 20/30 sand is e_{min}=0.533).

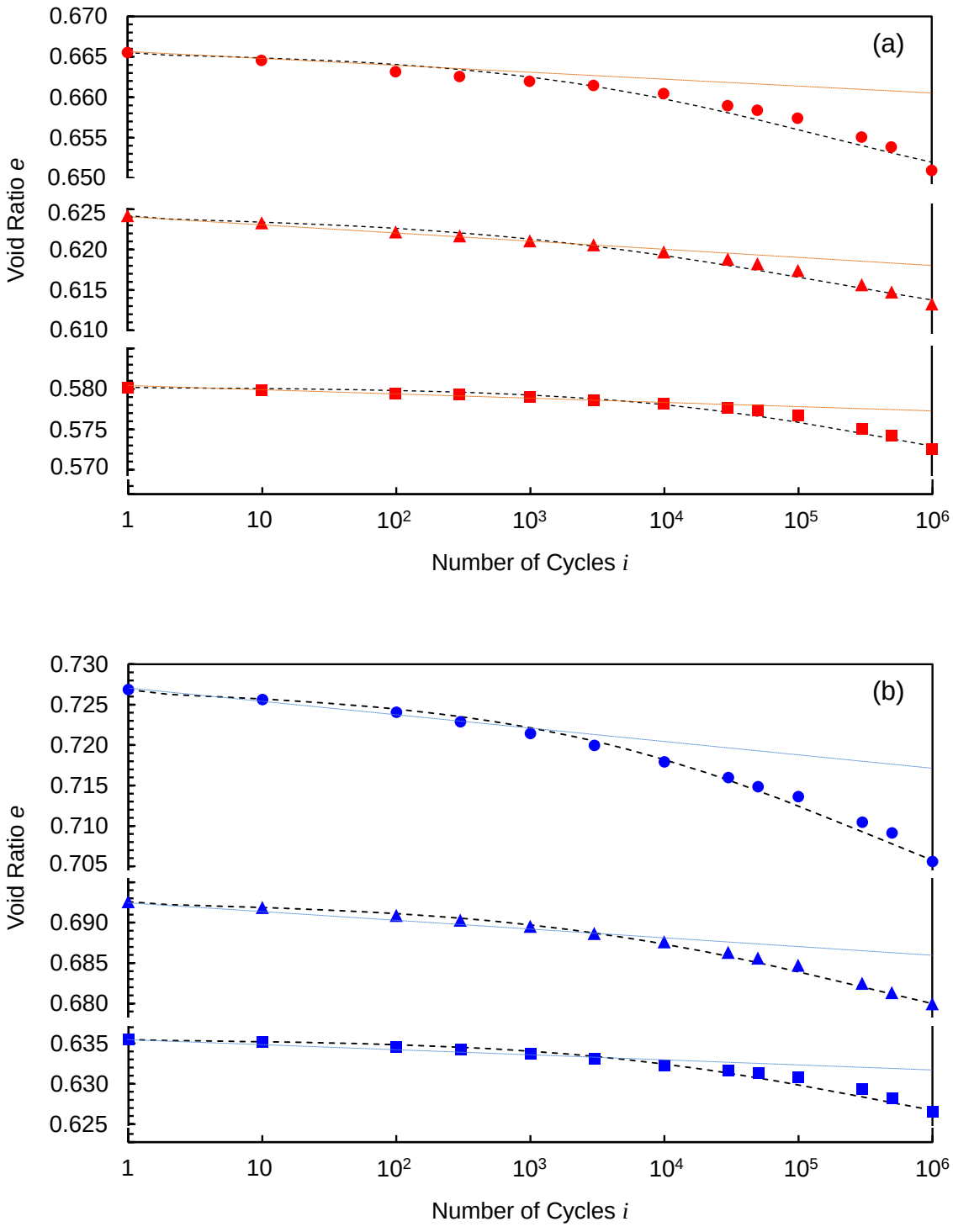

Figure 4.3. Evolution of void ratio during one million loading cycles against number of cycles *i*. (a) Ottawa 20/30 sand, (b) KAUST 20/30 sand. Test conditions: σ_o= 67 kPa, stress amplitude ratio $\Delta\sigma/\sigma_o$= 1.50 (from $\Delta\sigma$= 67-to-167 kPa).

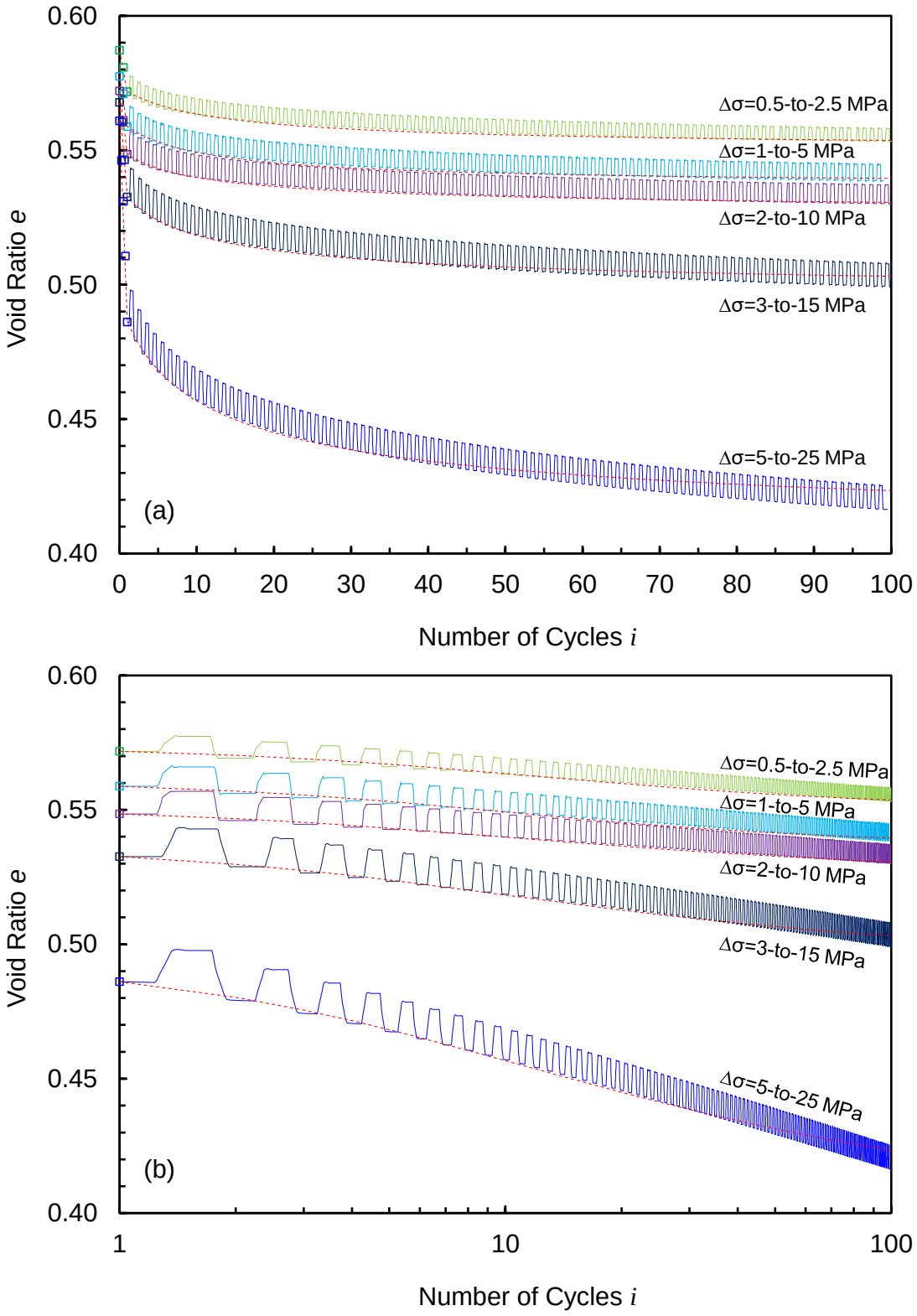

Figure 4.4. Evolution of void ratio against number of cycles *i* during high stress amplitude loading cycles. (a) Linear scale, (b) Logarithmic scale. Test conditions: stress amplitude ratio $\Delta\sigma/\sigma_o$= 4.0 for all specimens [refer to Table 4.2].

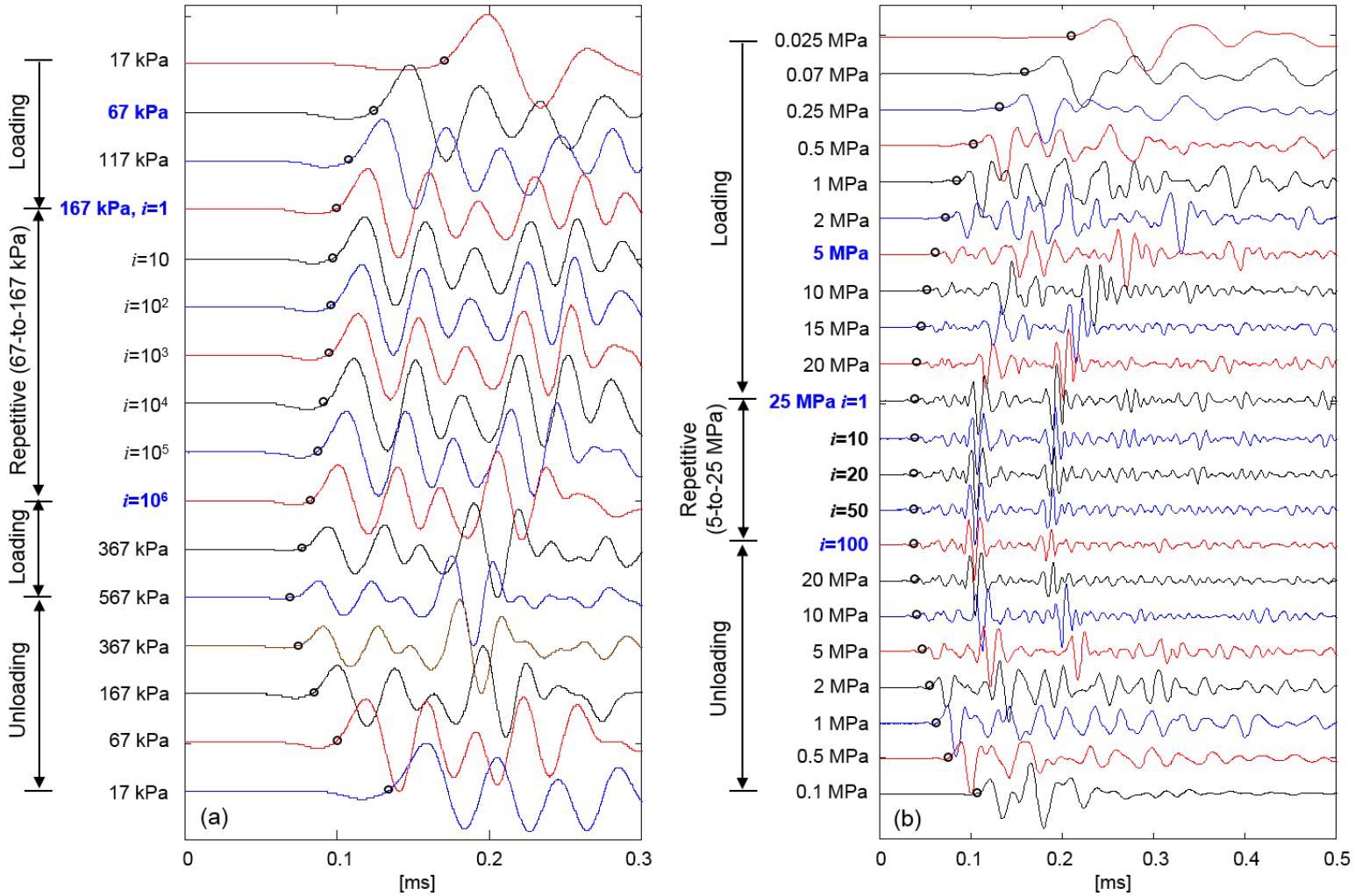

Figure 4.5. Cascade of shear wave signals. (a) One million loading cycles. Test conditions: σ_o=67 kPa, stress amplitude ratio $\Delta\sigma/\sigma_o$= 1.50 (from $\Delta\sigma$= 67-to-167 kPa). (b) High stress amplitude loading cycles. Test conditions: σ_o =5 MPa, stress amplitude ratio $\Delta\sigma/\sigma_o$= 4 (from $\Delta\sigma$= 5-to-25 MPa), and total number of cycles N= 100.

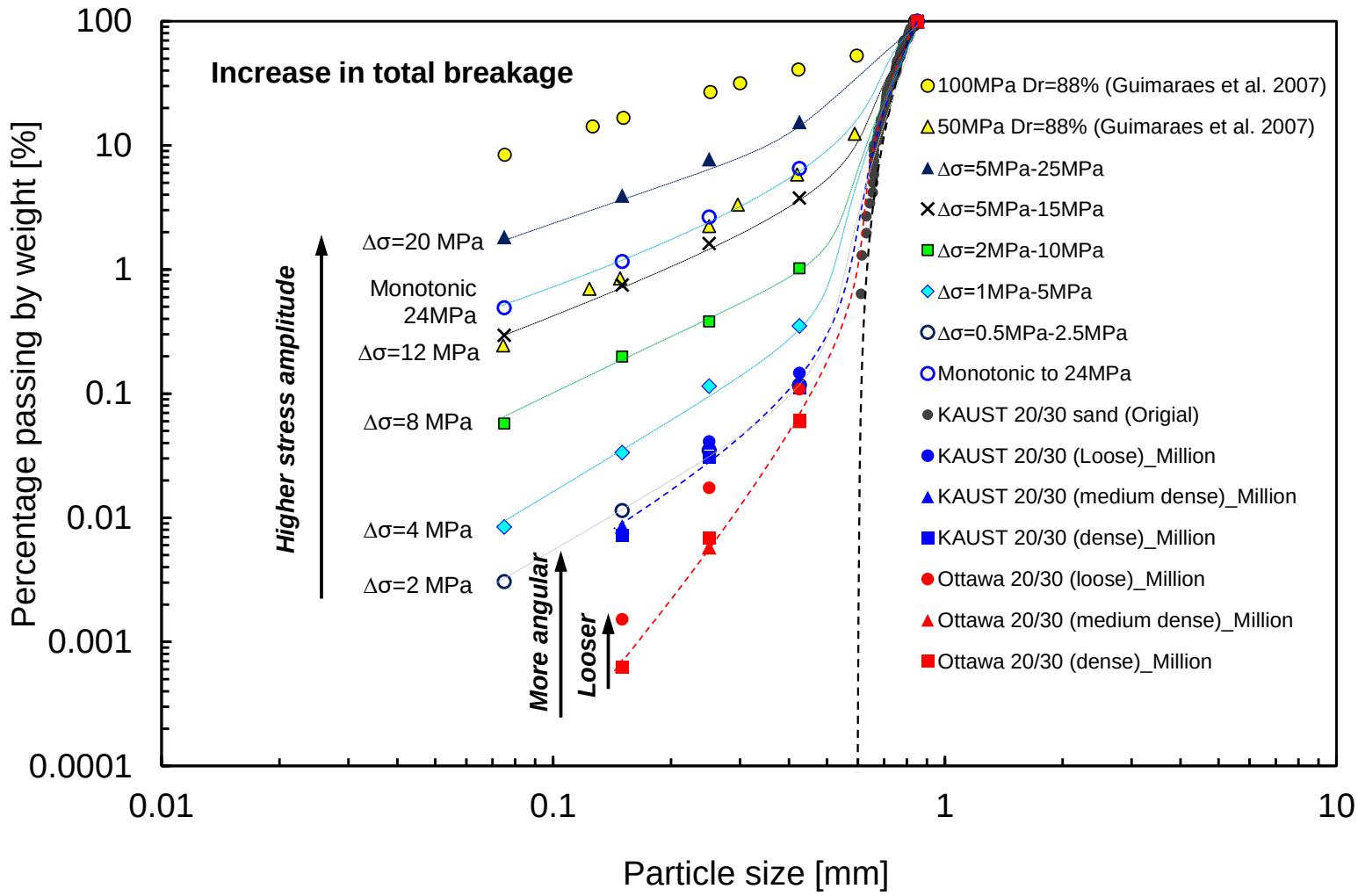

Figure 4.6. Particle size distribution curve after one million loading cycles and high stress amplitude loading cycles. Black circle indicates the original particle size distribution curve for KAUST 20/30 sand.

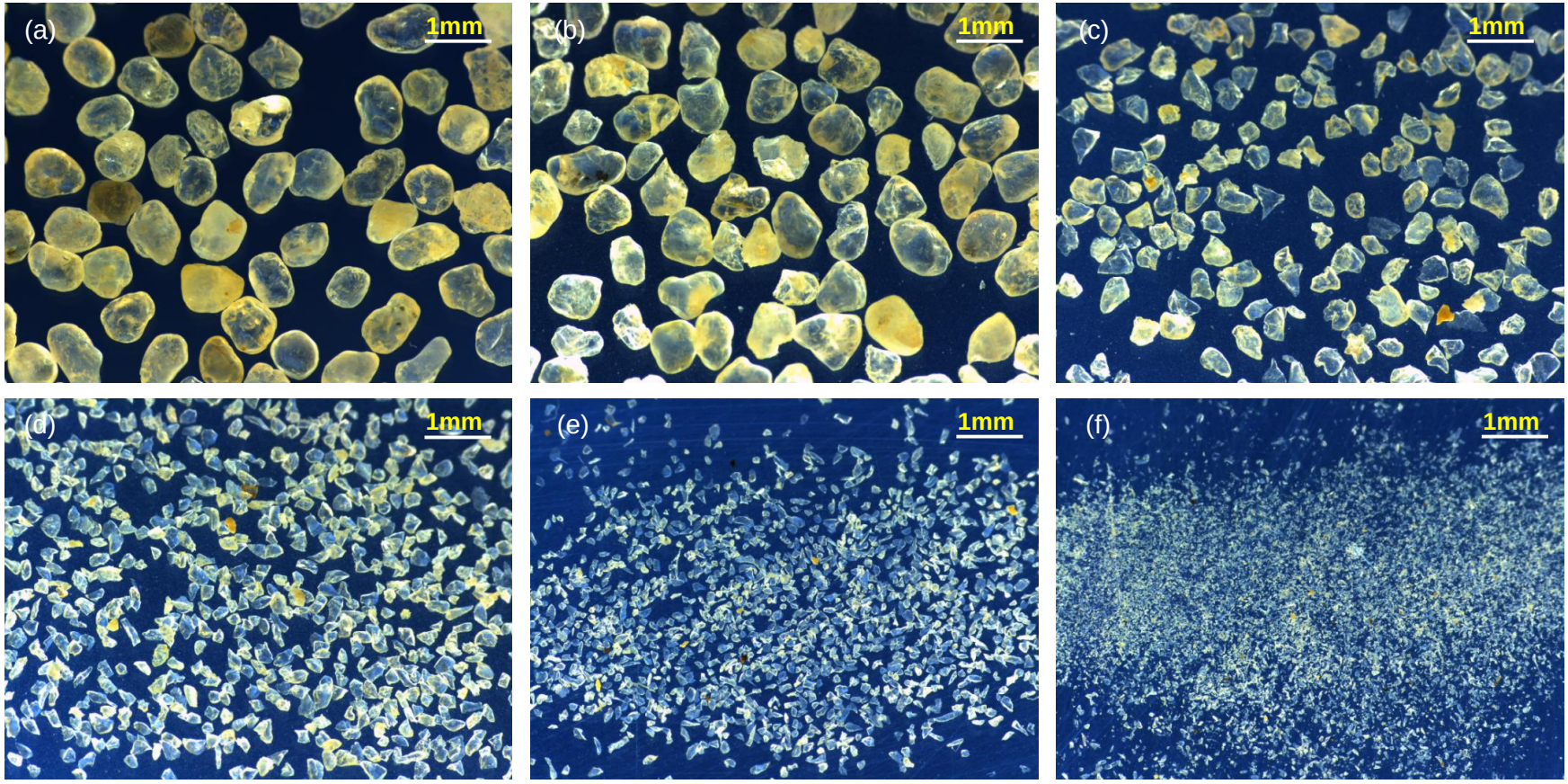

Figure 4.7. Microscopic images of KAUST 20/30 sand after high stress amplitude loading cycles. Test conditions: σ_o =5 MPa, stress amplitude ratio $\Delta\sigma/\sigma_o$= 4 (from $\Delta\sigma$= 5-to-25 MPa).

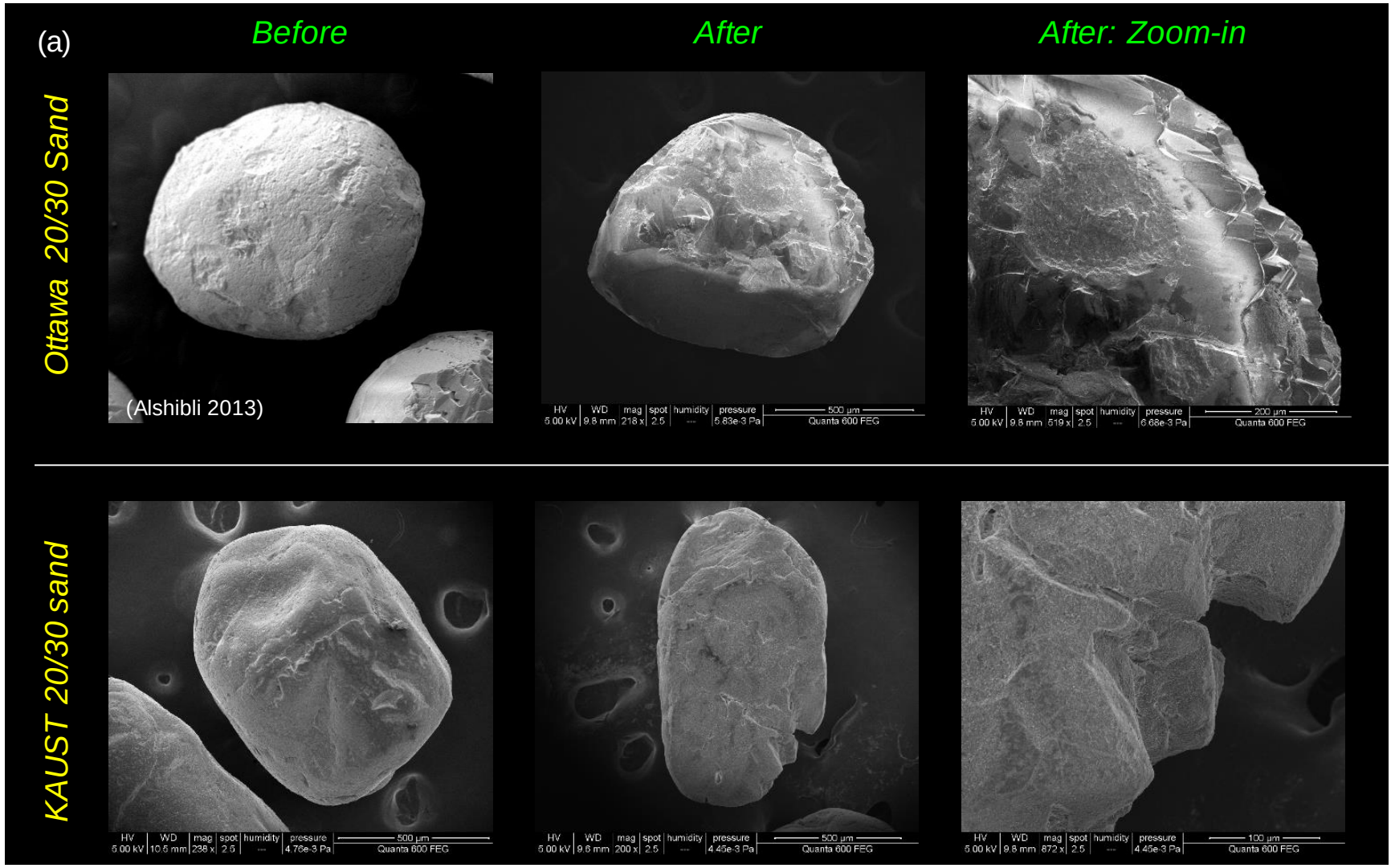
(a)
Before
After
After: Zoom-in
Ottawa 20/30 Sand
(Alshibli 2013)
HV 5.00 kV | WD 9.8 mm | mag 218 x | spot 2.5 | humidity --- | pressure 5.83e-3 Pa | 500 µm | Quanta 600 FEG
HV 5.00 kV | WD 9.8 mm | mag 519 x | spot 2.5 | humidity --- | pressure 6.68e-3 Pa | 200 µm | Quanta 600 FEG
KAUST 20/30 sand
HV 5.00 kV | WD 10.5 mm | mag 238 x | spot 2.5 | humidity --- | pressure 4.76e-3 Pa | 500 µm | Quanta 600 FEG
HV 5.00 kV | WD 9.6 mm | mag 200 x | spot 2.5 | humidity --- | pressure 4.45e-3 Pa | 500 µm | Quanta 600 FEG
HV 5.00 kV | WD 9.8 mm | mag 872 x | spot 2.5 | humidity --- | pressure 4.45e-3 Pa | 100 µm | Quanta 600 FEG

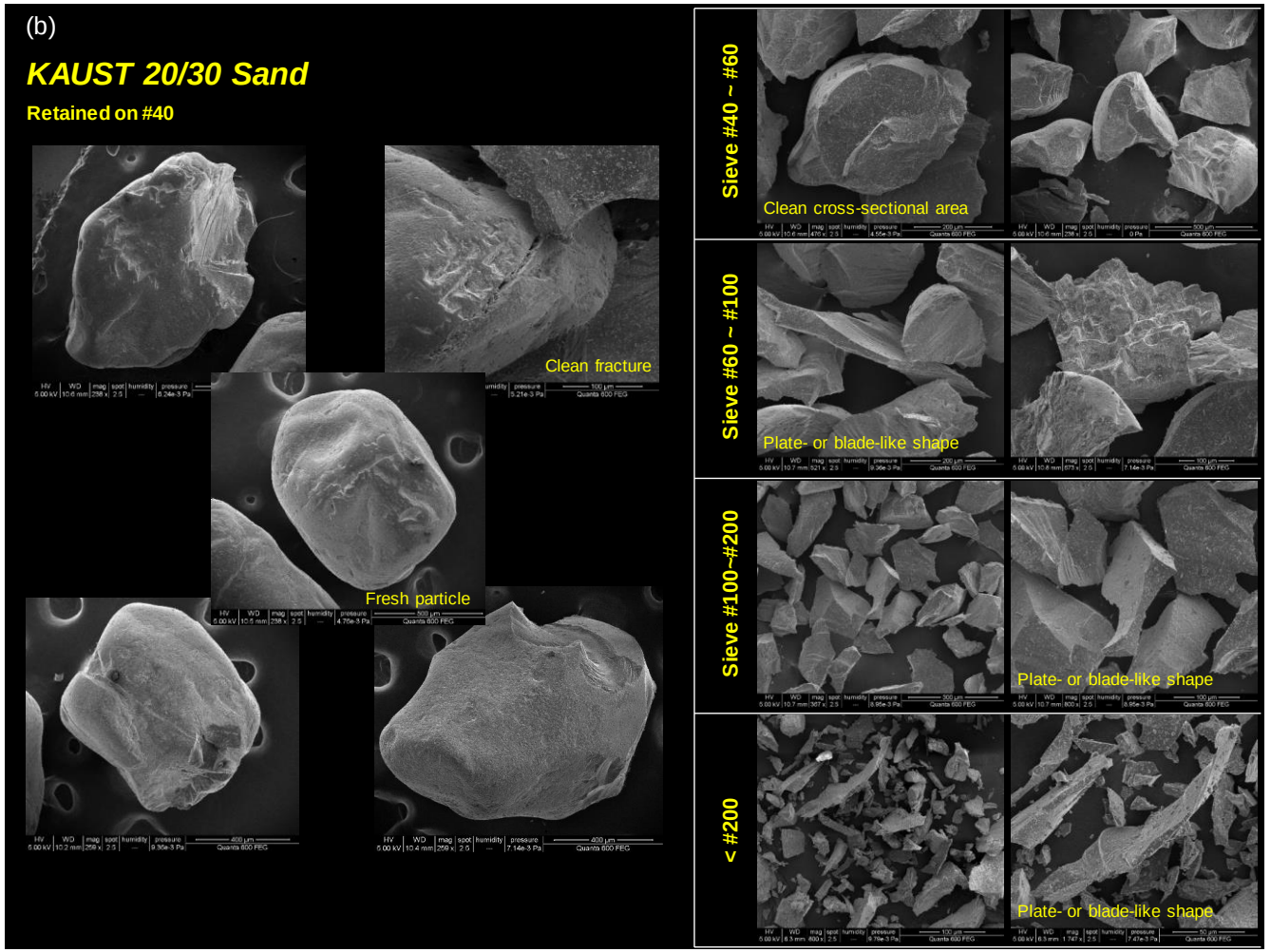

Figure 4.8. Scanning Electron Microscope SEM: (a) Low stress amplitude Δσ with large number of cycles for Ottawa 20/30 sand (local abrasion) and KAUST 20/30 sand (asperity breakage), (b) High stress amplitude Δσ with small number of cycles for KAUST 20/30 sand. Note that SEM image captures the clear fracture, clean cross-sectional area, and plate-like finer particles with shaper edges. In addition, the particle shape becomes more angular as the particle size becomes smaller.

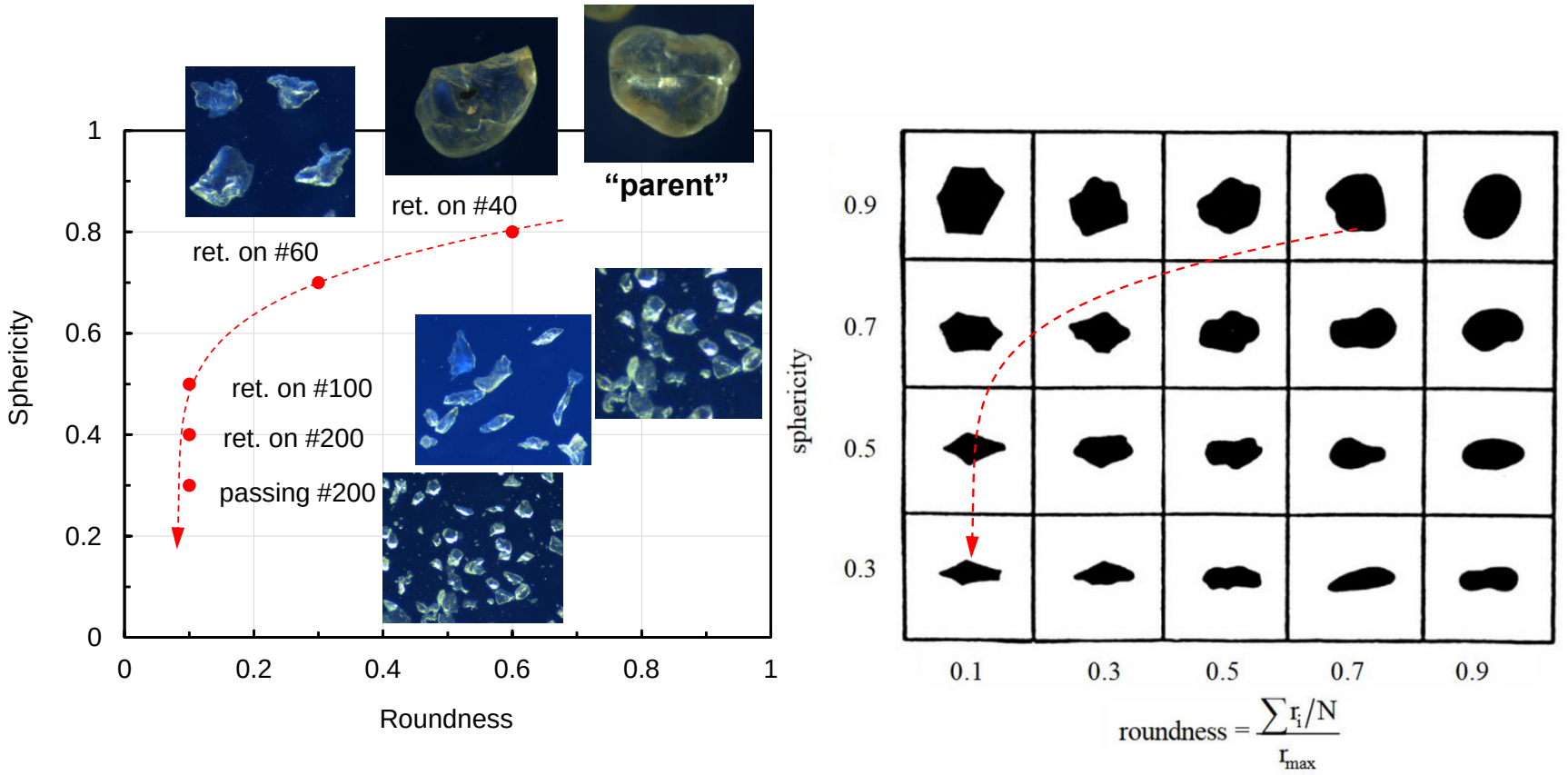

Figure 4.9. Variation of sphericity and roundness for fines produced during crushing [The chart obtained from Krumbein and Sloss (1963)].

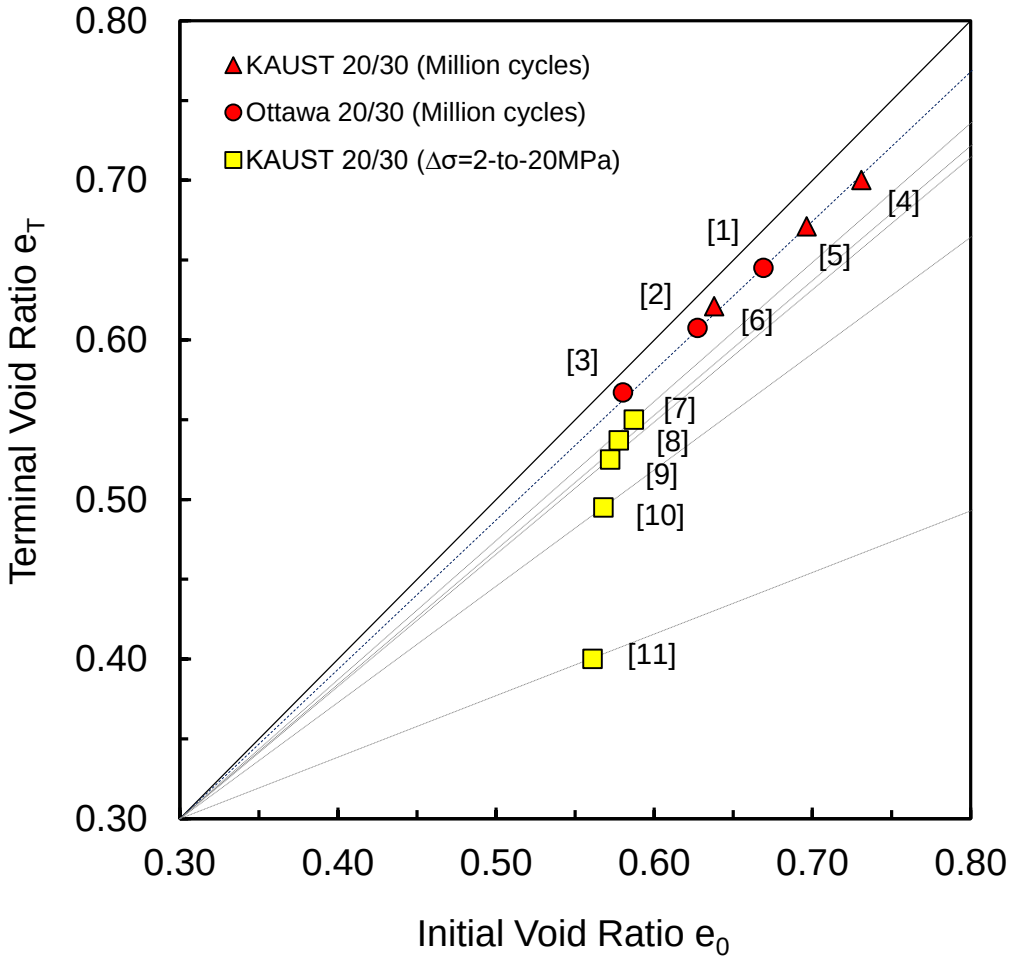

Figure 4.10. Terminal void ratio e_T versus initial void ratio e_0. Test conditions for million cycles: σ_o=67 kPa, stress amplitude ratio $\Delta\sigma/\sigma_o$= 1.50 (from $\Delta\sigma$=67-to-167 kPa). Test conditions for high stress amplitude loading cycles: σ_o =0.5-to-5 MPa, stress amplitude ratio $\Delta\sigma/\sigma_o$= 4 (refer to Table 4.2 for test conditions), and total number of cycles N= 100. [ ] indicates the Test No. in Table 4.2.

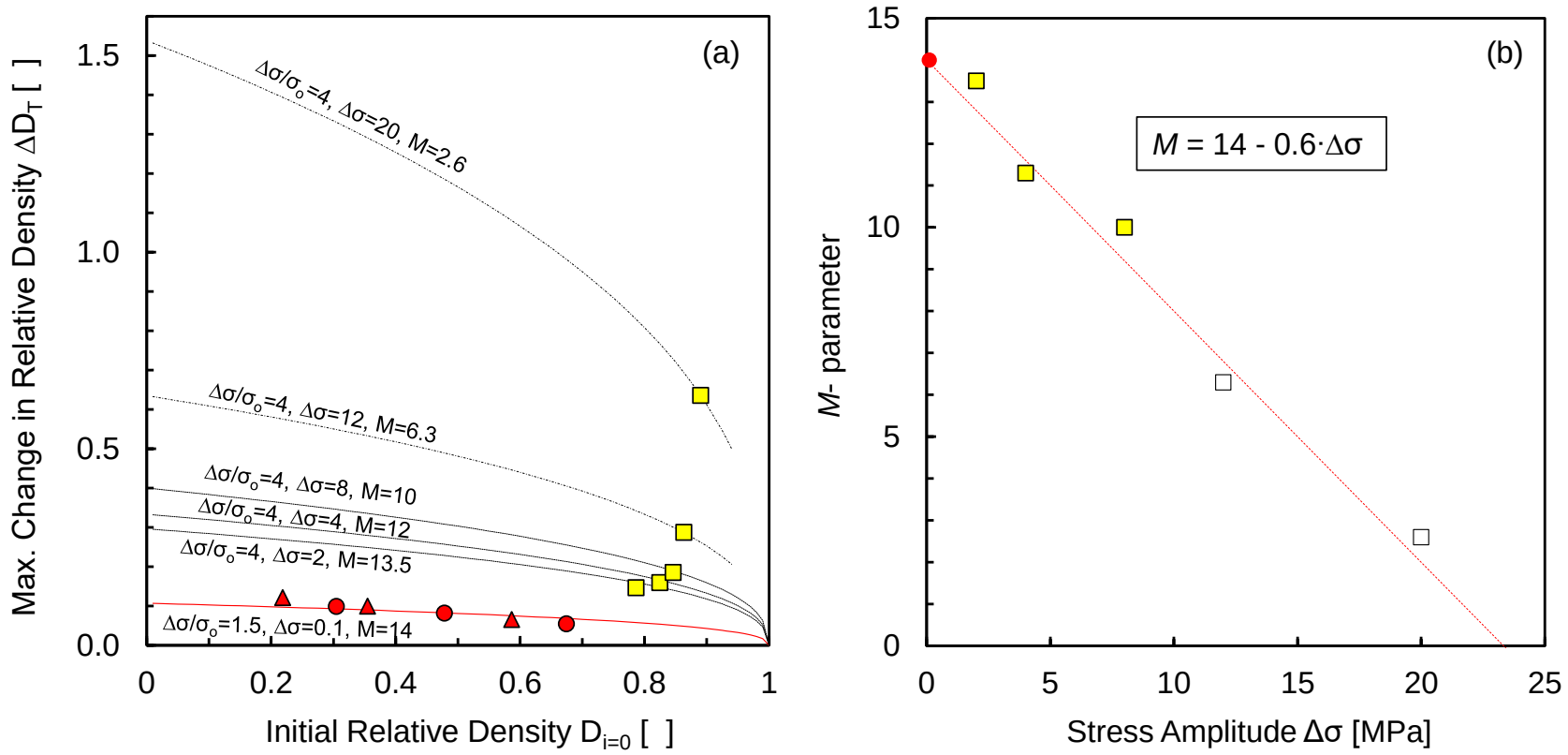

Figure 4.11. Estimation of maximum settlement due to the repetitive loading. (a) Maximum change in relative density ΔD_T versus initial relative density $D_{i=0}$ at i=0 (b) M-parameter with stress amplitude $\Delta\sigma$.

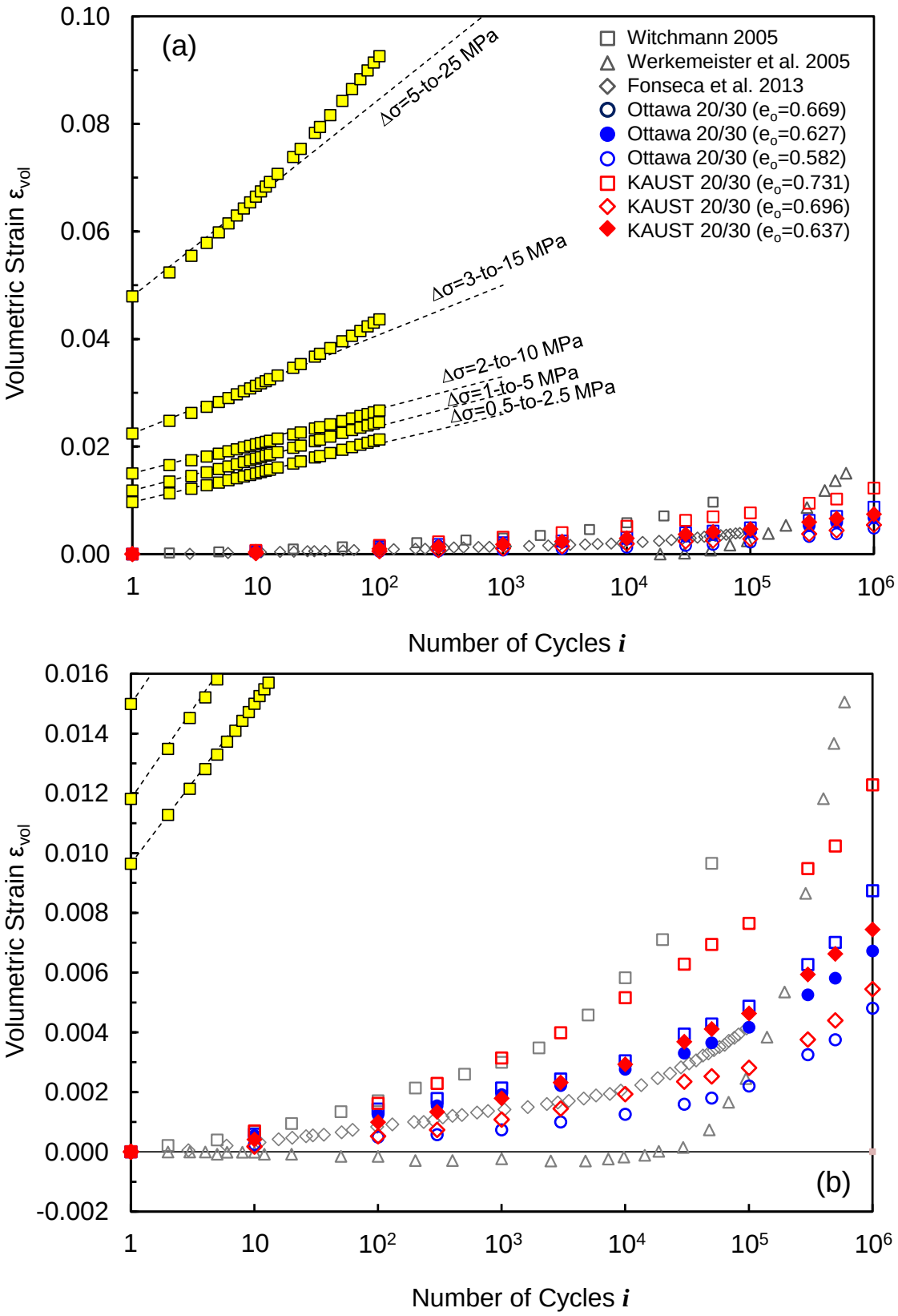

Figure 4.12. Volumetric strain ε_{vol} with number of cycles during one million of repetitive loading cycles and high stress amplitude loading cycles.

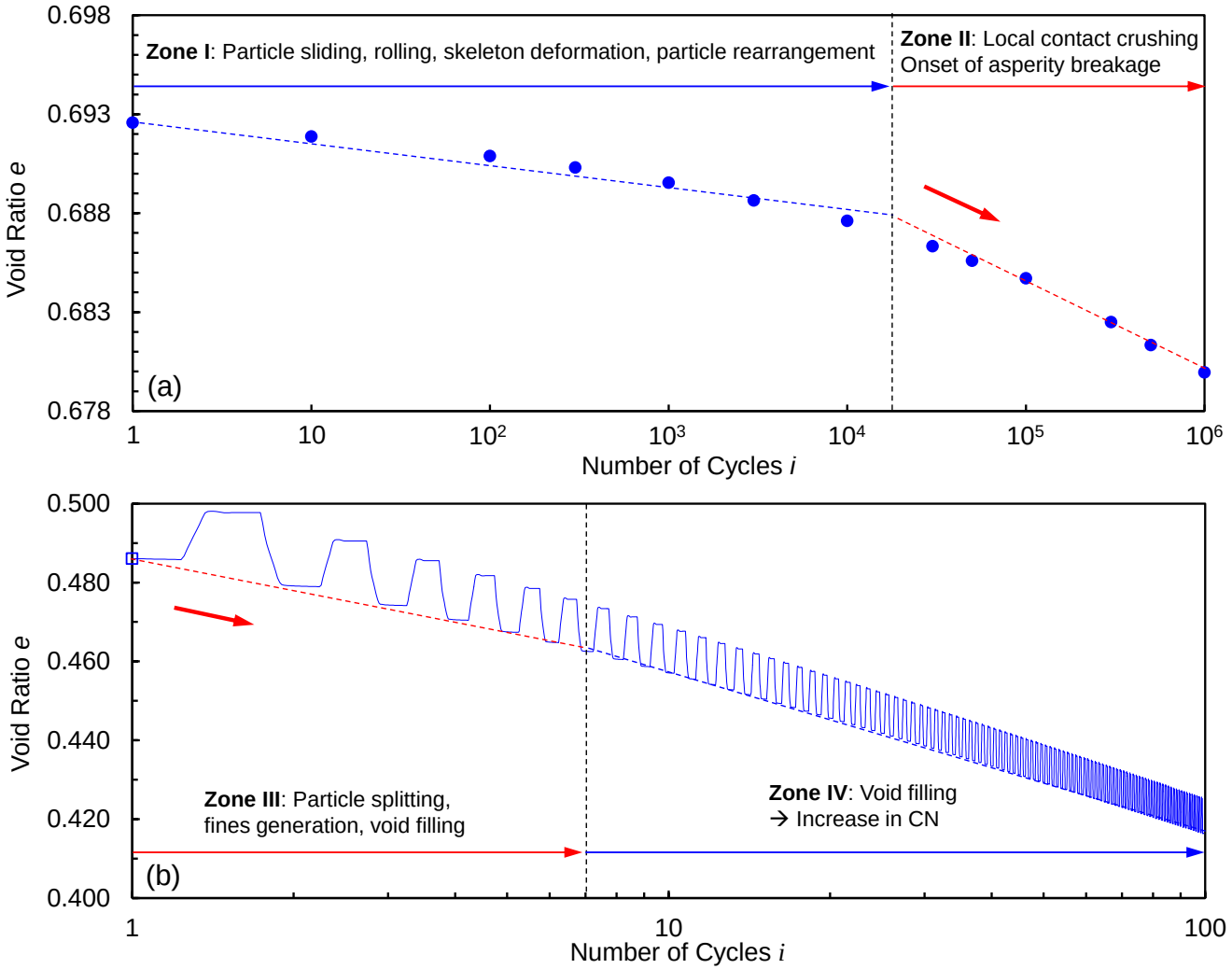

Figure 4.13. Void ratio evolution with number of cycles. (a) Million loading cycles. Test conditions: σ_o=67 kPa, stress amplitude ratio $\Delta\sigma/\sigma_o$= 1.50 (from $\Delta\sigma$= 67-to-167 kPa). (b) High stress amplitude loading cycles. Test conditions: σ_o =5 MPa, stress amplitude ratio $\Delta\sigma/\sigma_o$= 4 (from $\Delta\sigma$= 5-to-25 MPa).

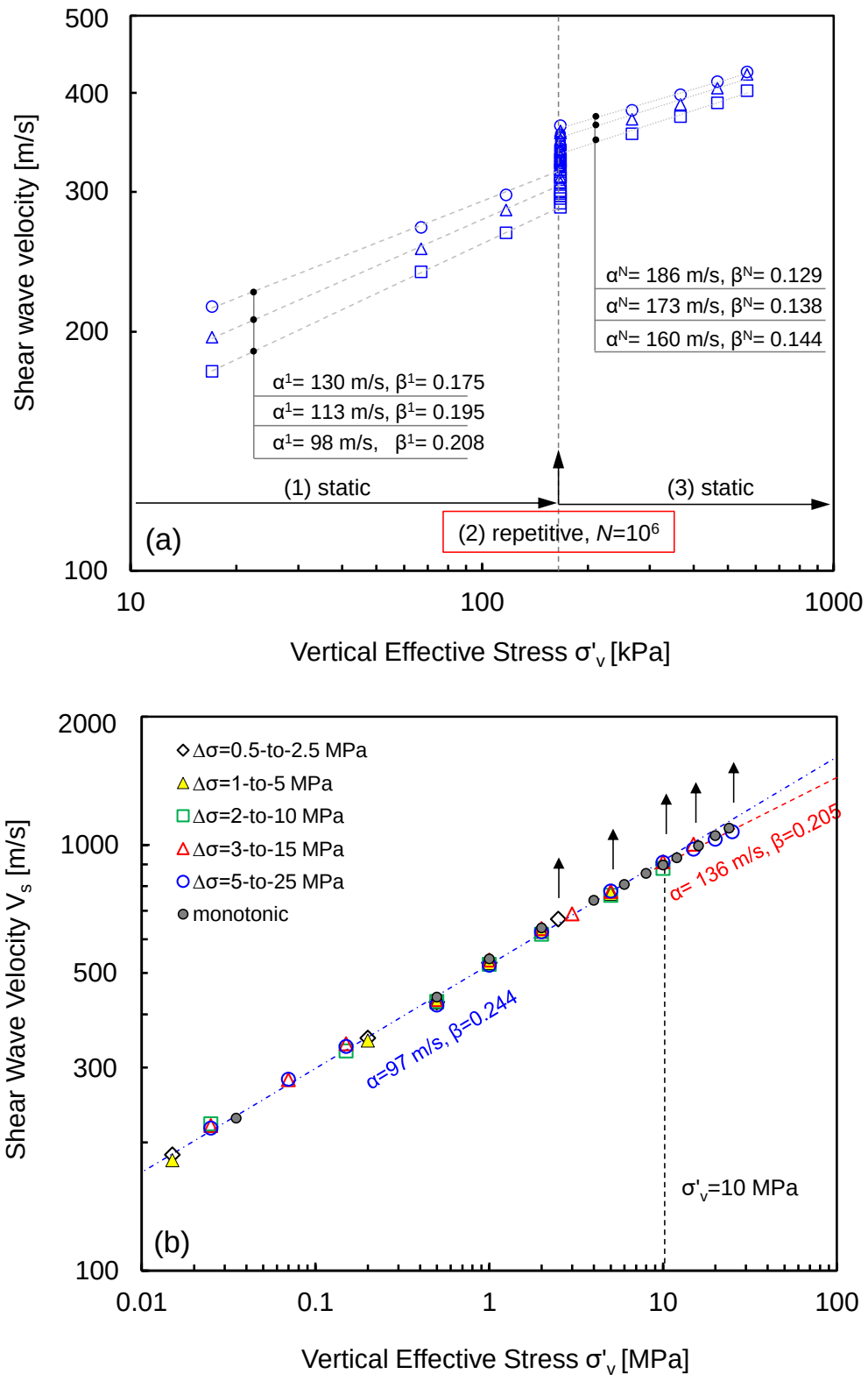

Figure 4.14. Shear wave velocity captured during the loading history. (a) Million cycles, (b) High stress amplitude loading cycles. The arrow indicates the initiation of loading cycles at a given stress $\sigma_o+\Delta\sigma$.

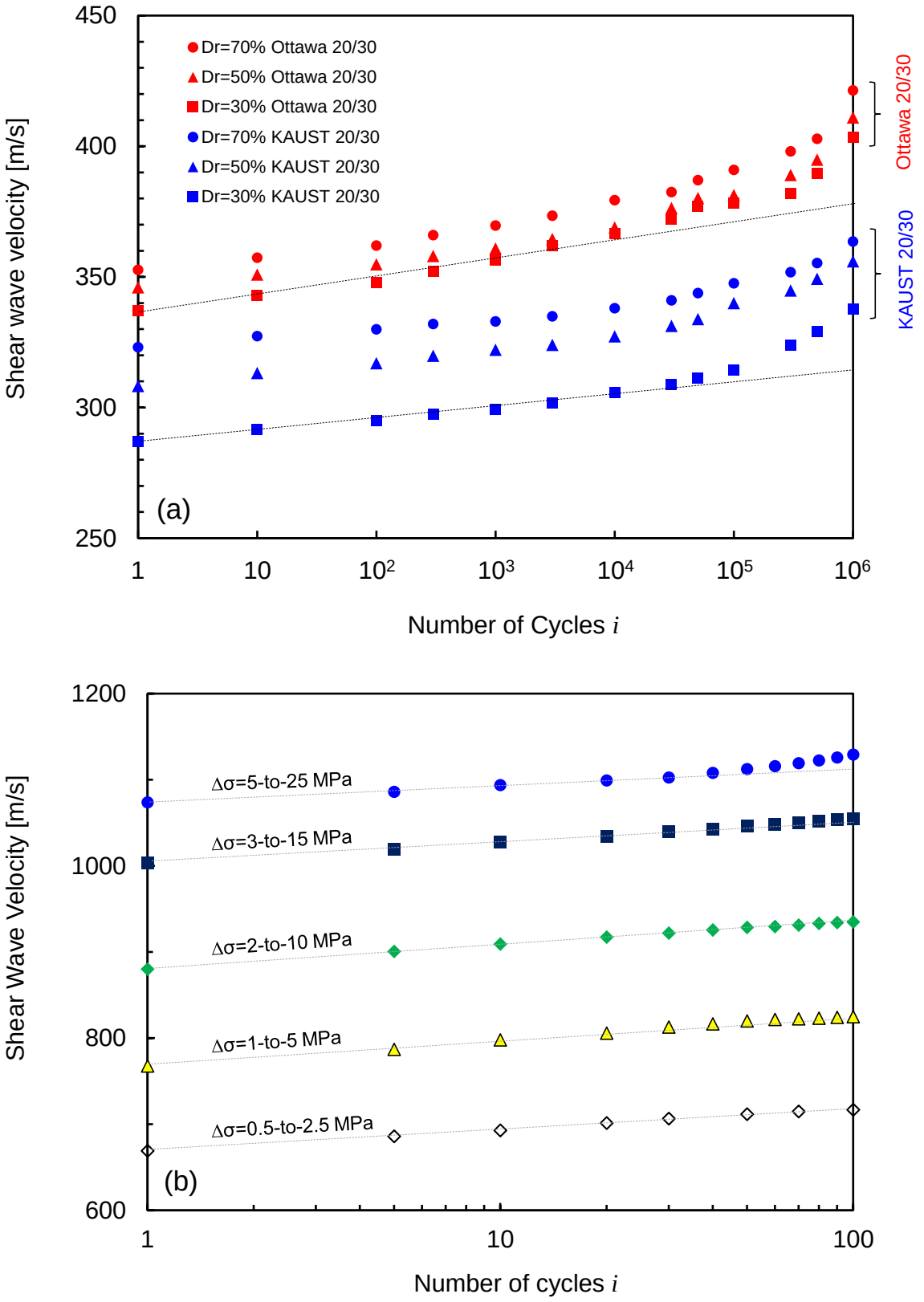

Figure 4.15. Evolution of the shear wave velocity with number of cycles. (a) Million loading cycles. (b) High stress amplitude loading cycles.

CHAPTER 5

LONG-TERM RESPONSE OF SAND-FINES MIXTURES SUBJECTED TO REPETITIVE MECHANICAL LOADS UNDER ZERO-LATERAL STRAIN CONDITIONS

5.1 Introduction

Soils often experience repetitive mechanical loads. The soil response to repetitive loads controls the long-term performance of geo-systems. Numerous studies reveal the remarkable features of plastic strain accumulation and void ratio evolution for mono-sized sands subjected to repetitive mechanical loads under different loading and boundary conditions (Brown 1996; Wichtmann and Triantafyllidis 2004; Wichtmann et al. 2005; Narsilio and Santamarina 2008; Andersen 2009; Pasten et al. 2014; Chong and Santamarina 2016).

However, it is important to understand the long-term response of coarse-fines mixtures subjected to repetitive mechanical loads due to the fact that: (1) soils are granular materials and consist of a wide range of grain sizes, then, the grain size distribution significantly affects the plastic strain accumulation (Wichtmann et al. 2005); (2) repetitive mechanical load-induced particle crushing results in a long-term accumulation of fines, and impacts the stiffness and strength in soil mixtures (Chapter 4 - Uygar and Doven 2006; Giannakos 2010; Indraratna et al. 2013); additional fines may favor the undrained failure in railway ballast (Indraratna et al. 1997; Indraratna et al. 2011); (3) repetitive mechanical loads alter the engineering properties and behavior of

soil mixtures that depend not only on fines-in-sand but also sand-in-fines (Uygar and Doven 2006, Thevanayagam et al. 2002); and (4) fines fractions affect cyclic thermo-mechanical coupled processes in energy-driven geo-systems.

In this study, we explore the long-term mechanical response of sand-fines mixtures subjected to repetitive loading under zero-lateral strain conditions. This study starts with the analysis of the "threshold fines fraction", followed by the experimental program. The discussion and analyses of results underline the role of fines-in-sand and sand-in-fines on the evolution of the void ratio and small strain stiffness in sand-fines mixtures subjected to repetitive mechanical loads. Finally, this study concludes with additional evidence to support the Revised Soil Classification System *RSCS* proposed last in Chapter 6.

5.2 Underlying Concept - Threshold Fines Fraction F_{th}

The engineering properties of soils depend on both the major and minor soil fractions due to the fact that soils evolve from a mixture of particles (Lade and Yamamuro 1997; Salgado et al. 2000; Carraro et al. 2009). Previous studies that investigated the effect of fines as the minor components in soil mixtures demonstrate that abrupt changes in the void ratio take place at the specific fines fraction known as the threshold fines fraction F_{th} (Thevanayagam 1998; Yang et al. 2006; Choo and Burns 2015; Zuo and Baudet 2015).

The mass fraction of fines $F_F=M_F/M_T$ in coarse-fine mixtures leads to the definition of the threshold fines fraction F_{th} based on gravimetric-volumetric relations

when fine grains completely occupy the voids between coarse grains in terms of the void ratio of fines e_f and coarse e_c fractions; for grains with the same specific gravities,

$$F_{th} = \frac{M_F}{M_T} = \frac{M_F}{M_C + M_F} = \frac{e_C}{1 + e_C + e_F} \qquad F_C = 1 - F_F \tag{5.1}$$

The packing conditions of fine and coarse components lead to the two threshold fines fractions. Densely-packed coarse-grains and loosely-packed fine grains result in the low threshold fines fraction $F_{th}|^L$. The inverse is true for the high threshold fines fractions $F_{th}|^H$ with coarse grains loosely packed and fine grains densely packed.

$$F_{th}\Big|^L = \frac{e_C^{\min}}{1 + e_C^{\min} + e_F^{\max}} \tag{5.2}$$

$$F_{th}\Big|^H = \frac{e_C^{\max}}{1 + e_C^{\max} + e_F^{\min}} \tag{5.3}$$

The low and high threshold fines fractions divide binary mixtures into three categories: coarse dominant $F_F < F_{th}|^L$, transitional $F_{th}|^L < F_F < F_{th}|^H$, and fines dominant $F_F > F_{th}|^H$ mixtures.

5.3 Experimental Study

This experimental program explores the evolution of the void ratio and small strain stiffness in sand-fines mixtures subjected to repetitive mechanical loading under zero-lateral strain conditions.

5.3.1 Materials

This study uses the KAUST 20/30 sand and silica flour to prepare sand-fines mixtures (KAUST 20/30 sand: diameter D=0.60~0.85mm, specific gravity G_s=2.65, maximum and minimum void ratios e_{max}=0.78 and e_{min}=0.53, and roundness R=0.60; silica flour: diameter d<75-μm, specific gravity G_s=2.65, maximum and minimum void ratios e_{max}=1.50 and e_{min}=0.80.

5.3.2 Maximum and Minimum Void Ratios

Figure 5.1 presents the variation of the maximum and minimum void ratios for sand-fines mixtures with different fines fractions by mass $F_F = M_F/(M_C+M_F)$. The sand-fines mixture with F_F=20% displays the smallest value for the maximum void ratio while the mixture with F_F=30% exhibits the lowest value for the minimum void ratio.

The estimates of the low and high threshold fines fractions lead to the $F_F|^L$=17.6% for e_{max} and $F_F|^H$=31.2% for e_{min} (Equations 5.2 and 5.3). This trend results from the fact that fines are relatively free to separate coarse grains apart for e^{max} while fines occupy the pores between coarse grains for e^{min}.

5.3.3 Specimen preparation

We prepare the sand-silt mixtures with different fines fractions F_F=0%, 10%, 20%, 30%, 60%, and 100% for the different initial relative densities D_r=40% and 70%. The maximum and minimum void ratios data assist to attain the target relative densities (Figure 5.1).

5.3.4 Instrumented Oedometer Cell

This study employs the tall floating ring oedometer cell to obtain the system alignment during repetitive loading (Figure 5.2, floating ring: ID = 52.5 mm, wall thickness t=3.9 mm, and height H=100 mm; caps: OD = 50.8 mm and height h = 50.8 mm).

Top and bottom caps include parallel-type bender elements for both the source and receiver to minimize crosstalk and provide increased shielding (Lee and Santamarina 2005). The dimensions of the bender elements are 12.7×8×0.7 (length × width × thickness in mm). A 5 mm cantilevered length of bender elements ensures enhanced soil contact. An LVDT (TransTek DC 0242) clamped to the top and bottom caps tracks changes in the specimen height.

5.3.5 Stress-controlled repetitive loading and data acquisition systems

Figure 5.2 presents the stress-controlled loading system. It consists of a stiff reaction frame, the tall floating ring oedometer cell, a pneumatic cylinder, and peripheral electronics. The PID controller (Proportional-integral-derivative controller) activates the sinusoidal stress amplitudes for the repetitive vertical loadings (see details in Park and Santamarina 2017a).

The data logger measures the vertical deformation of specimens (Keysight 34970A, Figure 5.2). The function generator sends the step input signal (V=10 volt, freq=20 Hz, Keysight 33210A). The mechanically-transformed shear waves pass through soils. The filter-amplifier establishes a 500 Hz high-pass and 200 kHz low-pass window (Krohn-Hite 3364). The computer saves the average signal from the oscilloscope after the

stacking of 1024 signals (Keysight DSOX 2014A-stacking in Santamarina and Fratta 2005).

5.3.6 Test procedure

The loading procedure involves four stages: (1) static step loading to σ_o=67kPa, (2) repetitive loading with stress amplitude $\Delta\sigma$=100kPa by $N=10^4$ cycles (i.e. $\Delta\sigma/\sigma_o$=1.50), (3) static step loading to the maximum vertical stress 505kPa, and (4) unloading. Note that shear wave measurements during the cyclic loading occur only at the same level of vertical effective stress $\sigma_0 + \Delta\sigma$ at the number of cycles i = 1, 10, 100, 300, 1000, 3000, and 10000. The loading cycle period is 12 seconds.

5.4 Experimental Results

This section presents the experimental results for six specimens with different fines fraction F_F=0%, 10%, 20%, 30%, 60%, and 100% (D_r=40%), subjected to repetitive loading with stress amplitude $\Delta\sigma/\sigma_o$=1.5.

5.4.1 Vertical Effective Stress σ'_v vs. Void Ratio

Figure 5.3 presents the change in void ratio for selected sand-fines mixtures F_F=0%, 30%, and 100% during the static-repetitive-static loadings history followed by the static unloading stage. The void ratio for the three mixtures decreases monotonically during the first static loading. The dotted circles capture the creep-induced deformation at constant stress. Repetitive loading cycles lead to larger contractions as the fines fraction increases.

5.4.2 Evolution of Void Ratio

Figure 5.4 shows the void ratio evolution versus the number of cycles for five sand-fines mixtures F_F=0%, 10%, 30%, 60%, and 100% (D_r=40%). Most changes in the void ratio occur in the first 100 cycles and the volume contraction becomes more pronounced as the fines fraction increases. The non-linear trends in e-log(i) plot for sand-fines mixtures capture the transition from coarse-controlled to fines-controlled deformation behavior.

Figure 5.4 also illustrates a modified hyperbolic model (red dotted line) matched to the test results (Modified from Chong and Santamarina 2016; Park and Santamarina 2017a). This model assists with estimates of the void ratio e_i after a given number of loading cycle i as follows:

$$e_i = e_T + (e_1 - e_T)\left[1+\left(\frac{i-1}{N^*}\right)^m\right]^{-1} \qquad \text{for } i \geq 1 \text{ and } m > 0 \qquad (5.4)$$

where m is a fitting constant, e_1 is measured after the 1st cycle, and the terminal void ratio e_T corresponds to the asymptotic void ratio as $i \rightarrow \infty$. The model parameter N^* captures the number of cycles where half of the asymptotic contraction (e_1-e_T)/2 occurs.

5.4.3 Shear Wave Velocity

Figure 5.5 presents the shear wave velocity measured during the static-repetitive-static loadings history for a sand specimen F_F=0%. The shear wave velocity is a function of the vertical σ'_z and horizontal σ'_x effective stresses with α- and β- parameters. The α-factor is the shear wave velocity at mean effective stress σ'_{mean}= 1 kPa, and the β-

exponent represents the stress sensitivity of the shear wave velocity (Roesler 1979; Yu and Richard 1984; Santamarina et al. 2001):

$$V_s = \alpha\left(\frac{\sigma_z^{'} + \sigma_x^{'}}{2\,kPa}\right)^{\beta} = \alpha\left(\frac{\sigma_z^{'}}{1kPa}\right)^{\beta}\left(\frac{1+K_0}{2}\right)^{\beta} \quad (5.5)$$

The shear wave velocity-stress relation reflects both the contact behavior and fabric changes (Cha et al. 2014). Detailed analyses for all specimens follow in the next section.

5.5 Analyses and Discussion

Analyses of the mechanical response of sand-fines mixtures subjected to repetitive loading uses the results of the 12 tests detailed in the previous section. These include sediment stiffness at small and large strain levels, terminal void ratio e_T, asymptotic contraction $\Delta e = e_o - e_T$, maximum changes in relative density ΔD_T, repetitive loading-induced volumetric strain, and estimate of K_o after cyclic loading.

5.5.1 Compression Index C_c – Large Strain Level

Figure 5.6 plots the compression index of all mixtures measured during the first static step loading stages with fines fraction F_F. The Revised Soil Classification System RSCS boundaries superimposed on the C_c vs. F_F properly capture the sand-dominant, transitional, and fines-dominant deformation behavior and anticipate the compressibility of the soil mixtures (see the similar trend in Cordero et al. 2017). Note that fines (F) will control fluid flow at the fines fraction F_F>17.6%.

5.5.2 Shear Wave Velocity V_s – Small Strain Level

Figure 5.7 presents the shear wave velocity V_s against fines fraction F_F measured during the "static-repetitive-static" loading for six sand-fines mixtures with different fines fractions F_F=0%, 10%, 20%, 30%, 60%, and 100% (initial relative density D_r=40%). The shear wave velocities for all specimens increase during the repetitive loading cycles from i=1-to-i=10^4. Furthermore, the role of fines on stiffness improvement becomes more remarkable as the fines consolidate with increasing in effective stress.

The RSCS boundaries superimposed on Figure 5.7 also anticipate the mechanical-controlling soil fraction for the small strain stiffness of sand-fines mixtures, i.e. either sand *S*, sand with fines *SF*, or fines *F* (See details in Park and Santamarina 2017b).

5.5.3 Maximum Change in Relative Density ΔD_T

The modified hyperbolic model captures the asymptotic terminal void ratio e_T [Equation 5.5 and Figure 5.4]. The ratio between the asymptotic contraction $\Delta e=e_o-e_T$ to the attainable void ratio range e_{max}-e_{min} leads to the estimate of the maximum change in relative density ΔD_T at $i\rightarrow\infty$ versus initial relative density $D_{i=0}$ at i=0 during repetitive loading (Chong and Santamarina 2016):

$$\Delta D_T = \frac{e_{i=o} - e_T}{e_{\max} - e_{\min}} \tag{5.6}$$

$$D_{i=0} = \frac{e_{\max} - e_{i=0}}{e_{\max} - e_{\min}} \tag{5.7}$$

Figure 5.8(a) plots these dimensionless parameters ΔD_T versus the initial relative density $D_{i=0}$ for all sand-fines mixtures under the constant stress amplitude ratio $\Delta\sigma/\sigma_o$=

1.5. Results shows that the maximum changes in relative density ΔD_T increases and the slope $\Delta D_T/D_{i=0}$ becomes steeper as the fines fraction increases.

For comparison, Figure 5.8(b) presents the maximum change in relative density ΔD_T data obtained from previous studies (mainly Ottawa 20/30 sand, roundness R=0.90). Results show that the stress amplitude ratio $\Delta\sigma/\sigma_o$ significantly controls the volume contraction during repetitive loading.

Figure 5.8 also presents a curve fitting model to predict the maximum change in relative density ΔD_T that depends on the stress amplitude ratio $\Delta\sigma/\sigma_o$, initial relative density $D_{i=0}$, and fines fraction F_i (note: we assume that a volume contraction does not take place at minimum void ratio e_{min}):

$$\Delta D_T = \frac{\left(\frac{\Delta\sigma}{\sigma_0}\right)\left[1-D_{i=0}\right]^n}{M} = \frac{\left(\frac{\Delta\sigma}{\sigma_0}\right)\left[1-D_{i=0}\right]^n}{b+(a-b)\left[\frac{\sqrt{1-F_F}}{1+\left(\frac{F_F}{c}\right)}\right]} \qquad (5.8)$$

where M is a model parameter determined by matching the fitting model to test results, and this is a function of fines fraction F_F with three model constants a, b, and c. The M-parameter corresponds to a value for pure sands (M=a for F_F=0), and is equal to constant b for pure fines (M=b for F_F=1) otherwise varies from a-to-b values for sand-fines mixtures (b<M<a for 0< F_F < 1). The n-parameter determines the curvature of the model.

Figure 5.8(c) presents the M-parameter versus fines fraction F_i. The curve fitting provides the three model constants a= 42, b= 7.5, and c= 0.1 for sand-fines mixtures in this study. The comparison of M-parameters captures the effect of particle shape on

deformation resistance during repetitive loading [Figure 5.8(a) and 5.8(b)]. The more angular sand attains a higher *M* value associated with smaller asymptotic contraction.

The changes in *M*-parameter captures the transition from the sand-to-fines controlled asymptotic trend at the fines fraction F_F=20%. The mixture with F_F=60% exhibits an even higher *M*-parameter compared to the pure fines F_F=100%. This result indicates that sands still contribute to the sediment stiffness although the sand floats in a fines-dominant mixture.

5.5.4 Volumetric Strain

Figure 5.9 presents the estimated vertical strains ε_z against fines fraction F_F. The vertical strains involve: (1) $\varepsilon_z = (e_o - e_T)/(1+e_o)$, (2) $\varepsilon_z = C_c \cdot \log[(\sigma_o+\Delta\sigma)/\sigma_o]/(1+e_o)$ during first initial static step loading where σ_o=67 kPa and $\Delta\sigma$=100 kPa, (3) $\varepsilon_z = (e_i^u - e_i^l)/(1+e_i^l)$ where e_i^u and e_i^l are void ratios for one single cyclic loading at the load cycle $i=10^4$, and (4) $\varepsilon_z = \Delta\sigma/M_{max}$ where $\Delta\sigma$ =100 kPa and the maximum constraint modulus M_{max} computed from the shear wave velocity obtained at the load cycle $i=10^4$ $M_{max} = 2\cdot(V_s^2\rho)(1-\nu)/(1-2\nu)$ assuming a small-strain Poisson's ratio ν=0.15.

The RSCS boundaries superimposed on the results highlights that all vertical strains estimated from different loading processes and mechanisms identify sand-dominant, transitional, and fines-dominant mixtures. The cyclic loading-induced vertical strain exceeds the vertical strain during the static step loading. The vertical strain decreases as the strain regime changes from a large-to-small strain level for all sand-fines mixtures. Note the maximum constraint modulus M_{max} bounds the maximum value of vertical strain ε_z at small strain level.

5.5.5 Shear Wave Velocity - Evolution of K_o

The shear wave velocity-stress relation before and after the repetitive loading stages captures the evolution of the coefficient of earth pressure K_o during repetitive loading (Figure 5.5). From the Equation 5.5,

$$\frac{V_s|_N}{V_s|_1} = \frac{\alpha|_N}{\alpha|_1} \frac{\left(\frac{\sigma'_z|_N}{1kPa}\right)^{\beta|_N}}{\left(\frac{\sigma'_z|_1}{1kPa}\right)^{\beta|_1}} \frac{\left(\frac{1+K_0|_N}{2}\right)^{\beta|_N}}{\left(\frac{1+K_0|_1}{2}\right)^{\beta|_1}} \tag{5.9}$$

Then,

$$K_0|_N = \frac{\sigma'_x}{\sigma'_z} = 2\left[\frac{V_s|_N}{V_s|_1}\frac{\alpha|_1}{\alpha|_N}\sigma'^{(\beta|_1-\beta|_N)}_z\left(\frac{1+K_0|_1}{2}\right)^{\beta|_1}\right]^{\frac{1}{\beta|_N}} - 1 \tag{5.10}$$

Figure 5.9 presents the estimated coefficient of earth pressure K_o versus the fines fraction F_F by assuming an initial $K_o|_1$= 0.5. The coefficient of earth pressure increases with an increase in the fines fraction at the fines fraction below F_F=30%. It indicates that the horizontal effective stress under zero-lateral strain conditions becomes larger due to the reduction of the fabric stability induced by fines-in-sand. Note that the coefficient of earth pressure at rest for a sand-fines mixture will decrease with the addition of fines in sands if the fines added reinforces the soil fabric, and also contributes to the frictional resistance (Lee et al. 2014).

5.5.6 Towards a Revised Soil Classification System RSCS

Experimental results and data analyses reveal that fines have a marked effect on both the repetitive loading-induced asymptotic contraction and small strain sediment

stiffness even when the fines fraction F_F is significantly lower than the F_F= 50% used in the Unified Soil Classification System USCS. Moreover, sands in the F_F=60% mixtures still influence the load-deformation response even when the sand-in-fines is at a void ratio $e > e^{max}$. These observations hint to the need for a physics-inspired and data-driven soil classification system, as advanced in Chapter 6.

5.6 Conclusions

Soils often consist of a broad range of grain sizes. This study investigates the role of fines on the evolution of the void ratio and small-strain stiffness in sand-fines mixtures when subjected to repetitive mechanical loads. The salient conclusions made in this study follow:

- The volumetric-gravimetric analysis defines the threshold fines fraction F_{th}. The low and high threshold fines fractions adequately bound the fines-controlled, the coarse-controlled, and transitional zone in sand-fines mixtures. Indeed, fines separate coarse grains apart or fines tends to occupy the pores between the coarse grains in the transitional zone.
- The void ratio evolution of sand-fines mixtures with different fines fractions exhibits asymptotic terminal void ratio e_T as the number of cycles increases. The ratio between the asymptotic contraction ($\Delta e = e_o - e_T$) to the attainable void ratio range ($e^{max} - e^{min}$) can be used to estimate the maximum change in the relative density ΔD_T during repetitive loading.

- The terminal void ratio e_T, asymptotic contraction $\Delta e=e_o-e_T$, and volumetric strain data trends capture the transition of the sand-to-fines controlled repetitive load-deformation behavior.
- The evolution of the shear wave velocity during repetitive loading allows us to estimate the coefficient of earth pressure at rest K_o. Results indicate that a horizontal effective stress under zero-lateral strain conditions becomes larger due to the reduction of the fabric stability by the addition of fines.
- The sediment stiffness at small and large strain levels plotted against fines fraction provides further evidence towards the Revised Soil Classification System RSCS developed in the following chapter.

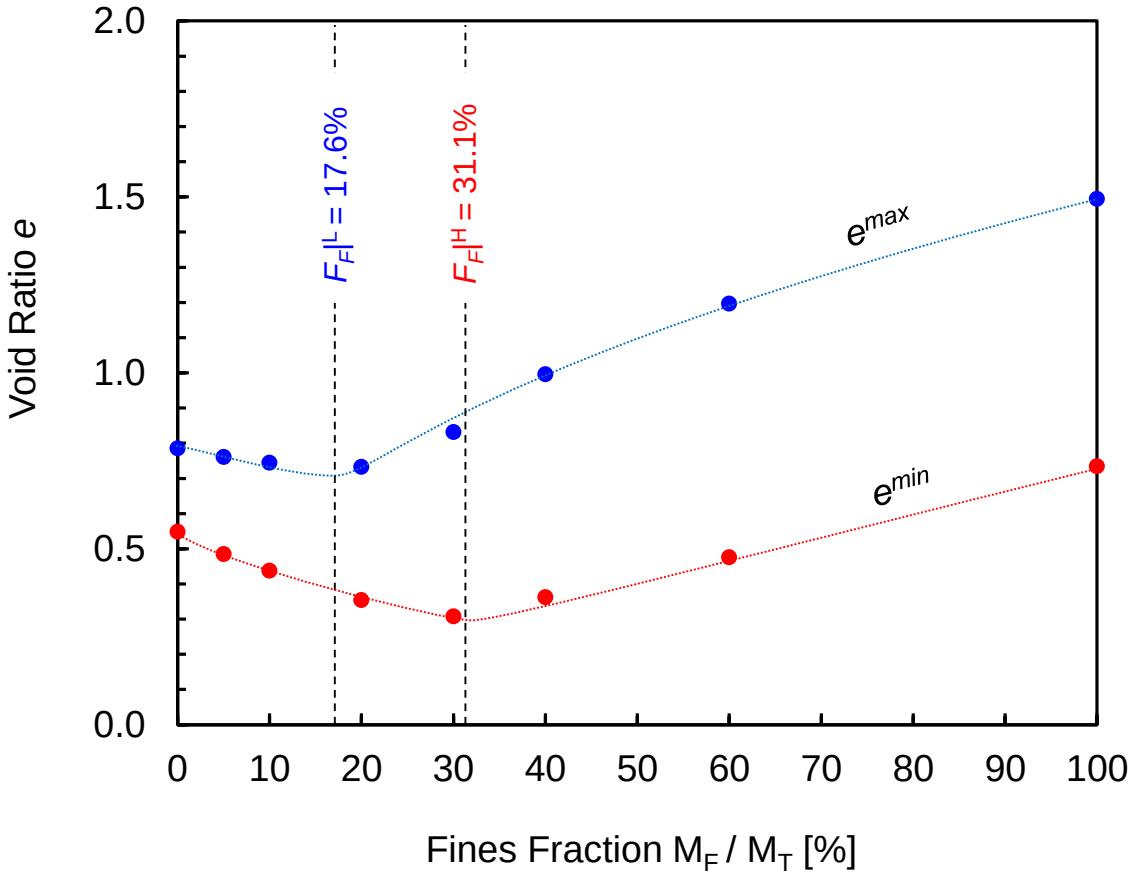

Figure 5.1. Maximum and minimum void ratios of sand-fines mixtures. Sand: e_C^{max}=0.78 and e_C^{min}=0.53. Fines: e_F^{max} =1.50 and e_F^{min}=0.73.

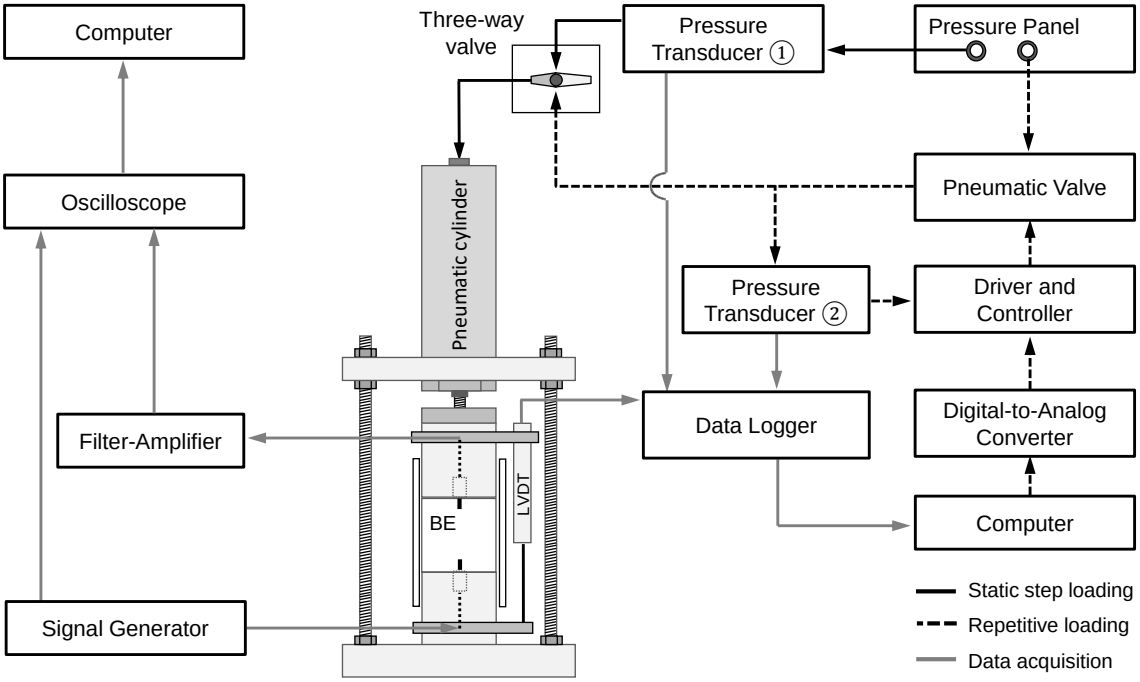

Figure 5.2. Device. Schematic diagram of the pneumatic system used for static and repetitive loading. The peripheral electronics are used to measure deformation and shear waves. The oedometer cell consists of a floating ring, top and bottom caps with bender elements BE, and LVDT clamps. Top and bottom cap dimensions: 50.8 mm diameter and 50.8 mm height. Floating ring dimensions: ID= 52.5 mm, OD= 60.3 mm, and 100 mm height.

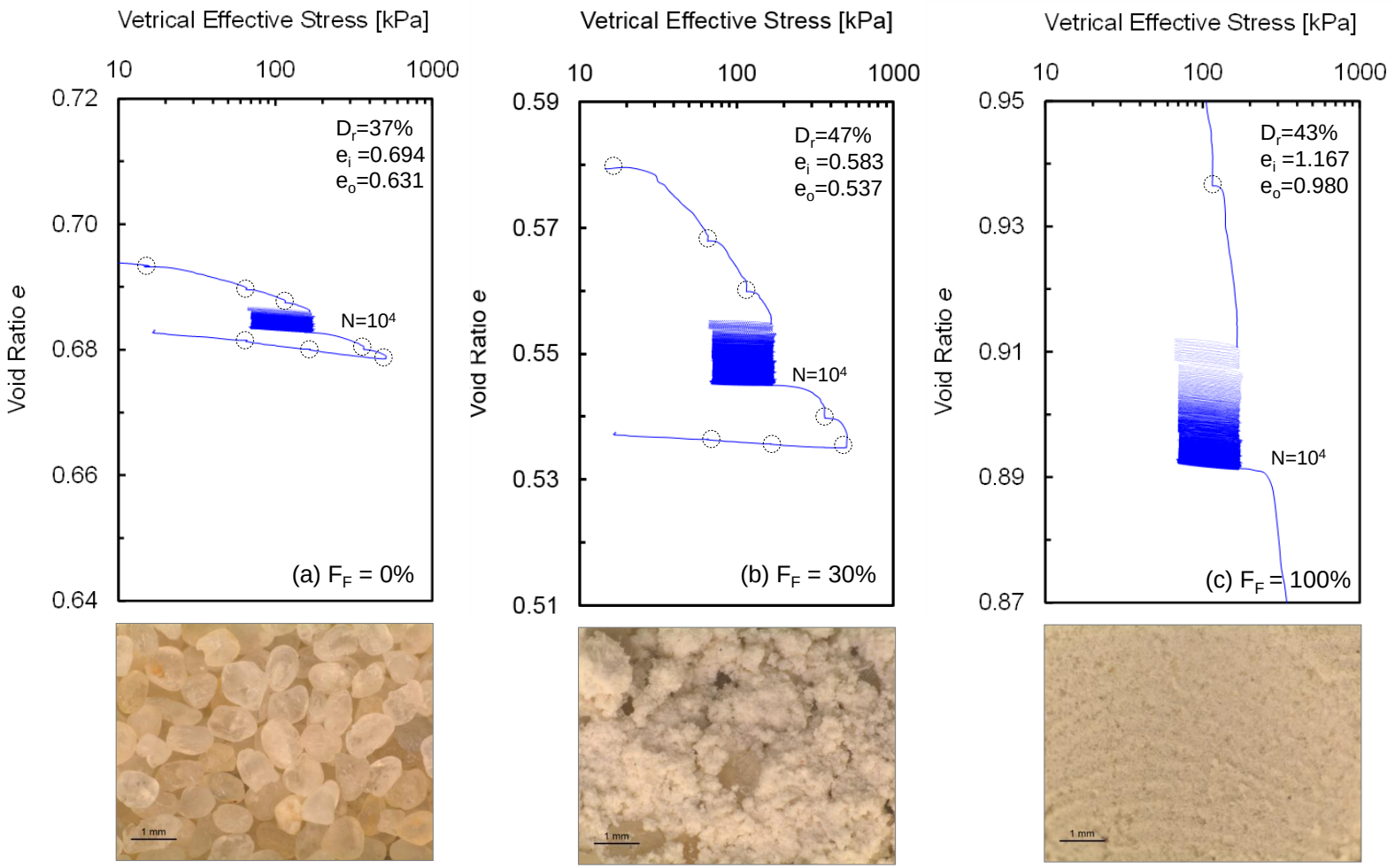

Figure 5.3. The change in void ratio during the static-repetitive-static loading history followed by the static unloading sequence. (a) Pure sand F_F=0% (b) Sand-fines mixture F_F=30%, and (c) Pure fines F_F=100%. Test conditions: σ_o= 67 kPa, stress amplitude ratio $\Delta\sigma/\sigma_o$= 1.50 (from 67-to-167 kPa).

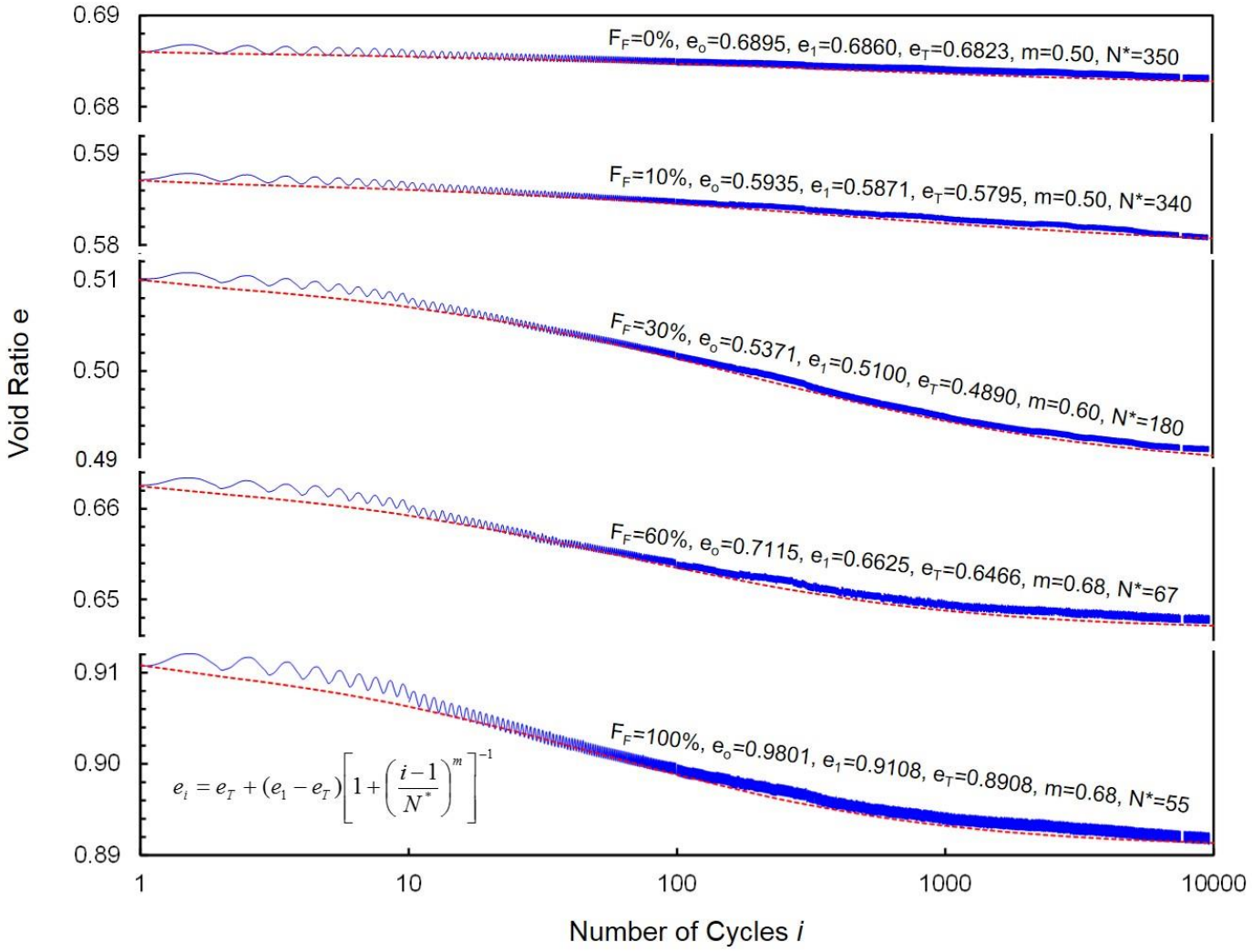

Figure 5.4. Void ratio evolution for sand-fines mixtures with number of cycles *i*. Test conditions: σ_o= 67 kPa, stress amplitude ratio $\Delta\sigma/\sigma_o$= 1.50 (from 67-to-167 kPa).

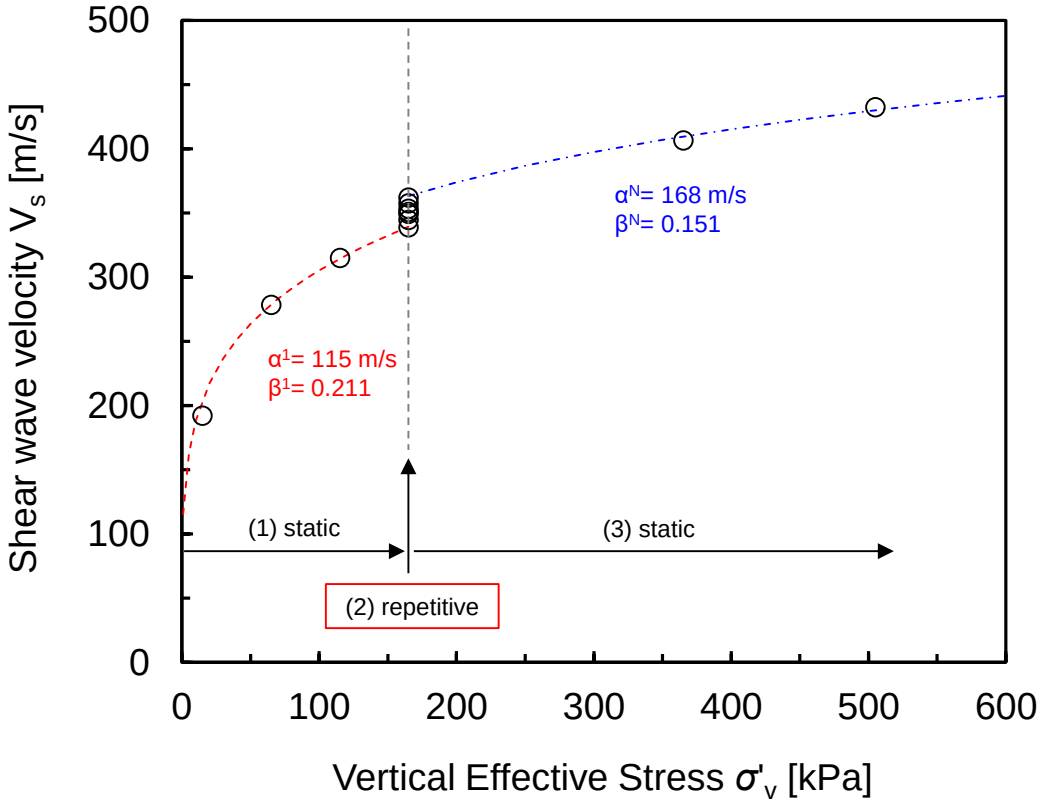

Figure 5.5. Shear wave velocity captured during the "static-repetitive-static" loading history followed by unloading (F_F=0%, D_r=37%). Test conditions: σ_0 =105 kPa, stress amplitude ratio $\Delta\sigma/\sigma_0$= 1.3 (from 105-to-243 kPa).

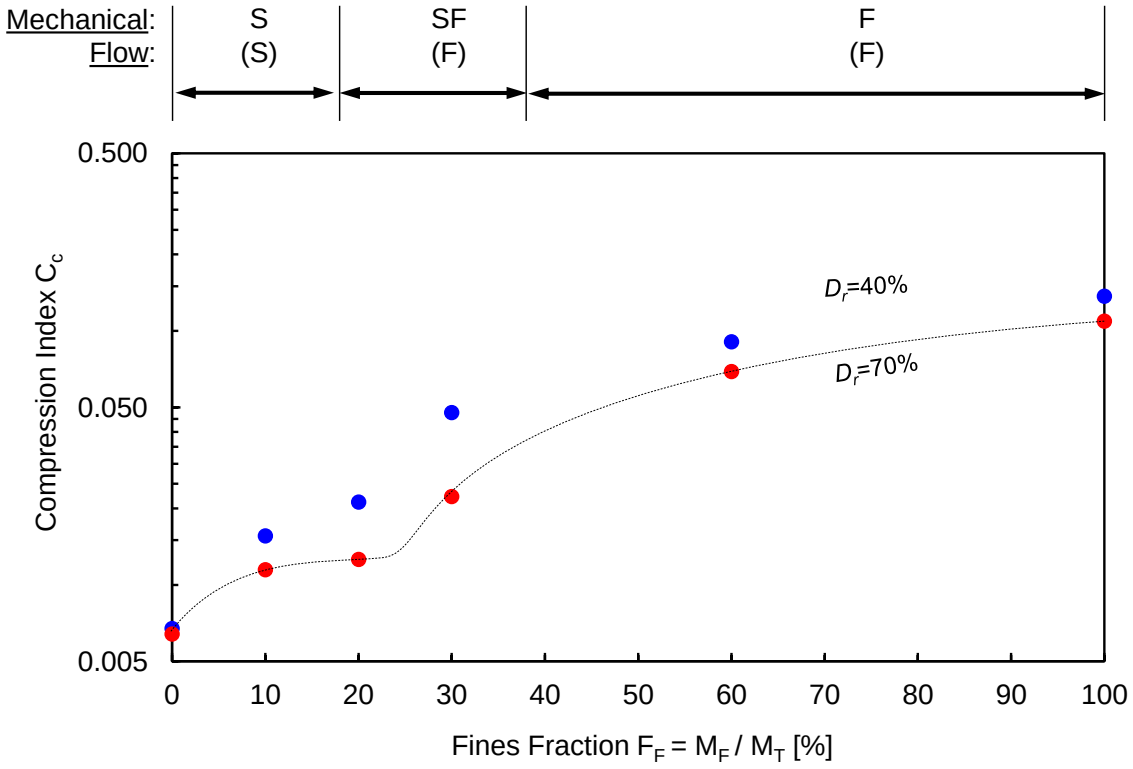

Figure 5.6. Compression index C_c during the first static step loading versus fines mass fraction F_F. Compressibility computed as $C=\Delta e/\log[(\sigma_o + \Delta\sigma)/\sigma_o]$. The RSCS shown at the top of the figure denotes the component(s) that controls the mechanical response and the component that controls fluid flow. Refer to Park and Santamarina (2017) for details.

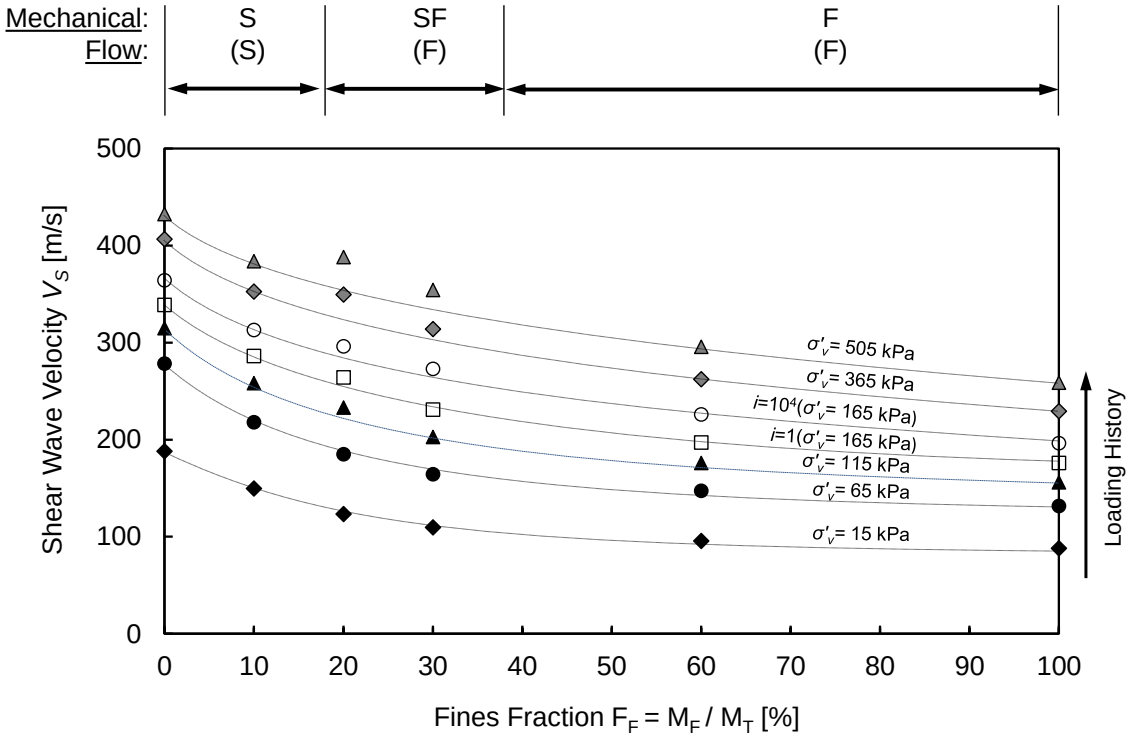

Figure 5.7. Shear wave velocity V_s during the static-repetitive-static loading history against fines mass fraction F_F. The RSCS shown at the top of the figure denotes the component(s) that controls the mechanical response and the component that controls fluid flow. Refer to Park and Santamarina (2017) for details.

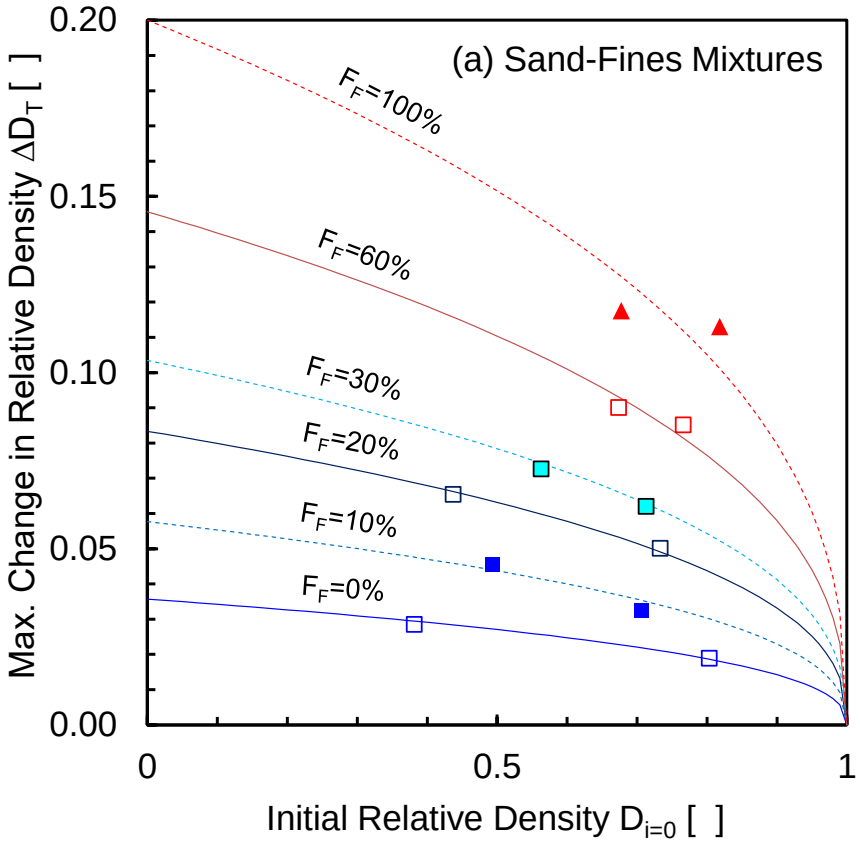
(a) Sand-Fines Mixtures
F_F=100%
F_F=60%
F_F=30%
F_F=20%
F_F=10%
F_F=0%
Max. Change in Relative Density ΔD_T [ ]
Initial Relative Density $D_{i=0}$ [ ]
0.20
0.15
0.10
0.05
0.00
0
0.5
1

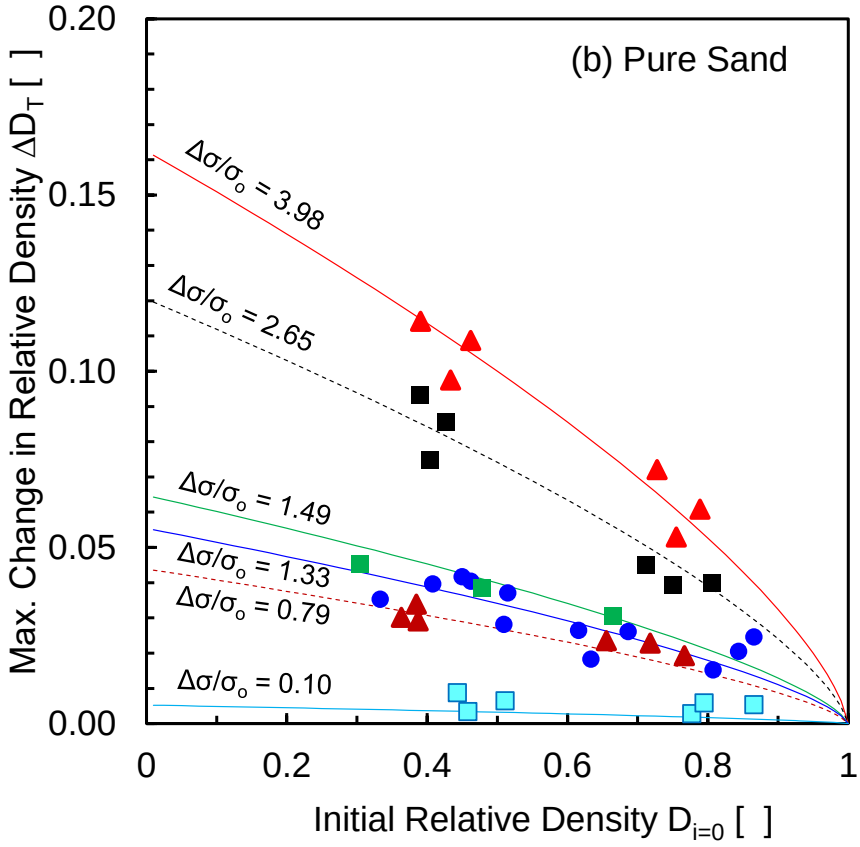
(b) Pure Sand
$\Delta\sigma/\sigma_o$ = 3.98
$\Delta\sigma/\sigma_o$ = 2.65
$\Delta\sigma/\sigma_o$ = 1.49
$\Delta\sigma/\sigma_o$ = 1.33
$\Delta\sigma/\sigma_o$ = 0.79
$\Delta\sigma/\sigma_o$ = 0.10
Max. Change in Relative Density ΔD_T [ ]
Initial Relative Density $D_{i=0}$ [ ]
0.20
0.15
0.10
0.05
0.00
0
0.2
0.4
0.6
0.8
1

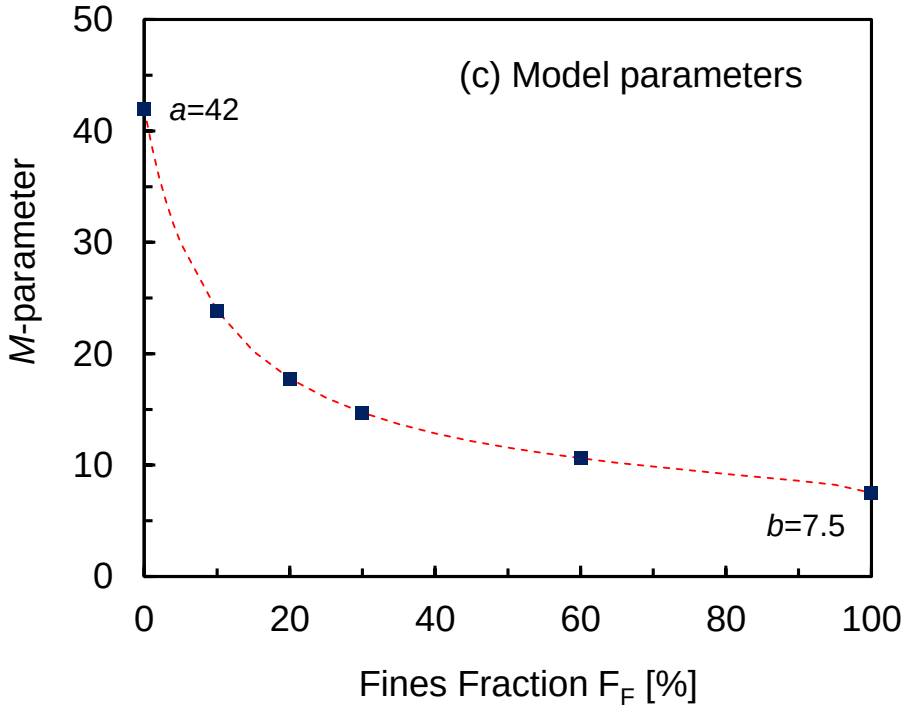

Figure 5.8. Estimation of maximum settlement due to the repetitive loading. (a) Sand-fines mixtures in this study. Note: variable=F_F, constant $\Delta\sigma/\sigma_o$=1.50, n=0.4, a=42, b=7.5, c=0.1 for all curves, (b) Pure sands data extracted from previous studies (mainly Ottawa 20/30 sands). Note: variable=$\Delta\sigma/\sigma_o$, constant F_i=0, n=0.7, M=20~22 for all curves, and (c) Model parameters: Variation of M-parameters with fines fraction F_F.

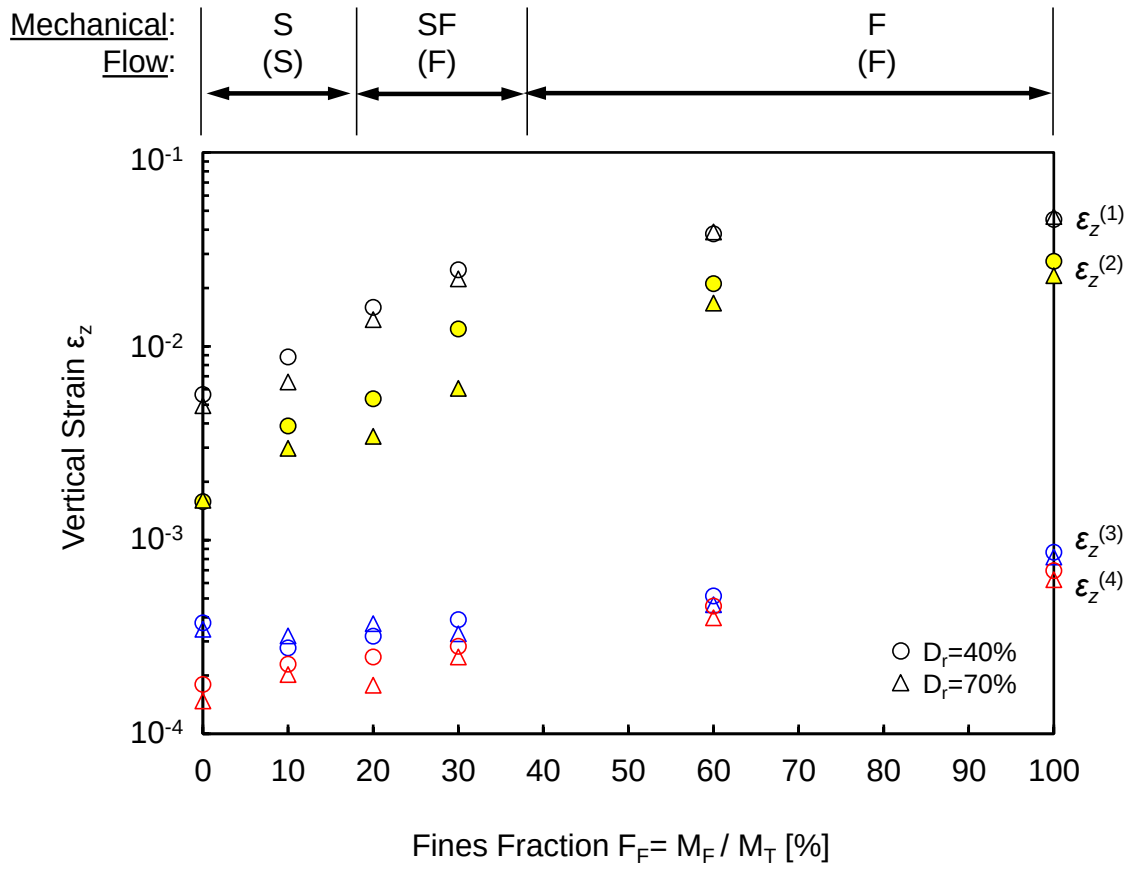

Figure 5.9. Vertical strains ε_z against fines fraction F_F. The vertical strains involve: $\varepsilon_z^{(1)}= (e_o-e_T)/(1+e_o)$, $\varepsilon_z^{(2)} =C_c\cdot\log[(\sigma_o+\Delta\sigma)/ \sigma_o]/(1+e_o)$ during first initial static step loading where σ_o=67 kPa and $\Delta\sigma$=100 kPa, $\varepsilon_z^{(3)}= (e_i^u-e_i^l)/(1+e_i^l)$ where e_i^u and e_i^l are void ratios for one single cyclic loading at the load cycle $i=10^4$, and $\varepsilon_z^{(4)}= \Delta\sigma/M_{max}$ where $\Delta\sigma$ =100 kPa and the maximum constraint modulus M_{max} computed from the shear wave velocity obtained at the load cycle $i=10^4$ $M_{max}= 2\cdot(V_s^2\rho)(1-\nu)/(1-2\nu)$ assuming a small-strain Poisson's ratio ν=0.15.

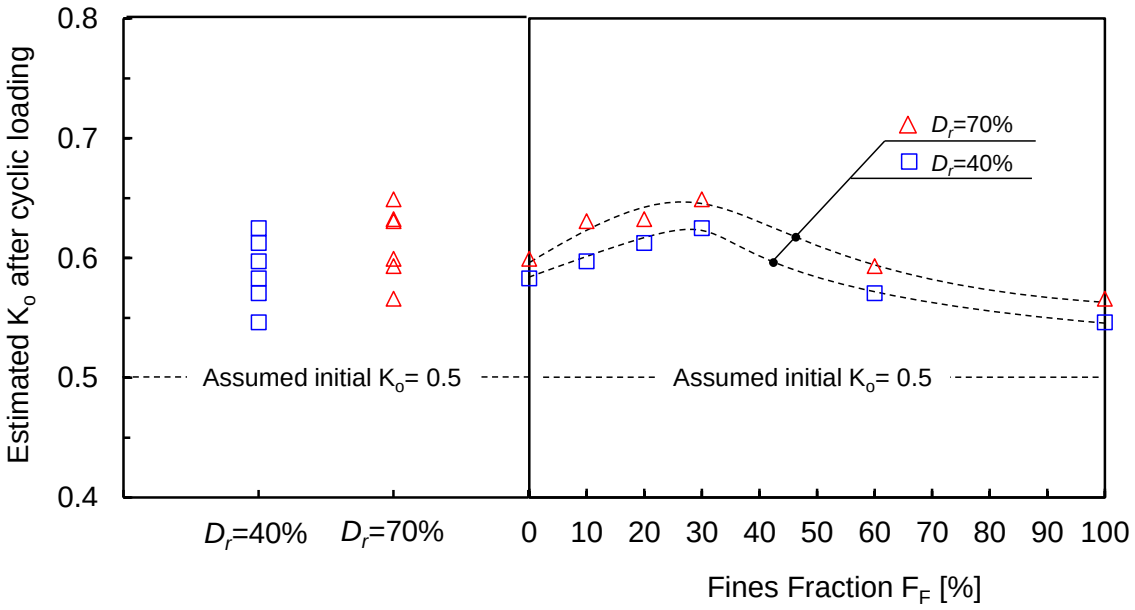

Figure 5.10. Coefficient of earth pressure at rest K_o after the load cycle $i=10^4$ estimated from velocity data.

CHAPTER 6

REVISED SOIL CLASSIFICATION SYSTEM FOR COARSE-FINE MIXTURES: PHYSICS-INSPIRED AND DATA-DRIVEN

6.1 Introduction

Soil classification enables geotechnical engineers to anticipate the properties and behavior of soils by grouping them into similar response categories based on their index properties (Casagrande 1948; Howard 1984; Das 2009; Dundulis et al. 2010; Kovačević and Jurić-Kaćunić 2014).

The Unified Soil Classification System USCS is the foundation for classification systems worldwide, from Japan and China (JGS0051 and GBT50145) to Mexico and Switzerland (SNV 70). The USCS places emphasis on particle size and uses the percentage retained on sieve No. 200 (75-μm) to separate coarse-grained soils (more than 50% retained) from fine-grained soils (more than 50% passing). Other classification systems use a lower boundary for fines, either 35% (USA's AASHTO, UK's BS5930, France's GTR; Australia's guidelines under review) or 40% (Deutche Norm DIN 18196, 2011).

Most classification systems, including the USCS, use a 50% split on sieve No. 4 (4.76mm) to classify coarse-grained soils as either gravels or sands. The German DIN norm classifies soils as 'gravel' when the fraction coarser than 2mm exceeds 40%.

A detailed analysis of the USCS and other soil classification systems highlighted above readily discloses great physical insight and understanding of soil behavior and their properties. However, both laboratory and field data gathered during the last century

indicate the need for a revised soil classification system. There are common limitations to all classification systems. First, they adopt fixed boundaries for coarse-fine mixtures despite the fact that fine-grained soils may exhibit a broad range of plasticity. Second, particle shape and grading affect the packing density of the coarse fraction; hence the relevance of both the coefficients of uniformity and curvature in the USCS, yet shape does not feature in any classification system. Third, the effect of plastic fines on mechanical and conduction properties is not properly captured by the 50% and the 5%-12% fines thresholds adopted in the USCS. Finally, current soil classification systems do not reflect the fact that pore-fluid chemistry plays a significant role in the behavior of fines.

The purpose of this study is to propose a Revised Soil Classification System RSCS for engineering purposes by providing a physics-inspired, data-driven approach that benefits from the experience gained in our discipline since the inception of current soil classification systems. This study starts with gravimetric-volumetric analyses to anticipate fines and sand fraction thresholds, summarizes a data-based analysis focused on the physical properties of soil mixtures, and concludes with a new methodology for soil classification.

6.2 Granular Mixtures – Triangular Textural Charts

A soil can be analyzed as a three-component mixture made of gravel, sand, and fines. Triangular textural charts then facilitate the grouping of similar soils (see Figure 6.1a for interpretation guidelines). Figure 6.1b depicts the essence of the USCS in such a triangular chart. This soil map does not capture additional classification details related to

the coefficients of uniformity and curvature for coarse grains and Atterberg limits for fine grains.

The gravimetric-volumetric analysis of mixtures allows for the systematic definition of threshold boundaries in these triangular charts. The simpler case of binary mixtures is presented first.

6.2.1 Binary Mixtures

Let us invoke gravimetric-volumetric relations to compute the mass fraction of fines F_F in coarse-fine mixtures when fine grains completely fill the voids between coarse grains (Figure 6.2). In terms of the void ratio of fines e_F and coarse e_C fractions, and assuming the same specific gravities (See Appendix A for the detailed mathematical solution),

$$F_F = \frac{M_F}{M_T} = \frac{M_F}{M_C + M_F} \approx \frac{e_C}{1 + e_C + e_F} \quad \text{and} \quad F_C = 1 - F_F \tag{6.1}$$

There are two threshold fines fractions (Figure 6.2). Densely-packed coarse grains filled with loosely-packed fine grains define the low threshold fines fraction $F_F|^L$. By contrast, loosely-packed coarse grains filled with densely-packed fine grains result in the high threshold fines fraction $F_F|^H$.

The low and high threshold fines fractions divide binary mixtures into three groups (Figure 6.2): coarse dominant $F_F < F_F|^L$, transitional $F_F|^L < F_F < F_F|^H$, and fines dominant $F_F > F_F|^H$ mixtures. This analysis applies to binary gravel-sand, gravel-fines, and sand-fines mixtures.

6.2.2 Threshold Ternary Mixtures: Gravel-sand-fines Mixtures

Let us extend the previous gravimetric-volumetric analysis to ternary gravel-sand-fines mixtures. In this case, sand packed at void ratio e_S fills the voids in the gravel e_G, and fines e_F fill the remaining pores within the gravel-sand mixture. Then, the computed gravel fraction F_G, sand fraction F_S, and fines fraction F_F are functions of their void ratios (Appendix A details the complete mathematical solution):

$$F_G = \frac{1}{\left(1 + \frac{e_G}{1+e_S} + \frac{e_S}{1+e_F}\frac{e_G}{1+e_S}\right)} \tag{6.2}$$

$$F_S = \frac{1}{\left(\frac{1+e_S}{e_G} + 1 + \frac{e_S}{1+e_F}\right)} \tag{6.3}$$

$$F_F = \frac{1}{\left(\frac{1+e_S}{e_G}\frac{1+e_F}{e_S} + \frac{1+e_F}{e_S} + 1\right)} \tag{6.4}$$

where $F_G + F_S + F_F = 1.0$. The combination of loose and dense packing conditions for each component leads to various threshold fractions, similarly to binary mixtures. These threshold values define a transitional zone in a triangular textural plot for ternary mixtures, rather than the line segment for binary mixtures shown in Figure 6.2.

6.3 Low and High Void Ratios – Correlations

The use of gravimetric-volumetric analyses to determine transition thresholds require estimates of "feasible" low and high void ratios for gravel *G*, sand *S*, and fines *F*.

Robust empirical relations between index properties and feasible void ratios can facilitate soil classification.

6.3.1 Gravel and Sand

As packing densities for gravels and sands are insensitive to effective stress, then, the threshold fractions derived from the packing states of gravels and sands are independent of effective stress as a first approximation. We adopt the maximum and minimum void ratios e^{max} and e^{min} to estimate the feasible range of void ratios gravels and sands may attain (see Figure 6.2).

Maximum and minimum void ratios decrease for rounder and well-graded sands and gravels. Indeed, roundness R and uniformity C_u determine e^{max} and e^{min} (Youd 1973):

$$e_C^{\max} = 0.032 + \frac{0.154}{R} + \frac{0.522}{C_u} \tag{6.5}$$

$$e_C^{\min} = -0.012 + \frac{0.082}{R} + \frac{0.371}{C_u} \tag{6.6}$$

where roundness R is the average radius of curvature of surface features $\sum r_i/N$ divided by the radius of the largest inscribed sphere r_{max}. Readily available software computes grain roundness R from grain images; for classification purposes, it is sufficient to visually compare grains against shape charts (chart in Krumbein and Sloss 1963; example in Cho et al. 2006). Alternatively, the value of e^{max} can be quickly determined using a container of known volume and a scale; and $e^{min}=0.74[e^{max} - 0.15(C_u-1)]$ is an adequate estimate of e^{min} (Cho et al. 2006).

6.3.2 Fines: Load Carrying

The void ratio of fines (i.e., silts and clays) depends on their plasticity and the applied effective stress. Effective stress is not a soil index property, but is a state variable. One may argue against the use of a state variable in soil classification; however, a sand-clay mixture that behaves as clay-dominant at low effective stress may transform into sand-dominant at high effective stress as clays consolidate and sand grains form the load-carrying skeleton (note: a similar notion underlies the equivalent liquidity index in Schofield 1980). Consequently, we select the void ratio of fines at pre-selected effective stress levels as equivalent index parameters that capture the packing condition of fines, analogous to the use of e^{max} and e^{min} for coarse grains.

The K_0-compression line at effective stress σ'= 10 kPa and σ'= 1 MPa defines two useful reference void ratios $e_F|^{10\text{kPa}}$ and $e_F|^{1\text{MPa}}$ that represent "soft" and "stiff" soil conditions relevant to near-surface engineering applications. Published correlations enable the prediction of reference void ratios in the absence of consolidation data during early soil classification (Burland 1990; Chong and Santamarina 2016):

$$e_F\Big|^{10kPa} = e_F\Big|^{1kPa} - C_c = 0.026\,LL + 0.07 \tag{6.7}$$

$$e_F\Big|^{1MPa} = e_F\Big|^{1kPa} - 3C_c = 0.011\,LL + 0.21 \tag{6.8}$$

These lower-bound estimates apply to non-sensitive clays or remolded conditions; they reflect that the void ratio at the liquid limit $e_F|^{\text{LL}}=G_sLL/100$ is a good estimator of the void ratio at σ'= 1 kPa, as $e_F|^{1\text{kPa}}\approx 5/4\,e_F|^{\text{LL}}=0.033LL$ (Chong and Santamarina 2016) and of the compressibility of fine-grained sediments C_c=0.007(LL-10) (Skempton and Jones

1944). For the proposed revised classification system, these estimates must use the liquid limit obtained for fines passing through sieve No. 200 (75-μm opening).

6.3.3 Fines: Flow Control

The presence of fines has a prevalent role on hydraulic conductivity even when fines are packed at a void ratio higher than $e_F|^{LL}$. In fact, fluid flow can exacerbate the effect of fines by dragging grains until they clog the soil by forming bridges at pore constrictions (Kenney and Lau 1985; Skempton and Brogan 1994; Valdes and Santamarina 2006; Valdes and Santamarina 2008; Shire et al. 2014).

In this context, the threshold fines fraction for fluid flow adopted in this classification is the fines content that causes a 100-times decrease in the hydraulic conductivity of otherwise clean sands and clean gravels. Fines and water may form a viscous slurry at low fines content. Analyses based on published data (Locat and Demers 1988; Palomino and Santamarina 2005; Pennekamp et al. 2010) and experiments conducted as part of this study indicate that such a slurry will exhibit ~100 times higher viscosity than water when the water content is approximately $\omega\% = \lambda \cdot LL$ where $\lambda = [2 \cdot \log(LL-25)] \geq 1.0$. Then, the void ratio of fines used to compute the threshold fines fraction for fluid flow $e_F|^{flow}$ is:

$$\begin{aligned} e_F\big|^{flow} &= \lambda \cdot e_F\big|^{LL} \\ &= \left[2\log\left(LL-25\right)\right] \cdot e_F\big|^{LL} \qquad \text{(where } \lambda \geq 1\text{)} \\ &\approx 0.05\, LL \cdot \log\left(LL-25\right) \end{aligned} \tag{6.9}$$

where $e_F|^{LL}$ is the void ratio of fines at the liquid limit.

6.4 Data Collection – Transitions in Dominant Behavior

Gravimetric-volumetric analyses in terms of the low and high void ratios identified above may not properly capture the transition from coarse-controlled to fines-controlled behavior because of multiple grain-scale and pore-scale mechanisms and processes.

This study gathered mixture properties from published studies to examine the transition in hydraulic conductivity, shear wave velocity, compression index, and shear strength. Table 6.1 presents each data set normalized between the properties for 100% coarse grains and 100% fines to facilitate the comparison across different soil types. In addition, we select an asymptotically consistent mixture model to fit all trends. The normalization function and mixture models are mathematically analogous for all *x*-properties (Table 6.1):

$$\frac{x_i - x_F}{x_C - x_F} = \frac{\sqrt{1 - F_i^6}}{1 + \left(\frac{F_i}{F_{th}}\right)^m} \tag{6.10}$$

where x_i corresponds to a coarse-fine mixture with fines fraction F_i, and x_C and x_F are the values of the property for 100% coarse and 100% fines fractions. The role of the numerator in the mixture model is to force the convergence of the normalized property to zero as $F_i \rightarrow 1$. The arithmetic mean $x_i=(x_C+x_F)/2$ takes place near the threshold fines fraction $F_i \approx F_{th}$. Table 6.1 illustrates mixture models fitted to the data to identify the threshold fractions F_{th} for all properties. The dataset includes porosity to gain an insight into the underlying processes related to granular packing. Observations for each physical property follow.

6.4.1 Porosity

Figure 6.3 illustrates the changes in porosity (a) with fines fraction in coarse-fines mixtures and (b) with sand fraction in gravel-sand mixtures. The minimum porosities are attained at F_F = 15% to 40% in coarse-fines mixtures, and at F_S = 20% to 40% in gravel-sand mixtures. In general, the porosity of mixtures decreases with increases in roundness (Youd 1973, Santamarina and Cho 2004; Cho et al. 2006), coefficient of uniformity C_u (Istomina 1957; Vukovic and Soro 1992), and relative size ratio R_d (McGeary 1961; Guyon et al. 1987; Marion et al. 1992; Thevanayagam 2007). Geometric models for idealized packings agree with these data-based observations (see examples in Koltermann and Gorelick 1995; Kamann et al. 2007).

6.4.2 Hydraulic Conductivity

Figure 6.4 presents normalized hydraulic conductivity data $\underline{\underline{k}}$ versus fines F_F and sand F_S fractions. While hydraulic conductivity varies in orders of magnitude, we opt for linear normalization to reflect the direct proportionality between the flow rate q and hydraulic conductivity k in engineering problems, as per Darcy's law $q=k$iA (i=hydraulic gradient, A= area). The hydraulic conductivity drops to the arithmetic mean value when the fines fraction is F_F = 2-to-7% in coarse-fines mixtures, and when the sand fraction is F_S = 5-to-17% in gravel-sand mixtures. While these threshold fractions arise from gap-graded mixture data, similar threshold values are expected for well-graded mixtures following the discussion on porosity trends in the previous section.

The data include mixtures with hydraulic conductivity smaller than the hydraulic conductivity of 100% fines in coarse-fines mixtures, or smaller than for 100% sand in

gravel-sand mixtures (this is clearly observed in logarithmic scale, but it is faint in the normalized scale used in Figure 6.4). Hydraulic conductivity values $k_{mix} < k_F$ reflect the increased tortuosity of flow paths caused by the presence of coarse grains "floating" in the porous medium made of the finer grains.

6.4.3 Small-Strain Stiffness (in terms of shear wave velocity)

Figure 6.5 shows normalized shear wave velocities $\underline{\underline{V_s}}$, as defined in Table 6.1, for coarse-fines mixtures against fines fraction F_F. The normalized shear wave velocities drop to the arithmetic mean value for threshold fines fractions between F_{th} = 5% and 36%. The transition from coarse-controlled to fines-controlled shear stiffness is influenced by effective stresses: as the vertical effective stresses increases, the threshold fines fraction F_{th} increases. Apparently, fines prevent the formation of a coarse-grain skeleton at low stress but consolidate at high stress levels. Figure 6.5b displays data for sand-mica mixtures in the absence of published data for gravel-sand mixtures. Results indicate that d_{sand}/L_{mica} affects the transition from coarse-controlled to fines-controlled mixtures, and the threshold fines fraction F_{th}.

6.4.4 Compression Index

Figure 6.6 presents the normalized compression index $\underline{\underline{C_c}}$ of coarse-fine mixtures graphed versus fines fraction F_F. The normalized compression index reaches the arithmetic mean compressibility at a fines fraction that varies from F_{th}= 10% to 65% as the liquid limit decreases from high plasticity clays to silts. The initial void ratio, particle shape, soil fabric, stress conditions, pore fluids, mineralogy, and the plasticity of fines all

affect the transition from coarse-controlled to fines-controlled compressibility (Kenny 1977; Maio and Fenelli 1994; Sridharan and Nagaraj 2000; Monkul and Ozden 2007; Thevanayagam 2007; Bandini and Sathiskumar 2009).

The threshold fines fraction for the sand-silt mixture is F_{th} = 65%, as illustrated by the open black square in Figure 6.6. Yet, mixtures near the minimum porosity (i.e., at a fines fraction $F_F \approx$ 30%) exhibit lower compressibility than the 100% sand specimen (this effect is concealed in the normalized scale used in Figure 6.6). Similarly, while coarse grains form a load-bearing skeleton when the fines fraction is lower than threshold values (Monkul and Ozden 2007; Evans and Valdes 2011), fines improve the stability of the soil matrix by hindering the buckling of the coarse-grain chains (Radjai et al. 1998; Lee et al. 2007b).

6.4.5 Shear Strength (in terms of tanϕ)

Figure 6.7 presents trends for the normalized tanϕ plotted against the fraction of fines and sand. The data in Figure 6.7 were obtained by various researchers using different test devices, and include peak, constant-volume, and residual friction angles. While diverse in origin, all trends show consistent transitions from coarse-controlled to fines-controlled shear strength. The threshold fraction characterizes the transition from coarse-controlled to fines controlled shear strength. The fines threshold is F_{th} = 10-to-42% in coarse-fines mixtures while the sand threshold is F_{th} = 47-to-70% in gravel-sand mixtures. The threshold fraction F_{th} decreases when the relative size ratio R_d increases, the liquid limit increases, the coarse grains become well-graded, and the particle shape becomes rounder. These trends reflect underlying changes in shear mechanisms, e.g.,

from rolling to sliding shear (Kenny 1967; Lupini et al. 1981; Maio and Fenelli 1994; Mitchell and Soga 2005; Santamarina and Shin 2009; Skempton 1985). The dominant mechanism depends on whether fines occupy the pores between coarse grains, or separate coarse grains apart (Monkul and Ozden 2007; Thevanayagam et al. 2002; Vallejo and Mawby 2000), and associated changes in the coordination number, rotational frustration and interlocking (Santamarina et al. 2001; Bareither et al. 2008; Cho et al. 2006).

Particle shape rather than size determines the constant volume friction angle (Cho et al. 2006). Therefore, angular fines could exhibit higher friction angle than well-rounded coarser particles. This applies to the dataset symbolized by the orange circle in Figure 6.7a. The normalization of $\tan\phi$ defined in Table 6.1 still assigns a value of 1.0 to the coarser component and 0 to the finer component.

The shear resistance of mixtures may exceed that of their components; in particular, the highest peak friction angles would be expected for highly dilative mixtures near minimum porosity (dataset illustrated by the open blue square in Figure 6.7b – Refer to Figure 6.3).

6.5 Observations

Gravimetric-volumetric packing analyses (Figure 6.2 and Equations 6.1-to-6.4), the selection of low and high "feasible" void ratios (Equations 6.5-to-6.9), and the data compilation discussed above and detailed in Figures 6.3-to-6.7 and Table 6.1 support the four observations that follow:

- The packing density and relative fraction of each component define the transition from coarse-controlled to fines-controlled mixtures, both for load carrying and fluid

flow.

- The maximum and minimum void ratios e^{max} and e^{min} for loose and dense sands and gravels depend on the coefficient of uniformity and particle shape.
- The packing of fines depends on the liquid limit and effective stress. We select three distinctive values in view of near-surface engineering applications: "soft" at $e_F|^{10kPa}$ and "stiff" at $e_F|^{1MPa}$ for mechanical response, and "viscous" at $\lambda \cdot e_F|^{LL}$ for fluid flow behavior where $\lambda=[2 \cdot \log(LL-25)]$, detailed in Equation 6.9.
- Volumetric-gravimetric analyses provide the underlying conceptual framework for soil classification boundaries. However, pore filling does not necessarily occur at either e^{max} or e^{min} due to pore and grain scale mechanisms and processes such as the effect of boundaries that the large grains impose on the smaller grains, i.e. a function of relative size ratio (Fraser 1935). Hence, physics-inspired analytical boundaries require data-driven corrections.

These analyses and data trends reveal two critical limitations in current soil classification methods as illustrated in Figure 6.1. First, the fines begin to control mechanical properties and hydraulic properties at lower fines fractions than the boundaries adopted in current soil classification systems. Second, the fixed boundaries used in existing classification methods do not account for particle shape and underestimate the impact of high plasticity fines.

Does the gravimetric-volumetric formulation provide adequate thresholds for well-graded soils? Experimental data are scarce, and analyses provide only partial answers even for the ideal packings of spherical particles. We conducted gravimetric-volumetric packing analyses for well-graded gravely-sandy soils, all with the same

coefficient of uniformity and particle shape (C_u=10 and roundness R=0.5), but with different median grain size (D_{50}=3.8-to-204mm). Results show a natural and gradual transition from gravel-dominant soils when the sand fraction is less than F_S<10%, to sand-dominant behavior when the sand fraction exceeds F_S>48%. Given these results, and in the absence of negative evidence, we adopt the gravimetric-volumetric analysis proposed above for the analysis of both gap-graded and well-graded soils. (Note: the gravimetric-volumetric analyses consider grain size of sand and gravel fractions separately from each other, hence, the coefficient of uniformity for the sand and gravel fractions are lower than the C_u for the whole soil mass).

6.6 Notable Mixtures and Classification Boundaries

Let's identify notable mixtures that mark the transitions between the soil components that control the mechanical response and fluid flow. These mixtures are specified in Table 6.2 and displayed in Figure 6.8 on the textural triangle. Notable mixtures discussed below assist with the definition of classification boundaries.

6.6.1 Mechanical Control

Densely-packed soil fractions control the mechanical response of a soil. For example, the gravel carries the load in a gravel-fines mixture when the gravel packing is dense at eGmin and fines are at a high void ratio e > eF|10kPa; this is mixture ① in Table 6.2 and Figure 6.8a. Other notable mixtures labeled ② and ④ follow a similar logic and procedure. Mass fractions are computed using Equations 6.1-to-6.9 in all cases.

Data-driven correction. Data-based thresholds F_{th} indicate that the coarse component in a mixture affects properties even when it is packed at a void ratio $e > e^{max}$ (similar observations in Holtz and Gibbs 1956; Vasil'eva et al. 1971; Fragaszy et al. 1992; Vallejo and Mawby 2000; Vallejo 2001; Simoni and Houlsby 2006; Kim et al. 2007). Correction factors for e^{max} match the theoretically predicted threshold fractions F_F with the threshold fractions F_{th} at the arithmetic mean value observed for the various physical properties (Figures. 6.3-to-6.7 and Table 6.1). Results support the correction factors listed below (included in Table 6.2a):

- gravel-sand mixtures (mixture ⑤): $\beta = 2.5$ ($e_G=\beta \cdot e_G^{max}$; $e_S=e_S^{min}$)
- gravel-fines mixtures (mixture ⑦): $\alpha = 1.3$ ($e_G=\alpha \cdot e_G^{max}$; $e_F= e_F|^{1MPa}$)
- sand-fines mixtures (mixture ⑧): $\gamma = 1.3$ ($e_S=\gamma \cdot e_S^{max}$; $e_F= e_F|^{1MPa}$)

Finally, we compute notable ternary mixtures ③, ⑥, and ⑨ as specified in Table 6.2a. Figure 6.8a displays all notable mixtures on the triangular chart.

These nine mixtures define boundaries for seven soil groups in terms of mechanical properties control (Figure 6.8a). A single component is dominant in three of the seven groups: *G*= gravel, *S*= sand and *F*= fines. The four other soil groups are mixtures in transitional conditions: *GS*, *SF*, *GF*, and *GSF*. Soils that fall within the ternary transitional group *GSF* may exhibit distinctly different soil properties as boundaries depend on the liquid limit of fines as well as the particle shape and coefficient of uniformity of both sands and gravels.

6.6.2 Fluid Flow Control

Notable mixtures that define flow-control thresholds are computed using the low viscosity criterion $e_F|^{flow} = \lambda \cdot e_F|^{LL}$ (Equation 6.9), and densely-packed gravel or sand. These conditions result in the mixtures ⑩, ⑪, ⑫, and ⑬, detailed in Table 6.2b and plotted in Figure 6.8b.

Finally, we select the mixture of densely-packed gravel e_G^{min} and loosely-packed sand e_S^{max} to define the boundary for sand-controlled hydraulic conductivity in gravel-sand mixtures (point ② in Table 6.2 and Figure 6.8b).

Altogether, points ②, ⑩, ⑪, ⑫, and ⑬ delimit the three distinct zones for flow control (Figure 6.8b): a large region controlled by the fines (*F*), a smaller region controlled by the sand (*S*), and the corner reserved for clean gravels (*G*).

6.6.3 Classification – Charts

Classification groups and nomenclature. Distinct differences between the textural charts for mechanical behavior control (Figure 6.8a) and for flow-control (Figure 6.8b) suggest the need for a two-name nomenclature whereby the first letters identify the component that controls mechanical properties, followed by a letter that identifies the component that controls flow (shown in parenthesis). For example, consider a *S(F)* soil: sand controls the mechanical properties but fines control its hydraulic conductivity.

The resulting 10 soil groups are summarized in Figure 6.9. The fines fraction in *F*, *GF*, *SF*, and *GSF* soils controls the hydraulic conductivity in these groups. While the two-name nomenclature *F(F)*, *GF(F)*, *SF(F)* and *GSF(F)* is redundant in these cases, it clearly states the distinct role of fines on both mechanical and flow properties. Clean

gravel *G(G)* and clean sand *S(S)* classifications can be augmented with "well-graded" or "poorly-graded" qualifiers used in the USCS.

Sample charts. Charts in Figure 6.10 capture mechanical control and flow control boundaries superimposed onto a single chart for each case. These charts reflect a wide range of soil conditions and include both angular-uniform and rounded-well-graded sands and gravels, in addition to fines of varying plasticity.

Threshold fractions are markedly different from those used in the USCS. For various combinations of roundness, coefficient of uniformity and fines plasticity, results indicate:

- gravel-sand mixtures: threshold sand fractions range between $F_S|^{L}$ = 12-to-24% and $F_S|^{H}$ = 45-to-65%,
- coarse-fines mixtures - mechanical control: the fines threshold varies between $F_F|^{L}$ = 3-to-27% and $F_F|^{H}$ = 12-to-50%,
- coarse-fines mixtures - flow control: the fines threshold varies from $F_F|^{flow}$ = 1% to 23%.

The predominant role of fines extends much further into the lower fines content than anticipated by the USCS (compare the RSCS charts in Figure 6.10 with the USCS chart in Figure 6.1b). In fact, the USCS has the closest resemblance to the triangular textural chart computed for low plasticity fines (such as kaolinite), and angular sands and gravels. Fines plasticity plays a critical role in the position of boundaries for both mechanical and hydraulic controls. In particular, well-graded rounded sands and gravels can form denser packings than uniform angular coarse grains, therefore a small mass fraction of fines is

needed to alter soil behavior in this case (e.g., compare classification charts in the lower row of Figure 6.10 against charts in the upper row).

These new classification charts incorporate the main parameters used by the USCS, that is: sieves No. 200 and No. 4, coefficient of uniformity C_u, and liquid limit *LL* of fines (The values of e^{max} and e^{min} implicitly consider the coefficient of curvature). Furthermore, the development of these charts recognizes the role of particle shape on the behavior of sands and gravels. It also considers the stress regime that the soil will be subjected to in near-surface geotechnical engineering projects.

Fines classification. The classification of fines could be completed using the standard Casagrande chart in the USCS. However, the revised classification RSCS adopts the new fines classification method proposed by Jang and Santamarina (2016) because it takes into consideration both the soil plasticity and its sensitivity to pore fluid chemistry. This classification is based on liquid limits obtained with deionized water, brine (high electrical conductivity), and kerosene (low dielectric constant). Fines fall into one of 12 groups: *NL*, *NI*, *NH*, *LL*, *LI*, *LH*, *IL*, *II*, *IH*, *HL*, *HI*, and *HH*, where the first capital letter indicates the soil plasticity [No, Low, Intermediate, High] and the second letter indicates the sensitivity of the soil response to changes in pore fluid chemistry [Low, Intermediate, High].

6.7 Revised Soil Classification System RSCS

The recommended procedure for soil classification follows:

[1] <u>*Input Parameters*</u>.

- Obtain the gravel fraction F_G (where G > sieve No. 4), sand fraction F_S (sieves No. 200 < S < No. 4) and fines fraction F_S (passing sieve No. 200) by mass.
- For gravel and for sand: determine e^{max} and e^{min} for each fraction. For estimates of e^{max} and e^{min}, use the coefficient of uniformity C_u and roundness R gathered for each fraction [Equations. 6.5 and 6.6]
- For fines: determine $e_F|^{10kPa}$, $e_F|^{1MPa}$, and $e_F|^{LL}$ or estimate these values from the liquid limit measured on the passing sieve No. 200 using the pore fluid that the soil is subjected to in the field [Equations. 6.7-to-6.9]

[2] <u>*Classification Chart*</u>. Compute a case specific chart using the notable mixtures ①-to-⑬ specified in Table 6.2. Computations and graphing schemes are built into the Excel-sheet included in the Supplementary Material associated with this manuscript (the file is available for download from the authors' websites).

- Determine the boundaries for the load-carrying component [①-to-⑨: Table 6.2a]
- Determine the boundaries for the flow-controlling component [⑩-to-⑬: Table 6.2b]

Alternatively, select the textural triangular chart in Figure 6.10 that most closely resembles the soil under consideration.

[3] <u>*Soil Classification*</u>. Plot the point that corresponds to the soil under consideration and determine its classification using the two-name nomenclature suggested above: first

letter(s) indicate the load carrying component, followed by a letter in parenthesis that denotes the component that controls flow. When appropriate, include the RSCS triangular chart as part of the report.

- Fines classification: Follow the classification procedure described in Jang and Santamarina (2016) to consider the fines plasticity and sensitivity to changes in pore fluid chemistry. This method requires additional liquid limit determinations for soil pastes mixed with brine and kerosene.

6.8 Conclusions

Soil classification is intended to help geotechnical engineers anticipate the properties and behavior of soils by grouping them into similar response categories based on index properties. Soil classification systems worldwide capture great physical insight. Yet, analyses and data trends reveal critical limitations in the boundaries for various soil groups adopted in classical soil classification systems. In particular, fines begin to play a significant role at threshold fractions that are smaller than boundaries adopted by the existing classification systems.

Classification boundaries can be defined by the void ratio that each fraction may attain. The revised classification adopts e^{max} and e^{min} for gravels and sands, and three distinctive values for fines: "soft" $e_F|^{10kPa}$ and "stiff" $e_F|^{1MPa}$ for the mechanical response, and "viscous" $\lambda \cdot e_F|^{LL}$ for the fluid flow behavior where $\lambda=[2 \cdot \log(LL-25)]$. There are robust correlations between these void ratios and index properties such as particle shape, coefficient of uniformity, and liquid limit.

Analytically-computed and data-adjusted threshold fractions point to very different values to those used as boundaries in the Unified Soil Classification System, both for mechanical-control and for flow-control. The boundaries in the USCS have some -albeit limited- resemblance to the RSCS boundaries computed for low plasticity clays (such as kaolinite), and angular sands and gravels.

Threshold fractions for mechanical-control and for flow-control are quite distinct. The revised soil classification system RSCS uses a two-name nomenclature whereby the first letters identify the component that controls mechanical properties, followed by a letter shown in parenthesis that identifies the component that controls flow.

Finally, the detailed classification of fines uses the new fines classification method proposed by Jang and Santamarina (2016) that takes into consideration the plasticity of fines and their sensitivity to pore fluid chemistry.

Table 6.1. Property normalization and fitting models

Trend with Fines	Property	Normalization and Fitting Trend	Threshold Fraction F_{th}		Notes
			Coarse-fine	Gravel-sand	
Saddle	Porosity (n)	$n = n_c \cdot \left[\exp\left(\sqrt{(F_i - F_{th})^2}\right)^a - b \right]$	15~40%	20~40%	F_{th} decreases with increasing relative size ratio R_d
Increases	Compression index (C_c)	$\underline{C_c} = \frac{C_{c,i} - C_{c,C}}{C_{c,F} - C_{c,C}} = 1 - \frac{\sqrt{1 - F_i^6}}{1 + \left(\frac{F_i}{F_{th}}\right)^m}$	10~65%	no data	F_{th} increases with decreasing liquid limit of fines
Decrease	Hydraulic conductivity (k)	$\underline{k} = \frac{k_i - k_F}{k_C - k_F} = \frac{\sqrt{1 - F_i^6}}{1 + \left(\frac{F_i}{F_{th}}\right)^m}$	2~7%	5~17%	F_{th} decreases with increasing relative size ratio R_d and angularity
	Shear wave velocity (V_s)	$\underline{V_s} = \frac{V_{s,i} - V_{s,F}}{V_{s,C} - V_{s,F}} = \frac{\sqrt{1 - F_i^6}}{1 + \left(\frac{F_i}{F_{th}}\right)^m}$	7~36%	no data	F_{th} increases with increasing relative size ratio R_d and increasing effective stress
	Shear strength (tanϕ)	$\underline{\tan\phi} = \frac{\tan\phi_i - \tan\phi_F}{\tan\phi_C - \tan\phi_F} = \frac{\sqrt{1 - F_i^6}}{1 + \left(\frac{F_i}{F_{th}}\right)^m}$	10~42%	47~70%	F_{th} decreases with increasing relative size ratio R_d and increasing fines plasticity

Note: The threshold fraction F_{th} is near the property arithmetic mean (except for porosity where it is selected as the fines content at minimum porosity).

Subscripts: *G* gravel, *S* sand, *F* fines.

Model parameters: *a*, *b*, and *m*.

Table 6.2. Notable mixtures used to define soil classification boundaries

Process	Controlling Fraction	Mixture No.	Packing Condition			Physical Background - Interpretation
			Gravel	Sand	Fines	
Load Carrying	Gravel-controlled	①	e_G^{min}	-	$e_F\|^{10kPa}$	Gravels carry the load if gravels are densely packed and fines experience σ'<10 kPa
		②	e_G^{min}	e_S^{max}	-	Gravels carry the load if gravels are densely packed and sands are loosely packed
		③	e_G^{min}	e_S^{max}	$e_F\|^{10kPa}$	Gravels carry the load if gravels are densely packed, sands are loose and fines feel σ'<10 kPa
	Sand-controlled	④	-	e_S^{min}	$e_F\|^{10kPa}$	Sands carry the load if sands are densely packed and fines experience σ'<10 kPa
		⑤	$2.5e_G^{max}$	e_S^{min}	-	Sands carry the load in sands are densely packed and contain very loose gravel at 2.5 e_G^{max}
		⑥	$2.5e_G^{max}$	e_S^{min}	$e_F\|^{10kPa}$	Sands carry the load in sands are densely packed and contain very loose gravel at 2.5 e_G^{max} and soft fines
	Fines-controlled	⑦	$1.3e_G^{max}$	-	$e_F\|^{1MPa}$	Fines carry the load when they are compact and contain loose gravel at 1.3 e_G^{max}
		⑧	-	$1.3e_S^{max}$	$e_F\|^{1MPa}$	Fines carry the load when they are compact and contain loosely packed sand at 1.3 e_S^{max}
		⑨	$2.5e_G^{max}$	$1.3e_S^{max}$	$e_F\|^{1MPa}$	Fines carry the load when they are compact and contain very loose gravels and sands
Fluid Flow	Fines-controlled	⑩	e_G^{min}	-	$\lambda e_F\|^{LL}$	The fraction for "clean" gravels and sands is computed by assuming that the coarse fraction is at e^{min} and that fines form a high viscosity fluid at a water content equal to $\lambda \cdot LL$, i.e., the void ratio of fines is $e_F\|^{flow} = \lambda \cdot e_F\|^{LL}$ where $\lambda = [2\log(LL-25)]$ (see text for details)
		⑪	e_G^{min}	e_S^{max}	$\lambda e_F\|^{LL}$	
		⑫	$2.5e_G^{max}$	e_S^{min}	$\lambda e_F\|^{LL}$	
		⑬	-	e_S^{min}	$\lambda e_F\|^{LL}$	

***Note**: G*=Gravel; *S*=Sand; *F*=Fines

Estimates: Values of e^{max}, e^{min}, $e_F|^{10kPa}$, $e_F|^{1MPa}$, and $e_F|^{LL}$ can be estimated from index properties (see Equations 6.5-to-6.9 in the text).

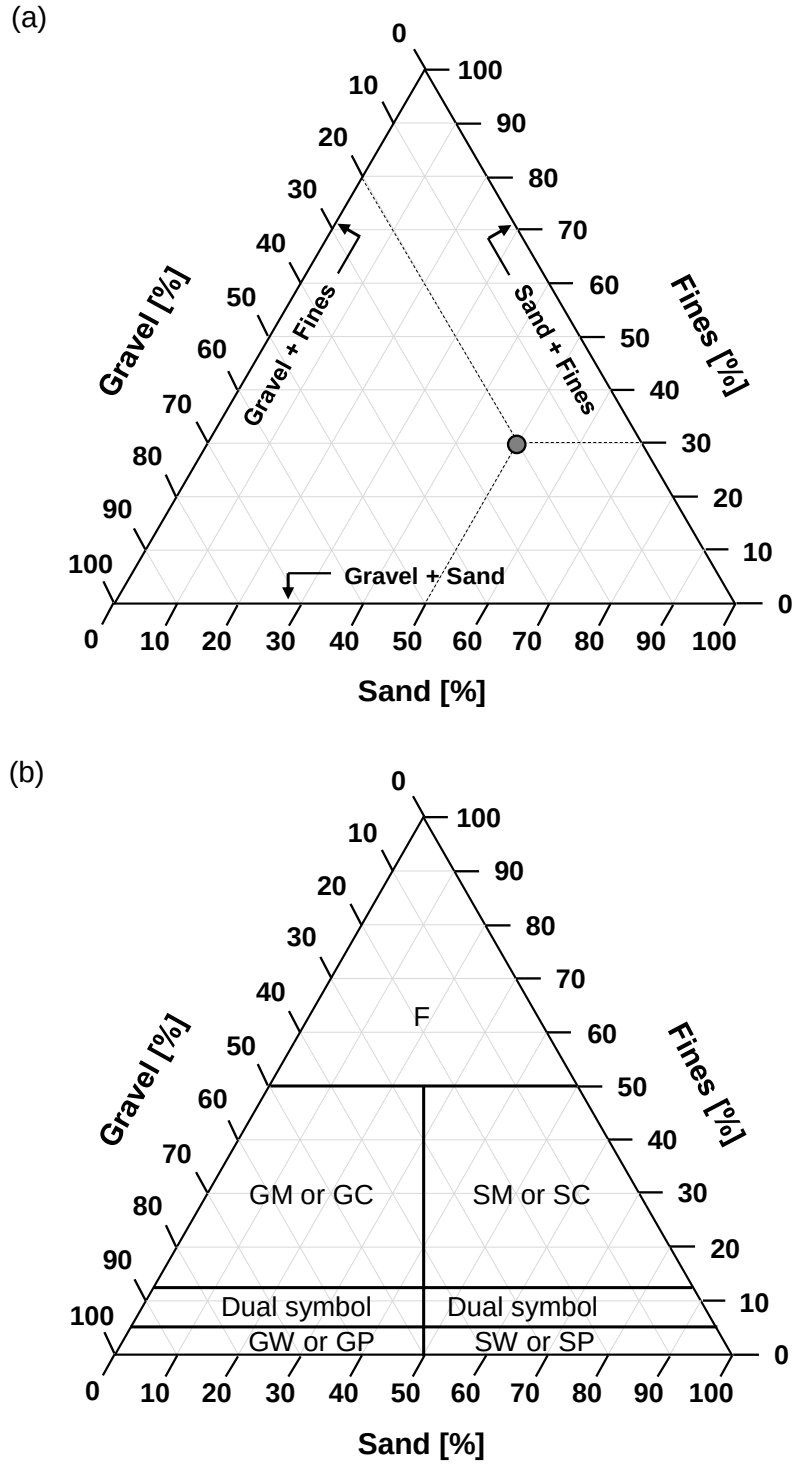

Figure 6.1. Soil classification systems: (a) Guide for the interpretation of triangular gravel-sand-fines charts; the example corresponds to gravel fraction F_G=20%, sand fraction F_S=50%, and fines fraction F_F=30%. (b) The Unified Soil Classification System (USCS).

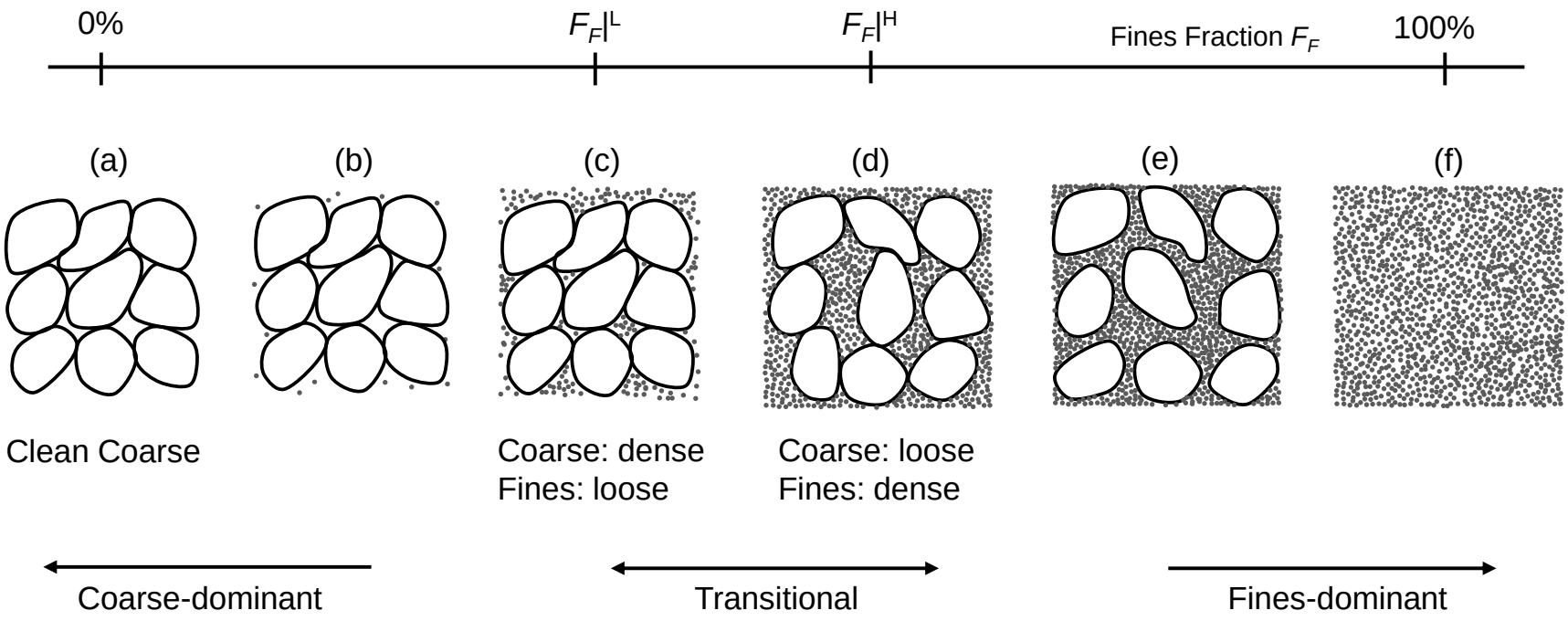

Figure 6.2. Coarse-fines mixtures: Threshold fractions. Coarse-dominant, transitional, and fines-dominant mixtures. These conceptual sketches apply to gravel-sand, gravel-fines and sand-fines mixtures.

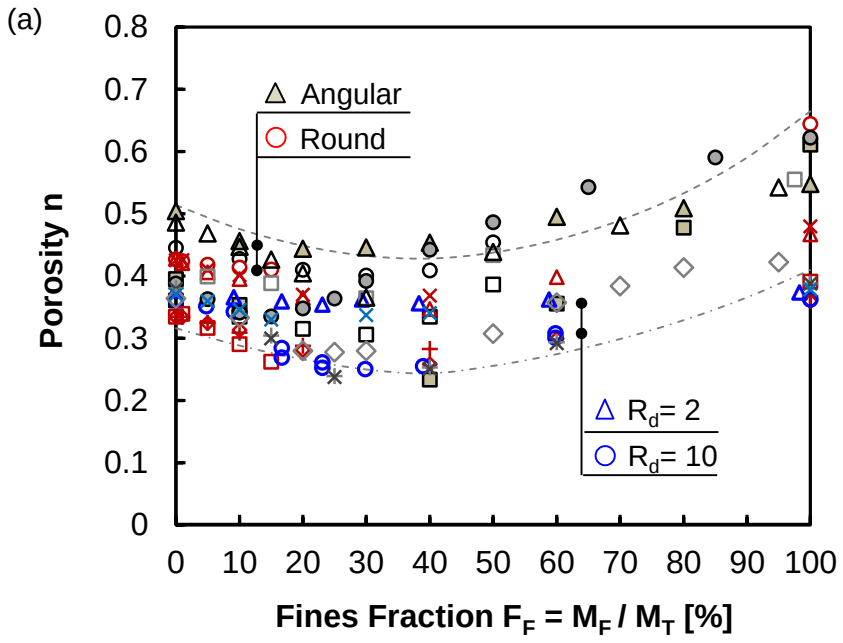

Data sources: ○ Han et al. 1986; ○,△ Goyon et al. 1987; ■ Knoll and Knight 1994; × Zlatovic and Ishihara 1995; ◇ Yamamuro and Covert 2001; + Thevanayagam et al. 2002; □ Konishi et al. 2007; × Thevanayagam et al. 2007; △ Yang 2004; □,○ Belkhatir et al. 2013; ○,△,×,◇,□ Choo 2013; ▲ Kang and Lee 2015 (Note that analogous data are found in Lade and Yamamuro 1997; Fourie and Papageogiou 2001; Shafiee 2008).

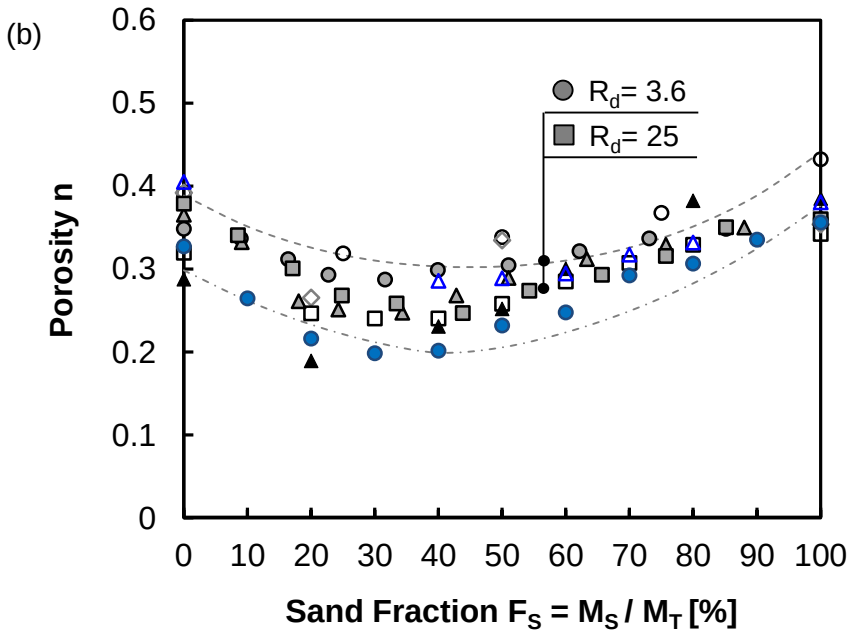

Data sources: ● Vallejo 2001; ○ Indrawan et al. 2006; △ Simoni and Housby 2006; ◇ Rahardjo et al. 2008; ▲, ■ Li 2009; ○,▲,□ Zhang et al. 2011 (Note that analogous data are found in Kamann et al. 2007; Donohue 2008).

Figure 6.3. Porosity: (a) Coarse-fine mixtures. (b) Gravel-sand mixtures. Note: $R_d = D_{50}/d_{50}$ is the relative size ratio (D_{50}=median grain size of coarser grains; d_{50}=median grain size of finer grains). For model -plotted as dashed line- refer to Table 6.1.

(a)

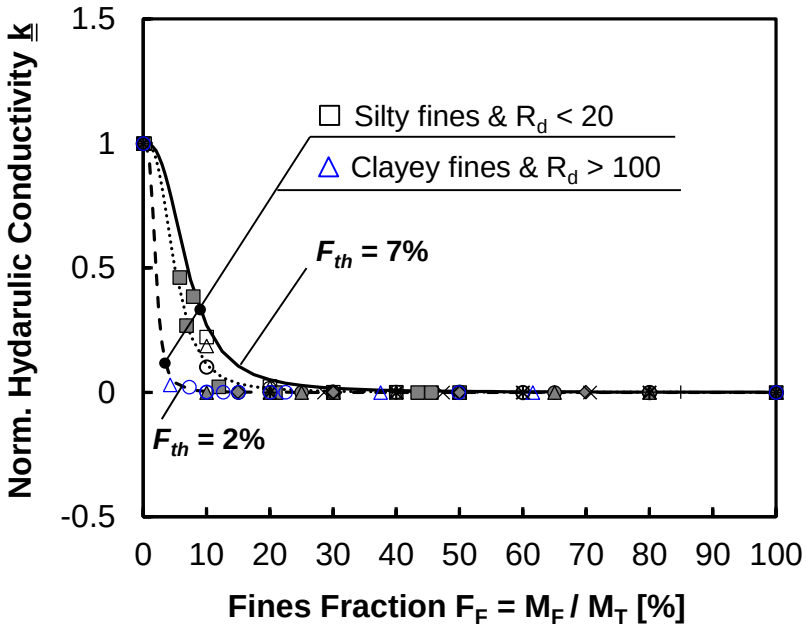

Data sources: ■ Marion 1990; ✶,+ Shelley and Daniel 1993; △ Knoll and Knight 1994; ▲, ● Sivapullaiah et al. 2000; ○ Crawford et al. 2008; × Shafiee 2008; ○ Tanaka and Toida 2008; ◆ Steiakakis et al. 2012; □,△ Belkhatir et al. 2013.

(b)

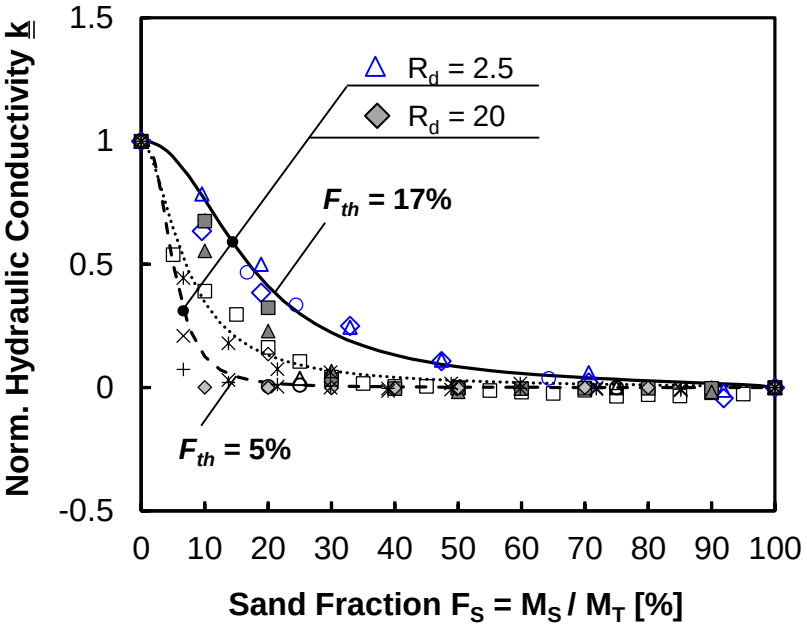

Data sources: ◇,■, ▲ Mason 1997; △,○ Indrawan et al. 2006; ○ Kamann et al. 2007; □ Donohue 2008; ● Rahardjo et al. 2008; ◆ Tanaka and Toida 2008; ×,✶,+ Zhang et al. 2011; ◇,△Lee and Koo 2014.

Figure 6.4. Normalized hydraulic conductivity: (a) Coarse-fine mixtures. (b) Gravel-sand mixtures. Note: $R_d = D_{50}/d_{50}$ is the relative size ratio (D_{50}=median grain size of coarser grains; d_{50}=median grain size of finer grains). Table 1 defines the normalization and the fitting model (plotted here as lines).

(a)

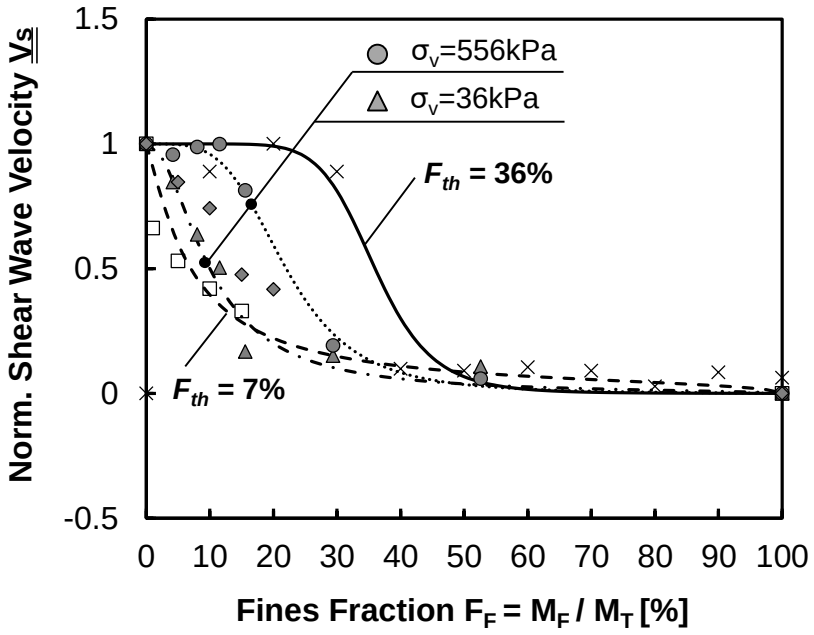

Data sources: ◆ Salgado et al. 2000; × Vallejo and Lobo-Guerrero 2005; ▲,● Lee et al. 2007b; □ Choo 2013 (*$V_{s,max}$ and $V_{s,min}$ are used for the normalization of symbol × only).

(b)

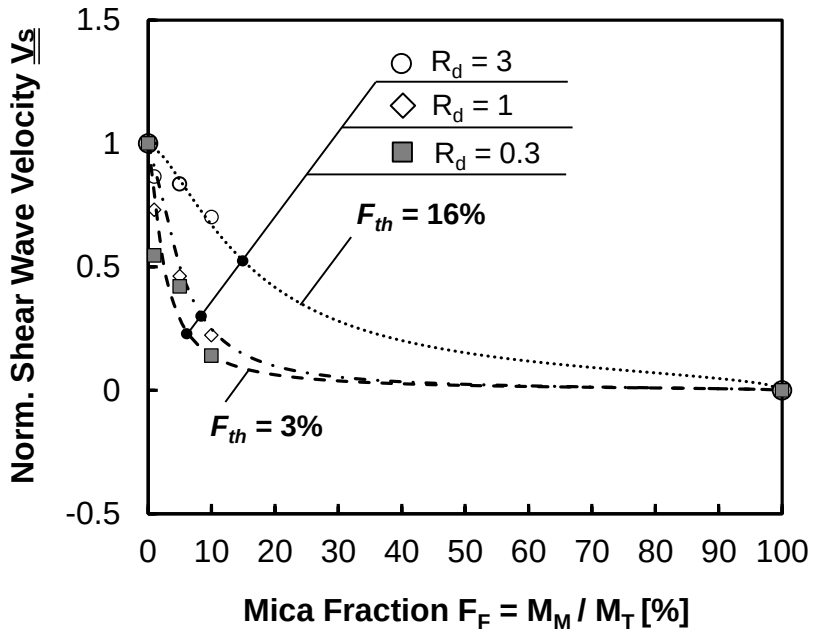

Data sources: ○,◇,■ Lee et al. 2007a.

Figure 6.5. Normalized shear wave velocity: (a) Coarse-fine mixtures. (b) Sand-mica mixtures. Note: $R_d = D_{50}/L_{mica}$ is the relative size ratio for sand-mica (D_{50}=median grain size of sand; L_{mica} = median mica particle length). F_{th} denotes the threshold mica fraction by weight. Table 6.1 defines the normalization and the fitting model (plotted here as lines).

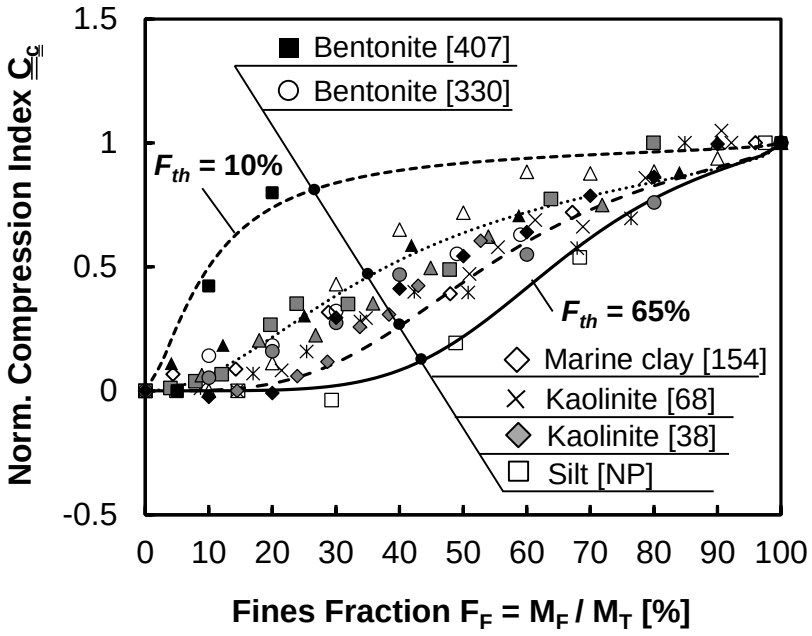

Data sources: ● Wagg and Kornard 1990; ○ Pandian et al. 1995; ■ Mollins et al. 1996; △ Kumar and Wood 1999; ◇ Monkul and Ozden 2007; □,▲,◇ Konishi et al. 2007; ✳,■,▲ Tiwari and Ajmera 2011; × Watabe et al. 2011; ◆ Simpson and Evans 2015.

Figure 6.6. Normalized compression index of coarse-fines mixtures versus fines fraction by mass. The number in square brackets [ ] indicates liquid limit *LL* of fine grains. Table 6.1 defines the normalization and the fitting model (plotted here as lines).

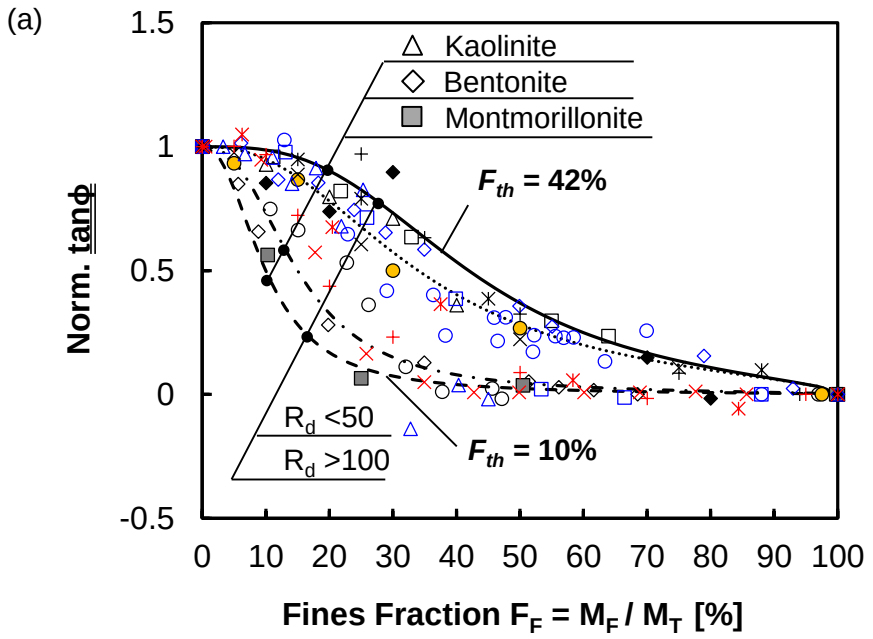

Data sources: △ Miller and Sowers 1958; ○ Kurata and Fujishita 1961; ◇ ■ Kenney 1977; □ Lupini et al. 1981; ○ Skempton 1985; □ Brown et al. 2003; + Yang 2004; × Tiwari and Marui 2005; ●: Konishi et al. 2007; ◇ Takahashi et al. 2007; △ Crawford et al. 2008; ×,✳,+ Tembe et al. 2010; ✳ Ueda et al. 2011; ◆ Simpson and Evans 2015.

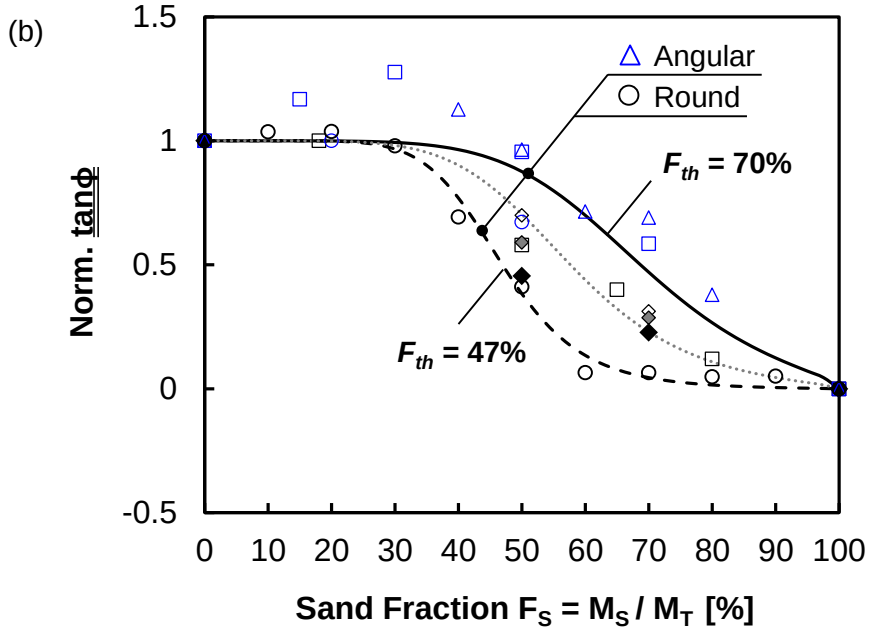

Data sources: ◇,◈,◆ Rathee 1981; □ Bortkevich 1982; ○ Vallejo 2001; △ Simoni and Housby 2006; ○ Rahardjo et al. 2008; □ Kumara et al. 2013.

Figure 6.7. Normalized shear strength in terms of tanϕ. (a) Coarse-fine mixtures. (b) Gravel-sand mixtures. Table 6.1 defines the normalization and the fitting model (plotted here as lines).

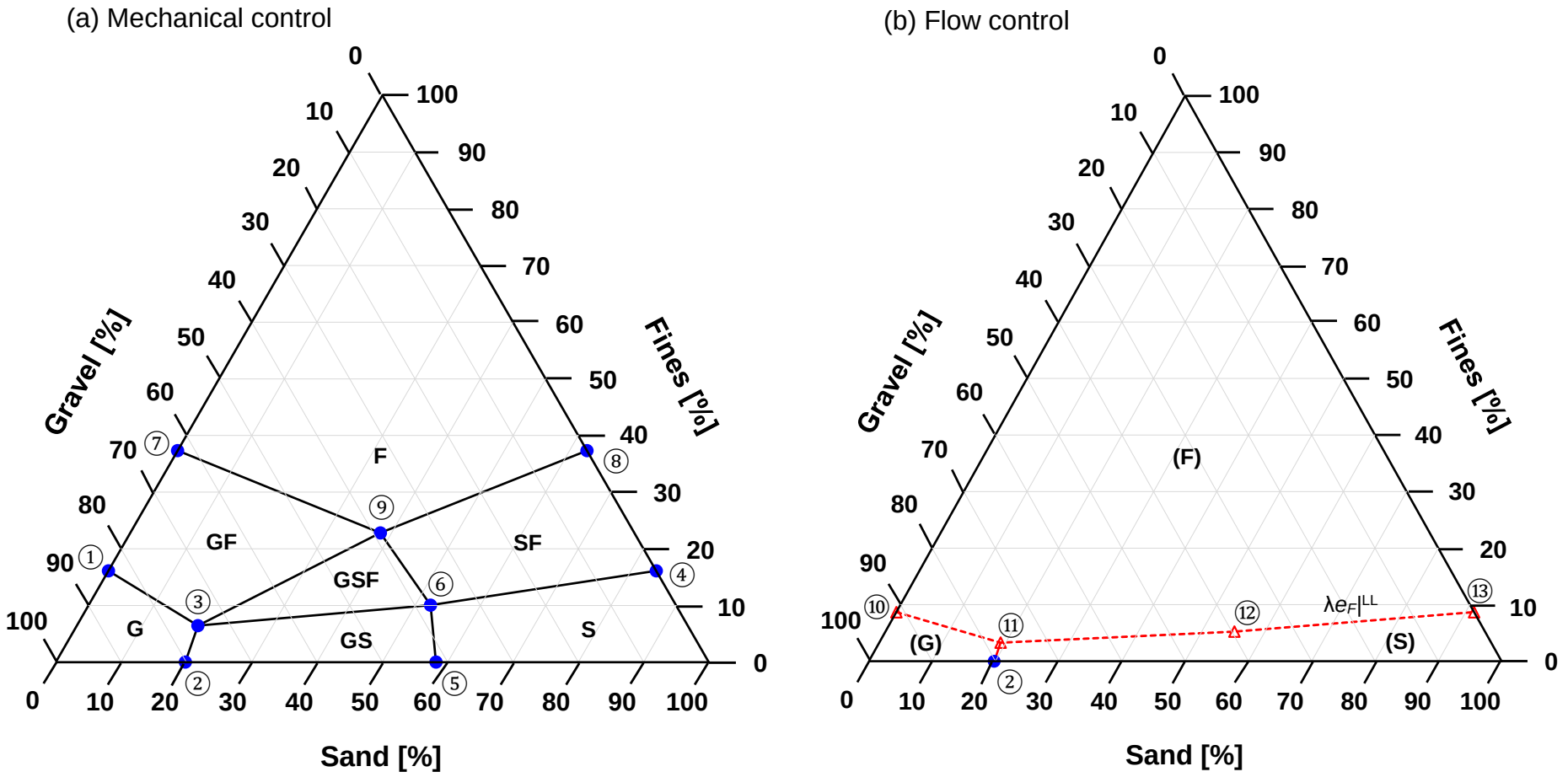

Figure 6.8. Notable mixtures and soil classification boundaries - ***Notation***: *G*=gravel, *S*=sand, and *F*=fines. (a) Mechanical control; *G*, *S*, and *F* indicate that a single fraction controls the mechanical response zone. *GF*, *SF*, *GS*, and *GSF* designate transition zones. (b) Flow control; fluid flow controlling fraction denoted as a single letter between parenthesis. Soil properties used for this chart: angular and uniform gravel e_G^{max}=0.81 and e_G^{min}=0.45; angular and uniform sand e_S^{max}=0.81 and e_S^{min}=0.45; fines resemble kaolinite with liquid limit *LL*=50, $e_F|^{10kPa}$=1.33, $e_F|^{1MPa}$=0.76, $e_F|^{LL}$=1.32, and λ=2.8. Note: flow-controlling fine fractions are F_F = 3.3% at point ⑪ and F_F = 5.2% at point ⑫.

Needed Input			
Gravel G	Fraction F_G	e_G^{max} and e_G^{min}	or roundness R and uniformity C_u
Sand S	Fraction F_S	e_S^{max} and e_S^{min}	or roundness R and uniformity C_u
Fines F	Fraction F_F	$e_F\|^{10kPa}$, $e_F\|^{1MPa}$, and $e_F\|^{LL}$	or liquid limit LL

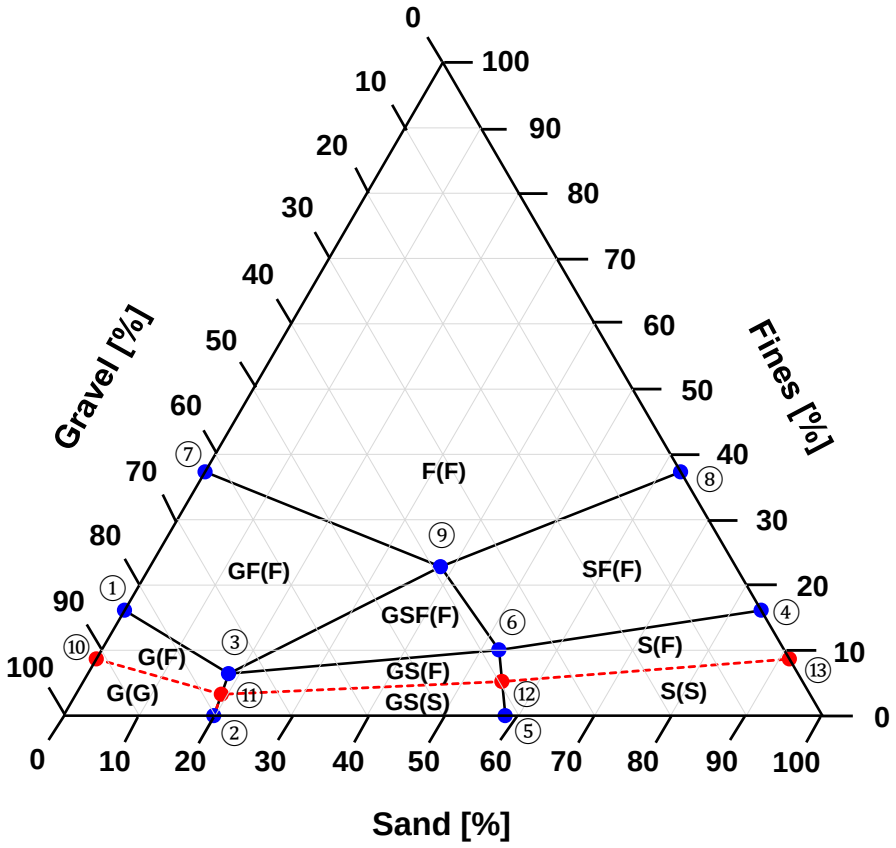

Group	Controlling Fraction		Description
	Mechanical Response	Fluid Flow	
F(F)	Fines	Fines	Fine-grained soil
GF(F)	Gravel & Fines	Fines	Transitional Mixture
SF(F)	Sand & Fines	Fines	Transitional Mixture
GS(F)	Gravel & Sand	Fines	Transitional Mixture
GSF(F)	Gravel-Sand-Fines	Fines	Transitional Mixture
G(F)	Gravel	Fines	Gravel with Fines
S(F)	Sand	Fines	Sand with Fines
G(G)*	Gravel	Gravel	Clean Gravel
S(S)*	Sand	Sand	Clean Sand
GS(S)	Gravel & Sand	Sand	Clean Gravel-Sand Mixture

Notes:

- (*) Specify well-graded or poorly-graded (Refer USCS). Well-graded G(G): $C_u \geq 4$ and $1 \leq C_c \leq 3$. Well-graded S(S): $C_u \geq 6$ and $1 \leq C_c \leq 3$.
- A soil group F or (F): Classify fines according to plasticity and sensitivity to pore-fluid chemistry.
- Recommendation: including triangular textural charts as part of standard reporting practice.

Figure 6.9. Soil classification boundaries: Mechanical control (blue points) and fluid flow control (red points). Soil properties used for this chart: angular and uniform gravel e_G^{max}=0.81 and e_G^{min}=0.45; angular and uniform sand e_S^{max}=0.81 and e_S^{min}=0.45; fines resemble kaolinite with liquid limit LL=50, $e_F|^{10kPa}$=1.33, $e_F|^{1MPa}$=0.76, $e_F|^{LL}$=1.32, and λ=2.8. Note: flow-controlling fine fractions are F_F = 3.3% at point ⑪ and F_F = 5.2% at point ⑫.

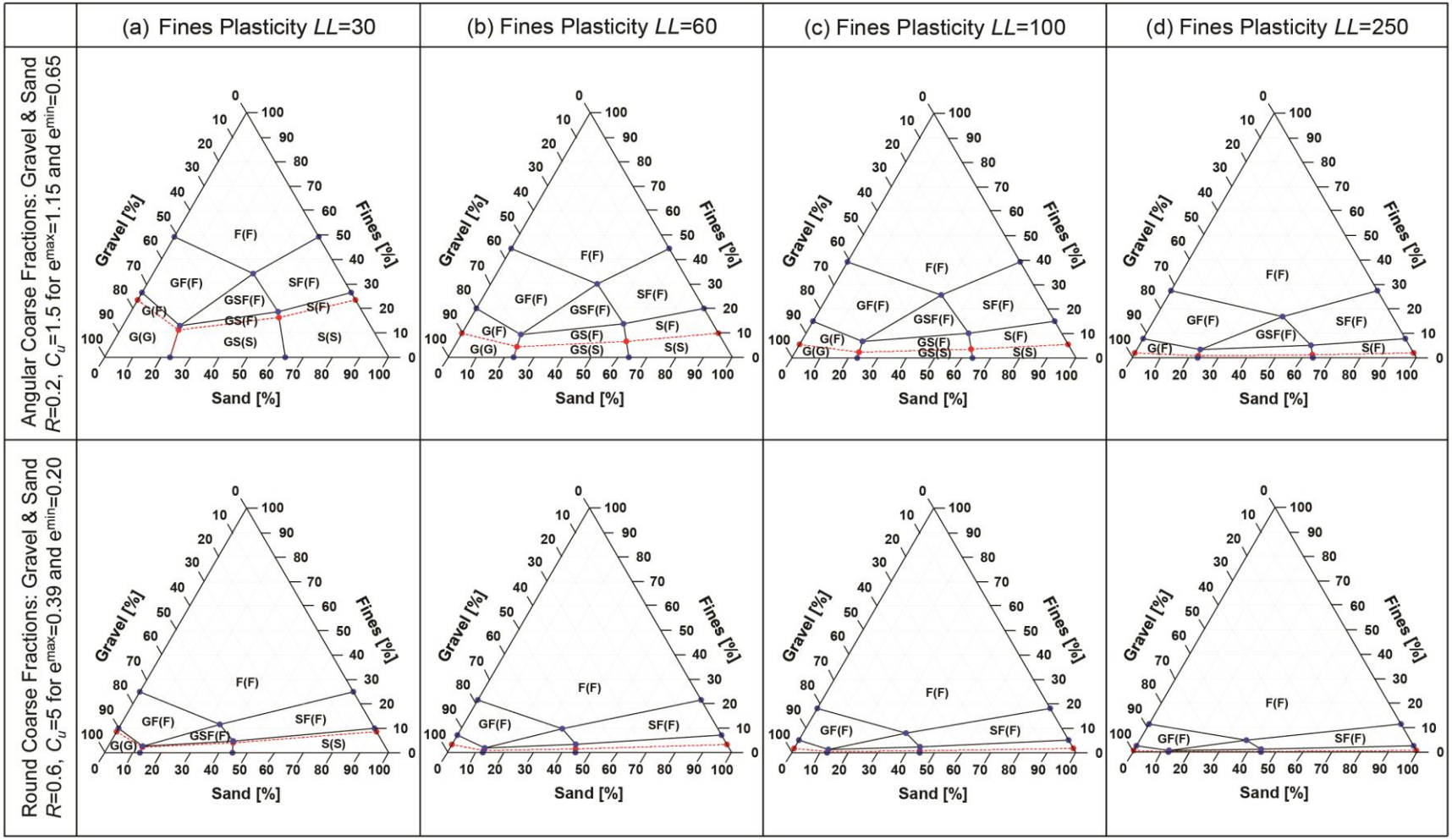

Figure 6.10. Revised soil classification system – Sample charts. *Angular gravel and sand* with (a) fines *LL*=30, (b) fines *LL*=60, (c) fines *LL*=100 and (d) fines *LL*=250. *Round gravel and sand* with (e) fines *LL*=30, (f) fines *LL*=60, (g) fines *LL*=100 and (h) fines *LL*=250. Refer to Figure 6.9 for missing nomenclature in small zones.

CHAPTER 7

CONCLUSIONS

The long-term performance of geotechnical systems depends on the soil response to all kinds of repetitive loads, including wind, waves, and traffic, chemical cyclic changes in pore fluid, thermal cycles, drying and wetting sequences, freeze-thaw cycles, and repetitive changes in pore water pressure. Repetitive loads induce the accumulation of permanent strain or the generation of excess pore water pressure. Consequently, there are associated changes in engineering properties (n, k, V_s, C_c, and ϕ).

7.1 Conclusions

The purpose of this research was to enhance the fundamental understanding of the long-term response of soils subjected to repetitive mechanical loads and to address the engineering implications. The main conclusions from this research follow.

Soil Response to Repetitive Changes in Pore Water Pressure under Deviatoric Loading

- The void ratio evolves towards the terminal void ratio e_T as the number of load cycles increases. The terminal void ratio is a function of the initial void ratio e_o, stress obliquity η, and cyclic pressure amplitude Δu_w.
- The soil subjected to high stress obliquity and large stress amplitude loading cycles will tend to be denser than *CSL*, and reach another volumetric terminal state where slip-down and roll-over is equally balanced (i.e. constant volume).

- Shakedown prevails with the small stress amplitude and low stress obliquity while ratcheting is dominant with the high stress obliquity and large stress amplitude.

Sand-K_o-Low Stress: Evolution of Void Ratio and Small Strain Stiffness

- The terminal void ratio e_T is a function of the initial void ratio e_o and the stress amplitude ratio $\Delta\sigma/\sigma_o$ under the K_o-condition.
- Changes in shear wave velocity track the evolution of the constraint modulus M_i during repetitive loadings. The maximum constraint modulus M_{max} computed from shear wave velocity V_s remains the upper bound for the sediment stiffness.
- Data provide a simple procedure to estimate the potential settlement a shallow foundation may experience when subjected to repetitive mechanical loads.

Sand-K_o-High Stress and One Million Cycles: Particle Crushing, Decementation, and Load-Deformation Relevant Analogues

- Sand particles subjected to a large number of cycles or high stress amplitude cycles tend to split through the inherent cleavage planes with more angular particle shape, finer particle size, and higher initial void ratio. Those factors increase the probability of crushing in a granular packing.
- Fatigue-induced asperity breakage is analogous to particle splitting or crushing. It describes the deformation mechanism associated with a “tipping point” for engineering purposes.

- Soil retains memory of their initial fabric even after a very large number of cycles or high stress amplitude cycles. A “tipping point” occurs at earlier cycles with a higher void ratio.
- The evolution of shear wave velocity during high stress amplitude cycles captures the role of fines produced on a sediment small strain stiffness.

Long-Term response of Sand-Fines Mixtures Subjected to Repetitive Mechanical Loads

- The ratio between the asymptotic contraction $\Delta e=e_o-e_T$ to attainable void ratio range $e_{max}-e_{min}$ estimates the maximum change in the relative density ΔD_T during repetitive loading.
- Trends for all volumetric changes in terms of e_T, $\Delta e=e_o-e_T$, and ε^{vol} capture the transition from sand- to fines- controlled behavior at the fines fraction $F_F < 50\%$.
- The evolution of the shear wave velocity during repetitive loads allows us to estimate the change in the coefficient of earth pressure at rest K_o.
- The sediment stiffness in small and large strain levels for coarse-fines mixtures encourages to revise current soil classification systems.

Revised Soil Classification System for Coarse-Fine Mixtures: Physics-Inspired and Data-Driven

- Detailed analyses of current soil classification systems reveal the great physical insight and understanding of soil behavior. However, there are several limitations in the current systems: fixed boundaries, 50% criteria, particle shape, and pore-fluid chemistry.

- The Revised Soil Classification System RSCS is proposed by providing a physics-inspired and data-driven approach.
- The RSCS classification boundaries are soil-specific and can be defined by the void ratio estimated from soil index properties (i.e. R, C_u, and LL).
- The RSCS uses a two-name nomenclature for mechanical- and flow- control fractions and classifies fines in terms of their plasticity and sensitivity to pore fluid chemistry.

7.2 Recommendations for Future Work

The studies addressed in this thesis can be extended to reflect other impotant phenomena associated with soil response to repetitive loads as follow:

- The critical state concept may not properly capture soil behavior under cyclic loading. Soils in the wet side may be denser than the critical state during repetitive loading.
- Proper model and algorism which do not accumulate the numerical error are required to enhance the understanding of soil behavior under repetitive loading condition.
- Constitutive models need to be capable of simulating ratcheting response and descrete element modelling is also required for particle scale analyses.
- The model also needs to be compatible with the repetitive load-deformation behavior caused by cyclic changes in pore fluid chemistry, thermal cycles, drying and wetting sequences, freeze-thaw cycles, and repetitive changes in pore water pressure.
- Quantification of factors affecting the stress concentration on particle contact is also required for further understanding of granular fatigue.

APPENDIX A: VOLUMETRIC-GRAVIMETRIC RELATIONS

A1. Binary Mixtures: Fines Fraction

Let us consider a binary mixture made of coarse and fine fractions. The coarse grains are packed at a void ratio e_C. The volume of voids between coarse grains V_{vC} is related to the volume of solids V_{sC} through the void ratio e_C

$$V_{vC} = e_C V_{sC} \tag{A1}$$

Fine grains packed at void ratio e_F fill the volume of voids between coarse grains V_{vC}. Then, the volume of solids in the fine grains V_{sF} is

$$V_{sF} = \frac{V_{vC}}{1+e_F} = \frac{e_C}{1+e_F} V_{sC} \tag{A2}$$

Let's define the mass fraction of fines as the mass of fines M_F divided by the total mass of fines and coarse fractions M_F+M_C; then,

$$F_F = \frac{M_F}{M_F + M_C} = \frac{1}{1+\frac{M_C}{M_F}} = \frac{1}{1+\frac{G_{sC}}{G_{sF}}\frac{V_{sC}}{V_{sF}}} \tag{A3}$$

where G_{sC} and G_{sF} are the specific gravities of coarse and fine fractions. Replacing Equation A2 in Equation A3,

$$F_F = \frac{1}{1+\frac{G_{s,C}}{G_{s,F}}\frac{1+e_F}{e_C}} \approx \frac{e_C}{1+e_C+e_F} \quad \text{(Approximately } G_{sC} \approx G_{sF}\text{)} \tag{A4}$$

The same equation can be used for gravel-sand, gravel-fines and sand-fines mixtures.

A2. Ternary Mixture: Gravel, Sand, and Fines Fractions

Let's extend the analysis to ternary gravel-sand-fines mixtures, where the gravel is packed at void ratio e_G. The sand packed at void ratio e_S fills the voids in the gravel V_{vG}. The remaining volume of voids is filled by the fines packed at void ratio e_F. From Equations A2 and A3:

$$M_F = \frac{e_S}{1+e_F} M_S \left(\frac{G_{sF}}{G_{sS}} \right) \tag{A5}$$

$$M_S = \frac{e_G}{1+e_S} M_G \left(\frac{G_{sS}}{G_{sG}} \right) \tag{A6}$$

Finally, the mass fraction of gravel F_G, sand F_S, and fines F_F relative to the total mass $M_G + M_S + M_F$ is obtained by successively invoking the previous two equations, A5 and A6. For clarity, let's consider to $G_{sG} \approx G_{sS} \approx G_{sF}$

$$F_G = \frac{M_G}{M_G + M_S + M_F} = \frac{1}{\left(1 + \frac{e_G}{1+e_S} + \frac{e_S}{1+e_F} \frac{e_G}{1+e_S} \right)} \tag{A7}$$

$$F_S = \frac{M_S}{M_G + M_S + M_F} = \frac{1}{\left(\frac{1+e_S}{e_G} + 1 + \frac{e_S}{1+e_F} \right)} \tag{A8}$$

$$F_F = \frac{M_f}{M_G + M_S + M_F} = \frac{1}{\left(\frac{1+e_S}{e_G} \frac{1+e_F}{e_S} + \frac{1+e_F}{e_S} + 1 \right)} \tag{A9}$$

Note that $F_G + F_S + F_F = 1.0$.

APPENDIX B: OBSERVATIONS RELEVANT TO THE RSCS

This appendix documents the closure prepared for discussion submitted to Park and Santamarina (2017b) reported in Chapter 6. This closure was prepared in collaboration with Gloria. M. Castro.

B1. Transition from Coarse-Controlled to Fines-controlled Behavior

The volumetric-gravimetric analysis for coarse-fine mixtures leads to the low threshold fines fraction $F_F|^L$ and the high threshold fines fraction $F_F|^H$ in terms of densely- and loosely- packed grains (from Equation. 6.1).

$$F_F\Big|^L = \frac{e_C^{\min}}{1 + e_C^{\min} + e_F^{\max}} \tag{B1}$$

$$F_F\Big|^H = \frac{e_C^{\max}}{1 + e_C^{\max} + e_F^{\min}} \tag{B2}$$

In designing the RSCS, we recognized that the packing of smaller grains between the pore spaces formed by the larger grains is different from packing conditions in bulk. Therefore, a data-based correction factor α is applied to the high threshold fines fraction $\alpha \cdot F_F|^H$ where α=1.3 for coarse-fines mixtures (Note: the factor is β=2.5 for gravel-sand mixtures in the original paper).

The low threshold $F_F|^L$ and data-adjusted high threshold fractions $\alpha \cdot F_F|^H$ are expected to bound the transition from fines- to coarse-controlled behavior. Figure B1 displays trends for maximum and minimum void ratios against the fines fraction F_F. The transition boundaries $F_F|^L$ and $\alpha \cdot F_F|^H$ are superimposed in each case. The threshold

fractions adequately capture the transitions from coarse-controlled to fines-controlled behavior. Either coarse, fines, or both fractions can be responsible for the mechanical control in transitional mixtures; this has implications on internal instability – explored next.

B2. Seepage-Induced Internal Instability

Liu et al. (2018) identify seepage data gathered for four binary mixtures and three ternary mixtures to test the RSCS. The underlying assumption being that internal instability during seepage implies that the fines are not load carrying. This is an insightful proposition indeed.

Further discussion requires a careful definition of internal instability, and its consistent application to the analysis of results reported by various studies. Previous studies associate internal instability to: (1) change in particle size distribution before and after testing, (2) change in the slope of the seepage velocity against the hydraulic gradient, (3) finer particles loss rate, (4) visual observations, and (5) changes in the local hydraulic gradient with time. In the context of this discussion, let's define "internal instability" as the fluid induced migration of fines out of a stable coarse-grained skeleton (in agreement with Moffat et al. 2011). Two corollaries follow from this definition. First, heave prior to internal instability destructures the coarse-grained skeleton and fines migration may follow even if the initial structure was stable prior to heave. Second, compaction and fines migration during fluid flow implies fines were part of the initial granular structure.

We carefully reviewed the seven soils in the three references cited by Liu et al. (2018) to identify the criteria used to assess internal instability and to extract

experimental details relevant to the analysis: particle size distribution for each soil fraction (F_G, F_S, and F_F), particle shape, extreme void ratios e^{max} and e^{min}, liquid limit, and experimental boundary conditions (i.e. confining boundary condition, effective stress level, vertical deformation, and flow direction). The main observations follow.

B2.1 Binary Mixtures

- *Soils A and B (from Skempton and Brogan 1994)*. The use of the sieve No. 4 (d= 4.76 mm) to separate gravel from sand classifies both soils as sands S(S). However, the fractions of these gap-graded, sub-angular gravel-sand specimens are best discriminated by a grain size d= 0.5 or 1 mm (Skempton and Brogan 1994 used d=2 mm); in this case, both soils A and B are classified as gravels G(G). In addition, heave destructures the granular skeleton and facilitates the migration of the finer fraction.
- *Soil HF01 (from Li 2008)*. This GS(S) soil sits near the S(S) boundary ($C_{u,\,G}$=1.5, $C_{u,S}$=17.2 and R_G=0.3, and R_S=0.3; particle shape: sub-angular for both gravel and sand).
- *Soil HF03 (from Li 2008)*. The soil experiences downward displacement (δ_v= 0.1~0.4 mm) during the increase in the hydraulic gradient. Therefore, the migrating finer particles were part of the initial load carrying skeleton, as expected for a soil with only F_G=19% gravel fraction. Indeed, this soil is a sand S(S), rather than a gravel G( ).

B2.2 Ternary Mixtures

- *Soil 14A (from Wan and Fell 2004).* This soil is made of very angular gravel ('blue metal', Sydney), very angular sand (as part of 'Basalt'), silica flour (LL=23), and kaolinite (LL=30). Detailed descriptions for each soil fraction found in Wan and Fell (2004) suggest the following index values: roundness R_G=0.20, uniformity $C_{u,G}$=1.82 for gravel; R_S=0.20, $C_{u,S}$=1.10 for sand; and liquid limit LL=30 for fines. The RSCS classifies soil 14A as a gravel, on the boundary between G(G) and G(F).
- *Soil 15 (from Wan and Fell 2004).* This soil experiences ~7% of material loss by suffusion, including both fines and sand grains. The remaining fines fraction F_F≈33% contributes to support loads. Our analysis classifies this soil as GF(F) assuming the following input parameters: roundness R_G=0.35, uniformity $C_{u,G}$=1.82 for very angular and sub-rounded gravel mixture; R_S=0.55, $C_{u,S}$=1.10 for 'Nepean sand' (in Payan et al. 2017); and liquid limit LL=30 for fines (Note: R_S=0.55 for sub-rounded grains).
- *Soil HF05 (from Li 2008).* The low gravel fraction F_G≈11% cannot form a primary soil skeleton to support loads, so, this soil cannot be classified as a gravel. This is a SF(F) soil (Adopted input parameters: roundness R_G=0.30, uniformity $C_{u,G}$=1.46 for gravel; R_S=0.30, $C_{u,S}$=4.44 for sand; and liquid limit LL=30 for fines). The original reference reports fines migration at a gradient i=7; this high gradient reflects the competition between drag forces and skeletal forces carried by particles subjected to effective stress.

B2.3 Discussion

The detailed analysis of each soil considered by Liu et al. (2018) and a careful review of previous studies on seepage-induced internal instability lead to the following observations:

- Internal stability by fines migration should not be determined through unconfined upwards seepage because seepage-induced heave and boiling inherently destructure the soil skeleton. Tests should impose effective stress controlled boundary conditions in order to identify the soil component(s) that controls the mechanical response. Then, the selective migration and loss of fines will confirm their lack of participation in the granular skeleton.
- Gradations that resemble the theoretical Fuller's curve (Fuller 1907) can attain self-filtering characteristics as the finer fractions successively fill the pores between coarser grains. Therefore, the deviation of a given grain size distribution from the Fuller's curve hints to the potential for internal instability, as suggested by Kenny and Lau (1985).
- The evaluation of internal stability for gap-graded soils should be determined by the properties of individual fractions rather than by an artificially imposed sieve size, such as sieves No. 200 or No. 4 in the USCS and RSCS.

B2.4 Complementary Study

We compiled data for 93 soils from published studies on seepage-induced internal instability (Kenny et al. 1984; Kenny and Lau 1985; Lafleur et al. 1989; Sun 1989; Aberg 1993; Burenkova 1993; Skempton and Brogan 1994; Chapuis et al. 1996; Wan and Fell

2004; Li 2008). The detailed analysis and classification of each soil (not reported here) suggest that soils that cluster into the GF(F), GS(S), and SF(F) classifications have a higher probability of experiencing internal instability. In particular, we can anticipate that fines migration is more likely to occur near the GF(F)-G(F) and SF(F)-S(F) boundaries where the coarser fraction forms the granular skeleton and the finer fraction is free to migrate. As soil classification boundaries are only indicative of on-going transitions, special attention is required for soils that fall near classification boundaries.

B3. Conclusions

The additional data collection and detailed analyses prompted by observations relevant to the RSCS show that:

- The low and high threshold fractions adopted in the proposed RSCS properly predict the coarse-controlled to fines-controlled transition.
- The analysis of gap-graded soils should be based on the grain size that best discriminates the soil fractions, rather than by a preselected sieve size e.g., No. 200 or No. 4 in the USCS and RSCS.
- Sediments that fall near the GF(F)-G(F) and SF(F)-S(F) boundaries are more likely to experience fines migration as the coarser fraction forms the granular skeleton and the finer fraction is free to migrate.

An Excel macro for the RSCS is available on the websites (egel.kaust.edu.sa). It simultaneously draws all RSCS-associated charts, identifies classification boundaries, and plots the point that represents the soil under consideration.

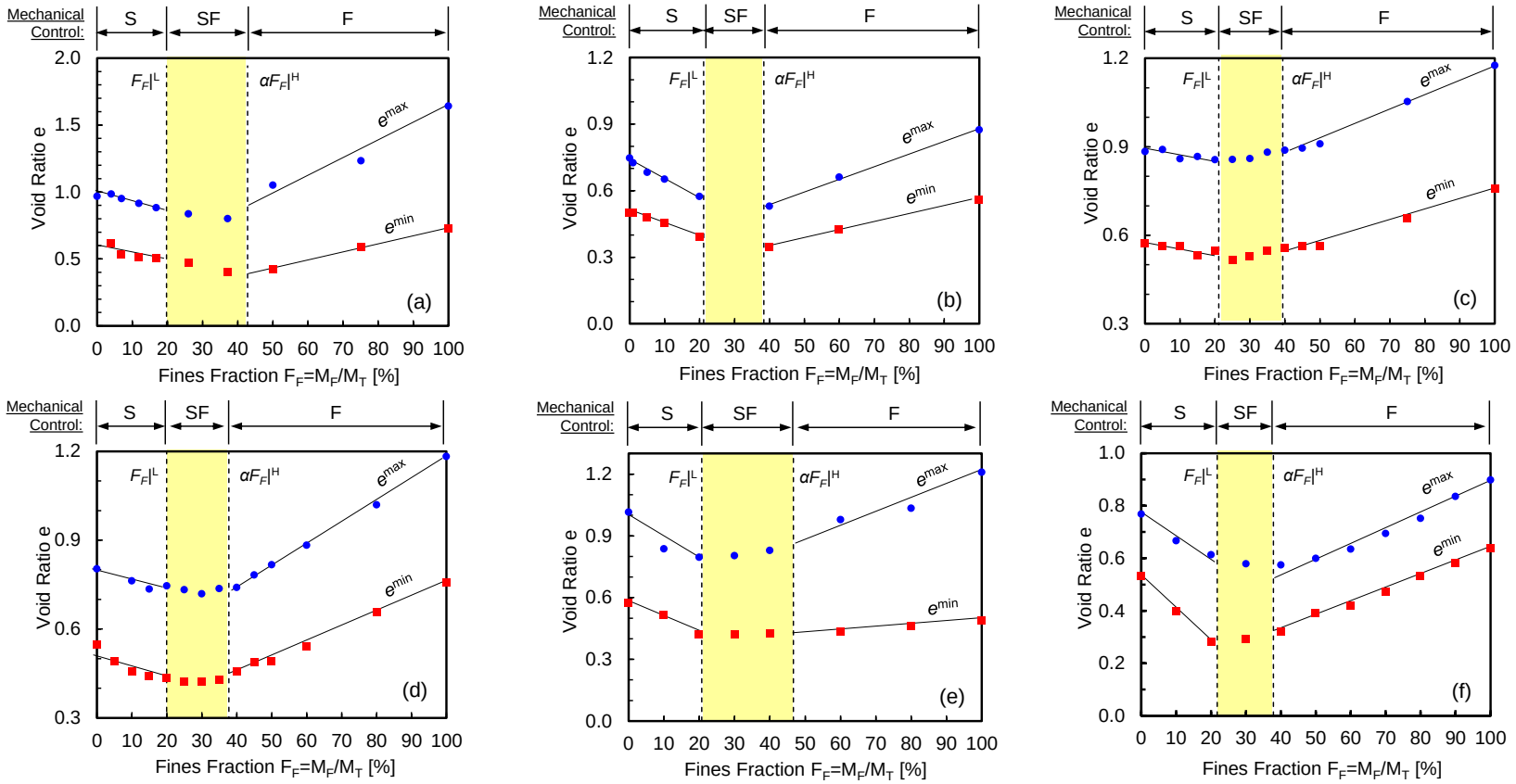

Figure B1. Maximum and minimum void ratios against fines fraction F_F extracted from: (a) Gutierrez (2005); (b) Choo and Burns (2015); (c) Lade and Yamamuro (1997); (d) Lade and Yamamuro (1997); (e) Kang and Lee (2015); (f) Fuggle et al. (2014). Note: α=1.3 in all cases.

APPENDIX C: MODEL: BOUNDING SURFACE PLASTICITY

The bounding surface plasticity model introduced by H. S. Yu (2007) is revisited here as an early effort towards modeling the soil response to repetitive loading.

C1. Introduction

The modified Cam-clay model is respected concept used to anticipate the load-deformation response of soils subjected to monotonic loading. However, the traditional plasticity only captures the purely elastic deformation behavior within a yield surface during unloading and reloading at the elasto-plastic state. However, this theory is not a robust method to demonstrate the soil behavior under repetitive loading conditions.

Appendix C describes the underlying concept of bounding surface plasticity and presents the constitutive model with all detrailed procedures to simulate the cyclic load-deformation behavior of one soil element in an Excel sheet.

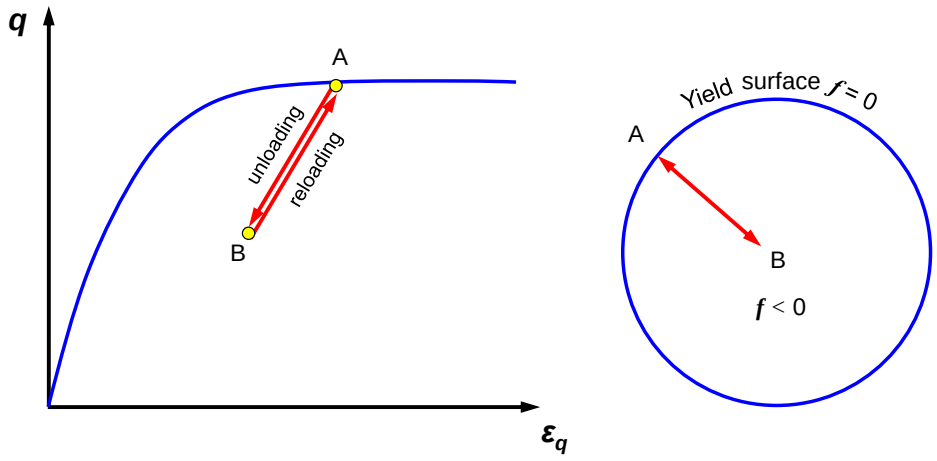

Figure C1. Idealized stress-strain response. Schematic drawings describe the unloading followed by reloading within a yield surface (Rahimi et al. 2017).

C2. Bounding Surface Plasticity - Underlying Concepts

C2.1 Definitions

We use the following definitions to describe the constitutive model based on bounding surface plasticity.

Yield surface: The limitation for elastically attainable stress state.

Loading surface: It represents the current stress state in p'-q space.

Bounding surface: It is same as the yield surface in conventional plasticity theory for the loading stage before any loading history (i.e. first isotropic loading or first shear loading). On the other hand, this bounding surface represents the image stress point for the loading surface during isotropic unloading followed by shear loading, shear unloading, and reloading.

Hardening rule. This rule governs the evolution of a yield surface.

Co-axiality: The plastic strain increment $\delta\varepsilon^p$ along the p'-q axes consists of the volumetric strain increment $\delta\varepsilon_p^p$ and shear strain increment $\delta\varepsilon_q^p$.

Normality: The plastic strain increment $\delta\varepsilon^p$ is normal to the plastic potential g.

Flow rule: The associated flow rule describes the assumption when the plastic potential g is expressed by the same function of yield surface f [i.e. $g(p, q)= f(p, q)$]. The non-associated flow rule defines the condition when $g(p, q) \neq f(p, q)$.

Consistency: This indicates that the stress state during plastic flow should remain on the subsequent yield surface (i.e. a loading applied from a plastic deformation state results in another plastic deformation state, Prager 1949).

C2.2 Underlying Concepts

Modeling of soils subjected to cyclic loading lead to the development of the concept of a bounding surface plasticity [Dafalias and Popov, 1975; Krieg 1975; Manzari and Dafalias 1997; Yu 2007; Hu et al. 2012]. This theory involves two surfaces: a loading surface and bounding surface F as shown in Figure C2. The bounding surface plasticity does not require tracking of the evolution of the yield surface (i.e. size and location) to estimate the plastic strain increment, but assumes a continuous yielding inside the bounding surface. The plastic modulus associated with permanent volumetric or shear strain accumulation depends on the distance δ between the current stress state and the image point on the bounding surface [plastic modulus $H= f(\delta)$ in Figure C2]. In other words, the plastic modulus decreases as the loading surface becomes closer to bounding surface, consequently, the more plastic strain increment occurs.

C3. Constitutive Model

This section details the constitutive model based on bounding surface plasticity and presents all procedures that describe the repetitive load-deformation response of soils under triaxial and drainage conditions. The key feature of this modeling is to divide the continuous cyclic stress path into separate loading events: (1) first loading, (2) first unloading, and (3) second loading followed by the same repeated loading sequences as illustrated in Figure C3. An Excel sheet facilitates this one-element modeling.

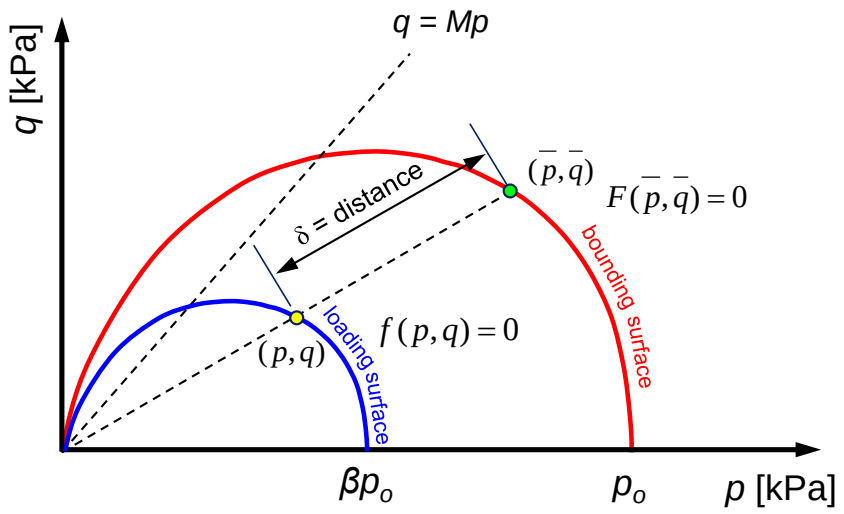

Figure C2. Bounding surface and loading surface. The yellow circle denotes the current stress state (p, q) on loading surface f and the green circle indicates the image point on bounding surface F. The β-value indicates that the distance δ=0 as $\beta \rightarrow 1$ while $\delta=\delta_{max}$ when $\beta \rightarrow 0$ (Yu 2007).

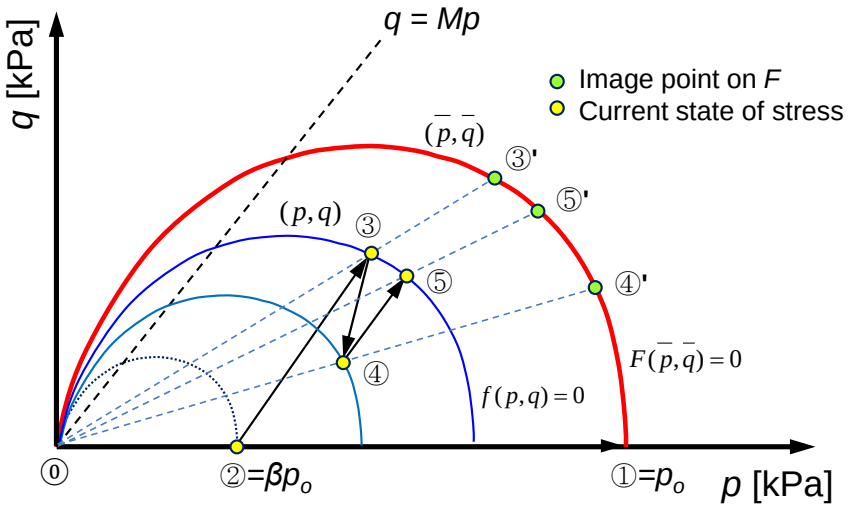

Figure C3. Schematic drawing to describe the division of the cyclic stress path into a separate loading event. F indicates the bounding surface (red line) and f denotes the loading surface (blue lines). Loading history: Hydrostatic loading: ⓪→①, Hydrostatic unloading: ①→②, First shear loading: ②→③, First shear unloading: ③→④, shear reloading: ④→⑤. The pre-consolidation pressure p_o defines the size of the bounding surface F while the β-value determines the initial size of the loading surface f (Yu 2007).

C3.1 Input Model Parameters

Table C1 summarizes all parameters associated with the constitutive model detailed in the next section and used in a simple example exercise at the end of this Appendix C.

Table C1. Soil Parameters (Values from Wang 2005; Yu et al. 2007).

Parameters	Symbol	Associated with	Used Value
Maximum void ratio	e_{max}	Minimum packing density	0.79
Minimum void ratio	e_{min}	Maximum packing density	0.46
e_{cs} at p'=1kPa	e_{cs}^{1kPa}	Critical state	0.796
Slope in e-lnp' space	λ_{cs}	Critical state	0.025
Compression index	λ	Initial loading	0.025
Recompression index	κ	Unloading	0.005
Poisson's ratio	ν		0.30
Initial void ratio	e_o	State parameter	0.81
Friction angle	ϕ_{cs}	Critical state	29.8^o
Slope in p'-q space	M	M = 6sinϕ_{cs}/(3-sinϕ_{cs})	1.19
Stress obliquity	η	$\eta = q/p'$	
Spacing ratio	r	$\zeta_R=(\lambda-\kappa)\ln r$ where $\frac{\eta}{M}=1-\frac{\xi}{\xi_R}$ ζ_R is a reference state parameter ($\zeta_R > 0$) that indicates a vertical distance between CSL and NCL.	19.2
Material constant	n	plastic flow rule	3.5
Material constant	m	plastic flow rule	1
Material constant	h	First loading	2
Material constant	ψ	First loading	1
Model constant	H_u	Unloading	1
Material constant	H_R	Reloading	5
Material constant	k	Shakedown controlling factor	1000

C3.2 Formulations for Repetitive Loading

This study defines the mean effective stress p'= (σ'_1+σ'_3)/2 and the deviatoric stress q= (σ'_1-σ'_3)/2 in terms of the effective axial σ'_1 and confining stress σ'_3, and the stress obliquity as $\eta=q/p'$.

C3.2.1 First Loading

Step 1. Define the bounding surface F and loading surface f (Figures C2 and C3).

$$F(\bar{p},\bar{q},\varepsilon_p^p)=\left(\frac{\bar{q}}{M\bar{p}}\right)^n+\frac{1}{\ln r}\ln\left(\frac{\bar{p}}{p_o}\right)=0 \qquad \text{(Bounding surface)} \qquad \text{(C1)}$$

$$f(p,q,\varepsilon_p^p)=\left(\frac{q}{Mp}\right)^n+\frac{1}{\ln r}\ln\left(\frac{p}{\beta\cdot p_o}\right)=0 \qquad \text{(Loading surface)} \qquad \text{(C2)}$$

Step 2. Define the plastic potential g

$$g(p,q)=m\ln\left[1+(m-1)\left(\frac{q}{Mp}\right)^n\right]+n(m-1)\ln\frac{p}{C} \qquad \text{(C3)}$$

where $m=\frac{2}{3}\frac{[M(6-M)]^n-(3M)^n}{\Lambda(6-M)(3M)^{n-1}}$ and Λ = (λ-κ)/λ. The m-parameter relates to a critical state constant. This plastic potential adopts the non-associate flow rule (i.e. $f \neq g$). The constant C determines the size of the plastic potential surface [$g(p, q)$=0 returns C].

Step 3. Compute bulk modulus B

$$B=\frac{p'(1+e_o)}{\kappa} \qquad \text{(C4)}$$

Step 4. Compute shear modulus G (where ν = Poisson's ratio).

$$G=\frac{3p'(1+e_o)(1-2\nu)}{2\kappa(1+\nu)} \qquad \text{(C5)}$$

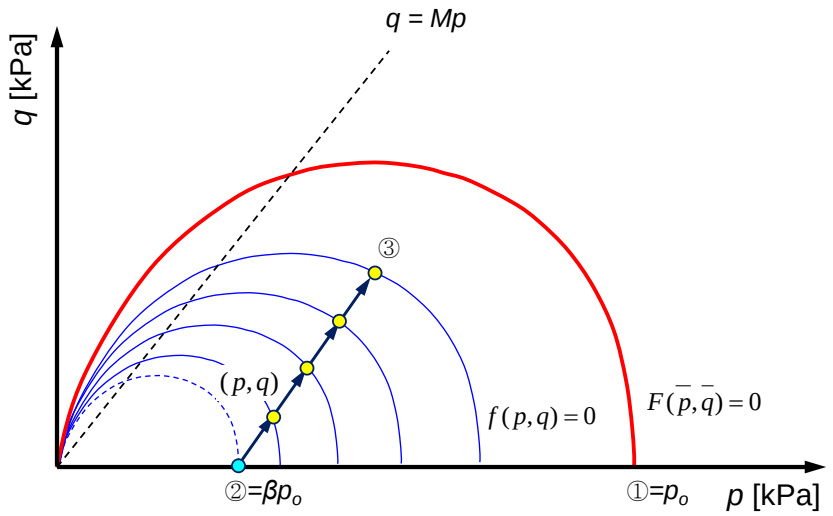

Figure C4. First shear loading. The effective stress path (=ESP) is divided into a number of equal stress increments.

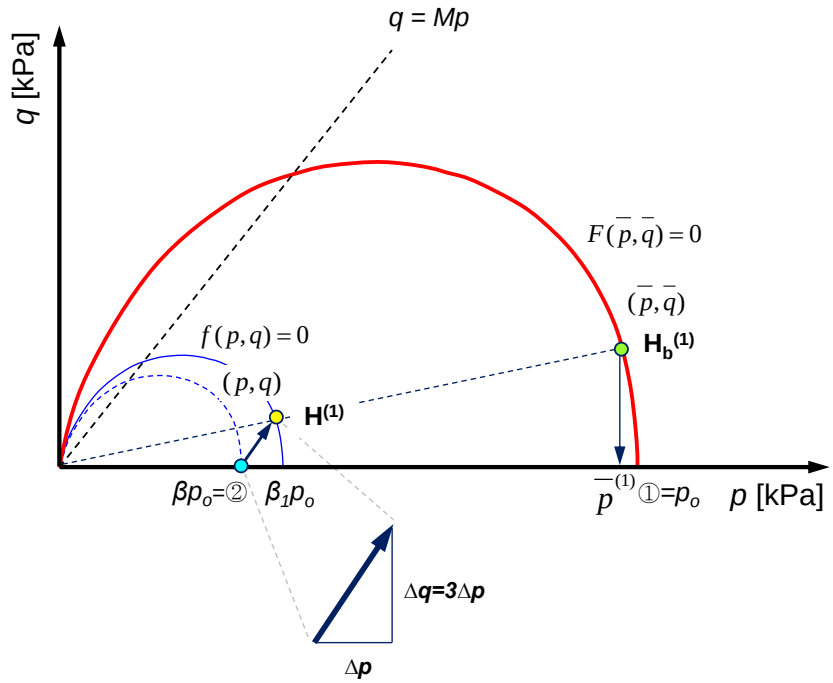

Figure C5. Loading surface f after one stress increment Δp. $H^{(1)}$ denotes the plastic modulus on the current loading surface and $H_b{}^{(1)}$ indicates the plastic modulus on the bounding surface. Note: $^{(1)}$ denotes the first stress increment. The yellow circle indicates the current state of stress and the green circle indicates the image point on the bounding surface.

Step 5. Divide the cyclic stress path into separate loading events [Figure C3].

Step 6. Divide the effective stress path (=ESP) into a number of equal stress increments (Δp, Δq) [Figure C4].

Step 7. Implement the one stress increment Δp and Δq [Figure C5].

Step 8. Compute the plastic modulus H at the current stress state after one loading step.

$$H = H_b + \frac{h}{p} \times \frac{(1-\beta)^{\psi}}{\beta} \tag{C6}$$

where ψ and h are material constants. The modulus H is a function of the plastic modulus H_b at the image point. The β-value estimates the distance between the current state of stress and its image point [see Figure C2].

Plastic modulus H_b at image point. This step requires obtaining the plastic modulus H_b at the image point. The plastic volumetric strain rate at the current stress state (p, q),

$$\Delta\varepsilon_p^p = \frac{1}{H}\left(\frac{\partial f}{\partial p}\Delta p + \frac{\partial f}{\partial q}\Delta q\right)\frac{\partial g}{\partial p} = \frac{1}{H_b}\left(\frac{\partial F}{\partial \bar{p}}\Delta \bar{p} + \frac{\partial F}{\partial \bar{q}}\Delta \bar{q}\right)\frac{\partial g}{\partial \bar{p}} \tag{C7}$$

The bounding surface should satisfy the *consistency condition*, $F = f(p, q, \varepsilon^p)$ that requires,

$$dF = \frac{\partial F}{\partial \bar{p}}\Delta \bar{p} + \frac{\partial F}{\partial \bar{q}}\Delta \bar{q} + \frac{\partial F}{\partial \varepsilon_p^p}\Delta\varepsilon_p^p = 0 \rightarrow \left(\frac{\partial F}{\partial \bar{p}}\Delta \bar{p} + \frac{\partial F}{\partial \bar{q}}\Delta \bar{q}\right) = -\frac{\partial F}{\partial \varepsilon_p^p}\Delta\varepsilon_p^p \tag{C8}$$

Replacing Equation C8 in Equation C7, then the plastic volumetric strain rate $\Delta\varepsilon_p^p$,

$$\Delta\varepsilon_p^p = \frac{1}{H_b}\left(-\frac{\partial F}{\partial \varepsilon_p^p}\Delta\varepsilon_p^p\right)\frac{\partial g}{\partial \bar{p}} \tag{C9}$$

Rearranging Equation C9 defines the plastic modulus H_b at the image point.

$$H_b = -\frac{\partial F}{\partial \varepsilon_p^p}\cdot\frac{\partial g}{\partial \bar{p}} = -\left(\frac{\partial F}{\partial p_o}\cdot\frac{\partial p_o}{\partial \varepsilon_p^p}\right)\frac{\partial g}{\partial \bar{p}} \qquad \text{(Chain rule)} \tag{C10}$$

The three terms in Equation C10 follow,

$$\frac{\partial F}{\partial p_o} = -\frac{1}{p_o \ln r} \tag{C11}$$

$$\frac{\partial p_o}{\partial \varepsilon_p^p} = \frac{(1+e_o)\,p_o}{\lambda-\kappa} \qquad \text{(Rowe's stress-dilatancy relation)} \tag{C12}$$

$$\frac{\partial g}{\partial \bar{p}} = \frac{(1+e_o)}{(\lambda-\kappa)}\frac{n(m-1)}{\bar{p}}\left[1-\frac{m\cdot\left(\frac{\bar{q}}{M\bar{p}}\right)^n}{1+(m-1)\left(\frac{\bar{q}}{M\bar{p}}\right)^n}\right] \tag{C13}$$

Finally, we can obtain the plastic modulus H_b at the image point,

$$H_b = \frac{n(m-1)(1+e_o)}{(\lambda-\kappa)\bar{p}\ln r}\left[1-\frac{m\left(\frac{q}{Mp}\right)^n}{1+(m-1)\left(\frac{q}{Mp}\right)^n}\right] \tag{C14}$$

Then (refer to Equations C1 and Figure C5),

$$\bar{p}^{(1)} = p_o \exp\left[-\left(\frac{q}{Mp}\right)^n \ln r\right] \qquad \text{where} \quad \bar{p} = \bar{p}^{(1)} \tag{C15}$$

β-parameter. This value estimates the distance between the current state of stress and its image point. The plastic modulus H satisfies that $H=H_b$ as $\beta \to 1$ while $H \to \infty$ when $\beta \to 0$ [Equation C6 and Figure C2]. The computation of β-value at the current stress state (p, q) follows (refer to Equation C2):

$$\beta_1 = \frac{p}{p_o \exp\left[-\left(\frac{q}{Mp}\right)^n \ln r\right]} \tag{C16}$$

Step 9. Determine the plastic volumetric strain increment $\Delta\varepsilon^{p}_{p}$ at the current stress state (p, q) by using Equations C6, C7, and C14. All three associated terms in Equation C7 are,

$$\frac{\partial f}{\partial p} = -\frac{n \cdot \left(\frac{q}{Mp}\right)^{n}}{p} + \frac{1}{p \ln r} \tag{C17}$$

$$\frac{\partial f}{\partial q} = -\frac{n \cdot \left(\frac{q}{Mp}\right)^{n}}{q} \tag{C18}$$

$$\frac{\partial g}{\partial p} = -\frac{(m-1)mn \cdot \left(\frac{q}{Mp}\right)^{n}}{\left[(m-1)\left(\frac{q}{Mp}\right)^{n} + 1\right]} + \frac{(m-1)n}{p} \tag{C19}$$

Step 10. Determine the plastic shear strain increment $\Delta\varepsilon^{p}_{q}$ at the current stress state (p, q).

$$\Delta\varepsilon^{p}_{q} = \Delta\varepsilon^{p}_{p} \frac{m\left(\frac{q}{p}\right)^{n-1}}{M^{n} - \left(\frac{q}{p}\right)^{n}} \qquad \leftarrow \frac{\Delta\varepsilon^{p}_{p}}{\Delta\varepsilon^{p}_{q}} = \frac{M^{n} - \left(\frac{q}{p}\right)^{n}}{m\left(\frac{q}{p}\right)^{n-1}} \tag{C20}$$

Note: Equation C20 has the same plastic flow rule as the modified Cam-clay model by choosing n=2 and m=1.

Step 11. Determine the elastic volumetric strain increment $\Delta\varepsilon^{e}_{p}$ [Equation C4 in Step 3].

$$\Delta\varepsilon^{e}_{p} = \frac{\Delta p}{B} \tag{C21}$$

Step 12. Determine the elastic shear strain increment $\Delta\varepsilon^{e}_{q}$ [Equation C5 in Step 4].

$$\Delta\varepsilon_q^e = \frac{\Delta q}{3G} \tag{C22}$$

Step 13. Calculate the total volumetric strain increment $\Delta\varepsilon_p$ [Equations C7 and C21].

$$\Delta\varepsilon_p = \Delta\varepsilon_p^e + \Delta\varepsilon_p^p \tag{C23}$$

Step 14. Calculate the total shear strain increment $\Delta\varepsilon_q$ [Equations C20 and C22].

$$\Delta\varepsilon_q = \Delta\varepsilon_q^e + \Delta\varepsilon_q^p \tag{C24}$$

Step 15. Calculate the total volumetric strain ε_p [Equation C23].

$$(\varepsilon_p)_{i+1} = (\varepsilon_p)_i + (\Delta\varepsilon_p)_{i+1} \tag{C25}$$

Step 16. Calculate the total shear strain ε_q [Equation C24]

$$(\varepsilon_q)_{i+1} = (\varepsilon_q)_i + (\Delta\varepsilon_q)_{i+1} \tag{C26}$$

After finishing *Step 16*, go back to *Step 7* to add one more stress increment (Δp, Δq) and conduct this iteration (*Steps 7*-to-1*6*) until the current stress reaches the desired stress level (i.e. ③ in Figure C4).

C3.2.2 First Unloading

Step 17. Determine the stress amplitude $\Delta\sigma$ and final stress state for the first shear unloading, and divide the effective stress path (=ESP) into a number of equal stress decrements (Δp, Δq) [Figure C6].

Step 18. Implement the one stress decrement Δp and Δq [Figure C7].

Step 19. Compute the plastic modulus H at the current stress state.

$$H = \frac{H_u}{1-\beta} \tag{C27}$$

where H_u is the model constant. Use Equation C16 for β-value calculation.

Step 20. Use the plastic modulus H in Equation C27 to compute the total volumetric strain ε_p and total shear strain ε_q after this one unloading step [Steps 9-to-16].

Step 21. After finishing *Step 20*, go back to *Step 17* to conduct one more stress decrement (Δp, Δq), and implement this iteration (*Steps 17*-to-*20*) until the current stress reaches the desired stress level.

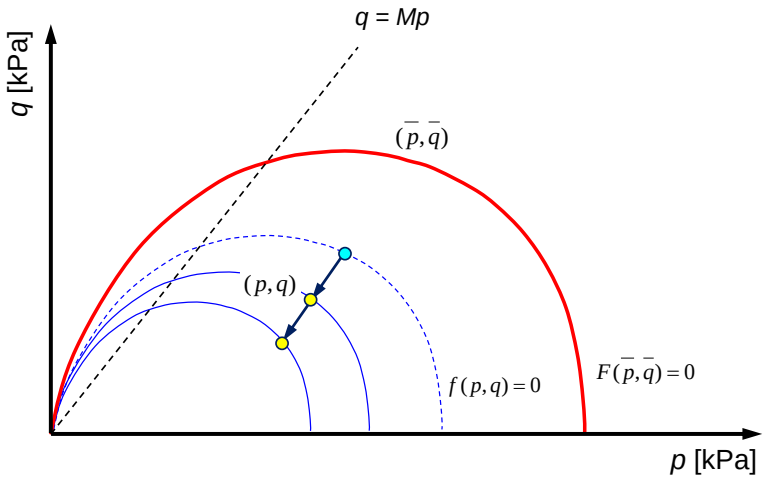

Figure C6. First shear unloading. The effective stress path (=ESP) is divided into a number of equal stress decrements.

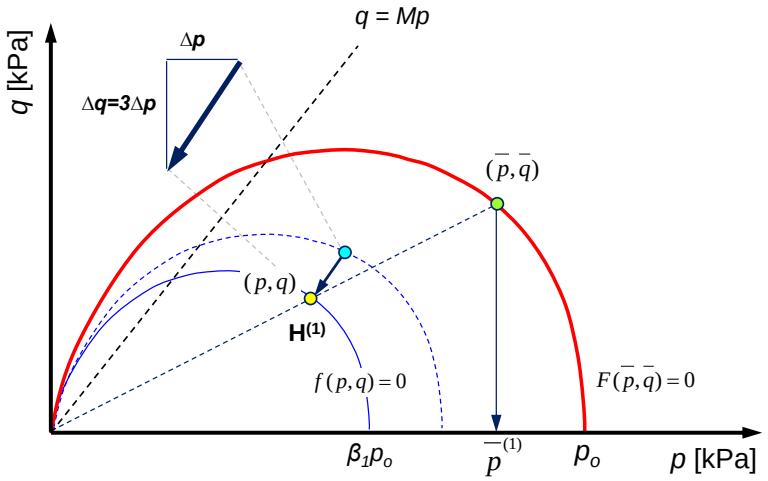

Figure C7. First shear unloading. Loading surface f after one stress decrement Δp.

C3.2.3 Reloading (or Second Loading)

Step 22. Divide the effective stress path (=ESP) corresponding to the stress amplitude $\Delta\sigma$ into a number of equal stress increments [Figure C8].

Step 23. Implement the one stress increment Δp and Δq [Figure C9].

Step 24. Compute the plastic modulus H at the current stress state [Figure C9].

$$H = H_b + H_R \times \left(\frac{1-\beta}{\beta}\right) \times (1+\varepsilon_q^p)^k \qquad \text{(C28)}$$

where H_R and k are model constants, and ε_q^p is the accumulated plastic shear strain.

Step 25. Use Equation C14 to obtain H_b and use Equation C16 for β-value calculation.

Step 26. Use the plastic modulus H in Equation C28 to compute the total volumetric strain ε_p and total shear strain ε_q after this one loading step [Go to *Steps 9-to-16*].

Step 27. After finishing *Step 26*, go back to *Step 23* to conduct one more stress increment (Δp, Δq) and implement this iteration (*Steps 23*-to-*26*) until the current stress increases to the desired stress level.

C3.2.4 Further Repetitive Loading – Increase in the Number of Cycles

An increase in the number of cycles for further repetitive loading can be carried out by iterating *Steps 17-to-27* as described in C4.2.2 and C4.2.3 with the pre-selected stress amplitude $\Delta\sigma$ in *Step 17*.

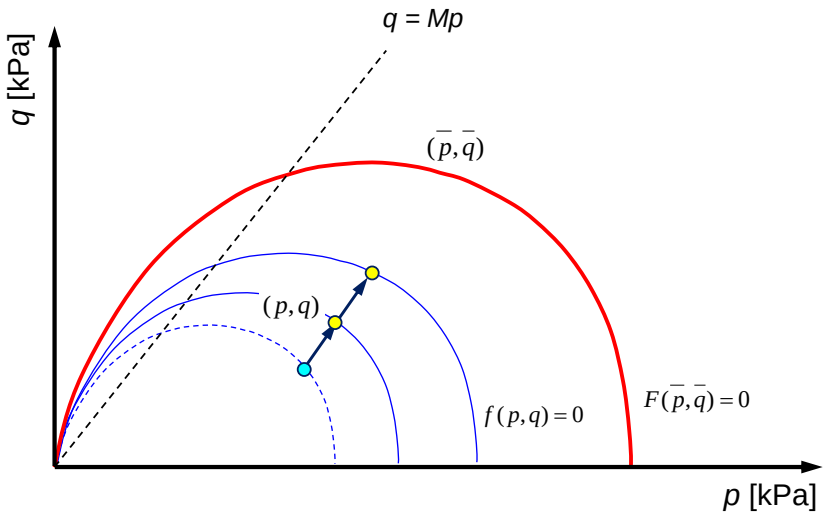

Figure C8. Second shear loading. The effective stress path (=ESP) is divided into a number of equal stress increments.

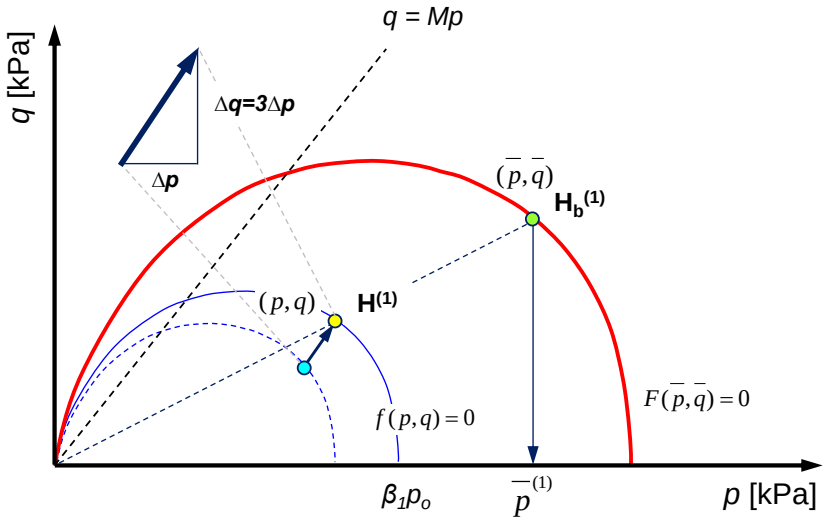

Figure C9. Second shear loading. Loading surface *f* after one stress increment Δp.

C4. Results and Considerations for Future Work

Figure C10 presents the simulation results in the p'-q-e-ε_d space for the contractive sand subjected to repetitive deviatoric stress Δq=30kPa during the number of cycles i=100. Soils parameters used for this simulation are summarized in Table C1. Results indicate that the bounding surface plasticity with the constitutive model (introduced by Yu 2007) is simple, but successfully describes the evolution of the void ratio and the asymptotic shear deformation response (i.e. shakedown) during repetitive loads. However, there are still pending questions and considerations to enhance the constitutive model as described in the section 7.2.

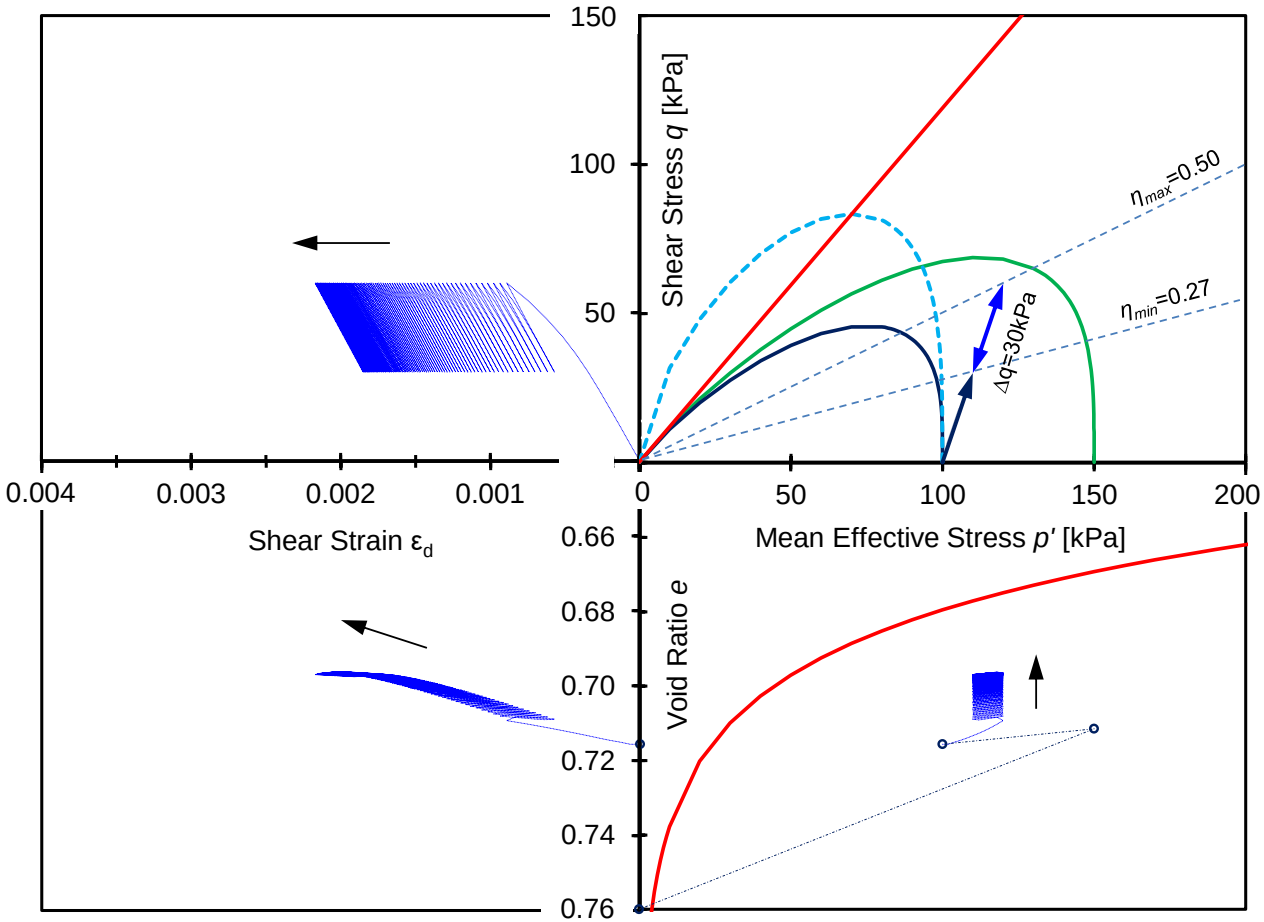

Figure C10. Load-deformation response of soil subjected to repetitive shear loading. Loading history: (1) preconsolidation at p_o'=150kPa, (2) hydrostatic unloading to 100kPa, (3) first shear loading to q=60kPa, and (4) initiation of repetitive loading with stress amplitude Δq=30kPa. Stress obliquity for repetitive loading η_{max}=0.50 and η_{min}=0.27. Notation: $p'=(\sigma_1'+\sigma_3')/2$, $q=(\sigma_1'-\sigma_3')/2$. Note: bounding surface (=green line), initial loading surface (=navy line), plastic potential (=blue dotted line), and critical state (=red line).

REFERENCES

Åberg, B. (1993). "Washout of grains from filtered sand and gravel materials." Journal of Geotechnical Engineering, 119(1), 36-53.

Achmus, M., Kuo, Y. S., and Abdel-Rahman, K. (2009). "Behavior of monopile foundations under cyclic lateral load. *Computer and Geotechnic*, 36(5), 725-735.

Albrecht, B. A. and Benson, C. H. (2001). "Effect of desiccation on compacted natural clays." *Journal of Geotechnical and Geoenvironmental Engineering*, 127(1), 67-75.

Alonso-Marroquin, F., and Herrmann, H. J. (2004). "Ratcheting of granular materials." *Physical Review Letters*, 92(5), 054301.

Alonso-Marroquín, F., García-Rojo, R. and Herrmann, H. J. (2004). "Micromechanical Investigation of granular ratcheting." *Proc., Int. Conf. Cyclic Behavior of Soils and Liquefaction Phenomena*, Bochum, Germany, 3-9.

Andersen, K. H. (2009). "Bearing capacity under cyclic loading-offshore, along the coast, and on land." *Canadian Geotechnical Journal*, 46(5), 513-535.

Association Suisse de Normalization (1959). *SNV 70 055*. Soil classification, Zurich.

ASTM (2011). "Standard practice for classification of soils for engineering purposes (unified soil classification system)." *ASTM D2487*, West Conshohocken, PA.

ASTM (2009). "Standard practice for classification of soils and soil-aggregate mixtures for highway construction purposes." *ASTM D3282*, West Conshohocken, PA.

ASTM (2016). "Standard test methods for maximum index density and unit weight of soils using a vibratory table." *ASTM D4253*, West Conshohocken, PA.

ASTM (2016). "Standard test methods for minimum index density and unit weight of soils and calculation of relative density." *ASTM D4254*, West Conshohocken, PA.

Bandini, P. and Sathiskumar, S. (2009). "Effects of silt content and void ratio on the saturated hydraulic conductivity and compressibility of sand-silt mixtures." *Journal of Geotechnical and Geoenvironmental Engineering*, 135(12), 1976-1980.

Bareither, C. A., Edil, T. B., Benson, C. H., and Mickelson, D. M. (2008). "Geological and physical factors affecting the friction angle of compacted sands." *Journal of Geotechnical and Geoenvironmental Engineering*, 134(10), 1476-1489.

Belkhatir, M., Schanz, T., and Arab, A. (2013). “Effect of fines content and void ratio on the saturated hydraulic conductivity and undrained shear strength of sand–silt mixtures.” *Environmental Earth Sciences*, 70(6), 2469-2479.

Bortkevich, S. V. (1982). “Density of placing sand-gravel and pebble soils in dams.” *Power Technology and Engineering*, (formerly Hydrotechnical Construction), 16(6), 324-328.

Brown, S. F. (1996). “Soil mechanics in pavement engineering.” *Géotechnique*, 46(3), 383-426.

Brown, K. M., Kopf, A., Underwood, M. B., and Weinberger, J. L. (2003). “Compositional and fluid pressure controls on the state of stress on the Nankai subduction thrust: A weak plate doundary.” *Earth and Planetary Science Letters*, 214(3), 589-603.

BSI (British Standards Institution). (1999). “Code of practice for site investigations.” *BS 5930*, London.

Burenkova, V. V. (1993). “Assessment of suffusion in non-cohesive and graded soils.” Filters in geotechnical and hydraulic engineering. Balkema, Rotterdam, 357-360.

Burland, J. B. (1990). “On the compressibility and shear strength of natural clays.” *Géotechnique*, 40(3), 329-378.

Carraro, J. A. H., Prezzi, M. and Salgado, R. (2009). “Shear strength and stiffness of sands containing plastic or nonplastic fines.” *Journal of Geotechnical and Geoenvironmental Engineering*, 135(9), 1167-1178.

Casagrande, A. (1936). “Characteristics of cohesionless soil affecting the stability of slopes and earth fills.” J. Boston Soc. Civ. Engng, 13–32.

Casagrande, A. (1948). “Classification and identification of soils.” *Transactions of the American Society of Civil Engineers*, 113(1), 901-930.

Castro G., Poulos, S. J., France, J. W. and Enos, J. L. (1982): “Liquefaction induced by cyclic loading.” NASA STI/Recon Technical Report N, 83.

Cha, M., Santamarina, J. C., Kim, H. S. and Cho, G. C. (2014). “Small-strain stiffness, shear-wave velocity, and soil compressibility.” *Journal of Geotechnical and Geoenvironmental Engineering*, 140(10), p.06014011.

Chai, J. C. and Miura, N. (2002). Traffic-load-induced permanent deformation of road on soft subsoil. *Journal of Geotechnical and Geoenvironmental Engineering* 128(11), 907-916.

Chamberlain, E. J., Iskandar, I. and Hunsicker, S. E. (1990). "Effect of freeze-thaw cycles on the permeability and macrostructure of soils." *Cold Region Research and Engineering Laboratory*, 90(1), 145-155.

Chang, W. J., Shou, S. H., and Huang, A. B. (2017). "Mechanism of subsidence from pore pressure fluctuation in aquifer layers." *Proc. 19th Int. Conf. Soil Mechanics and Geotechnical Engineering*, Seoul (Accepted).

Chapuis, R. P., Contant, A. and Baass, K. A. (1996). Migration of fines in 0-20 mm crushed base during placement, compaction, and seepage under laboratory conditions. Canadian Geotechnical Journal, 33(1), 168-176.

Cho, G. C., Dodds, J., and Santamarina, J. C. (2006). "Particle shape effects on packing density, stiffness, and strength: Natural and crushed sands." *Journal of Geotechnical and Geoenvironmental Engineering*, 132(5), 591-602.

Cho, G. C. and Santamarina, J. C. (2001). "Unsaturated particulate materials - particle-level studies." *Journal of Geotechnical and Geoenvironmental Engineering*, 127(1), 84-96.

Chong, S. H. and Santamarina, J. C. (2016). "Sands subjected to vertical repetitive loading under zero lateral strain: Accumulation models, terminal densities, and settlement." *Canadian Geotechnical Journal*, 53(22), 2039-2046.

Chong, S. H., and Santamarina, J. C. (2016). "Soil compressibility models for a wide stress range." *Journal of Geotechnical and Geoenvironmental Engineering*, 142(6), p.06016003.

Choo, H. (2013). "Engineering behavior and characterization of physical-chemical particulate mixture using geophysical measurement techniques." Ph.D. thesis, Georgia Institute of Technology, Atlanta, GA.

Choo, H. and Burns, S. E. (2015). "Shear wave velocity of granular mixtures of silica particles as a function of finer fraction, size ratios and void ratios." *Granular Matter*, 17(5), 567-578.

Chu, J., Leroueil, S. and Leong, W. K. (2003). "Unstable behaviour of sand and its

implication for slope instability." *Canadian Geotechnical Journal, 40*(5), 873-885.

Collins, I. F., Wang, A. P. and Saunders, L. R. (1993). "Shakedown theory and the design of unbound pavements." *Road and Transport Research*, 2(4), 28-39.

Coop, M. R., Sorensen, K. K. and Freitas, T. B. (2004). "Particle breakage during shearing of a carbonate sand." *Géotechnique*. 54 (3), 157–163.

Cordero, J. A., Useche, G., Prat, P. C., Ledesma, A., and Santamarina, J. C. (2017). "Soil desiccation cracks as a suction-contraction process." *Géotechnique Letter*, 7(3), 272-278.

Crawford, B. R., Faulkner, D. R., and Rutter, E. H. (2008). "Strength, porosity, and permeability development during hydrostatic and shear loading of synthetic quartz-clay fault gouge." *Journal of Geophysical Research: Solid Earth*, 113(B3).

da Fonseca, A.V., Rios, S., Amaral, M.F. and Panico, F. (2013). "Fatigue cyclic tests on artificially cemented soil." *Geotechnical Testing Journal*, 36(2), 227-235.

Dafalias, Y. F. and Popov, E. P. (1975). "A model of nonlinearly hardening materials for complex loadings." *Acta Mechanica*, 21, 173-192.

Dai, S., Wuttke, F., and Santamarina, J. C. (2013). "Coda wave analysis to monitor processes in soils." *Journal of Geotechnical and Geoenvironmental Engineering*, 139(9), 1504-1511.

D'Appolonia, D. J., and D'Appolonia, E. E. (1967). "Determination of the maximum density of cohesionless soils." *Proc. 3rd Asian Regional Conf. on Soil Mech. Found. Eng*., 1, 266–268.

Das, M. D. (2009). *Principles of geotechnical engineering*, Cengage Learning, Stamford, CT.

Deutche Norm DIN18196. (2011). *Erd-und grundbau—bodenklassifikationfür-bautechnischezwecke*, BeuthVerlag GmbH, Berlin.

Di Donna, A., and Laloui, L. (2015). "Response of soil subjected to thermal cyclic loading: Experimental and constitutive study." *Engineering Geology*, 190, 65-76.

Djordjevic, N. and Morrison, R. (2006). "Exploratory modelling of grinding pressure within a compressed particle bed." *Minerals Engineering*, 19(10), 995-1004.

Donohue, T. (2008). "Permeability and the structure of porosity in particulate materials." Ph.D. thesis, The University of Newcastle, Australia.

Dundulis, K., Gadeikis, S., Gadeikytė, S., Urbaitis, D., and Prunskienė, L. (2010). "Problems of usage of soil classification systems for sand soils of Lithuania." *The 10th International Conference*.

Evans, T. M., and Valdes, J. R. (2011). "The microstructure of particulate mixtures in one-dimensional compression: Numerical studies." *Granular Matter*, 13(5), 657-669.

Feda, J. (2002). "Notes on the effect of grain crushing on the granular soil behaviour." *Engineering Geology*, 63(1), 93-98.

Fourie, A. B., and Papageorgiou, G. (2001). "Defining an appropriate steady state line for Merriespruit gold tailings." *Canadian Geotechnical Journal*, 38(4), 695-706.

Fragaszy, R. J., Su, J., Siddiqi, F. H., and Ho, C. L. (1992). "Modeling strength of sandy gravel." *Journal of Geotechnical Engineering*, 118(6), 920-935.

Fraser, H. J. (1935). "Experimental study of the porosity and permeability of clastic sediments." *The Journal of Geology*, 910-1010.

Fuggle, A. R., Roozbahani, M. M. and Frost, J. D. (2014). "Size effects on the void ratio of loosely packed binary particle mixtures." In Geo-Congress 2014: Geo-characterization and Modeling for Sustainability. 129-138.

Fuller, W. B. (1907). "The law of proportioning concrete." Transactions, American Society of Civil Engineers, 59, 67-143.

GBT50145. (2007). *Standard for engineering classification of soil*, China Planning Press, Beijing.

Giannakos, K. (2010). "Loads on track, ballast fouling, and life cycle under dynamic loading in railways." *Journal of Transportation Engineering*. 136(12), 1075–1084.

GTR Classification. (1992). "Technical guidelines on embankment and capping layers construction." LCPC, France.

Guimaraes, M. S., J. R. Valdes, Palomino, A. M., and Santamarina, J. C. (2007). "Aggregate production: Fines generation during rock crushing." *International Journal of Mineral Processing*, 81(4), 237–247.

Gutierrez, M. (2005). "Mixture theory characterization and modeling of soil mixtures." First Japan-U.S. workshop on testing, modeling, and simulation, Boston,

Massachusetts, United States, edited by Jerry A. Yamamuro, P. E. and Junichi Koseki, 600-616.

Guyon, E., Oger, L., and Plona, T. J. (1987). "Transport properties in sintered porous media composed of two particle sizes." *Journal of Physics D: Applied Physics*, 20(12), 1637-1644.

Han, D. H., Nur, A., and Morgan, D. (1986). "Effects of porosity and clay content on wave velocities in sandstones." *Geophysics*, 51(11), 2093-2107.

Holtz, W. G., and Gibbs, H. J. (1956). "Triaxial shear tests on pervious gravelly soils." *Journal of the Soil Mechanics and Foundations Division, 82*(1), 1-22.

Howard, A. K. (1984). "The revised ASTM standard on the unified classification system." *Geotechnical Testing Journal*, 7(4), 216–222.

Hu, C., Liu, H. and Huang, W. (2012). "Anisotropic bounding-surface plasticity model for the cyclic shakedown and degradation of saturated clay." *Computers and Geotechnics*, 44, 34-47.

Huang, A. W. (2016). The seventh James. K. Mitchell lecture: Characterization of silty/sand soils. *Australian Geomechanics Journal*, 51(4), 1-23.

Huang, Y. T., Huang, A. B., Kuo, Y. C. and Tsai, M. D. (2004). "A laboratory study on the undrained strength of a silty sand from Central Western Taiwan." *Soil Dynamics and Earthquake Engineering*, 24(9), 733-743.

Indraratna, B., Ionescu, D., Christie, H. D. and Choudhury, R. N. (1997). "Compression and degradation of railway ballast under one-dimensional loading." *Australian Geomechanics Journal,* 32(4), 48-61.

Indraratna, B., Khabbaz, H. and Lackenby, J. (2003). "Behaviour of railway ballast under dynamic loads based on large-scale triaxial testing." In AusRAIL PLUS 2003, 17-19 November 2003, Sydney, NSW, Australia.

Indraratna, B., Khabbaz, H., Salim, W., and Christie, D. (2006). "Geotechnical properties of ballast and the role of geosynthetics in rail track stabilization." *Ground Improvement,* 10(3), 91–101.

Indraratna, B. and Nimbalkar, S. (2013). "Stress-strain degradation response of railway ballast stabilized with geosynthetics." *Journal of Geotechnical and Geoenvironmental Engineering*, 139(5), 684-700.

Indraratna, B., Salim, W. and Rujikiatkamjorn, C. (2011). *Advanced rail geotechnology: Ballasted track*. Boca Raton, FL, USA: CRC Press.

Indraratna B, Tennakoon N, Nimbalkar S, Rujikiatkamjorn C. (2013). "Behaviour of clay fouled ballast under drained triaxial testing." *Géotechnique,* 63(5), 410–419.

Indrawan, I. G. B., Rahardjo, H., and Leong, E. C. (2006). "Effects of coarse-grained materials on properties of residual soil." *Eng. Geol*., 82(3), 154-164.

Ishihara, K. (1996). *Soil behaviour in earthquake geotechnics*, Clarendon Press; Oxford University Press, Oxford, New York.

Istomina, V. S. (1957). "Seepage stability of the soil." Translated from Russian, Moscow.

Jang, J., and Santamarina, J. C. (2016). "Fines classification based on sensitivity to pore-fluid chemistry." *Journal of Geotechnical and Geoenvironmental Engineering*, *142*(4), p.06015018.

Jardine, R. J. (1992). "Some observations on the kinematic nature of soil stiffness." *Soils and Foundation*, 32(2), 111-124.

JGS0051. (2009). "Method of classification of geomaterials for engineering purposes." Japanese Geotechnical Society, Tokyo.

Kamann, P. J., Ritzi, R. W., Dominic, D. F., and Conrad, C. M. (2007). "Porosity and permeability in sediment mixtures." *Groundwater*, 45(4), 429-438.

Kang, M., and Lee, J. S. (2015). "Evaluation of the freezing–thawing effect in sand–silt mixtures using elastic waves and electrical resistivity." C*old Regions Science and Technology*, 113, 1-11.

Kelly, R. B., Houlsby, G. T., and Byrne, B. W. (2006). "A comparison of field and laboratory tests of caisson foundations in sand and clay." *Géotechnique* 56 No. 9, 617-626.

Kenney, T. C. (1967). "The influence of mineral composition on the residual strength of natural soils." *Proc. Geotech. Conf*., Shear strength properties of natural soils and rocks, Oslo, 1, 123-129

Kenney, T. C. (1977). "Residual strengths of mineral mixtures." University of Toronto, Department of Civil Engineering. *Proc. 9th Int. Conf. Soil Mech*., Tokyo 1, 155-160.

Kenney, T. C., Lau, D., and Clute, G. (1984). ‘‘Filter tests on 235mm diameter specimens of granular materials.’’ Tech. Rep. 84-07, Dept. of Civ. Eng., University of Toronto, Toronto.

Kenney, T. C., and Lau, D. (1985). “Internal stability of granular filters.” *Canadian Geotechnical Journal,* 22(2), 215-225.

Kim, H. K., Cortes, D. D., and Santamarina, J. C. (2007). “Flow test: Particle-level and macroscale analyses.” *ACI Material Journal,* 104(3), 323-327.

Knoll, M. D., and Knight, R. (1994). “Relationships between dielectric and hydrogeologic properties of sand-clay mixtures.” *In 5th Int. Conf. Ground Penetrating Radar*.

Kolisoja, P. (1998). “Large scale dynamic triaxial tests III.” Tampere University of Technology.

Koltermann, C. E., and Gorelick, S. M. (1995). “Fractional packing model for hydraulic conductivity derived from sediment mixtures.” *Water Resources Research,* 31(12), 3283-3297.

Konishi, Y., Hyodo, M., and Ito, S. (2007). “Compression and undrained shear characteristics of sand-fines mixtures with various plasticity.” JSCE *Journal of Geotechnical and Geoenvironmental Engineering,* 63(4), 1142-1152 (in Japanese).

Kovačević, M. S., and Jurić-Kaćunić, D. (2014). “European soil classification system for engineering purposes.” *Građevinar*, 66(09), 801-810.

Krieg, R. D. (1975). “A practical two-surface plasticity theory.” *Journal of Applied Mechanics,* 42, 641-646.

Krumbein, W. C., and Sloss, L. L. (1963). *Stratigraphy and sedimentation,* 2nd Ed., Freeman and Company, San Francisco.

Kumar, G. V., and Wood, D. M. (1999). “Fall cone and compression tests on clay-gravel mixtures.” *Géotechnique,* 49(6), 727-739.

Kumara, J., Hayano, K., Shigekuni, Y., and Sasaki, K. (2013). “Physical and mechanical properties of sand-gravel mixtures evaluated from DEM simulation and laboratory triaxial test.” *International Journal of GEOMATE,* 4(2), 546-551.

Kurata, S., and Fujishita, T. (1961). “Research on the engineering properties of sand-clay mixtures.” *Report of the Port Harbour Research Institute,* 11(9), 389-424.

Lade, P. V. and Yamamuro, J. A. (1996). “Undrained sand behavior in axisymmetric tests at high pressures.” *Journal of Geotechnical Engineering*, 122(2), 120-129.

Lade, P. V., and Yamamuro, J. A. (1997). “Effects of nonplastic fines on static liquefaction of sands.” *Canadian Geotechnical Journal*, 34(6), 918-928.

Lafleur, J., Mlynarek, J., and Rollin, A. L. (1989). “Filtration of broadly graded cohesionless soils.” Journal of Geotechnical Engineering, ASCE, 115(12), 1747-1769.

Lee, H., and Koo, S. (2014). “Liquid permeability of packed bed with binary mixture of particles.” *Journal of Industrial and Engineering Chemistry*, 20(4), 1397-1401.

Lee, J., Lee, D., and Park, D. (2014). “Experimental investigation on the coefficient of lateral earth pressure at rest of silty sands: effect of fines. *Geotechnical Testing Journal*, 37(6), 967-979.

Lee, J. S., Dodds, J., and Santamarina, J. C. (2007b). “Behavior of rigid-soft particle mixtures.” *Journal of materials in civil engineering*, 19(2), 179-184.

Lee, J. S., Guimaraes, M., and Santamarina, J. C. (2007a). “Micaceous sands: Microscale mechanisms and macroscale response.” *Journal of Geotechnical and Geoenvironmental Engineering*, 133(9), 1136-1143.

Lee, J. S., and Santamarina, J. C. (2005). “Bender elements: performance and signal interpretation.” *Journal of Geotechnical and Geoenvironmental Engineering* 131(9), 1063-1070.

Lee, K. L. and Farhoomand, I. (1967). “Compressibility and crushing of granular soil in anisotropic triaxial compression.” *Canadian Geotechnical Journal*, 4(1), 68-86.

Leroueil, S., Chu, J. and Wanatowski, D. (2009). “Slope instability due to pore water pressure increase.” *Proc., 1st Italian Workshop on Landslides*, Naples, 8-10.

Li, M. (2008). “Seepage induced instability in widely graded soils.” Ph.D thesis, The University of British Columbia, Canada.

Li, W., Igoe, D., and Gavin, K. (2015). “Field tests to investigate the cyclic response of monopiles in sand.” *Proc. Institution of Civil Engineers-Geotechnical Eng*. 168(5), 407-421.

Li, Y. (2009). “Experimental study of shear behavior of soils with abundant coarse particles associated with slip zones of large landslides in the three gorges reservoir.” Ph.D. thesis, The University of Hong Kong.

Locat, J., and Demers, D. (1988). “Viscosity, yield stress, remolded strength, and liquidity index relationships for sensitive clays.” *Canadian Geotechnical Journal, 25*(4), 799-806.

Long, J. H., and Vanneste, G. (1994). “Effects of cyclic lateral loads on piles in sand.” *Journal of Geotechnical Engineering*, 120(1), 225-244.

Lupini, J. F., Skinner, A. E., and Vaughan, P. R. (1981). “The drained residual strength of cohesive soils.” *Géotechnique*, 31(2), 181-213.

Maio, C. D, and Fenellif, G. B. (1994). “Residual strength of kaolin and bentonite: The influence of their constituent pore fluid.” *Géotechnique*, 44(2), 217-226.

Marion, D., Nur, A., Yin, H., and Han, D. H. (1992). “Compressional velocity and porosity in sand-clay mixtures.” *Geophysics*, 57(4), 554-563.

Manzari, M. T. and Dafalias, Y. F. (1997). “A critical state two-surface plasticity model for sands.” *Géotechnique*, 47(2), 255-272.

Mason, T. (1997) “Hydrodynamics and sediment transport on a macro-tidal, mixed (sand and shingle) beach.” Ph.D. thesis, University of Southampton.

Mayne, P. W., and Kulhawy, F. H. (1982). “K_0-OCR relationships in soil.” *Journal of the Soil Mechanics and Foundations Division*, 108(6), 851-872.

McDowell, G. R. (1999). “Micromechanics of clastic soil.” Proceedings of the International Workshop on Soil Crushability. Ube, Yamaguchi, Japan, 138–157.

McGeary, R. K. (1961). “Mechanical packing of spherical particles.” *Journal of the American ceramic Society*, 44(10), 513-522.

Mesri, G. and Vardhanabhuti, B. (2009). “Compression of granular materials.” *Canadian Geotechnical Journal*, 46(4), 369-392.

Michalowski, R. L. (2005). “Coefficient of earth pressure at rest.” *Journal of Geotechnical and Geoenvironmental Engineering*, 131(11), 1429-1433.

Miller, E. A., and Sowers, G. F. (1958). “The strength characteristics of soil-aggregate mixture and discussion.” *Highway Research Board Bulletin*, No.183, 16-32.

Mitchell, J. K. and Soga, K. (2005). *Fundamentals of Soil Behavior*, Wiley, Hoboken, NJ.

Moffat, R., Fannin, R. J. and Garner, S. J. (2011). "Spatial and temporal progression of internal erosion in cohesionless soil." *Canadian Geotechnical Journal*, 48(3), 399-412.

Mohamad, R. and Dobry, R. (1986). "Undrained monotonic and cyclic triaxial strength of sand," *Journal of Geotechnical Engineering*, ASCE, 112(10), 941-958.

Mollins, L. H., Stewart, D. I., and Cousens, T. W. (1996). "Predicting the properties of bentonite-sand mixtures." *Clay Minerals*, 31(2), 243-252.

Monismith, C. L. (2004). "Evolution of long-lasting asphalt pavement design methodology: a perspective." International Symposium of Design and Construction of Long Lasting Asphalt Pavements, Auburn University.

Monkul, M. M., and Ozden, G. (2007). "Compressional behavior of clayey sand and transition fines content." *Engineering Geology*, 89(3), 195-205.

Mueth, D. M., Debregeas, G. F., Karczmart, G. S., Eng, P. J., Nagel, S. R., and Jaeger, H. M. (2000). "Signatures of granular microstructure in dense shear flows." *Nature*, 406(6794), 385-389.

Musso, G., Morales, E. R., Gens, A., and Castellanos, E. (2003). "The role of structure in the chemically induced deformations of FEBEX bentonite." *Applied Clay Science*, 23(1), 229-237.

Nakata, Y., Kajiwara, T., and Yoshimoto, N. (2013). "Collapse behavior of slope due to change in pore water pressure." *Proc., 18th Int. Conf. Soil Mechanics and Geotechnical Engineering*, Paris, 2225-2228.

Narsilio, A. and Santamarina, J. C. (2008). "Terminal densities." *Géotechnique* 58(8), 669-674.

Ni, Q., Tan, T. S., Dasari, G. R., and Hight, D. W. (2004). "Contribution of fines to the compressive strength of mixed soils." *Géotechnique*, 54(9), 561-569.

Oda, M., and Kazama, H. (1998). "Microstructure of shear bands and its relation to the mechanics of dilatancy and failure of dense granular soils." *Géotechnique*, 58(4), 465–481.

Olson, S. M., Stark, T. D., Walton, W. H. and Castro, G. (2000). "1907 static liquefaction flow failure of the north dike of Wachusett dam." *Journal of Geotechnical and Geoenvironmental Engineering*, 126(12), 1184-1193.

Omidvar, M., Iskander, M. and Bless, S. (2012). "Stress-strain behavior of sand at high strain rates." *International Journal of Impact Engineering*, 49, 192-213.

Orense, R., Farooq, K. and Towhata, I. (2004). "Deformation behavior of sandy slopes during rainwater infiltration." *Soils and Foundation*, *44*(2), 15-30.

Page, D., Dillon, P., Vanderzalm, J., Toze, S., Sidhu, J., Barry, K., Levett, K., Kremer, S. and Regel, R. (2010). "Risk assessment of aquifer storage transfer and recovery with urban stormwater for producing water of a potable quality." *Journal of Environmental Quality*, 39(6), 2029-2039.

Palomino, A. M., and Santamarina, J. C. (2005). "Fabric map for kaolinite: effects of pH and ionic concentration on behavior." *Clays and Clay Minerals*, 53(3), 211-223.

Pandian, N. S., Nagaraj, T. S., and Raju, P. N. (1995). "Permeability and compressibility behavior of bentonite-sand/soil mixes." *Geotechnical Testing Journal*, 18(1), 86-93.

Papadopoulos, E., Cortes, D., and Santamarina, J. C. (2016). "In-situ assessment of the stress-dependent stiffness of unbound aggregate bases: application in inverted base pavements." *International Journal of Pavement Engineering*, 17(10), 870-877.

Park, J. and J. C. Santamarina (2017a). "Long-term response of sands subjected to repetitive mechanical loads: Evolution of void ratio and small strain stiffness." *Géotechnique* (under review).

Park, J. and Santamarina, J. C. (2017b). "Revised soil classification system for coarse-fine mixtures." *Journal of Geotechnical and Geoenvironmental Engineering*, 143(8), p.04017039.

Pasten, C., and Santamarina, J. C. (2011). "Energy geo-storage—analysis and geomechanical implications." *KSCE Journal of Civil Engineering*, 15(4), 655-667.

Pasten, C., and Santamarina, J. C. (2014). “Thermally induced long-term displacement of thermoactive piles.” *Journal of Geotechnical and Geoenvironmental Engineering*, 140(5), p.06014003.

Pasten, C., Shin, H., and Santamarina, J. C. (2014). “Long-term foundation response to repetitive loading.” *Journal of Geotechnical and Geoenvironmental Engineering*, 140(4), p.04013036.

Paute, J-L., Hornych, P., and Beraben, J.-P. (1993). “Repeated load triaxial testing of granular materials on the French network of Laboratoires des Ponts et ChausseÂes.” *Flexible Roads*, Balkema, 53-64.

Payan, M., Senetakis, K., Khoshghalb, A., and Khalili, N. (2017). “Effect of gradation and particle shape on small-strain Young’s modulus and Poisson’s ratio of sands.” *International Journal of Geomechanics*, 17(5), p.04016120.

Peng, J., Clarke, B. G., and Rouainia, M. (2006). “A device to cyclic lateral loaded model piles.” *Geotechnical Testing Journal*, 29(4), 341-347.

Pennekamp, J. G. S., Talmon, A. M., and van Kesteren, W. G. M. (2010). “Determination of non-segregating tailings conditions.” *Proc., Wodcon XIX*, 9-14.

Prager, W. (1949). “Recent developments in the mathematical theory of plasticity.” *Journal of Applied Physics*, 20(3), 235-241.

Qi, J., Ma, W., and Song, C. (2008). “Influence of freeze–thaw on engineering properties of a silty soil.” C*old Regions Science and Technology*, 53(3), 397-404.

Radjai, F., Wolf, D. E., Jean, M., and Moreau, J. J. (1998). “Bimodal character of stress transmission in granular packing.” *Physical Review Letters*, 80, 61-64.

Rahardjo, H., Indrawan, I. G. B., Leong, E. C., and Yong, W. K. (2008). “Effects of coarse-grained material on hydraulic properties and shear strength of top soil.” *Engineering Geology*, 101(3), 165-173.

Rahimi, M., Chan, D., and Nouri, A. (2017). “Constitutive model for cyclic behaviour of cohesionless sands.” *Geomechanics and Geoengineering*, 12(1), 36-47.

Rahman, M. M., Lo, S. R. and Gnanendran, C. T. (2008). “On equivalent granular void ratio and steady state behaviour of loose sand with fines.” *Canadian Geotechnical Journal*, *45*(10), 1439-1456.

Rathee, R. K. (1981). “Shear strength of granular soils and its prediction by modeling techniques.” *Journal of the Institution of Engineers* (India), 64-70.

Roesler, S. K. (1979). “Anisotropic shear modulus due to stress anisotropy.” *Journal of the Geotechnical Engineering Division*, 105(7), 871-880.

Roshankhah, S. (2015). “Physical properties of geomaterials with relevance to thermal energy geo-systems” Ph.D. thesis, Georgia Institute of Technology, Atlanta, GA.

Sadrekarimi, A. and Olson, S. M. (2010). “Particle damage observed in ring shear tests on sands.” *Canadian Geotechnical Journal*, 47(5), 497-515.

Salgado, R., Bandini, P., and Karim, A. (2000). “Shear strength and stiffness of silty sand.” *Journal of Geotechnical and Geoenvironmental Engineering*, 126(5), 451-462.

Santamarina, J. C., and Cho, G. C. (2001). “Determination of critical state parameters in sandy soils-simple procedure.” *Geotechnical Testing Journal*, 24(2), 185–192.

Santamarina, J. C., and Cho, G. C. (2004). “Soil behaviour: The role of particle shape.” *Advances in geotechnical engineering: The Skempton Conference*, R. J. Jardine, D. M. Potts, and K. G. Higgins, eds., Vol. 1, Thomas Telford, London, 604–617.

Santamarina, J. C., and Fratta, D. (2005). *Discrete signals and inverse problems: an introduction for engineers and scientists*. John Wiley & Sons.

Santamarina, J. C., Klein, K. A., and Fam, M. A. (2001). *Soils and waves: Particulate materials behavior, characterization and process monitoring*, Wiley, Chichester, U.K.

Santamarina, J. C., and Shin, H. (2009). “Friction in granular media.” *Meso-scale Shear Physics in Earthquake and Landslide Mechanics*. CRC Press, London, 157-188.

Sawicki, A., and Swidzinski, W. (1995). “Cyclic compaction of soils, grains and powders.” *Powder Technology*. 85(2), 97-104.

Schofield, A. N. (1980). “Cambridge geotechnical centrifuge operations.” *Géotechnique*, 30(3), 227-268.

Schofield, A. N. and Wroth, P. (1968). *Critical state soil mechanics*. London, McGraw-Hill.

Shafiee, A. (2008). “Permeability of compacted granule–clay mixtures.” *Engineering Geology*, 97(3), 199-208.

Sharp, R. W., and Booker, J. R. (1984). “Shakedown of pavements under moving surface loads.” *Journal of Transportation Engineering*, 110(1), 1-14.

Shelley, T. L., and Daniel, D. E. (1993). “Effect of gravel on hydraulic conductivity of compacted soil liners.” *Journal of Geotechnical Engineering*, 119(1), 54-68.

Shire, T., O’Sullivan, C., Hanley, K. J., and Fannin, R. J. (2014). “Fabric and effective stress distribution in internally unstable soils.” *Journal of Geotechnical and Geoenvironmental Engineering*, 140(12), p.04014072.

Silver, M. L., and Seed, H. B. (1971). “Volume changes in sands during cyclic loading.” *Journal of Soil Mechanics and Foundations Div*. 97(9), 1171-1182.

Simoni, A., and Houlsby, G. T. (2006). “The direct shear strength and dilatancy of sand–gravel mixtures.” *Geotechnical and Geological Engineering*, 24(3), 523-549.

Simpson, D. C., and Evans, T. M. (2015). “Behavioral thresholds in mixtures of sand and kaolinite clay.” *Journal of Geotechnical and Geoenvironmental Engineering*, 142(2), p.04015073.

Sivapullaiah, P. V., Sridharan, A., and Stalin, V. K. (2000). “Hydraulic conductivity of bentonite-sand mixtures.” *Canadian Geotechnical Journal*, 37(2), 406-413.

Skempton, A. W. (1985). “Residual strength of clays in landslides, folded strata and the laboratory.” *Géotechnique*, 35(1), 3-18.

Skempton, A. W., and Brogan, J. M. (1994). “Experiments on piping in sandy gravels.” *Géotechnique*, 44(3), 449-460.

Snieder, R. (2006). “The theory of coda wave interferometry.” *Pure and Applied geophysics*, 163(2-3), 455-473.

Skempton, A. W., and Jones, O. T. (1944). “Notes on the Compressibility of Clays.” *Journal of the Geological Society*, 100(1-4), 119-135.

Skempton, A. W. and Brogan, J. M. (1994). “Experiments on piping in sandy gravels.” *Geotechnique*, 44(3), 449-460.

Sridharan, A., and Nagaraj, H. B. (2000). “Compressibility behaviour of remoulded, fine-grained soils and correlation with index properties”. *Canadian Geotechnical Journal*, 37(3), 712-722.

Steiakakis, E., Gamvroudis, C., Komodromos, A., and Repouskou, E. (2012). “Hydraulic conductivity of compacted kaolin–sand specimens under high hydraulic gradients.” *Electronic Journal of Geotechnical Engineering*, 17.

Stokoe, K. H., Darendeli, M. B., Andrus, R. D., and Brown, L. T. (1999). “Dynamic soil properties: laboratory, field and correlation studies.” *Proc. 2nd International Conf. on Earthquake Geotech. Eng., Lisbon, Balkemia, Rotterdam* 3, 811-846.

Sun, B. C. (1989). “Internal Stability of Clayey to Silty Sands.” Ph.D. thesis, University of Michigan, Ann Arbor, USA.

Takahashi, M., Mizoguchi, K., Kitamura, K., and Masuda, K. (2007). “Effects of clay content on the frictional strength and fluid transport property of faults.” *Journal of Geophysical Research: Solid Earth*, 112(B8).

Tanaka, T., and Toida, M. (2008). “Characteristics and method of estimating permeability of bentonite-sand-gravel mixture.” *Doboku Gakkai Ronbunshuu C (Online),* 64(1), 101-110.

Taylor, D. W. (1948). *Fundamentals of soil mechanics*. New York: Wiley.

Tembe, S., Lockner, D. A., and Wong, T. F. (2010). “Effect of clay content and mineralogy on frictional sliding behavior of simulated gouges: Binary and ternary mixtures of quartz, illite, and montmorillonite.” *Journal of Geophysical Research: Solid Earth*, 115(B3).

Thevanayagam, S. (1998). “Effect of fines and confining stress on undrained shear strength of silty sands.” *Journal of Geotechnical and Geoenvironmental Engineering*, 124(6), 479-491.

Thevanayagam, S. (2007) “Intergrain contact density indices for granular mixes – I: Framework.” *Earthquake engineering and engineering vibration*, 6(2), 123–134.

Thevanayagam, S., Shenthan, T., Mohan, S., and Liang, J. (2002). “Undrained fragility of clean sands, silty sands, and sandy silts.” *Journal of Geotechnical and Geoenvironmental Engineering*, 128(10), 849-859.

Tiwari, B., and Ajmera, B. (2011). “Consolidation and swelling behavior of major clay minerals and their mixtures.” *Applied Clay Science*, 54(3), 264-273.

Tiwari, B., and Marui, H. (2005). “A new method for the correlation of residual shear strength of the soil with mineralogical composition.” *Journal of Geotechnical and Geoenvironmental Engineering*, 131(9), 1139-1150.

Truong, Q. H., Eom, Y. H., Byun, Y. H. and Lee, J. S. (2010). “Characteristics of elastic waves according to cementation of dissolved salt.” *Vadose Zone Journal*, 9(3), 662-669.

Tsuha, C. D. H. C., Foray, P. Y., Jardine, R. J., Yang, Z. X., Silva, M. and Rimoy, S. (2012). “Behaviour of displacement piles in sand under cyclic axial loading.” *Soils and Foundations*, 52(3), 393-410.

Ueda, T., Matsushima, T. and Yamada, Y. (2011). “Effect of particle size ratio and volume fraction on shear strength of binary granular mixture.” *Granular Matter*, 13(6), 731-742.

Uygar, E. and Doven, A. G. (2006). “Monotonic and cyclic oedometer tests on sand at high stress levels.” *Granular Matter*, 8(1), 19-26.

Valdes, J. R. (2002). “Fines migration and formation damage.” Ph.D. thesis, Georgia Institute of Technology, Atlanta, GA.

Valdes, J. R., and Santamarina, J. C. (2006). “Particle clogging in radial flow: Microscale mechanisms.” *SPE Journal*, 11(02), 193-198.

Valdes, J. R., and Santamarina, J. C. (2008). “Clogging: Bridge formation and vibration-based destabilization.” *Canadian Geotechnical Journal*, 45(2), 177-184.

Vallejo, L. E. (2001). “Interpretation of the limits in shear strength in binary granular mixtures.” *Canadian Geotechnical Journal*, 38(5), 1097-1104.

Vallejo, L. E., and Lobo-Guerrero, S. (2005). “The elastic moduli of clays with dispersed oversized particles.” *Engineering geology*, 78(1), 163-171.

Vallejo, L. E., and Mawby, R. (2000). “Porosity influence on the shear strength of granular material–clay mixtures.” *Engineering Geology*, 58(2), 125-136.

Vasil'eva, A. A., Mikheev, V. V., and Lobanova, G. L. (1971). “How the strength properties of gravel soils depend on the type and state of the sand filling the pores.” *Soil Mechanics and Foundation Engineering*, 8(3), 167-171.

Viklander, P. (1998). “Permeability and volume changes in till due to cyclic freeze/thaw.” *Canadian Geotechnical Journal*. 35(3), 471-477.

Vucetic, M., and Dobry, R. (1991). Effect of soil plasticity on cyclic response. *Journal of Geotechnical Engineering*, 117(1), 89-107.

Vucetic, M. (1994). "Cyclic threshold shear strains in soils." *Journal of Geotechnical Engineering*, 120(12), 2208-2228.

Vukovic, M. and Soro, A. (1992). "Determination of hydraulic conductivity of porous media from grain-size composition." *Water Resour. Publications*, Littleton, Colorado.

Wagg, T. B., and Konrad, J. M. (1990). "Index properties of clay–silt mixtures." *43rd Canadian Geotechnical Conference*, Québec City, Canada, (2), 705–710.

Waite, W. F., Santamarina, J. C., Cortes, D. D., Dugan, B., Espinoza, D. N., Germaine, J., Jang, J., Jung, J. W., Kneafsey, T. J., Shin, H. and Soga, K. (2009). "Physical properties of hydrate-bearing sediments." *Reviews of geophysics*, 47(4). *RG4003.*

Wan, C. F. and Fell, R. (2004). "Experimental investigation of internal instability of soils in embankment dams and their foundations." University of New South Wales, School of Civil and Environmental Engineering.

Wang, J. (2005). "The stress-strain and strength characteristics of Portaway sand." Ph.D. thesis, University of Nottingham, Nottingham, UK.

Watabe, Y., Yamada, K., and Saitoh, K. (2011). "Hydraulic conductivity and compressibility of cixtures of nagoya clay with sand or bentonite." *Géotechnique*, 61(3), 211-219.

Werkmeister, S. (2003). "Permanent deformation behaviour of unbound granular materials in pavement constructions." Ph.D. thesis, Technischen Universita¨t, Dresden, Germany.

Werkmeister, S., Dawson, A.R. and Wellner, F. (2005). "Permanent deformation behaviour of granular materials." *Road materials and pavement design*, 6(1), 31-51.

Wichtmann, T. (2005). "Explicit accumulation model for non-cohesive soils under cyclic loading." Ph.D. thesis, Ruhr Univ. Bochum, Bochum, Germany.

Wichtmann, T., Niemunis, A. and Triantafyllidis, T. (2004). "Strain accumulation in sand due to drained uniaxial cyclic loading." *Proc., Int. Conf. Cyclic Behaviour of Soils and Liquefaction Phenomena*, Bochum, Germany, 233-246.

Wichtmann, T., Niemunis, A. and Triantafyllidis, T. (2005). “Strain accumulation in sand due to cyclic loading: Drained triaxial tests.” *Soil Dynamics and Earthquake Engineering*, 25(12), 967-979.

Wichtmann, T., Rondón, H. A., Niemunis, A., Triantafyllidis, T., and Lizcano, A. (2010). Prediction of permanent deformations in pavements using a high-cycle accumulation model. *Journal of Geotechnical and Geoenvironmental Engineering*, 136(5), 728-740.

Wichtmann, T., and Triantafyllidis, T. (2004). “Influence of a cyclic and dynamic loading history on dynamic properties of dry sand, part II: cyclic axial preloading.” *Soil Dynamics and Earthquake Engineering*, 24(11), 789-803.

Yamamuro, J. A., and Covert, K. M. (2001). “Monotonic and cyclic liquefaction of very loose sands with high silt content.” *Journal of Geotechnical and Geoenvironmental Engineering*, 127(4), 314-324.

Yang, S. (2004). “Characterization of the properties of sand–silt mixtures.” Ph.D. thesis, Norwegian University of Science and Technology, Trondheim, Norway.

Yang, S. L., Lacasse, S., and Sandven, R. F. (2006). “Determination of the transitional fines content of mixtures of sand and non-plastic fines.” *Geotechnical Testing Journal*, 29(2), 102-107.

Youd, T. L. (1970). “Densification and shear of sand during vibration.” *Journal of the Soil Mechanics and Foundations Division*, 96(3), 863-880.

Youd, T. L. (1973). “Factors controlling maximum and minimum densities of sands.” *ASTM Special Technical Publication*, 523, 98–112.

Yu, H. S. (2007). *Plasticity and geotechnics*. Springer, New York

Yu, H. S., Khong, C., and Wang, J. (2007). “A unified plasticity model for cyclic behaviour of clay and sand.” *Mechanics Research Communications*, 34(2), 97-114.

Yu, P. and Richart Jr, F. E. (1984). “Stress ratio effects on shear modulus of dry sands.” *Journal of Geotechnical Engineering*, 110(3), 331-345.

Zhang, Z. F., and Ward, A. L. (2011). “Determining the porosity and saturated hydraulic conductivity of binary mixtures.” *Vadose Zone Journal*, 10(1), 313-321.

Zlatović, S., and Ishihara, K. (1995). “On the influence of nonplastic fines on residual strength.” *Proc., 1st Int. Conf. on Earthquake Geotechnical Engineering*, IS-Tokyo, 95, 239-244.

Zuo, L., and Baudet, B. A. (2015). “Determination of the transitional fines content of sand-non plastic fines mixtures.” *Soils and Foundations*, 55(1), 213-219.